

DISS. ETH NO. 29031

Electronic and magnetic properties of solvated electron precursor systems

A thesis submitted to attain the degree of
DOCTOR OF SCIENCES of ETH ZÜRICH
(Dr. sc. ETH Zürich)

presented by

Jonathan Vinzent Barnes

M. Sc. Universität Leipzig
born on 31.08.1991
citizen of Germany

accepted on the recommendation of

Prof. Dr. Ruth Signorell, examiner
Prof. Dr. Gunnar Jeschke, co-examiner

2023

Abstract

The understanding of the solvation of electrons and their degree of delocalisation in that state have been of fundamental interest ever since first discovered in alkali metal ammonia solutions. Neutral, alkali metal-doped clusters serve as ideal model systems to study solvated electrons in their size-dependent properties. The presented work focuses on the characterisation of electronic properties via angle-resolved photoelectron spectroscopy and of their magnetic properties by Stern-Gerlach deflection. The combination of both experimental techniques reveals information on the solvated electron binding energy, electron orbital and spin angular momenta as well as the cluster rotational angular momentum.

We report measurements of electron binding energies and photoelectron anisotropies in angle-dependent photoelectron spectra of lithium-doped dimethyl ether clusters as a function of cluster size distribution. Neutral singly doped lithium clusters are studied in the range from bare lithium atom to an average cluster size of 63 dimethyl ether molecules. We explain trends in electron binding energies and photoemission anisotropies on the bases of density functional calculations of $\text{Li}(\text{CH}_3\text{OCH}_3)_n$ clusters. The results of lithium-doped clusters are compared to a previous study [1, 2] performed in our group on $\text{Na}(\text{CH}_3\text{OCH}_3)_n$ clusters. The comparison reveals similar trends of electron binding energies and photoemission anisotropies with increasing cluster size. Yet, structural and electronic differences arise from the alkali metal substitution. In highly symmetric clusters, the highest occupied molecular orbital can delocalize over an extended region and form a symmetric charge distribution of mainly *s*-character, resulting in a pronounced photoemission anisotropy. The photoelectron angular distributions of $\text{Li}(\text{CH}_3\text{OCH}_3)_n$ reveal pronounced *s*-character at $n = 4, 5$ and 6 . These cluster sizes are referred to as magic clusters for the photoelectron anisotropy.

Photoelectron studies of cluster size distributions are limited in their details of cluster size-resolved photoelectron contributions. Size-resolved measurements of electron binding energies and photoemission anisotropies of neutral $\text{Na}(\text{NH}_3)_n$ clusters are achieved with photoelectron-photoion-coincidence-spectroscopy, for photon energies in the range of $5.5\text{eV} - 9.9\text{eV}$. Photoelectron kinetic energy spectra in combination with *ab initio* calculations show three distinct ionisation pathways of the single solvated electron, each of the pathways is dominant in a certain photon energy range. One of the ionisation pathways occurs via an autoionisation process after resonant excitation of the neutral

state. The excitation process is proposed to be characterised by an electron transfer of an NH_3 molecule lone pair to the singly occupied molecular orbital. This excited state is characterised by a doubly occupied orbital, the so called solvated dielectron. The excited, solvated dielectron subsequently decays by electron transfer processes with the emission of low kinetic energy electrons.

Besides studying the electronic states of the clusters, we exploit their magnetic character due to the unpaired electron in magnetic deflection experiments on molecular beams. The paramagnetic properties of sodium-doped clusters with ammonia, water, methanol and dimethyl ether for cluster sizes $n = 1 - 4$ are characterised by their deflection behaviour when traversing a magnetic field gradient. The spatial deflection is compared to molecular dynamics simulations based on the Zeeman interaction of a spin $1/2$ system. The comparison of experiment and simulation reveals unperturbed magnetic properties of a spin $1/2$ system for the smallest clusters NaNH_3 and NaH_2O . All larger clusters, in contrast show reduced deflection compared to simulations of a spin $1/2$ system. Deviations from a spin $1/2$ deflection behavior are attributed to a reduction of magnetic moment due to intracluster spin-relaxation processes. Determining effective magnetic moments for these clusters allows us to identify trends in their paramagnetic properties. The observed trends are discussed in terms of spin and rotational angular momentum interactions of the thermally accessible rovibrational density of states. We used density functional methods to determine the lowest energy cluster geometries and the rovibrational states with the harmonic oscillator and rigid rotor approximation. With this approach we find that the dominant mechanism of intracluster spin-relaxation processes in sodium-doped clusters is governed by the thermal population of spin-rotational coupled Zeeman states.

Zusammenfassung

Das Verständnis der Solvatisierung von Elektronen und deren Delokalisierungsgrad in diesem Zustand, ist seit ihrer ersten Entdeckung in Alkalimetall Ammoniak Lösungen von wissenschaftlichen Interesse. Neutrale Alkalimetall-dotierte Cluster dienen als ideale Modellsysteme, um systemgrößenabhängige Eigenschaften zu studieren. Die vorliegende Arbeit befasst sich mit der Charakterisierung der elektronischen und magnetischen Eigenschaften dieser Cluster mittels winkelaufgelöster Photoelektronenspektroskopie beziehungsweise Stern-Gerlach Deflektion. Die Kombination beider Messtechniken ermöglicht es, Rückschlüsse über die Bindungsenergie, den Orbital- und Spindrehimpuls des solvatisierten Elektrons, als auch den Rotationsdrehimpuls des Clusters zu ziehen.

Wir berichten über Messungen der Elektronenbindungsenergien und Photoelektronenanisotropien von Lithium-dotierten Dimethylether Clustern in Abhängigkeit ihrer Grössenverteilungen unter Verwendung winkelaufgelöster Photoelektronenspektren. Hierzu wurden neutrale, einfach dotierte Lithiumcluster im Grössenbereich von einzelnen Lithiumatomen bis zu einer durchschnittlichen Clustergrösse von 63 Dimethylether Molekülen untersucht. Wir erklären beobachtete Trends in der Elektronenbindungsenergien und Photoemissionsanisotropien auf der Grundlage von Dichtefunktionalrechnungen an $\text{Li}(\text{CH}_3\text{OCH}_3)_n$ Clustern. Die gezeigten Resultate werden mit früheren Studien aus unserer Gruppe [1, 2] über $\text{Na}(\text{CH}_3\text{OCH}_3)_n$ Clustern verglichen. Der Vergleich zeigt ein ähnliches clustergrößenabhängiges Verhalten in Bezug auf die Bindungsenergie und Photoemissionsanisotropie. Jedoch bewirkt der Alkalimetallaustausch strukturelle und elektronische Unterschiede. In hochsymmetrischen Clusterstrukturen kommt es zur Delokalisierung des höchsten besetzten Molekülorbitals über einen ausgedehnten räumlichen Bereich und zur symmetrischen Ladungsverteilung mit hauptsächlich *s*-Charakter, was zu einer ausgeprägten Photoemissionsanisotropie führt. Die Winkelverteilungen der Photoelektronen von $\text{Li}(\text{CH}_3\text{OCH}_3)_n$ zeigen ausgeprägten *s*-Charakter für die Clustergrößen $n = 4, 5$ und 6 . Diese Grössen werden als magische Cluster in ihrer Photoelektronenanisotropie bezeichnet.

Photoelektronenstudien an Clustergrössenverteilungen sind limitiert in ihrer Auflösung der einzelnen Clustergrössenbeiträge. Grössenaufgelöste Messungen von elektronischen Bindungsenergien und Photoemissionsanisotropien an neutralen $\text{Na}(\text{NH}_3)_n$ Clustern wurden mittels Photoelektron-Photoion-Koinzidenz-Spektroskopie, mit Photonenergien zwischen $5.5\text{ eV} - 9.9\text{ eV}$, gemessen. Spektren der kinetischen Elektronen nach Anregung in Kombination mit *ab initio* Rechnungen legen drei verschiedene Ionisationspfade nahe, wobei jeder

Pfad in einem bestimmten Photonenenergiebereich dominant ist. Einer dieser Pfade läuft über die resonante Anregung des neutralen Zustandes und anschliessende Autoionisation ab. Wir vermuten dass der Anregungsprozess durch einen Elektronentransfer vom freien Elektronenpaar eines Ammoniak-Moleküls zum einfach besetzten Molekülorbital des solvatisierten Elektrons beschrieben ist. Der angeregte Zustand ist durch ein zweifach besetztes Molekülorbital charakterisiert, welches als solvatisiertes Dielektron bezeichnet wird. Das angeregte solvatisierte Dielektron zerfällt anschliessend durch Elektronentransferprozesse und die Emission von Elektronen mit niedriger kinetischer Energie.

Neben Studien über die elektronischen Zustände dieser Cluster, ist es möglich den magnetischen Charakter des ungepaarten Elektrons in magnetischen Deflektionsexperimenten an Molekularstrahlen zu untersuchen. Dazu charakterisieren wir die paramagnetischen Eigenschaften von Natrium-dotierten Ammoniak, Wasser, Methanol und Dimethylether Clustern mit $n = 1 - 4$ Molekülen in ihrem Ablenkverhalten während der Interaktion mit einem inhomogenen Magnetfeld. Das Ablenkungsverhalten wird mit Molekulardynamiksimulationen, welche auf der Zeeman-Wechselwirkung eines Spin $1/2$ Systems basieren, verglichen. Der Vergleich von Experiment und Simulation zeigt unveränderte magnetische Eigenschaften des Spin $1/2$ Systems für die kleinsten Cluster NaNH_3 und NaH_2O . Alle grösseren Cluster zeigen hingegen reduzierte Deflektion. Die Abweichungen vom Spin $1/2$ Deflektionsverhalten werden auf ein reduziertes magnetisches Moment zurückgeführt, welche wahrscheinlich durch Intracluster-Spinrelaxationsprozesse ausgelöst werden. Die Bestimmung effektiver magnetischer Momente für diese Cluster ermöglicht es uns, Trends in deren paramagnetischen Eigenschaften zu identifizieren. Die beobachteten Trends werden im Hinblick auf Spin- und Rotationsdrehimpulswechselwirkungen der thermisch zugängliche Rotationsschwingungszustandsdichten diskutiert. Unter Verwendung von Dichtefunktionalmethoden werden energieoptimierte Clusterstrukturen und dazugehörige Schwingungen und Rotationen in der Näherung eines harmonischen Oszillators und starren Rotators berechnet. Unter diesen Annahmen stellen wir fest, dass der bestimmende Mechanismus der Intracluster-Spinrelaxationsprozesse in Natrium-dotierten Clustern durch die thermische Besetzung von Spin-Rotations gekoppelten Zeeman-Zuständen bestimmt ist.

Acknowledgement

The work presented in this thesis was done in collaboration with several people, whom I would like to thank on this occasion.

Foremost I want to express my gratitude to Prof. Dr. Ruth Signorell, who gave me the opportunity to work on several exciting and challenging projects. The guidance and advice received from you are greatly appreciated. I enjoyed our discussions which were always very helpful to improve knowledge on both sides. I am especially thankful for the advice received in the preparation for talks at conferences. Thanks a lot for the support and patience throughout my time in your group. I am looking forward to meet you and your group as a guest.

Also I would like to thank my co-examiner Prof. Dr. Gunnar Jeschke, for the first theoretical estimations of spin-relaxation times, which were the first fundamental steps in realizing the deflector project. I also want to thank you, for reviewing this thesis. Thanks a lot to Dr. Daniel Klose and Sergei Kuzin of the Jeschke Group, for the very helpful discussion towards the end of my PhD. Furthermore I want to thank Prof. Evangelos Miliordos for the help with quantum chemical calculations and to have had you as guest in Zurich.

In general I am thankful to all the members of the Signorell group, I could share ideas, laughs and coffees with. Yet some members I want to emphasize, since they greatly influenced my time and the projects I was involved. I thank Dr. Bruce Yoder for guidance, exchange of creative ideas, reassurance in difficult times, open ears for any kind of worries and of course for your great sense of humour. Thanks a lot for all the corrections of my drafts and helping me improve in my writing. I thank Dr. Loren Ban foremost for being a friend and supporting me with all the problems I had, especially with these computers. Also I want to thank Dr. Egor Chasovskikh for sharing your great practical and technical skill set. I am very grateful to have worked with Dr. Martin Beck, your technical knowledge and deep insight into physical problems were of significant importance, in order to get the deflector running. I want to also thank you for teaching me, what ‘patience’ actually means. With this I want to thank Dr. David Luckhaus for the introduction into DFT calculations, as well as for providing and regularly updating the code for the MD simulations. I thank Dr. Sebastian Hartweg for teaching me in my first steps on the deflector project, showing me helpful experimental tricks in the lab, the time at SOLEIL synchrotron and of course providing a first draft on the solvated dielectron project. I wish you all the the best with

your young family.

Towards the end of my PhD, I had the opportunity to supervise the semester project of Dario Stolba and the master thesis of Edith Simmen. I thank both of you for the great help and your interesting questions, I genuinely enjoyed working with both of you. Furthermore, I want to thank my successors on the deflector project Dominique Borgeaud and Dr. HuanYu Yang. The exchange in the last couple of months helped the project to grow significantly. I wish you all the best with this project and other things to come.

All the experimental work would have not been possible with the extraordinary technical support from David Stapfer and Markus Steger from the mechanical and electronic workshops. David, thank you so much for rebuilding parts of the deflector, constructing complicated laser ablation bodies, refurbishing source flanges, helping to install new chambers and all the other technical problems we had in the lab. Markus, only with your redesigns and modifications of the deflector's electronic circuit, we were able to carry out successful measurements. I also want to thank you for measuring the magnetic field pulses and explaining me the electronic details of the deflector setup. I am also thankful to Dani Zindel for always taking care of any chemical problems and for synthesizing the deuterated dimethyl ether.

With this I want to thank some influences outside of academia, which provided balance to my life and gave me a wider perspective. I want to thank Veit and Andrea for supporting my eager to learn, scientific curiosity and all the books you gifted me. I want to thank my closest friends here in Zurich Loren, Ella, Louise, Oskar, Dianer and Tom to reassure me what actually matters.

In the end I would like to thank my family for their unique sense of humour and their realistic perspective on abstract thinking.

Contents

Abstract	I
Zusammenfassung	III
Acknowledgement	V
1 Introduction	1
2 Methods & experimental setups	5
2.1 Cluster formation and alkali metal-doping	5
2.1.1 Cluster formation - supersonic expansion	5
2.1.2 Alkali metal-doping	8
2.2 Light sources	11
2.2.1 Ultraviolet laser light sources	11
2.2.2 DESIRS beamline radiation at SOLEIL synchrotron	11
2.3 Pulsed Stern-Gerlach velocity map imaging photoion spectrometer	12
2.3.1 Pulsed Stern-Gerlach deflector	13
2.3.2 Photoion velocity map imaging - velocity dependent deflection	20
2.3.3 TOF mass spectrometry - deflection measurements	22
2.4 Velocity map imaging photoelectron spectrometer	25
2.4.1 Time-of-flight mass spectrometry	27
2.4.2 Photoelectron velocity map imaging	28
2.5 Photoelectron-photoion-coincidence-spectrometer	29
3 Theory & Modelling	33
3.1 Atoms and clusters in magnetic fields	33
3.1.1 Zeeman effect in atoms	33
3.1.2 Zeeman effect in sodium-doped clusters	34
3.1.3 The force field of an inhomogeneous magnetic field	35
3.1.4 Avoided crossing model	36
3.1.5 Spin relaxation model	38
3.1.6 Molecular Landé factor	40
3.2 Modelling of the pulsed Stern-Gerlach deflection	40
3.2.1 2D Space-Time Model	41
3.2.2 Molecular Dynamics Model	42

3.3	Angle-resolved photoelectron spectroscopy	51
3.3.1	Photoelectron angular distribution	51
3.3.2	Velocity map imaging of photoelectrons	53
3.3.3	Image reconstruction	54
3.4	Momentum transfer of alkali metal-doping	57
4	Magnetic deflection of neutral sodium-doped ammonia clusters	61
4.1	Introduction	62
4.2	Methods	64
4.2.1	Experimental setup	64
4.2.2	Measured velocity distributions of $\text{Na}(\text{NH}_3)_n$	69
4.2.3	Modelling of the magnetic deflection	70
4.3	Results	73
4.3.1	Coil contributions to the deflection of NaNH_3	73
4.3.2	Deflection ratios for $\text{Na}(\text{NH}_3)_n$: Experiment vs. MD simulations	74
4.4	Discussion	80
4.5	Conclusion	83
4.6	Supplementary Information	84
4.6.1	Mechanical deflector design	84
4.6.2	Electronic deflector design	84
4.6.3	Deflection of effusive Na atoms	85
5	Magnetic deflection of neutral $\text{Na}(\text{H}_2\text{O})_n$, $\text{Na}(\text{MeOH})_n$ and $\text{Na}(\text{DME})_n$ clusters	89
5.1	Introduction	89
5.2	Experimental & Computational Methods	90
5.3	Results for $\text{Na}(\text{H}_2\text{O})_n$ clusters	91
5.3.1	Magnetic deflection of NaH_2O	91
5.3.2	Magnetic deflection of $\text{Na}(\text{H}_2\text{O})_{2-4}$	94
5.4	Results for $\text{Na}(\text{MeOH})_n$ clusters	94
5.4.1	Magnetic deflection of NaMeOH	94
5.4.2	Magnetic deflection of $\text{Na}(\text{MeOH})_{2-4}$	95
5.5	Results for $\text{Na}(\text{DME})_n$ clusters	96
5.5.1	Magnetic deflection of NaDME	96
5.5.2	Magnetic deflection of $\text{Na}(\text{DME})_2$	98
5.5.3	Magnetic deflection of $\text{Na}(\text{DME})_3$	99
5.6	Summary	101
6	Comparison of $\text{Na}(\text{H}_2\text{O})_n$, $\text{Na}(\text{NH}_3)_n$, $\text{Na}(\text{MeOH})_n$ and $\text{Na}(\text{DME})_n$	103
6.1	Summarized magnetic deflection results	104
6.2	Modelling of an effective magnetic moment	105
6.3	Discussion	109

6.3.1	Thermally accessible vibrational states	111
6.3.2	Average number of rotational states within ΔE_{Zeeman}	118
6.3.3	Average number of rovibrational states within ΔE_{Zeeman}	122
6.4	Outlook	124
6.5	Summary	127
7	How solvated dielectrons and their electron transfer mediated decay govern the ionization dynamics of metal-ammonia solutions	129
7.1	Introduction	129
7.2	Experimental Methods	130
7.3	Computational Methods	131
7.4	Results & Discussion	132
7.5	Supplementary Information	143
7.5.1	Time-of-flight mass spectra	143
7.5.2	Electron binding energies and photoelectron spectra	144
8	Magic numbers for the photoelectron anisotropy in Li-doped dimethyl ether clusters	149
8.1	Introduction	150
8.2	Experiment	151
8.3	DFT Calculations	152
8.4	Results for $\text{Li}(\text{CH}_3\text{OCH}_3)_n$ clusters	153
8.5	Comparison of $\text{Li}(\text{CH}_3\text{OCH}_3)_n$ and $\text{Na}(\text{CH}_3\text{OCH}_3)_n$ clusters	159
8.6	Summary	162
8.7	Supplementary information	163
9	Conclusion & outlook	167
	Bibliography	170
A	Magnetic deflection results	191
B	Quantum chemical calculations	203
B.1	Cluster structures	203
B.2	Harmonic frequency calculations	205

Chapter 1

Introduction

Ever since the first discovery of concentration-dependent colours in alkali metal ammonia solutions by Davy in 1808 and rediscovery by Weyl in 1864 [3], there has been scientific interest in studying these solutions. In 1907, Krause [4] identified the high electrical conductivity of these solutions, blue colour when dilute and copper colour when concentrated, as being due to the presence of solvated electrons. In these solutions a variety of diamagnetic and paramagnetic species are thought to exist *e.g.* solvated electrons, solvated metal atoms, electron-cation pairs and bipolarons [5, 6, 7, 8]. Recent experimental and theoretical studies on solvated electrons were motivated by their potential relevance in liquid-phase chemistry [9, 10, 11], organic synthesis as a reducing agent [12] and radiation damage in aqueous systems [9, 11, 13, 14, 15], as well as their importance in biology and atmospheric processes [13, 15, 16].

Alkali metal doped solvent clusters provide an experimental and theoretical model system to study properties of excess electrons as a function of system size [17, 18, 19, 20, 21, 22, 23, 24, 25, 26, 1, 2, 27] (and references therein). The work presented in this thesis uses photoelectron spectroscopy (PES) and Stern-Gerlach deflection to study the electronic and magnetic properties of neutral alkali metal-doped solvent clusters $M(\text{Sol})_n$ with $n = 1 - 6$ (M : Li, Na; Sol : H_2O , NH_3 , CH_3OH , CH_3OCH_3). PES is an experimental technique which allows for the study of the electronic structure of matter, nearly independent of aggregation state and material [28, 29]. The photoelectron kinetic energies contain information on the electronic states of the material, reflecting their chemical composition and structure. Resolving the photoelectron angular distributions (PAD) [26, 30, 31] of emitted electrons represented by a final state $|f\rangle$ gives insight on the orbital character, respectively the orbital angular momentum of the initial electronic state $|i\rangle$ [32, 33, 34, 35, 36]. Angle-resolved photoelectron spectroscopy (ARPES) of neutral clusters is still not a commonly applied technique due to difficulties in size-selection [37, 38, 39], determination of size distributions [25, 40, 23] and demanding modelling of PAD [41, 42, 43, 33, 44]. Alkali metal-doping with subsequent photoionisation provides a nearly destruction-free method of size determination [40].

Size-resolved PAD are achieved with photoelectron-photoion-coincidence-spectroscopy

(PEPICO) [45, 46, 47]. Conservation of energy and momentum during the photoionisation process defines the internal energy of the photoion by the initial energy of the neutral species, the photon energy, the ionisation energy and the kinetic energy of the electron. Much faster photoelectrons are detected on the nanosecond timescale which define the internal clock, whereas photoions are detected microseconds later. The momentum and energy conservation correlates the photoions and photoelectrons, and the photoelectrons are assigned to their cluster size. In chapter 7 we present a PEPICO study of small sodium-doped ammonia clusters. With a combination of size-selected PAD and *ab initio* calculations we show three distinct ionisation pathways of the singly solvated electron accompanied by the formation of the electronic ground state cluster cation. One pathway proceeds via the formation of spin-paired solvated dielectrons, which may subsequently decay on ultrafast timescales via an electron transfer mediated decay (ETMD) [48, 49, 50, 51], and form the corresponding cationic cluster.

In chapter 8 we present an ensemble study of the solvated electron precursor system $\text{Li}(\text{CH}_3\text{OCH}_3)_n$ ($1 \leq n \leq 175$). We characterise various cluster size distributions in their ionisation energy of the highest occupied molecular orbital (HOMO), as well as the symmetry of the initial electronic state. In clusters of high symmetry, the HOMO is typically delocalized over the entire cluster, which forms symmetric charge distributions of high *s*-character [1, 52, 53, 2]. The photoelectron anisotropy of $\text{Li}(\text{CH}_3\text{OCH}_3)_n$ clusters reveals magic numbers at $n = 4, 5$ and 6 . These cluster sizes correspond to the completion of the first coordination shell, and can be considered as isomeric motifs of the first coordination shell. Previous work in our group [1] found magic numbers in the photoelectron anisotropy at $n = 4$ and 6 for sodium-doped ammonia and dimethyl ether clusters, respectively. Yet, for sodium-doped water and methanol clusters no magic numbers were found. Performing cluster size-dependent PAD studies on alkali metal-doped clusters, provide a molecular level understanding of solvated electron formation and their dependence on system size [5, 1, 2, 27]. Furthermore, an understanding of the HOMO symmetry could provide information on possible minor spin-orbit contributions.

The formation of solvated spin-paired electrons as a function of alkali metal concentration in sodium-doped nanodroplets [54] and liquid bulk solutions [55] is of recent interest. Probing spin-pairing effects via PES is limited in its application due to similar electron kinetic energies of the involved electronic species. However, investigating differences in magnetic properties of alkali metal-doped clusters is likely to be a favourable approach to probe spin-pairing effects. Distinguishing diamagnetic (singlet) and paramagnetic (triplet) states using SG deflection is suggested here as a first experimental approach. The original SG experiment was designed to determine the quantisation of the electron spin in silver atoms [56]. In atoms the total electronic angular momentum J is composed of the orbital angular momentum L and its intrinsic spin angular momentum S . The Zeeman effect results from the coupling of the net angular momentum to an external magnetic field B . The quantised projection of the total angular momentum onto the magnetic field axis is

expressed as M_J . Each J component has $2J + 1$ sublevels ($M_J = +J, \dots, 0, \dots, -J$), with their characteristic Zeeman energy, which is proportional to the magnetic field strength B and the atomic Landé factor g . In a SG experiment each Zeeman level corresponds to an individual deflecting beamlet [57]. In general polyatomic molecules, additional degrees of freedom like vibrations and rotations (neglecting nuclear spins) may contribute to the net angular momentum. The molecular Zeeman effect is due to the same fundamental cause as in atoms, although usually at least contributions of the rotational angular momentum must be considered. Theoretical investigations of the diatomic case were performed by Hill [58] and later Schadee [59]. An overview of the theory in diatomic molecules is given by Berdyugina and Solanki [60], where analytical solutions of molecular Landé factors g_J in the limiting Hund's cases (a) and (b) are evaluated. Gedanken *et. al* [61, 62] showed the importance of spin-rotation interaction in Stern-Gerlach deflection experiments of oxygen and nitrogen oxide radicals. For instance, O_2 in its lowest rotational level ($R = 1$) exhibited nine spatially separated peaks characterised by M_J [61]. Amirav and Navon [63, 64] found that paramagnetic molecules and stable radicals (TEMPO: 2,2,6,6-tetramethyl-piperidine-*N*-oxyl and DTBN: di-*t*-butyl nitroxide) would be deflected less than predicted. Their interpretation being that fast intramolecular spin relaxation (ISR) induced by spin-orbit coupling causes a loss of net magnetic orientation and according depletion in observable deflection magnitude. Gedanken *et al.* [62] disputed these interpretations, since their magnetic deflection spectra of TEMPO combined with line-profile calculations did not support the interpretation of ISR processes occurring while traversing the deflector. Yet, in the case of the large chromium complex $Cr(CF_3COCHCOCF_3)_3$ Gedanken and co-workers [65] interpreted the complete indifference to the magnetic field gradient of the SG deflection pattern, in the manner of Amirav and Navon [63, 64], and stated the possibility of a characteristic relaxation time $\tau < 1 \times 10^{-6}$ s.

For large paramagnetic molecular and cluster systems the density of Zeeman-like levels becomes so high that quantum chemical calculations are prohibitively expensive. Various groups [66, 67, 68] developed more simplified theoretical models in order to explain SG deflection experiments within terms of ISR processes caused by several spin flip processes while conserving the total angular momentum. De Heer and co-workers [69, 70, 71, 72] observed one-sided deflection towards high field for Fe_m , Co_m and Ni_m clusters ($m = 10 - 1000$), which was interpreted as rapid ISR processes [66]. More recent studies show similar deflection behaviour for metal-organic sandwich clusters [73, 74, 75, 76] and paramagnetic metal superatoms [77, 78, 79, 80].

Correct interpretations of SG deflection and their underlying effects for cluster systems, are still a challenge in itself. Singly sodium-doped clusters are promising model systems as several characteristic properties can be exploited, in order to understand their magnetic properties as a function of system size. In the case of $m_S = \pm 1/2$ systems zero field splitting terms are vanishing and high symmetry HOMOs suggest minor contributions of spin-orbit coupling. In the presented work, hyperfine effects from couplings to the core spins are

neglected, although Fuchs *et al.* [81] demonstrated that nuclear spins diminish the electron spin coherence in metal clusters. In a first approximation, we reduce the dominating interactions to spin-rotational couplings. Quantification of SG deflection magnitudes of $\text{Na}(\text{NH}_3)_n$ (chapter 4), $\text{Na}(\text{H}_2\text{O})_n$, $\text{Na}(\text{MeOH})_n$ and $\text{Na}(\text{DME})_n$ clusters (chapter 5) are achieved in comparison to predictions based on a molecular dynamics model (chapter 3). Combining SG deflection and detection via photoion velocity map imaging [82] allows us to directly record velocity dependent deflection data. We find superparamagnetic deflection behaviour for NaNH_3 and NaH_2O , whereas all other clusters showed significantly reduced deflection. The relative deflection trends of the sampled clusters are discussed in terms of thermally accessible rovibrational states. Spin-rotational coupling causes the formation of avoided crossings between Zeeman-like levels of the same total angular momentum J , and contributes to the cluster Landé factor g_J of each J state. The combination of both effects as a function of populated rotational states are expected to represent the SG deflection behaviour of sodium-doped clusters. Comparing the different clusters in their deflection behaviour and their thermally accessible rovibrational states reveals that the magnetic properties are dominated by the density of rotational states. Within the presented work we describe the rovibrational states with the harmonic oscillator and rigid rotor approximation and evaluate the population of vibrational and rotational states with estimated vibrational ($50 \text{ K} \leq T_{\text{vib}} \leq 200 \text{ K}$) and rotational ($10 \text{ K} \leq T_{\text{rot}} \leq 50 \text{ K}$) temperatures.

Chapter 2

Methods & experimental setups

2.1 Cluster formation and alkali metal-doping

2.1.1 Cluster formation - supersonic expansion

The clusters studied in this work were generated via supersonic expansion of neat gases or gas mixtures into vacuum. During an expansion from a high pressure (~ 1 bar) reservoir into vacuum ($\sim 1 \times 10^{-7}$ bar), the sample gas is accelerated to supersonic velocities. Since the initial thermal energy is converted into directed kinetic energy the sample gas rapidly cools. The cooling process causes supersaturation of the expansion gas and subsequent condensation [83]. Weakly bound molecular clusters are formed, bound via van der Waals interactions, dipole-dipole interactions, higher order multipole electrostatic interactions and induced interactions [84]. The degree of cooling is characterised by the number of two-body collisions undergone by a given molecule. The number of two-body collisions can be increased by rising the quantity $p_0 \cdot d$, where p_0 is the stagnation pressure and d the nozzle diameter [85, 86]. To further enhance cluster formation it is possible to co-expanded a carrier gas (*e.g.* He or N₂) which causes more efficient cooling. Previous studies [87, 88, 89, 90] showed that higher stagnation pressures and lower source temperatures support condensation and cause formation of larger clusters. Yet, it is difficult to predict optimal cluster formation conditions, and controlled cluster generation techniques are still to be developed. Vapour pressures, specific heat capacities, source temperatures, nozzle geometries, gas compositions and chamber pressures influence the formation of clusters. The directed flow of a supersonic expansion is characterised by its velocity distribution in molecular beam direction. Foremost we are able to influence the beam velocity by varying the carrier gas and source temperatures. In general, a heavier carrier gas causes a slower molecular beam and a higher source temperature a faster beam. A representation of the carrier gas effect is shown in Fig. 2.1.1a for experimental cluster velocity distributions (see subsection 2.3.2) of NaMeOH with N₂ ($m_{\text{N}_2} = 28$ u) or He ($m_{\text{He}} = 4$ u) as carrier gas. With the light noble gas the cluster beam is approximately 250 m/s faster compared to the N₂ seeded expansion. Fig. 2.1.1b shows the velocity distributions of the toluene dimer

$(\text{C}_6\text{H}_5\text{CH}_3)_2$ generated with a room temperature nozzle or a heated nozzle of 100°C . The higher temperature source conditions generate a cluster beam which is approximately 60 m/s faster.

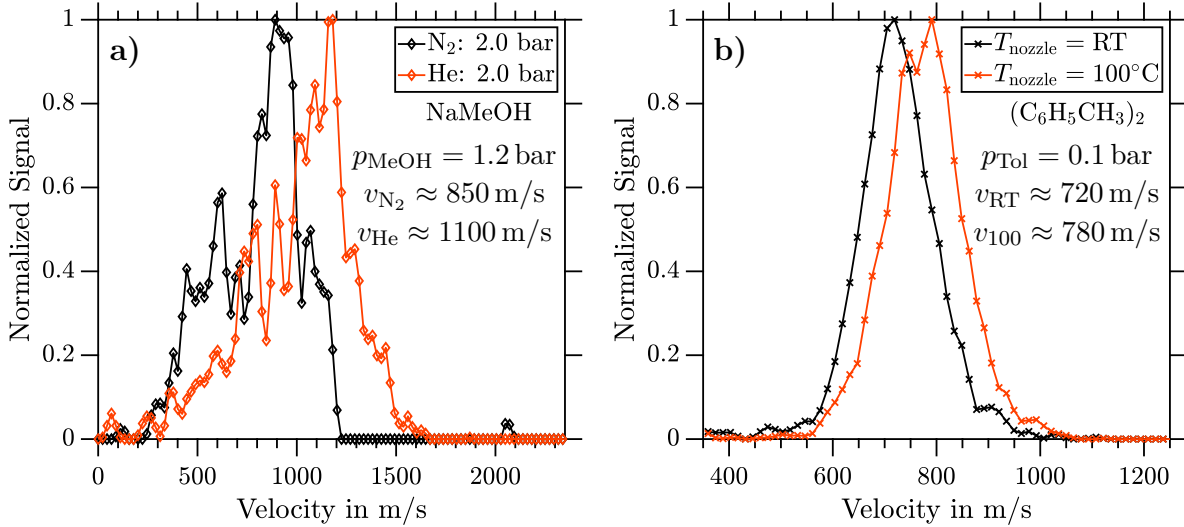


Fig. 2.1.1: (a) Velocity distributions of NaMeOH with N₂ carrier gas (black squares: $p_{\text{N}_2} = 2.0$ bar, $v_{\text{N}_2} \approx 850$ m/s, FWHM ≈ 490 m/s) and He carrier gas (red squares: $p_{\text{He}} = 2.0$ bar, $v_{\text{He}} \approx 1100$ m/s, FWHM ≈ 450 m/s). (b) Velocity distributions of $(\text{C}_6\text{H}_5\text{CH}_3)_2$ with $T_{\text{nozzle}} = \text{RT}$ (black crosses: $v_{\text{RT}} \approx 720$ m/s, FWHM ≈ 150 m/s) and $T_{\text{nozzle}} = 100^\circ\text{C}$ (red crosses: $v_{100} \approx 780$ m/s, FWHM ≈ 170 m/s).

Controlling the cluster beam velocity distributions allows us to vary the experimental time scale. This especially benefits the magnetic deflection studies presented in chapter 4, chapter 5 and chapter 6, since the cluster velocities define the interaction time with the magnetic field. In the presented work, clusters were generated via either continuous or pulsed supersonic expansion. In the following we discuss experimental properties of both cluster generation techniques.

Continuous supersonic expansion

In order to generate a continuous supersonic expansion we use a $1/4''$ stainless steel tubing with a laser drilled hole of $d = 25 - 100$ μm orifice diameter. The flow of the expansion gas is controlled by the orifice diameter and backing pressure. The gas throughput into the source chamber is limited by the pumping capacity. We typically perform experiments with source chamber pressures $\leq 1 \times 10^{-3}$ mbar (see Fig. 2.3.1 and Fig. 2.4.1). Fig. 2.1.2 depicts cluster size distributions of $\text{Na}(\text{NH}_3)_n$ clusters for various backing pressures and two different nozzle diameters d (see subsection 2.4.1 for time-of-flight (TOF) mass spectrometry and subsection 2.1.2 for alkali metal doping).

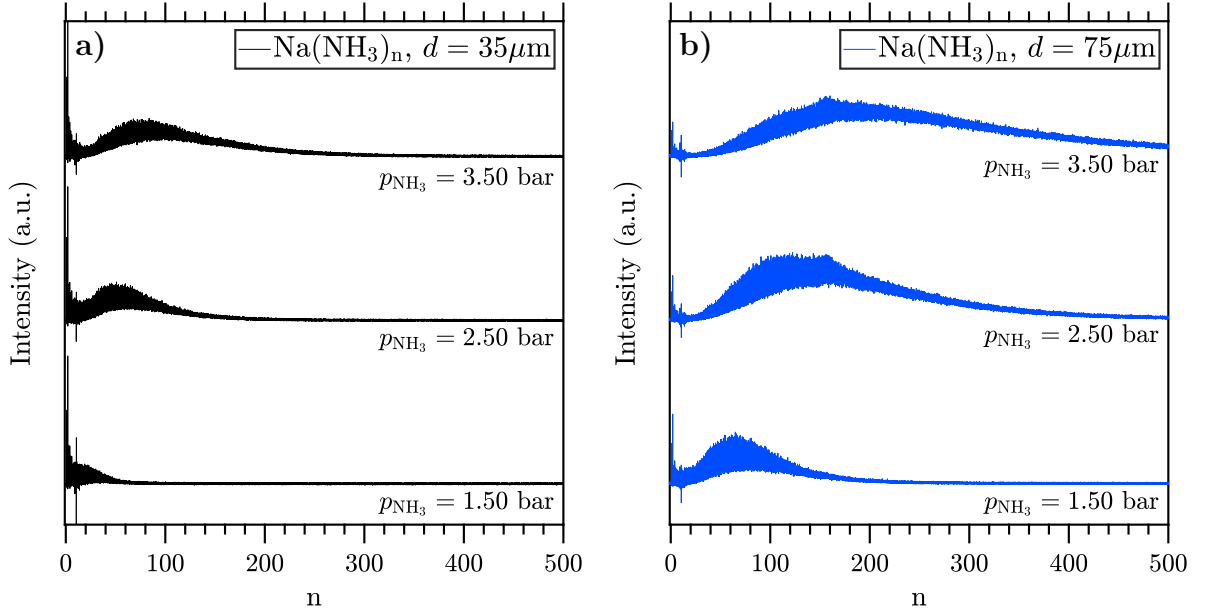


Fig. 2.1.2: TOF mass spectra of $\text{Na}(\text{NH}_3)_n$ clusters for various NH_3 backing pressures and nozzle diameters of: (a) $d = 35 \mu\text{m}$ and (b) $d = 75 \mu\text{m}$.

By varying the gas flow as a function of backing pressure p_{NH_3} and nozzle diameter d , we are able to control the average cluster size $\langle n \rangle$ of the cluster size distribution (see subsection 2.4.1 for determination of $\langle n \rangle$). The cluster size distributions and furthermore the cluster velocity distributions of a continuous cluster beam are independent of the ionisation time. In other words, at each point in time in the ionisation region the full information of cluster sizes and beam velocities is present.

Pulsed supersonic expansion

In the presented work pulsed supersonic expansions were generated with the Even-Lavie (EL) valve [91] operated at 1–20 Hz repetition rates. This allows us to work at significantly higher backing pressures before reaching the pressure limit in the source chamber. Due to the pulsed manner of the expansion, the relative time of valve t_{EL} and the detection/laser timing t_{L} are synchronized to retrieve cluster signals. Fig. 2.1.3a displays representative experimental TOF mass spectra of $\text{Na}(\text{H}_2\text{O})_n$ clusters (see subsection 2.1.2 for the alkali metal doping process) as a function of the relative time delay $\Delta t_{\text{L-EL}} = t_{\text{L}} - t_{\text{EL}}$ (see Fig. 2.3.10 for a schematic sketch of the timing sequence).

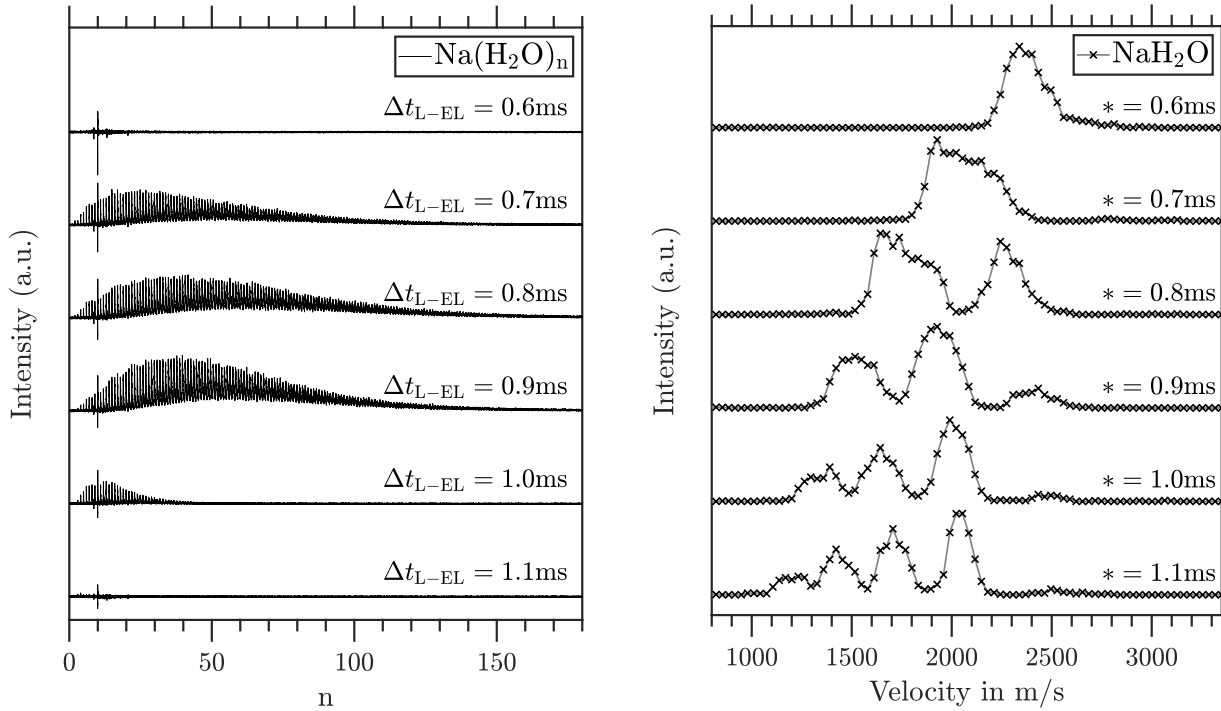


Fig. 2.1.3: Na(H₂O)_n clusters generated via pulsed supersonic expansion for various relative time delays Δt_{L-EL} . (a) TOF mass spectra (see section 2.4.1). (b) Experimental NaH₂O velocity distributions (see section 2.3.2), where * refers to Δt_{L-EL} .

We are able to control the detectable cluster size distribution by tuning the relative timing Δt_{L-EL} . The relative timing defines the observable cluster velocities. Shorter relative timings sample clusters which reach the ionisation region first, the faster clusters. With longer relative timings, we therefore should sample slower cluster velocities. Yet, due to the mechanical motion of the plunger in the EL-valve [91], several recoils occur and subsequently the valve opens several times per trigger pulse. The time separation of the recoils, allows different velocity components of each rebound to reach the detection region simultaneously. We observe these mechanical plunger recoils as distinct peaks in our experimental cluster velocity distributions (see subsection 2.3.2 for determination of cluster velocities), as shown in Fig. 2.1.3b. We use this experimental artefact to our advantage and simultaneously sample a range of velocity components of the cluster beam. This allows us to record magnetic deflection data of various velocity components, by simple changing the relative time delay Δt_{L-EL} (see chapter 5).

2.1.2 Alkali metal-doping

Alkali metal-doping of molecular clusters is a technique which was originally demonstrated by Bobbert *et al.* [92] and later extended in our research group [40, 25], to address the issue of cluster fragmentation upon ionisation and the determination of cluster size distributions. Alkali metal-doping of weakly bound solvent clusters is achieved via collisions of alkali metal atoms in a pickup cell (see Fig. 2.1.4). The interaction of alkali metal atom and

solvent molecules causes a significant decrease of the ionization energy < 5 eV of the alkali metal valence electron. This allows for a nearly destruction free ionisation of the clusters using UV light. This form of ionisation yields in more accurate measurements of cluster size distributions, since fragmentation processes are suppressed [40]. Furthermore studying alkali metal-doped solvent clusters sparked scientific interest, since these clusters serve as model systems to study electron solvation [5] and references therein. Alkali metal-doped clusters in molecular beams offered a controlled alternative to study size-dependent electronic [1, 2, 27] and magnetic properties [93].

A schematic representation of the alkali metal doping process is shown in Fig. 2.1.4 where the alkali metal vapour pressure is controlled by the oven temperature T_{oven} .

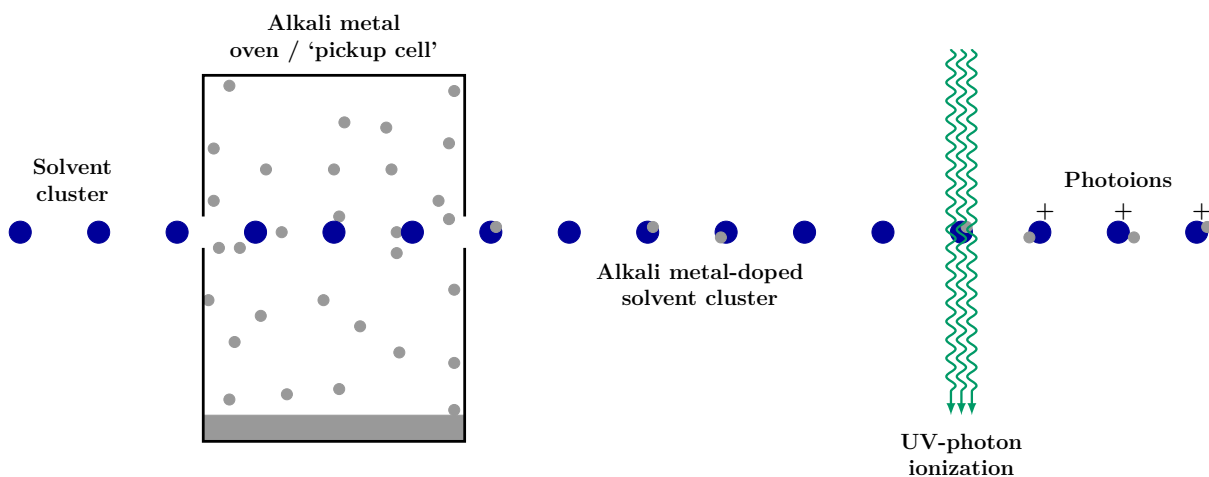


Fig. 2.1.4: Sketch of the alkali metal-doping process of molecular clusters.

The efficiency of the doping process depends on two major aspects: Firstly, on the collision probability of the alkali metal atom M with the molecular cluster $(\text{Sol})_n$. Secondly, on the lifetime of the newly formed alkali metal-doped species $M(\text{Sol})_n$ which must be longer than the experimental time scale. The collision probability to form $M(\text{Sol})_n$ is described by a Poisson distribution [94, 95].

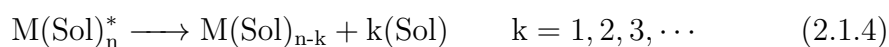
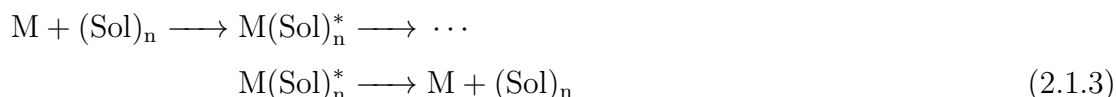
$$P_m = \frac{\langle m \rangle^m}{m!} \cdot \exp(-\langle m \rangle), \quad (2.1.1)$$

where m is the number of collisions and the average number of collisions $\langle m \rangle$ is given by

$$\langle m \rangle = \bar{n} L \sigma F. \quad (2.1.2)$$

Hereby \bar{n} denotes the number density of alkali metal atoms, L the length of the pickup cell, σ the collision cross-section and F is a parameter which takes the relative velocities of the cluster beam and alkali metal atoms into account (see section 3.4). In the presented work the density of alkali metal atoms \bar{n} is controlled via the oven temperature, with which it is possible to control signal intensities and degrees of doping. Since σ increases with cluster size, larger clusters are more likely to form alkali metal-doped species. Inelastic collisions

between the metal atom and solvent cluster can result in further processes, which influence the doping efficiency. Part of the collision energy can be converted into translational energy and internal energy of the activated collision complex $M(\text{Sol})_n^*$. The internal excess energy can be further redistributed into two different fragmentation processes. On one hand it is possible to stabilise the complex via dissociation of the alkali metal atom. This process is more likely for smaller clusters with less internal degrees of freedom to redistribute their collisional energy. On other hand, cluster stabilisation can be achieved by evaporative cooling of one or more solvent molecules. The competing mechanisms of collisional energy redistribution are summarised in the following reactions.



The conservation of momentum after the collision processes define the resulting velocity distribution of the clusters. A representative experimental velocity distributions (see subsection 2.3.2 for the evaluation of molecular beam velocities) are shown in Fig. 2.1.5 for the toluene dimer. With a cold oven ($T_{\text{oven}} = \text{RT}$) the vapour pressure of sodium is so low that no collisions occur in the pickup cell. The velocity distribution is merely defined by the supersonic expansion conditions. With a heated oven ($T_{\text{oven}} = 210^\circ\text{C}$) sodium collisions are possible and the initial velocity distribution is perturbed.

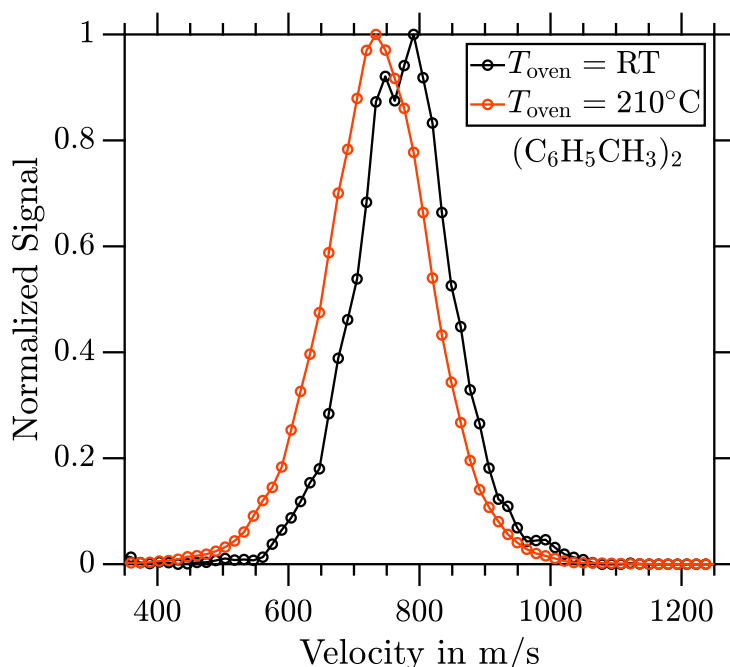


Fig. 2.1.5: Experimental cluster velocity distributions of $(\text{C}_6\text{H}_5\text{CH}_3)_2$ with a cold (black circles: $T_{\text{oven}} = \text{RT}$) and heated (red circles: $T_{\text{oven}} = 210^\circ\text{C}$) sodium oven.

The collisions of Na and $(\text{C}_6\text{H}_5\text{CH}_3)_2$ are characterised by velocity shift towards slower

velocities with $\Delta v \sim 50$ m/s. A possible explanation for the observed velocity shift is given in section section 3.4. Tab. 2.1.1 summarises working conditions of T_{oven} used throughout this work to generate single and multi-doped lithium- or sodium-doped solvent clusters.

Tab. 2.1.1: Oven temperatures for Li-doping and Na-doping applied in this work.

Alkali metal	Li		Na	
Doping degree	single	multi	single	multi
$T_{\text{oven}} / ^\circ\text{C}$	340 – 380	390 – 450	170 – 200	210 – 250

2.2 Light sources

2.2.1 Ultraviolet laser light sources

For experiments described in chapter 4 and chapter 5, photoionization was achieved with UV light 266 nm (4.66 eV), generated by the fourth harmonic of a pulsed (20 Hz) nanosecond (~ 7 ns) Nd:YAG laser (Quantel Ultra). The propagation direction and the linear polarisation vector were aligned parallel to the detection plane (see Fig. 2.3.1). The laser power could be varied by rotating the polarisation via the angle of the half-wave plate relative to the Glan-laser prism.

Single photon ionisation of bare sodium atoms was achieved with pulsed (20 Hz) nanosecond (~ 7 ns) 212 nm (5.85 eV) laser light, created by tripling the 636 nm output of a dye laser (Radiant Dyes Narrow Scan). Where the dye laser was pumped by 532 nm light from a Nd:YAG laser (Continuum powerlite), and used DCM (4-(Dicyanomethylene)-2-methyl-6-(4-dimethylaminostyryl)-4H-pyran) as a laser dye. Third harmonic generation was possible by doubling the frequency in a non-linear crystal, and additionally performing sum frequency generation (SFG) of the second harmonic and the residual fundamental in a further non-linear crystal. Once more the linear polarisation of the laser light was set by passing through a Glan-laser prism. In the given case the laser power was adjustable by detuning the second non-linear crystal which causes a reduced conversion efficiency.

2.2.2 DESIRS beamline radiation at SOLEIL synchrotron

For experiments described in chapter chapter 7, photoionization was achieved with VUV light generated at the DESIRS beamline at the French national synchrotron facility SOLEIL. Nahon *et al.* [96] present detailed conceptualisation and performance of the DESIRS beamline. Nevertheless we summarise the most important technical aspects for the experiments we carried out. In an undulator, highly relativistic electrons (2.75 GeV) follow an oscillating motion due to an alternating magnetic field. The magnetic fields are induced by pure electromagnets. The acceleration and deceleration of the oscillating electrons causes emission of electromagnetic radiation. The radiation frequency depends

on the strength and the spatial period of the magnetic fields. The DESIRS beamline undulator is 10 m long and consists of 14 periods of 640 mm length. Controllable driving currents of the electromagnetic coils leads to possible photon energies of 5 – 40 eV. The set of coils used in the undulator defines the polarisation vector of the emitted radiation. The polarisation vector can either be set to horizontal or vertical orientation. Furthermore, by using multiple sets of coils with fixed phase relation it is possible to generate circular and elliptical polarisations. Since higher harmonics of a desired wavelength are also generated in the undulator, suppression of these unwanted harmonics are achieved with a rare gas filter. Before entering the experimental chamber, the required wavelength is selected with a 6.65 m long grating monochromator. With the described beamline, photon energies with a minimal bandwidth of 1/50 000 and adjustable polarisation can be generated. For the presented work, the polarisation vector was linear with perpendicular alignment in regard to the electron and ion extraction axis. The photon energies were varied between 5 and 20 eV.

2.3 Pulsed Stern-Gerlach velocity map imaging photoion spectrometer

Parts of this section have been previously published in ref. [93] which is presented in its entirety in chapter 4. The pulsed Stern-Gerlach setup used to study the size-dependent magnetic properties of $\text{Na}(\text{NH}_3)_n$ (presented in chapter 4), $\text{Na}(\text{H}_2\text{O})_n$, $\text{Na}(\text{MeOH})_n$ and $\text{Na}(\text{DME})_n$ clusters (presented in chapter 5) is shown in Fig. 2.3.1.

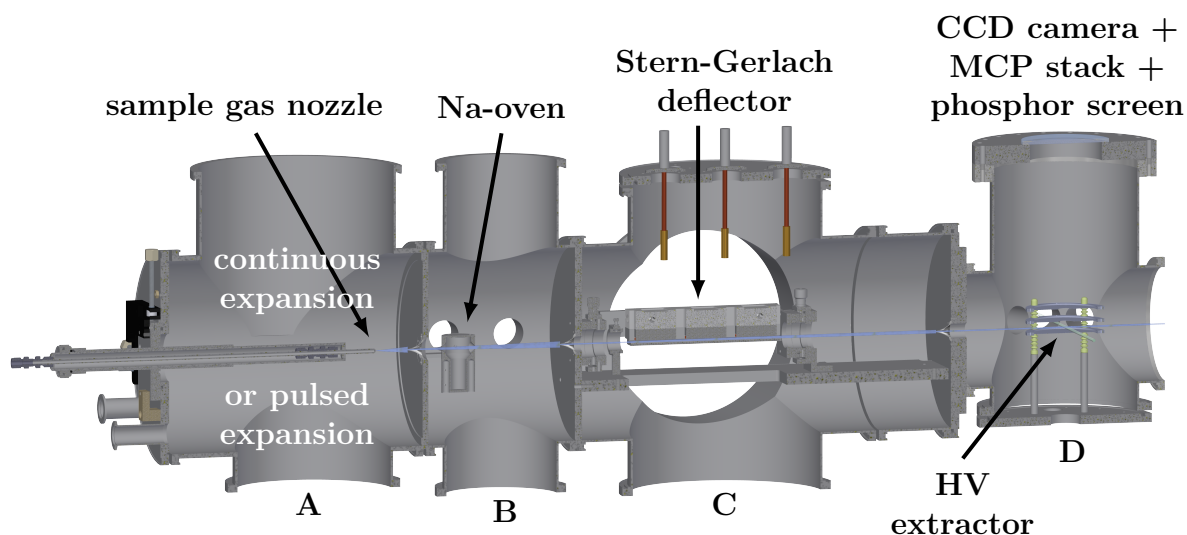


Fig. 2.3.1: Sketch of the experimental setup consisting of the source chamber (A), the Na-oven chamber (B), the deflection chamber (C) and the ionization/detection chamber (D). The figure is adapted with permission from [93] Copyright ©2021 Royal Society of Chemistry.

The experimental setup consists of four chambers (A-D) which are separated by skimmers

to ensure differential pumping conditions and a well-defined molecular beam. In the source chamber (A) solvent clusters are generated via supersonic expansion, which is described in subsection 2.1.1. After traversing the source chamber, the solvent cluster beam passes a 2 mm diameter skimmer before entering the sodium oven chamber (B). The solvent clusters are doped with sodium atoms inside the oven via collisions (see subsection 2.1.2). The resulting sodium-doped solvent clusters pass through a 1.5 mm diameter skimmer to enter the deflection chamber (C). This chamber houses the pulsed Stern-Gerlach deflector and the sodium-doped clusters interact with the magnetic field gradient. The non-deflecting cluster beam is separated by 2 mm diameter detection skimmer from the deflecting cluster beam. The remaining cluster beam enters the detection chamber (D) and reaches the interaction region where the clusters are ionised by 266 nm (4.66 eV) UV light (see subsection 2.2.1) and are subsequently detected. For the detection of photoion kinetic energies, velocity map imaging is applied (see subsection 2.3.2). Time-of-flight (TOF) based mass spectra signals are used to gain qualitative and quantitative cluster information and further quantify magnetic deflection (described in subsection 2.3.3). The following subsection 2.3.1 emphasises the mechanical and electronic design of the pulsed Stern-Gerlach deflector.

2.3.1 Pulsed Stern-Gerlach deflector

The pulsed Stern-Gerlach deflector was built in a collaboration with the group of Prof. Edvardas Narevicius at the Weizmann Institute of Science in Israel. The Narevicius group designed and machined the deflector parts, designed and built the essential electronic circuits to operate the deflector and simulated magnetic fields for several proposed flight channel cross sections. Design of the deflector and extending the existing velocity map imaging spectrometer (described in section 2.4) with the deflector were achieved in our group, as were all further deflection measurements. The mechanical and electronic design described in the following sections were adapted from the supplementary information of Barnes *et al.* [93].

Mechanical deflector design

The dimensions of the deflector and its position in the deflector chamber are shown in Fig. 2.3.2. The metal body parts of the deflector are machined from magnetic steel (1080 carbon steel).

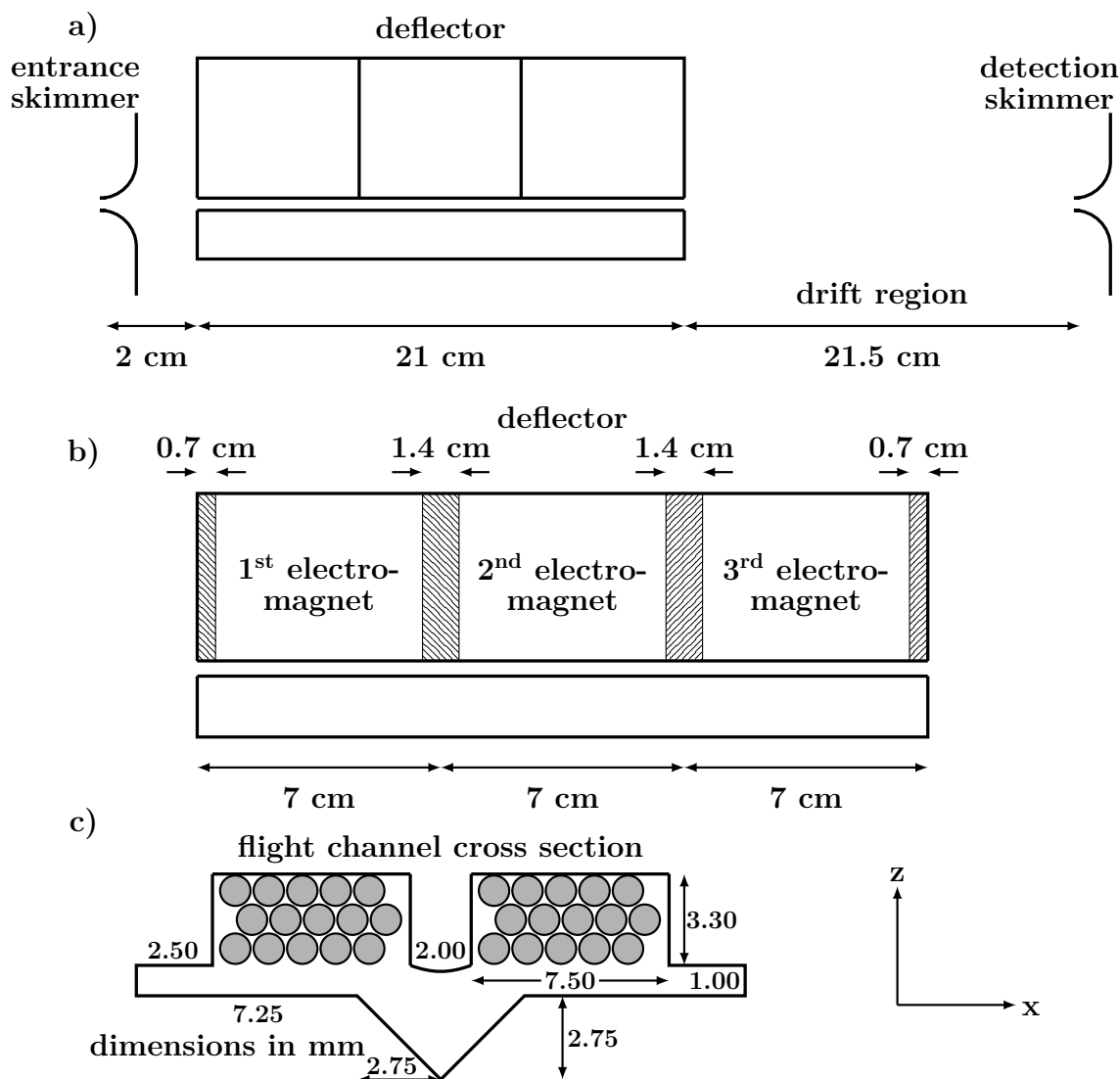


Fig. 2.3.2: (a) Side view of the deflector chamber with dimensions along the molecular beam propagation axis. (b) Side view of the deflector consisting of three electromagnets with the relevant dimensions. (c) Cross section of the deflector flight channel and the axis system. The figure is adapted with permission from [93] Copyright ©2021 Royal Society of Chemistry.

The assembled deflector with a length of 21 cm, consists of three electromagnets of 7 cm in length. Each electromagnet is composed of a metal body on which a coil, manufactured from 15 turns of insulated copper wire is mounted. Fig. 2.3.2c is a sketch of the cross section of the deflector with relevant dimensions. In addition 2.3.3a shows a photograph of the deflector front with its magnetic steel body, aluminium cooling plate and flight channel. The rounded metal bridge, situated in the centre of each coil is 5.6 cm long and 2 mm wide, acts as a pole shoe. With the chosen geometry the flight channel reaches a maximum height of 3.75 mm. The asymmetric geometry of the flight channel causes an inhomogeneous magnetic field with a gradient in z -direction. In the centre of the flight channel ($x = 0$) the gradient $\partial B/\partial z$ is nearly constant. The gradient in x -direction produces a focusing effect for one spin component and divergence for the opposite spin component. Fig. 2.3.3b displays the vector addition of the magnetic field gradients ($\partial B/\partial x + \partial B/\partial z$), which were

obtained from COMSOL simulations.

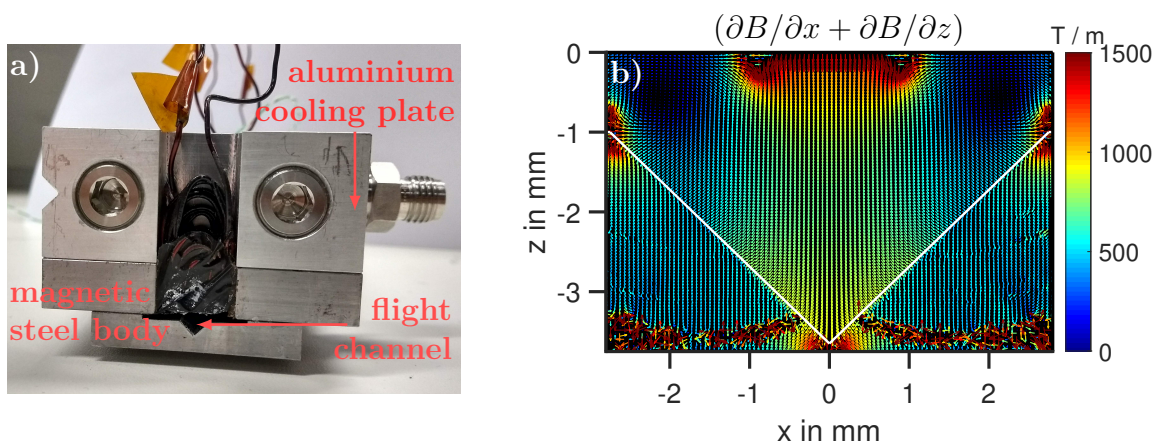


Fig. 2.3.3: (a) Photograph of the deflector front, with its aluminium cooling plate, magnetic steel body and flight channel. (b) Magnetic field gradient $(\partial B/\partial x + \partial B/\partial z)$ obtained from a COMSOL simulation with 1000 A electromagnetic current.

The electromagnetic coils are set in epoxy for mechanical protection and increased heat conductivity to the steel bodies. All three bodies are mounted onto a single, liquid-cooled aluminium plate. With a cooling liquid mixture of 30% glycol and 70% water, the aluminium plate is cooled to $-10\text{ }^{\circ}\text{C}$ by a closed-cycle chiller. Monitoring the pressure in the deflection chamber ($\sim 1 \times 10^{-7}$ mbar) and realising constant pressure conditions, while operating the deflector ensures stable temperature conditions of the deflector during measurements. The rear ends of the deflector are each mounted onto x, z -translation stages, to achieve fine alignment of the flight channel relative to the molecular beam. The detection skimmer positioned 21.5 cm after the deflector exit defines the selectivity of non-deflected species.

Electronic deflector design

Each electromagnet is driven by a 3-stage Pulse Forming Network (PFN) circuit designed to generate a square pulse of 1000 A with a FWHM of $270\text{ }\mu\text{s}$. A TDK-Lambda Genesis 1000-10 ($U_{\text{max}} = 1000\text{ V}$ and $I_{\text{max}} = 10\text{ A}$) power supply is used to charge the capacitors (simplified to C_{PFN} in Fig. 2.3.4) of each PFN circuit. A simplified sketch of the electronic circuit to operate the deflector is shown in Fig. 2.3.4.

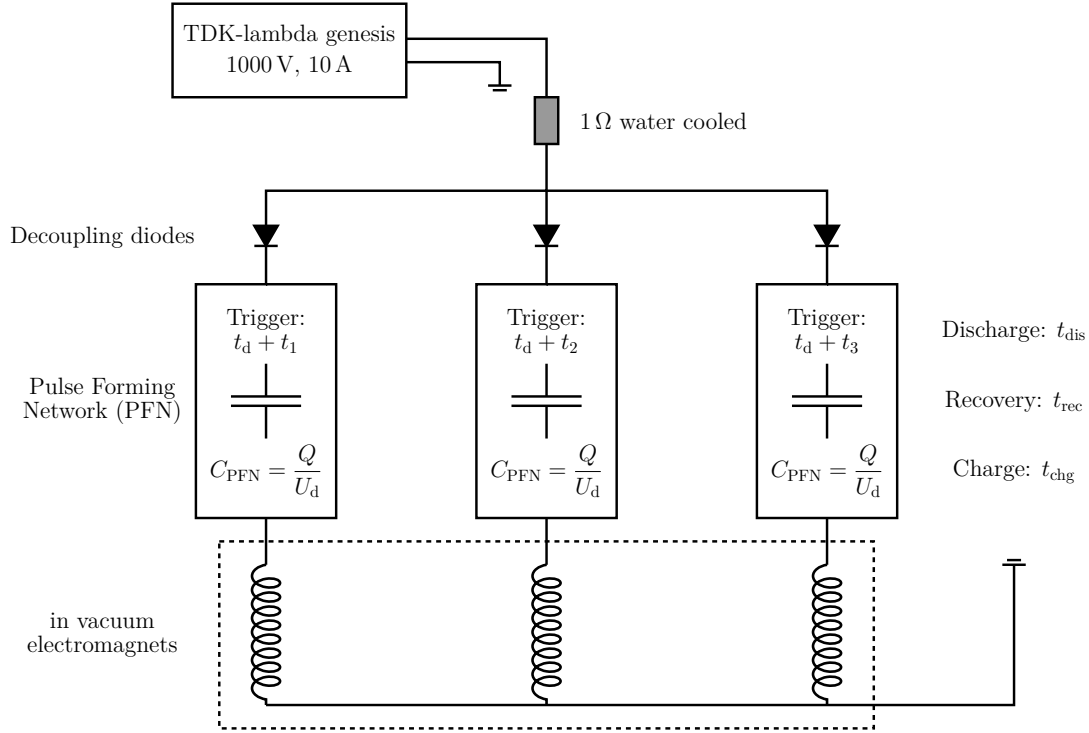


Fig. 2.3.4: Schematic representation of the electronic circuit used to generate magnetic fields of the pulsed Stern-Gerlach deflector.

The 1 Ω resistor is used to limit peaks arising in the charging currents of the power supply. Decoupling diodes are implemented to control the current direction and to protect the power supply. High power thyristors are used to switch the PFN circuits. The thyristor is a bistable switch which is opened by a trigger pulse and closes if the current through the switch falls below a threshold value. The trigger pulse sequence for each PFN circuit is generated by a home built time delay device. This device uses a master offset t_d of a delay generator (Stanford Research Systems DG535) as an internal time zero. The auxiliary trigger signals of charge, discharge and recovery, relative to t_d are programmed in our home built delay device. For deflection experiments, each electromagnet is triggered individually, with time delays t_1 , t_2 and t_3 relative to the master trigger t_d . We achieve this via a Complex Programmable Logic Device (CPLD) board and a micro controller (μC) board, schematically shown in Fig. 2.3.5.

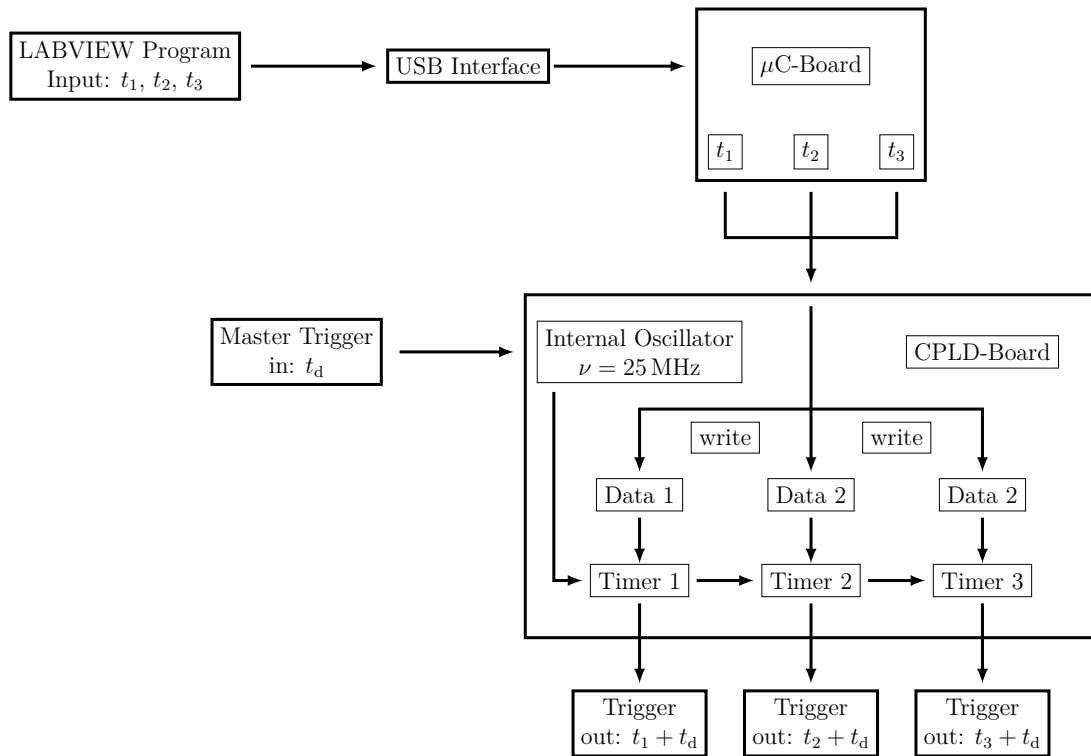


Fig. 2.3.5: Schematic representation of our home built delay device, composed of a μC -board and a CPLD-board.

The μC -board is controlled via a USB interface and a self written LABVIEW program in which individual coil trigger timings are set and the triggering of the PFN circuit is controlled. With the μC -board we are able to write relative timings t_1 , t_2 and t_3 to the CPLD-board, which introduces an additional individual time offset for the auxiliary trigger signals of each PFN circuit. An internal oscillator of 25 MHz operates as an internal clock for all three timers. The trigger pulse scheme implemented in the CPLD-board is shown in Fig. 2.3.6a and the corresponding voltage on the PFN capacitor C_{PFN} is displayed in Fig. 2.3.6b.

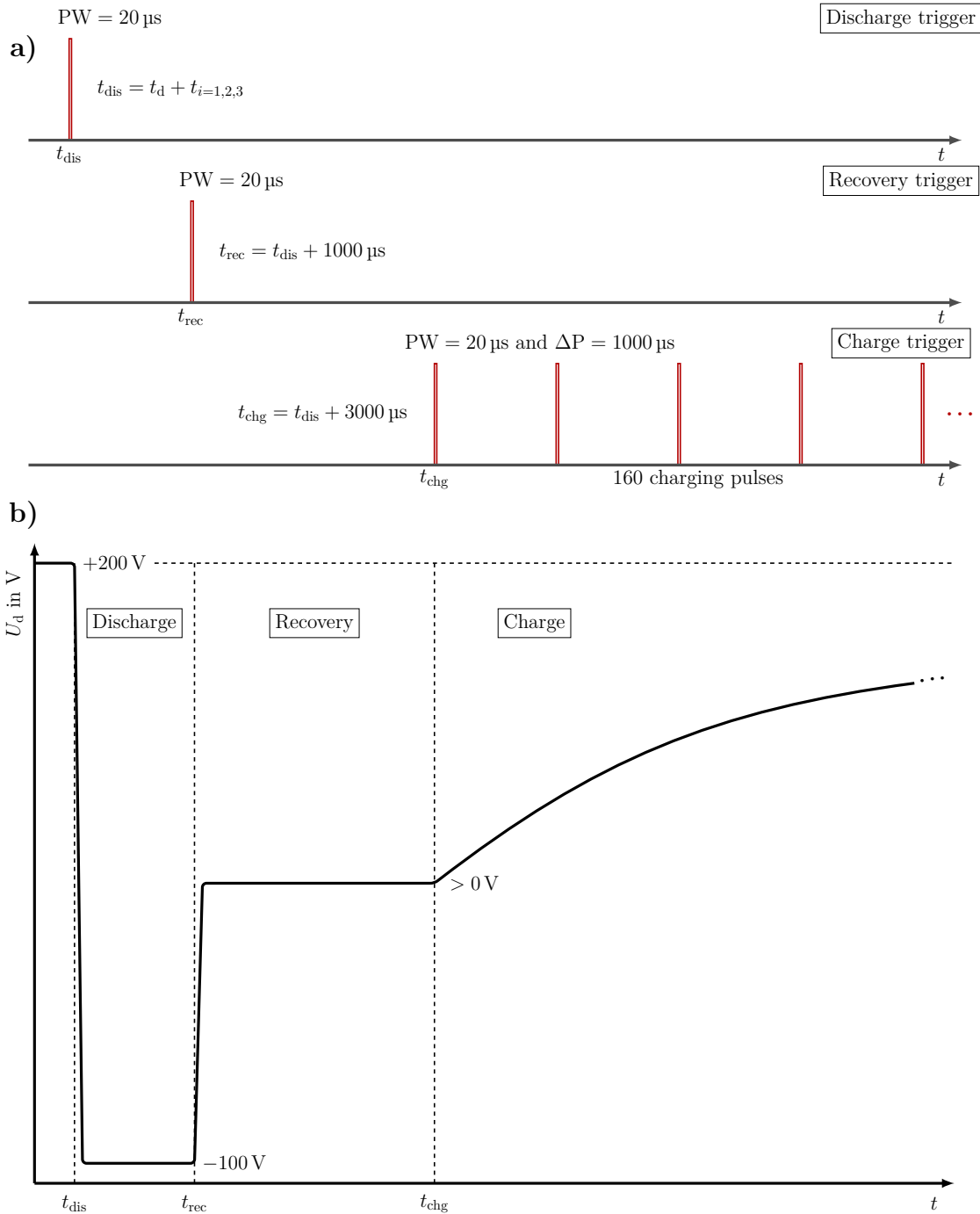


Fig. 2.3.6: (a) Schematic representation of the trigger pulse scheme programmed into the CPLD to control the PFNs. The discharge pulse (top panel) initiates the electromagnetic current pulse, the recovery pulse (mid panel) resets the voltages on the capacitors to a slightly positive voltage value and the charging pulses (bottom panel) start the charging process of the capacitors. (b) Schematic representation of the voltage over the PFN capacitor C_{PFN} . The current pulse is emitted between t_{dis} and t_{rec} .

The charging trigger initiates the charging process of the capacitors within the PFN circuit. Followed by a discharge trigger which starts the discharge of the capacitors and the emission of a surge current pulse to one of the deflector's electromagnets. The discharge through the inductive coil causes a negative voltage on the capacitors. With a recovery

trigger it is possible to reset this voltage to a slightly positive value, which supports the following charging process.

With the employed power supply, we were required to introduce an additional capacitor circuit of 1.25 mF before the 1 Ω resistor to suppress instabilities in the charging behaviour. Additional serial resistors before the 1 Ω resistor helped to further limit peak currents of the power supply and control the charging behaviour of the capacitors. These additional electronic components allowed us to reduce the load on the power supply at the cost of slightly increased charging times. The actual performance when driving the electromagnet (of about 32 μ H impedance and 75 m Ω resistance) was verified by measuring the current pulses and resulting magnetic field pulses in the flight channel with a Hall-probe for various charging voltages U_d . The measured magnetic field responses are displayed in Fig. 2.3.7.

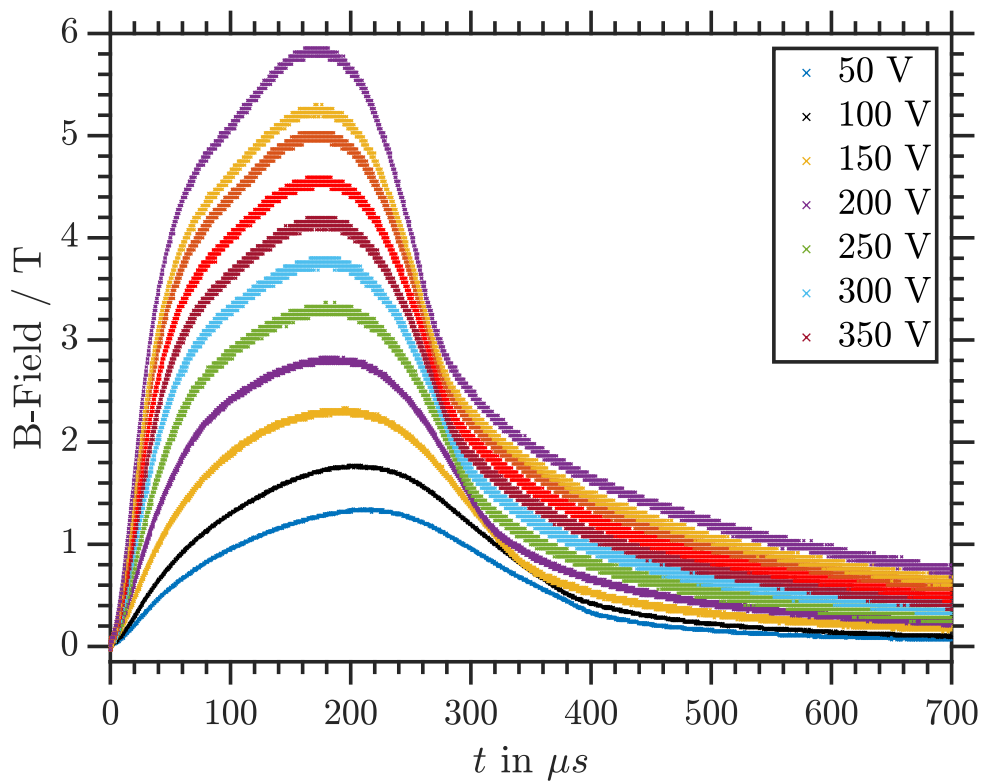


Fig. 2.3.7: Measured magnetic field responses in the deflector flight channel for various charging voltages U_d .

With the current deflector design we are able to collect data at a repetition rate of 5 Hz with a charging voltage up to 150 V (corresponds to 300 A peak pulse). With the current experimental setup working at higher charging voltages is only possible if the repetition rate is reduced. The limit in repetition rate and peak pulse current arises from thermal loads generated in the in-vacuum coils that cannot be efficiently dissipated by our cooling method. Attempts to operate with higher thermal loads are prevented by the onset of outgassing, accompanied by a total loss of signal at a chamber pressure of approximately 1.0×10^{-4} mbar. We attribute this loss of signal to obstruction of the flight channel. Since this mechanism of signal extinction would compete with signal loss due to deflection, we choose repetition rates that maintain the pressure increase in the deflector chamber

$< 3.0 \times 10^{-8}$ mbar (from the base pressure). Tab. 2.3.1 summarizes the repetition rates f , charging voltages U_d and deflector currents I_d to operate the deflector.

Tab. 2.3.1: Operating conditions of the pulsed Stern-Gerlach deflector setup used in this work.

f in Hz	5	5	5	2	1	1	1
U_d in V	50	100	150	200	250	300	350
I_d in A	100	200	300	400	500	600	700

2.3.2 Photoion velocity map imaging - velocity dependent deflection

Highest possible magnetic deflection in our pulsed Stern-Gerlach setup is achieved by synchronising the time between electromagnetic current trigger timings t_1, t_2, t_3 and the laser timing t_L . These relative time delays must be set evaluated as a function of the cluster velocity distributions. Extracting photoions perpendicular to the molecular beam propagation axis (see Fig. 2.3.8a) under optimised velocity map imaging (VMI) conditions (summarised in Tab. 2.3.2) allows us to determine cluster velocity distributions in the propagation direction of the molecular beam (v_y). Note, that the experimental principles of VMI for photoelectrons are explained in section subsection 2.4.2. Size-selection is achieved via time-of-flight based mass-gating to only detect the cluster size of interest [30], shown in Fig. 2.3.8b. Velocities of the neutral clusters in the molecular beam correspond to the displacement of the impinging photoions in the detector plane.

Tab. 2.3.2: Optimised VMI extraction conditions for photoion imaging all electrostatic potentials are given in V.

V_R	V_E	$V_{MCP, high}$	$V_{MCP, low}$	V_A
8000	5630	2000	1500	6000

With the given voltages of the repeller V_R , the extractor V_E , the MCP stacks $V_{MCP, high}$, $V_{MCP, low}$ and the anode (phosphor screen) V_A . The acquired photoion images were rotated by 1° to correct for a slight imperfection in the CCD camera alignment. The recorded ion signal five pixels above and below the center line (in total 11 pixels) were summed to retrieve the total ion signal as a function of the displacement in pixels. The displacement from the image center r (white cross in Fig. 2.3.8b) in pixels can be related to the neutral cluster's velocity v_y , by the following equation.

$$v_y = \sqrt{\frac{2 \cdot C \cdot V_R \cdot r^2}{m}} \quad (2.3.1)$$

Where C is a setup dependent calibration constant and m is the cluster mass. Fig. 2.3.8c displays an example cluster velocity distribution after converting the photoion image shown in Fig. 2.3.8b from pixel coordinates into velocity coordinates via Eq. 2.3.1.

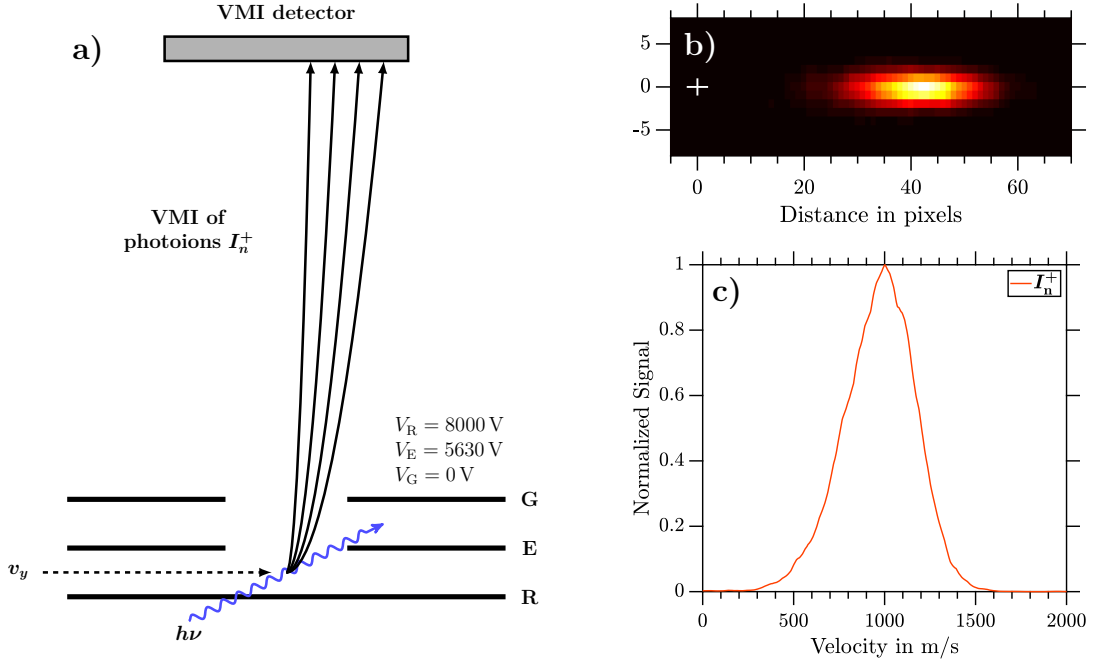


Fig. 2.3.8: (a) Sketch of perpendicular extraction of photoions I_n^+ relative to the molecular beam axis (y -axis). (b) Measured ion image with distances given in pixels at $V_R = 8000$ V, the white cross represents the image center. (c) Experimental velocity distribution retrieved from the ion image.

The average calibration constant $\langle C_{i,j} \rangle$ is determined from several VMI measurements of various cluster sizes m_j at different repeller voltages ($V_{R,i} = 8$ kV, 7 kV and 5 kV). For a single VMI $C_{i,j}$ is determined by

$$C_{i,j} = \frac{E_{\text{kin}}}{r^2 \cdot V_{R,i}} = \frac{m_j \cdot v_{\text{pixel}}^2}{2 \cdot r^2 \cdot V_{R,i}}. \quad (2.3.2)$$

Where the velocity v_{pixel} in pixels per second is calculated via the displacement r and the ion's arrival time at the detector t_{TOF} .

$$v_{\text{pixel}} = \frac{r}{t_{\text{TOF}}} \quad (2.3.3)$$

The dimensions of $\langle C_{i,j} \rangle$ is converted into $[\text{kgm}^2/\text{Vs}^2\text{pixel}^2]$ with the factor k in $[\text{m}^2/\text{pixel}^2]$, which is retrieved from the detector diameter 40 mm measured in pixels.

$$C = \langle C_{i,j} \rangle \cdot k \quad (2.3.4)$$

As mentioned above, with the evaluated cluster beam velocities we are able to synchronise the deflector trigger timings t_1 , t_2 and t_3 relative to the laser trigger t_L . A global optimization of the coil trigger timings is performed in order to achieve highest possible

deflection. The optimisation procedure is described in subsection 3.2.1. Operating the deflector with optimal trigger timings and recording photoions with VMI extraction conditions produces velocity dependent deflection data when compared to deflector ‘off’ measurements. The comparison of the photoion images of NaDME with the deflector switched ‘off’ (Fig. 2.3.9 a) and deflector ‘on’ (Fig. 2.3.9b) illustrates the described technique. Fig. 2.3.9c depicts the calibrated velocity distributions of both ion images.

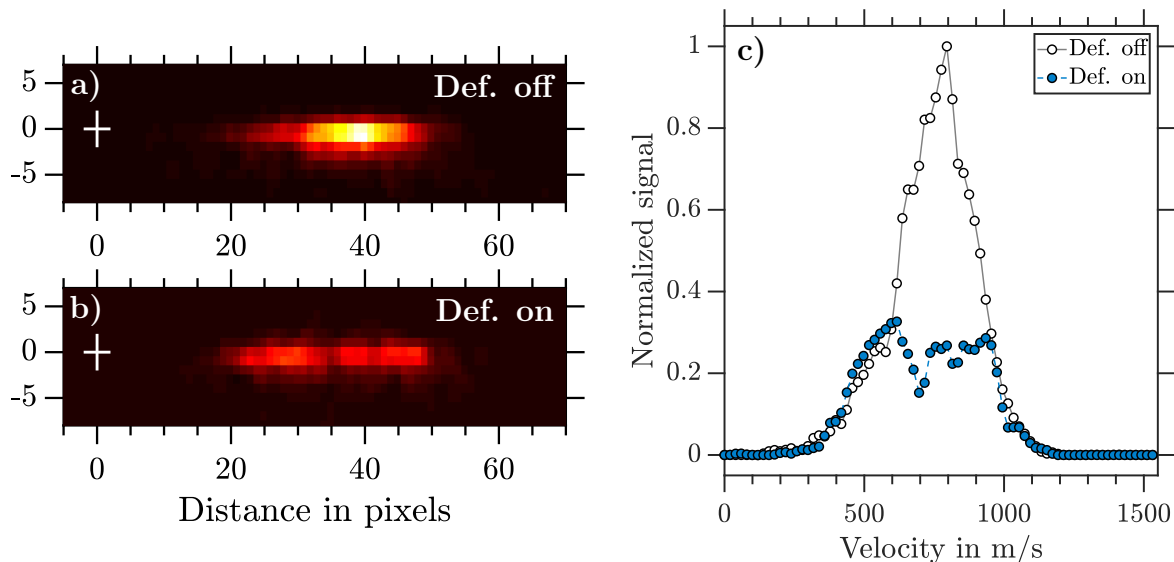


Fig. 2.3.9: (a) NaDME ion image measured in perpendicular extraction at $V_R = 8$ kV while the deflector is ‘off’. (b) NaDME ion image measured while the deflector is ‘on’ with $I_d = 700$ A. The distances of the VMIs are given in pixels. (c) Retrieved velocity distributions of both photoion VMIs.

In a similar fashion, we investigated the deflection contribution of each electromagnetic coil individually, as is presented in chapter 4 for NaNH_3 clusters. The deflection results of $\text{Na}(\text{H}_2\text{O})_n$, $\text{Na}(\text{MeOH})_n$ and $\text{Na}(\text{DME})_n$ presented in chapter 5 are based on photoion VMI measurements. Additional deflection measurements for the investigated sodium-doped solvent clusters are based on time-of-flight mass spectrometry, which is described in the following.

2.3.3 TOF mass spectrometry - deflection measurements

Time-of-flight (TOF) measurements are carried out under optimized TOF extraction conditions summarized in Tab. 2.3.3. We thereby obtain qualitative and quantitative information of the molecular beam, respectively the different cluster sizes and their absolute signal.

Tab. 2.3.3: Optimized TOF extraction conditions.

V_R	V_E	V_{MCP}	V_A
8000 V	6520 V	2200 V	3000 V

Magnetic deflection of paramagnetic clusters is expected to be identified as TOF-signal depletion. In order to investigate deflection induced signal depletion, we choose to record a series of TOF spectra with varied deflector timing t_d relative to the ionising laser timing t_L . The time sequence of a deflection measurement is schematically shown in Fig. 2.3.10.

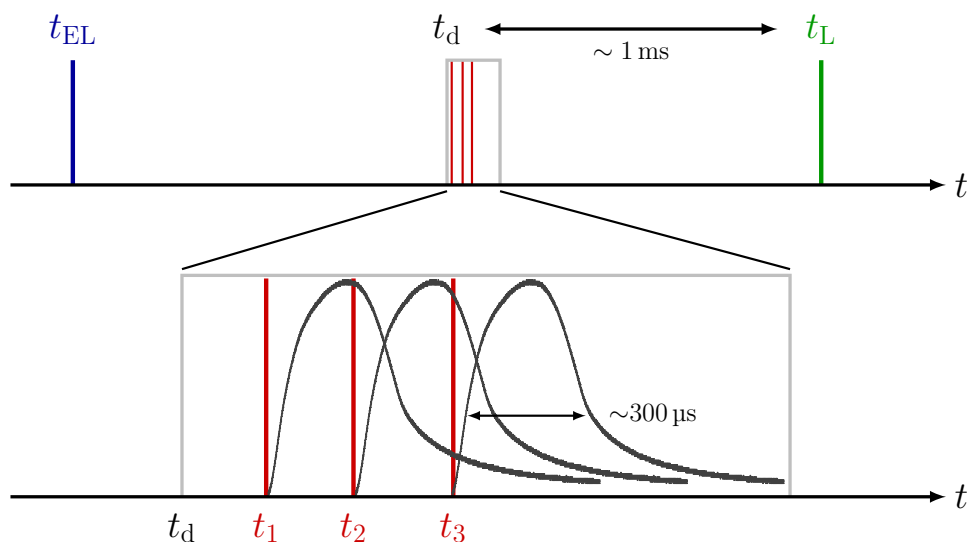


Fig. 2.3.10: Sketch of the timing sequence of the pulsed deflection experiment. The relative timing between deflection t_d and ionization t_L is varied for various TOF measurements. In the case of $\text{Na}(\text{H}_2\text{O})_n$ clusters a pulsed EL-valve was used to generate clusters. The EL-valve trigger timing t_{EL} is set constant during a deflection measurement. The deflector consists of three individual coils, which are operated with their individual trigger timings t_1 , t_2 and t_3 relative to t_d . The lower sketch shows the experimentally measured magnetic field pulses for each coil trigger timing. The figure is adapted with permission from [93] Copyright ©2021 Royal Society of Chemistry.

Each recorded TOF spectrum is transformed from time-scale into m/z -scale, which is described in subsection 2.4.1. The baseline of each TOF trace was fitted using a piecewise cubic Hermite interpolation method and the baseline as well as the background were subtracted (see Fig. 2.3.11a). In addition we applied a Savitzky-Golay finite impulse response smoothing filter with 4th order polynomial and integrated the TOF mass signals (see Fig. 2.3.11b).

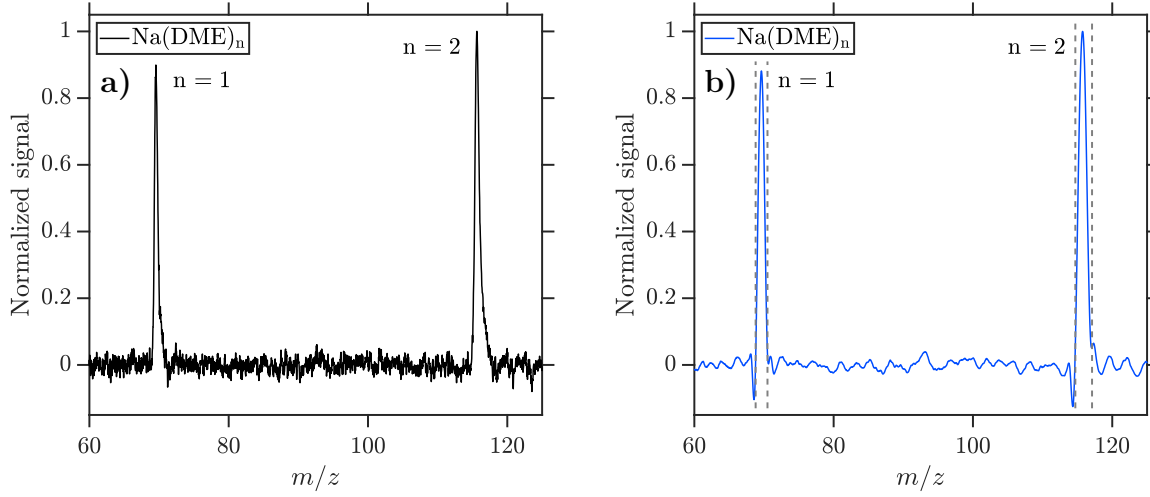


Fig. 2.3.11: (a) Baseline corrected and background subtracted NaDME and Na(DME)₂ TOF signals. (b) Smoothed TOF signals with the integration limits shown as dashed lines.

Relative integrated TOF mass signals θ_{rel} are defined as the ratio of the integrated mass signal with the deflector switched ‘on’ θ_{on} and the deflector switched ‘off’ θ_{off} .

$$\theta_{\text{rel}} = \frac{\theta_{\text{on}}}{\theta_{\text{off}}} \quad (2.3.5)$$

Evaluating θ_{rel} for various t_d is characterised by a relative signal dip with a distinct minima (see Fig. 2.3.12a). The minima of θ_{rel} are analysed as deflection ratios γ_d for different magnetic field strengths which are proportional to the deflector currents I_d (see Fig. 2.3.12b).

$$\gamma_d = 1 - \theta_{\text{rel}} = 1 - \frac{\theta_{\text{on}}}{\theta_{\text{off}}} \quad (2.3.6)$$

If $\gamma_d = 1$, 100% deflection is achieved and would correspond to $\theta_{\text{rel}} = 0$. Thus no cluster signal would be detected. A graphical representation of the deflection evaluation is schematically shown in Fig. 2.3.12.

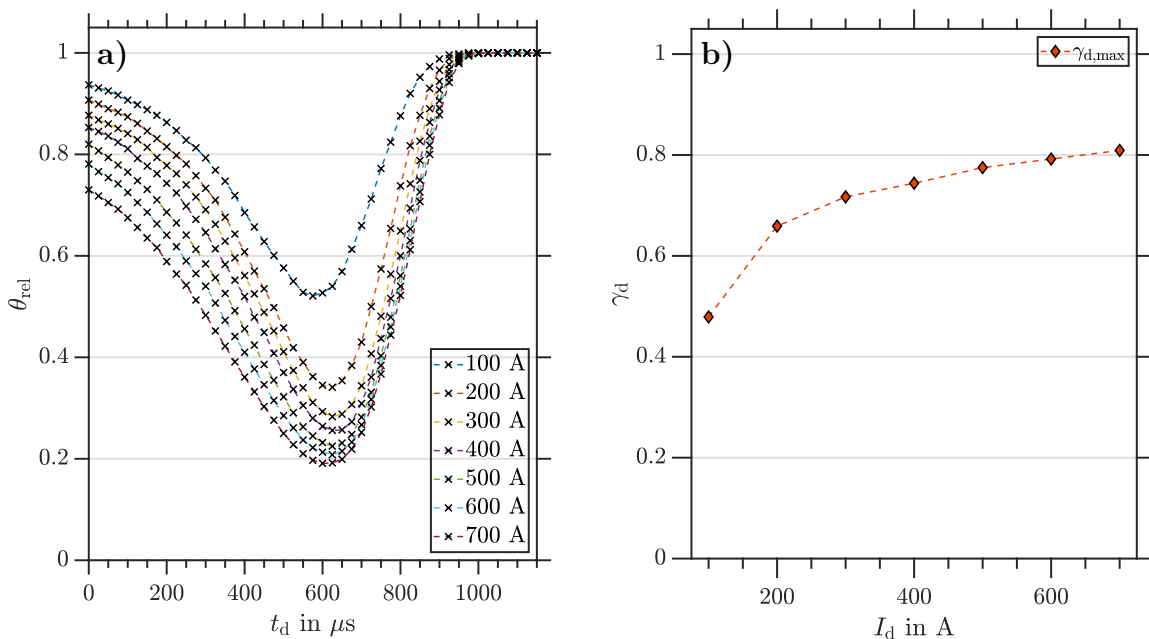


Fig. 2.3.12: The presented data is obtained from MD simulations of hypothetical particles (see subsection 3.2.2): (a) Relative integrated ion signal θ_{rel} as a function of the relative deflector trigger timing t_d with deflector currents $I_d = 100 - 700$ A. (b) Maximal deflection ratio $\gamma_{d,\text{max}}$ (corresponds to minima of θ_{rel}) as a function of the deflector current I_d .

2.4 Velocity map imaging photoelectron spectrometer

The experimental setup used to study the electronic properties of $\text{Li}(\text{DME})_n$ clusters, presented in chapter 8 is shown in Fig. 2.4.1 and has been previously described [26, 31, 30, 2, 40, 25, 97]. For convenience the main aspects are repeated here. The experimental setup consists of three chambers (A-C) separated by skimmers, for a well defined molecular beam and to maintain differential pumping conditions.

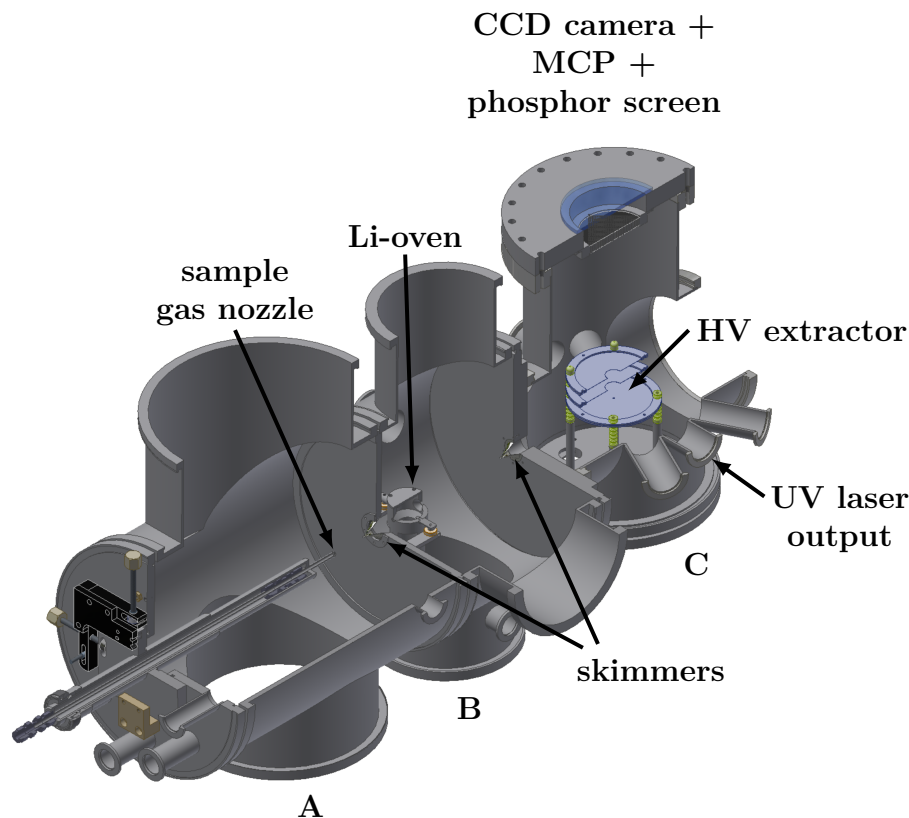


Fig. 2.4.1: Sketch of the experimental setup consisting of the source chamber (A), the Li-oven chamber and the ionization/detection chamber (C).

The source chamber (A) holds the EL-valve to generate $(\text{DME})_n$ clusters via pulsed supersonic expansion of a He/DME gas mixture into vacuum (see subsection 2.1.1). By varying the expansion conditions (stagnation pressure, gas composition and source temperatures) and EL-valve drive settings (pulse width and trigger timing) the solvent cluster size distribution could be controlled. The oven chamber (B) contains the temperature controlled Li-oven, where the doping process of $(\text{DME})_n$ occurs (see subsection 2.1.2) to form $\text{Li}(\text{DME})_n$ clusters. The last chamber is referred to as the detection chamber (C), where the Li-doped clusters are ionized with 266 nm pulse from a Nd:YAG laser (see subsection 2.2.1) and subsequently the photoelectrons (see subsection 2.4.2) and photoions are accelerated by Wiley-McLaren type extractor optimized for either TOF conditions (see Tab. 2.4.1) or VMI conditions (see Tab. 2.4.2). The extraction optics consist of three round metal plates spaced by 15 mm. The ionisation region is located between the repeller and extractor plate. Where the extraction region and a 20 cm field-free drift region are shielded by two concentric μ -metal cylinders. For the given experimental setup the molecular beam axis and the ion flight axis are perpendicular. The perpendicular configuration is useful for measurements of cluster beam velocities (see subsection 2.3.2) and to prevent deposition of non-volatile or low-volatile compounds onto the detector. The position sensitive detector is composed of a pair of 40 mm diameter microchannel plates (MCPs) in a chevron stack which are coupled to a phosphor screen (Photonis USA, Inc; APD) followed by a CCD camera. The front of the MCP assembly is held at ground

and the back plate is biased at up to 2400 V and can be used to ‘gate’ the detector. When gating, we use a high voltage switch (Behlke) to vary the MCP bias voltage by 500 V to ensure that the gain is only high when ions of interest reach the detector. The CCD camera records the luminescences of the screen. Individual frames (12 bit grayscale image, 1/3 inch sensor, 1024×768 pixel) are taken for each laser shot, summed up in real time using NuAcq software [98] and saved to the computer connected to the CCD camera.

2.4.1 Time-of-flight mass spectrometry

The cluster size distributions were determined by mass spectrometry under optimized TOF conditions, which are summarized in Tab. 2.4.1.

Tab. 2.4.1: Optimized TOF extraction conditions.

V_R	V_E	V_{MCP}	V_A
15 000 V	12 330 V	1650 V	3000 V

TOF focusing conditions are defined by the ratio $V_E/V_R \sim 0.8$, with the given settings it is possible to correct for their width in arrival times due to a distribution of the birth coordinates in the ionization volume. Increasing V_R with a constant V_E/V_R allows to measure larger cluster size distributions in a perpendicular extraction configuration. With a perpendicular setup, care must be taken to ensure that the full cluster size distribution fits onto the detector. Otherwise, size-dependent studies of electronic cluster properties become invalid. The mass to charge ratio m/z of the cluster size distributions was calibrated with given equation.

$$m/z = (t_{TOF} - t_0)^2/c \quad (2.4.1)$$

where t_{TOF} is the cluster specific time-of-flight, t_0 the laser trigger timing and c an experimental setup constant. The detection screen functions as an anode which records the signal current generated in the MCPs. The time-dependent current signal is transformed via a homebuilt capacitive decoupling circuit to a time dependent voltage signal. The data is then displayed on an oscilloscope and saved to the computer. Fig. 2.4.2 shows an example TOF mass spectrum of $\text{Li}(\text{DME})_n$ clusters.

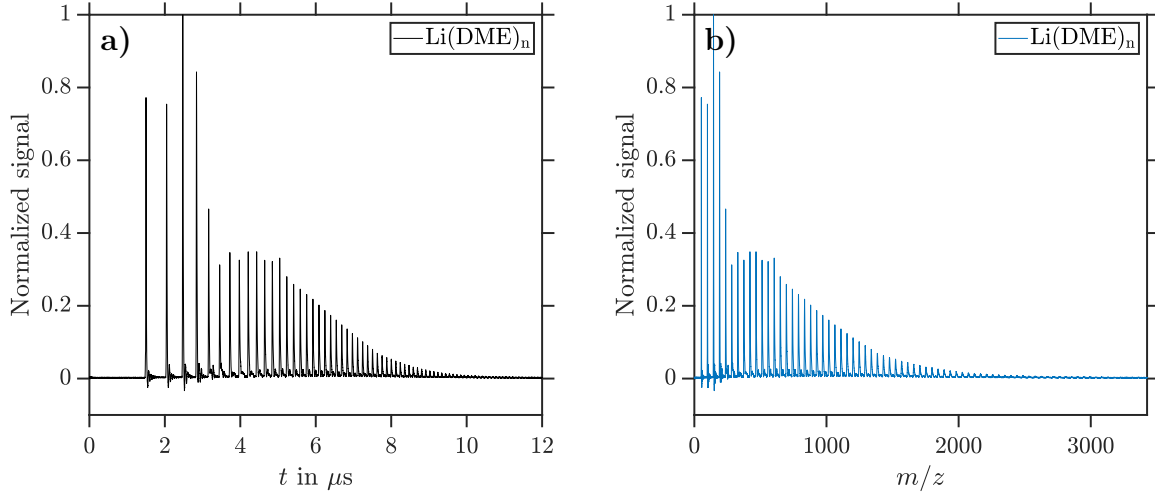


Fig. 2.4.2: (a) TOF-signal of $\text{Li}(\text{DME})_n$ clusters. (b) Corresponding calibrated m/z -signal with equidistant peak spacing ($\text{DME} = 46m/z$).

The cluster size distributions are characterized by an average cluster size $\langle n \rangle$ for cluster size $n > 4$. This is a valid approach, since the photoelectron energy spectrum is resolved for small $\text{Li}(\text{DME})_n$ clusters ($n = 1 - 4$).

$$\langle n \rangle = \frac{\sum_{n=5}^{n_{\max}} A_n \cdot n}{\sum_{n=5}^{n_{\max}} A_n} \quad (2.4.2)$$

A_n is the integrated area of each mass peak n , throughout this work the integration was carried out in time-space.

2.4.2 Photoelectron velocity map imaging

The theory and concepts of velocity map imaging, as well as the applied image reconstruction methods to obtain photoelectron binding energies and photoelectron angular distribution parameters β are discussed in section 3.3. In this section we focus on the experimental techniques, to record velocity map images. Photoelectrons are accelerated under optimized VMI conditions (see Tab. 2.4.2) to achieve kinetic energy focusing at the detector plane.

Tab. 2.4.2: Optimized VMI extraction conditions.

V_R	V_E	$V_{\text{MCP, high}}$	$V_{\text{MCP, low}}$	V_A
-3000 V	-2125 V	1750 V	1250 V	6000 V

The optimal energy focusing conditions are determined by the extraction ratio $V_E/V_R \sim 0.7$. Varying V_R while maintaining the extraction ratio, controls the image size and energy resolution of the VMI in the detector plane. Hereby the size of the image is limited by the screen diameter, for a successful measurement it has to be assured that the photoelectrons of highest kinetic energy are still detectable. Recorded VMIs are reconstructed and

evaluated using the pBASEX [99] and MEVIR [100] algorithm (see section 3.3). The electron kinetic energies E_{kin} are determined by the displacement r in pixels of the image center spot.

$$E_{\text{kin}} = r^2 \cdot V_{\text{R}}/C \quad (2.4.3)$$

where C is a setup dependent calibration constant, which is determined from a recorded VMI of lithium atoms with its radius r and known ionization potential (shown in Fig. 2.4.3). The theory in order to determine the radius of a Newton sphere projected onto a two dimensional detector plane is described in subsection 3.3.2.

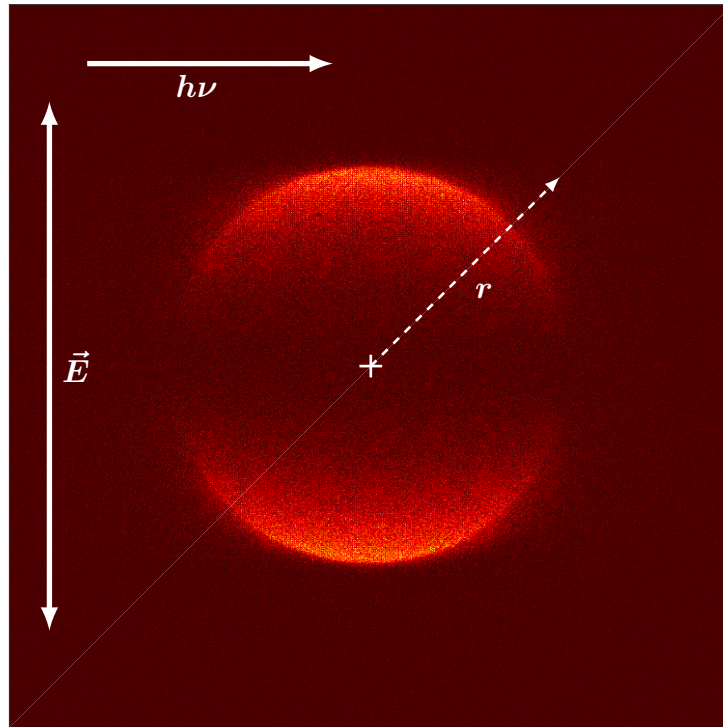


Fig. 2.4.3: Experimental photoelectron VMI of Li. The bold arrows indicate the electric field vector and the propagation axis of the laser light. The dashed arrow shows the radial displacement from the center of the image, shown as white cross.

2.5 Photoelectron-photoion-coincidence-spectrometer

The double imaging photoelectron-photoion-coincidence (i^2 PEPICO) spectrometer used in this work to study $\text{Na}(\text{NH}_3)_n$ (see chapter 7) has been previously described by Garcia, Tang and Nahon [96, 46]. The experimental setup is located at the DESIRS (dichroïsme et spectroscopie par interaction avec le rayonnement synchrotron) beamline of SOLEIL synchrotron and is schematically shown in Fig. 2.5.1.

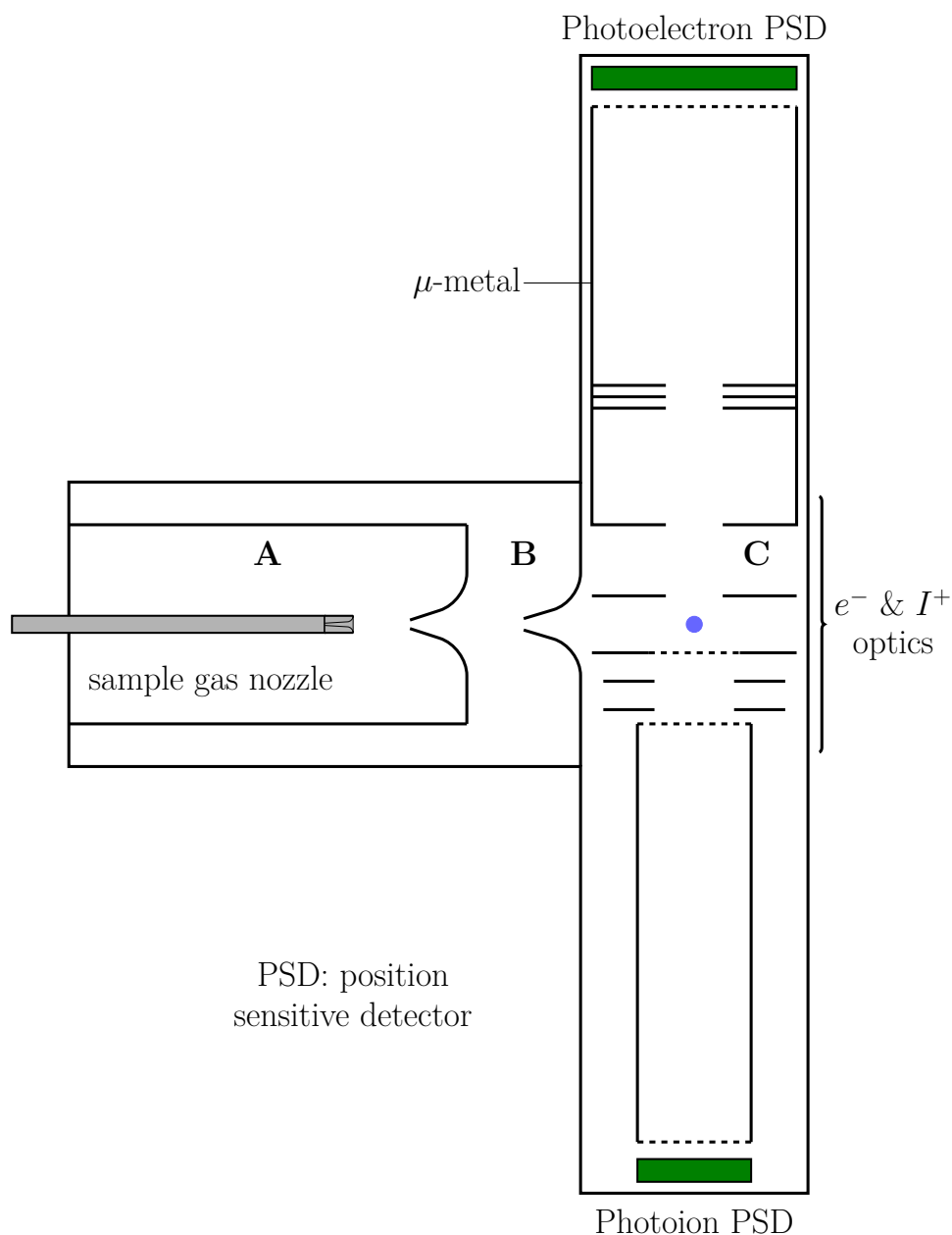


Fig. 2.5.1: Schematic representation of the double imaging photoelectron-photoion-coincidence-spectrometer at DESIRS beamline of SOLEIL synchrotron. The figure is adapted from [101] with permission of S. Hartweg.

The experimental setup is composed of three consecutive vacuum chambers (A-C). In the presented studies small aperture nozzles were installed in source chamber (A) in order to generate continuous supersonic molecular beams. The sample gas nozzle is fixed on a computer controlled x, y, z manipulator to adjust the molecular beam position in vacuum and in real-time. An additional temperature controlled Na-oven was installed in the source chamber (A) to generate sodium-doped clusters (see subsection 2.1.2). After traversing a first skimmer, the molecular beam enters the double-skimmer differential chamber (B). The position of the first skimmer separating both chambers is adjustable in vacuum by another computer controlled x, y, z -manipulator. A thin sliding valve behind the second skimmer is used to isolate the ionisation chamber when chambers (A) and

(B) are vented. After passing through a second skimmer, the molecular beam enters the detection chamber (C) and reaches the center of the DELICIOUS III spectrometer which corresponds to the photoionisation region. Here molecular clusters cross with the synchrotron beam in perpendicular orientation, resulting photoelectrons and photoions are extracted and accelerated vertically in opposite directions by a modified Wiley-McLaren TOF [102] device and detected via VMI [82]. From position sensitive photoion detection and their TOF, recorded with respect to the arrival time of the corresponding electron, it is possible to reconstruct the three dimensional photoion momentum distribution [46]. A second position sensitive detector is used to record photoelectron VMIs which can be processed with ion mass- and momentum-selection filters. With this technique it is possible to retrieve fully cluster size resolved electron VMIs and thus gain cluster size-dependent electronic properties. An Abel inversion algorithm was used to treat electron images to get the electron angular distribution and photoelectron spectra. In the recorded photoion image the different cluster masses are additionally separated spatially. This allows to furthermore filter out for example background signals, by choosing a spatial region of interest.

Chapter 3

Theory & Modelling

3.1 Atoms and clusters in magnetic fields

The theory and models presented in the following sections have been adapted by the works of various groups. The theory on the Zeeman effect for atoms and molecular systems (see sections 3.1.1 and 3.1.2)) is based on the review by Jansen and Merkt [103] (and references therein). The main aspects of the avoided crossing model (see section 3.1.4), is adapted from Xu *et al.* [104, 68]. The thermodynamic based spin relaxation model (see section 3.1.5), refers to the interpretations given by Knickelbein [66] and others [105, 106, 107]. The molecular Landé factor of diatomic systems described in section 3.1.6, is adapted from the theoretical work of Berdyugina and Solanki [60] (and references therein).

3.1.1 Zeeman effect in atoms

The Zeeman effect describes the energy splitting of a state into several components in the presence of an external magnetic field. The initial energy states at zero-field are represented by the Hamiltonian \hat{H}_0 and the interaction with the external magnetic field \mathbf{B} is described by the Zeeman Hamiltonian \hat{H}_{Zeeman} . The Zeeman levels are eigenstates of the resulting Hamiltonian, given by

$$\hat{H} = \hat{H}_0 + \hat{H}_{\text{Zeeman}}, \quad (3.1.1)$$

where the atomic Hamiltonian in the absence of the field \hat{H}_0 is composed of the electronic energy, the spin-orbit interaction and the hyperfine interaction. In terms of the Russell-Saunders (or spin-orbit) coupling approximation (for atoms with small nuclear charges), spin-orbit and hyperfine interactions can be treated for each electronic state separately. The Zeeman interaction is then described by

$$\hat{H}_{\text{Zeeman}} = \frac{\mu_B}{\hbar} (g_L \hat{\mathbf{L}} + g_S \hat{\mathbf{S}}) \mathbf{B} - \frac{\mu_N}{\hbar} g_N \hat{\mathbf{I}} \mathbf{B} \quad (3.1.2)$$

where μ_B is the Bohr magneton, $g_L = 1$ the Landé factor of the orbital angular momentum \mathbf{L} , $g_S \approx 2.00232$ the Landé factor of the free electron spin angular momentum \mathbf{S} , μ_N the

nuclear magneton, g_N the Landé factor of the nuclear spin angular momentum \mathbf{I} and \hbar the reduced Planck constant. The nuclear magneton μ_N is approximately 10^3 smaller than μ_B , we therefore neglect contributions of the nuclear spin term for all following considerations. The magnetic moment $\boldsymbol{\mu}$, within sole spin-orbit coupling, is expressed by

$$\boldsymbol{\mu} = -\frac{\mu_B (g_L \mathbf{L} + g_S \mathbf{S})}{\hbar}, \quad (3.1.3)$$

and the Zeeman energy splitting ΔE_{Zeeman} is given by

$$\Delta E_{\text{Zeeman}} = -\boldsymbol{\mu} \cdot \mathbf{B}. \quad (3.1.4)$$

The interaction of the magnetic moment with the magnetic field causes each total angular momentum state $\mathbf{J} = \mathbf{L} + \mathbf{S}$ level to split into $2J + 1$ Zeeman components with its projections onto the magnetic field axis $M_J = -J, -J + 1, \dots, J - 1, J$. In the case of s -electrons, $L = 0$ and the magnetic moment is purely composed of the electronic spin \mathbf{S} . The corresponding Zeeman effect causes a splitting into $2S + 1$ components, with their projection $m_S = -S, \dots, +S$ onto the magnetic field axis. For example, sodium atoms Na ($3s^1$) show a Zeeman diagram consisting of two Zeeman levels according to their spin states $m_S = -1/2$ and $+1/2$.

3.1.2 Zeeman effect in sodium-doped clusters

Unlike atoms, molecules and clusters have additional vibrational and rotational degrees of freedom which may contribute to the total angular momentum \mathbf{J} . The total angular momentum \mathbf{J} for a general molecule or cluster is said to consist of four different angular momenta, namely the angular momentum of molecular rotations \mathbf{R} , orbital angular momentum of electrons \mathbf{L} , spin angular momentum of electrons \mathbf{S} and spin angular momentum of nuclei \mathbf{I} . Calculating the Zeeman states with contributions of all four angular momenta is demanding, since angular momenta couplings are possible among all four angular momenta. Methods to calculate the Zeeman effect of an asymmetric-top free radical, with contributions of the four angular momenta are summarised by Sears [108]. For sodium-doped clusters we introduce the following approximations to simplify the couplings of angular momenta to the dominant contributions. As mentioned above, in a first approximation we neglect contributions of the nuclear spin term. In addition we assume $L \approx 0$, this is reasoned by former angle-resolved photoelectron studies of sodium-doped clusters [1, 2] which showed mainly s -character for the highest occupied molecular orbital (HOMO) of the solvated electron. We thus expect minor contributions from the spin-orbit coupling term and pronounced angular momenta contributions of \mathbf{S} and \mathbf{R} . Within these assumptions the Zeeman interaction for sodium-doped clusters is given by

$$\hat{H}_{\text{Zeeman}} = \frac{\mu_B}{\hbar} (g_R \hat{\mathbf{R}} + g_S \hat{\mathbf{S}}) \mathbf{B} \quad (3.1.5)$$

where g_R is the Landé factor corresponding to the rotational angular momentum. For given case, \mathbf{R} and \mathbf{S} add to form \mathbf{J} with corresponding Zeeman energies expressed by

$$E(J, M_J) = \frac{\mu_B}{\hbar} g_J M_J B \quad (3.1.6)$$

where g_J represents the molecular Landé factor and M_J is the projection of the total angular momentum onto the magnetic field axis. Approximated solutions of g_J in the limiting Hund's cases (a) and (b) for diatomic systems are shown in section 3.1.6.

3.1.3 The force field of an inhomogeneous magnetic field

In the case of an inhomogeneous magnetic field a cluster in a state M_J with corresponding magnetic moment μ_J will experience a force \mathbf{F} , defined in the direction of the negative Zeeman potential gradient.

$$\mathbf{F} = \nabla (\boldsymbol{\mu}_J \cdot \mathbf{B}) = -\mu_B g_J M_J \begin{pmatrix} \partial B / \partial x \\ \partial B / \partial y \\ \partial B / \partial z \end{pmatrix} \quad (3.1.7)$$

In the case of free spin 1/2 particles the force is expressed in similar manner, although with $\mu_J = \mu_0$, $g_J = g_S$ and $M_J = m_S$. In our experiments the main component of the magnetic field gradient is defined in the z -direction. The resulting force component in z is described by

$$F_z = -\mu_z \frac{\partial B}{\partial z} \quad (3.1.8)$$

with the projection of the magnetic moment μ_z onto the gradient axis. The resulting force causes an acceleration in z -direction for $m_S = +1/2$ (low-field seeking) and $m_S = -1/2$ (high-field seeking) particles. A spin 1/2 particle beam traversing the magnetic field gradient orthogonal with velocity v_y results in two diverging beamlets corresponding to their spin state m_S . While particles with a total spin of $S = 0$ do not experience any force and the cluster beam trajectories are not affected by the magnetic field gradient. The described deflection trajectories for $m_S = \pm 1/2$ are visualised in Fig. 3.1.1.

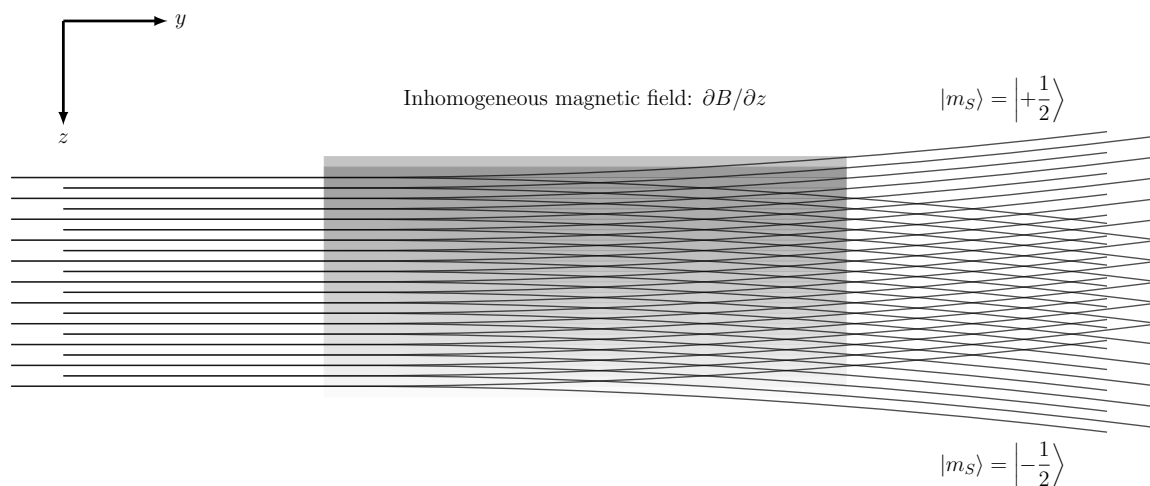


Fig. 3.1.1: Graphical representation of cluster beam trajectories with the spin states $m_S = -1/2$ and $m_S = +1/2$, traversing an inhomogeneous magnetic field with a gradient in z -direction ($\partial B/\partial z$). The figure is adapted with permission from [93] Copyright ©2021 Royal Society of Chemistry.

The x, z coordinates of the individual spin states $m_S = -1/2$, $S = 0$ and $m_S = +1/2$, obtained from MD simulations (see subsection 3.2.2) after experiencing the magnetic field gradient are shown in Fig. 4.2.4 of chapter 4. An aperture of suitable size in the x, z plane, allows for magnetic selection regarding the deflection in z -direction of the particles. For clusters with a distribution of populated M_J states, an effective broadening of the molecular beam is expected, which in our experiments would be observed as reduced deflection.

The number of Zeeman levels $E(J, M_J)$ for large paramagnetic clusters increase significantly, due to small rotational constants which result in dense rotational states (see chapter 6). Quantum chemical calculations of spin-rotational Zeeman-like levels becomes increasingly time consuming for larger cluster systems. We therefore choose to describe clusters by their density of thermally accessible rovibrational states and discuss trends in terms of the simplified avoided crossing model and spin relaxation model, presented in the following.

3.1.4 Avoided crossing model

The avoided crossing model is based on the sole coupling of rotation and spin angular momentum. Within this assumption spin-rotation coupling causes an increase in the total number of Zeeman-like levels from $2S + 1$ to $(2S + 1)(2R + 1)$ given by [109]

$$\sum_{J=|R-S|}^{R+S} 2J + 1 = (2S + 1)(2R + 1). \quad (3.1.9)$$

where corresponding Zeeman energies are expressed as $E(J, M_J)$. In the case of vanishing spin-rotational coupling, the corresponding eigenstates are described as uncoupled (diabatic) with $\mathbf{J} = \mathbf{S}$ and $m_S = \pm 1/2$ Zeeman splitting is expected (neglecting all other contributions

of angular momenta). However, the states are in general spin-rotational coupled and the cluster Zeeman levels form coupled (adiabatic) states [104, 68]. For two states ϕ_i and ϕ_j with same \mathbf{J} but different \mathbf{R} and \mathbf{S} the spin-rotation coupling causes an interaction of the two levels and the formation of avoided crossings between the intersecting states. The Hamiltonian at the avoided crossing can be expressed as a perturbation of the uncoupled (diabatic) states E_i and E_j ,

$$\hat{H}_{\text{AVC}} = \begin{bmatrix} E_i & \Delta_{SR} \\ \Delta_{SR} & E_j \end{bmatrix} \quad (3.1.10)$$

$\Delta_{SR} \equiv \langle \phi_i | \hat{H}_{\text{couple}} | \phi_j \rangle$ is the matrix element that corresponds to the spin-rotation coupling. Two important aspects for spin-rotational coupled states are noted. At the avoided crossing, the total magnetisation of the two levels is conserved and the spin state of each of the two adiabatic states reverse their sign after the avoided crossing. The latter transition between adiabatic states is commonly known as ‘spin flip’ process where the total angular momentum $\Delta J = 0$ is conserved. For systems with $m_S = \pm 1/2$ ‘spin flips’ are defined by $\Delta m_S = \pm 1$, subsequently the rotational angular momentum will change its quantum number $\Delta M_R = \pm 1$ to conserve \mathbf{J} , given by

$$|R, M_R\rangle |S, m_S\rangle \xrightarrow{\text{spin flip}} |R, M_R + \Delta M_R\rangle |S, m_S - \Delta m_S\rangle. \quad (3.1.11)$$

Where m_S and M_R specify projections of the angular momenta \mathbf{S} and \mathbf{R} onto a fixed axis, which we choose in direction of the external magnetic field gradient z -axis. In the case of a spin 1/2 system ‘spin flips’ are only allowed for neighbouring rotational states. In a two-level system, the probability of traversing E_i and E_j adiabatically p_{ad} can be estimated by the Landau-Zener formula [68, 110]. The Landau-Zener formula is an analytical solution of the equation of motion describing the transition dynamics of a two-level system. Analytical solutions are found within the Landau-Zener approximation which consists of the following simplifications. The perturbation parameter Δ_{LZ} is a known linear function of time, the energy separation of the diabatic states varies linearly with time and the spin-rotational coupling Δ_{SR} matrix elements are independent of time.

$$p_{\text{ad}} = 1 - \exp\left(-\left(\frac{\Delta_{SR}}{\Delta_{\text{LZ}}}\right)^2\right) \quad (3.1.12)$$

$$\Delta_{\text{LZ}}^2 = \mu_B \hbar |\Delta m_S| dB/dt. \quad (3.1.13)$$

While traversing the deflector with an approximate time-dependent magnetic field change $dB/dt \sim 1 \times 10^3 \text{ T/s}$ and estimated values of $\Delta_{SR} \sim 10 \times 10^{-7} \text{ eV}$ [68] $p_{\text{ad}} \approx 1$ is obtained. Thus it is expected that the avoided crossings are traversed adiabatically and the spin state is able to always flip. For sodium-doped clusters with rotational constants in the range of $\langle B \rangle_{\text{rot}} \approx 0.05 - 4 \text{ cm}^{-1}$ (see Tab. 6.3.2-6.3.5), dense rotational levels $\rho_{\text{rot}} \sim 1/\langle B \rangle_{\text{rot}}$

are expected within Zeeman energy splitting $\Delta E_{\text{Zeeman}} = 2g_S\mu_B SB_{\text{max}} \approx 5.6 \text{ cm}^{-1}$, at $B_{\text{max}} = 6 \text{ T}$. We thus expect several avoided crossings among the Zeeman levels and effects on the observed deflection behaviour due to changes in the cluster trajectories, induced by spin flip processes. Xu *et. al* [68] showed that several traversed avoided crossings among adiabatic states can be expressed as so called average net state. It was reasoned that in magnetic field ranges $\Delta B \sim \text{mT}$ fine details of the adiabatic states cannot be resolved in current Stern-Gerlach deflection experiments. Nevertheless, averaging the adiabatic states over the experimental magnetic field range ΔB results in average net states which are described as follows: At low fields, the average net states exhibit parabolic behaviour and at high fields linear correlations. Note that the average slope at a given magnetic field strength resembles the effective net magnetic moment. Since all of the average states decrease with increasing field, asymmetric deflection to one side is expected for spin-rotational coupled systems with dense rotational levels. Walter de Heer and co. workers [104, 68] experimentally observe one-sided deflection and discuss their findings in terms of the avoided crossing model. For cluster with dense rotational energies thermally accessible, we would expect a corresponding distribution of intrinsic effective magnetic momenta, with $\mu_{\text{eff}} \leq \mu_0$. In our experiments this would be observed as molecular beam broadening and reduced deflection when compared to the free $m_S = \pm 1/2$ system. A quantitative description of the expected deflection behaviour derived from the avoided crossing model is given in [68]. Assuming a Boltzmann distribution of cluster energy states a distribution of the magnetisation follows

$$P(\bar{\mu}_z) = \left| \frac{\rho(E_0) \cdot \exp(-E_0/k_B T)}{\partial \bar{\mu}_z / \partial E} \right|, \quad (3.1.14)$$

where the density of states is given by $\rho(E_0)$. For high magnetic fields $\bar{\mu}_z$ saturates at a single value $\mu = g_J\mu_B J$ and the distribution of $\bar{\mu}_z$ is described by a delta function. Whereas at low fields the magnetization distribution depends on the thermal excitation of the degrees of freedom and analytical solutions can only be given in specific cases [68]. For thermal population of high density of states the avoided crossing model predicts similar magnetization distributions as the spin relaxation model (SRM) [66, 105, 106, 107]. Xu *et al.* [68] state that the SRM is the high density of states limit of the avoided crossing model.

3.1.5 Spin relaxation model

The SRM determines the intrinsic magnetic moment of an isolated cluster via the thermodynamics based analysis of the average magnetic moment projected on the magnetisation axis (z -direction) $\bar{\mu}_z$. At higher temperatures the state density acts as a heat bath to exchange angular momentum and energy in order to allow for spin relaxation processes [104, 66, 105, 106, 107]. This model assumes thermal equilibrium among the Zeeman-like levels [111]. Where the statistical thermodynamic based Brillouin model $\mathcal{B}_J(\eta)$ of

paramagnetism describes the magnetisation as a function of temperature of the intrinsic magnetic moment $\mu = g\mu_B J$.

$$\bar{\mu}_z = \mathcal{B}_J(\eta)\mu \quad (3.1.15)$$

$$\bar{\mu}_z = \left[\frac{2J+1}{2J} \coth\left(\frac{2J+1}{2J}\eta\right) - \frac{1}{2J} \coth\left(\frac{\eta}{2J}\right) \right] \mu \quad (3.1.16)$$

with $\eta = \mu B/k_B T_{\text{rot}}$. In the limit of $J \rightarrow \infty$ the Brillouin function reduces to the Langevin function $\mathcal{L}(\eta)$.

$$\bar{\mu}_z = \lim_{J \rightarrow \infty} \mathcal{B}_J(\eta)\mu = \mathcal{L}(\eta)\mu = \left(\coth(\eta) - \frac{1}{\eta} \right) \mu \quad (3.1.17)$$

In the low-field limit $\eta \rightarrow 0$ ($\mu B \ll k_B T_{\text{rot}}$) the average magnetic moment in z -direction reduces to Curie's Law

$$\bar{\mu}_z = \lim_{\eta \rightarrow 0} \mathcal{L}(\eta)\mu = \mu^2 B/3k_B T_{\text{rot}}. \quad (3.1.18)$$

In the high-field limit ($\mu B \gg k_B T_{\text{rot}}$) the average magnetic moment along the magnetisation axis is described by

$$\bar{\mu}_z = \mu. \quad (3.1.19)$$

The different thermodynamics-based analytical functions are shown in Fig. 3.1.2.

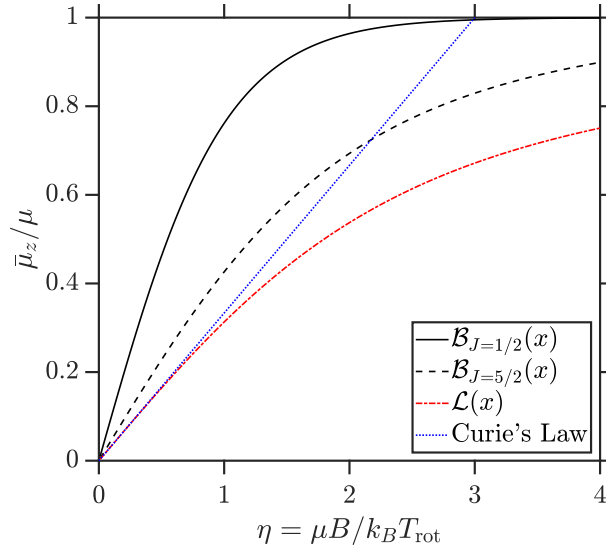


Fig. 3.1.2: Average magnetic moment in z -direction $\bar{\mu}_z/\mu$, as described by the Brillouin function $\mathcal{B}_J(\eta)$, the Langevin function $\mathcal{L}(\eta)$ and Curie's Law.

For clusters with dense rovibrational eigenstates and high internal temperatures, a thermodynamic description of the magnetisation distribution becomes significantly more valid. In Stern-Gerlach experiments of such systems, only a weak broadening of the molecular beam was observed [112, 113, 69, 114, 80]. Within our experiments we would observe cluster systems with similar deflection behaviour as slightly or non-deflected.

3.1.6 Molecular Landé factor

We here present the molecular Landé factor g_J for a diatomic system as has been approximated by Berdyugina and Solanki [60]. We aim to provide a qualitative trend of how g_J evolves towards higher J and contribute to the deflection behaviour of sodium-doped clusters. Theoretical investigations on the molecular Zeeman effect for diatomic [58, 59, 115, 60, 103] and polyatomic [116, 108, 117] systems have been carried out by various groups. An overview of the theory of the molecular Zeeman effect for diatomic systems in the limiting Hund's coupling cases (a) and (b), as well as for the intermediate coupling case (a-b) are given by Berdyugina and Solanki [60]. In Hund's coupling case (a), the angular momenta of electron orbital and spin are coupled to the internuclear axis and interact very weakly with the rotational angular momentum. In Hund's case (b) the orbital angular momentum is coupled to the molecular axis, whereas the electron spin is decoupled or very weakly coupled to the axis [118]. The molecular Landé factor g_J in both cases includes contributions from the electron spin angular momentum, orbital angular momentum and rotational angular momentum. The corresponding expression in Hund's case (a) is given by [60]

$$g_J^{(a)} = \frac{(g_L \Lambda + g_S \Sigma) \Omega}{J(J+1)} \quad (3.1.20)$$

with the projection of the spin angular momentum onto the internuclear axis Σ , Λ is the projection of the orbital angular momentum onto the internuclear axis and Ω is the corresponding projection of the total angular momentum. Whereas in Hund's case (b) the molecular Landé factor can be approximated by [60]

$$g_J^{(b)} = \frac{g_L}{2J(J+1)} \left[\frac{\Lambda^2 (J(J+1) + R(R+1) - S(S+1))}{R(R+1)} \right] + \frac{g_S}{2J(J+1)} [J(J+1) - R(R+1) + S(S+1)] \quad (3.1.21)$$

For example, in a diatomic systems where $\Lambda = 0$ and $S \neq 0$, the coupling of spin and rotations is described by Hund's case (b) [119, 118]. The cluster Landé factor g_J for both limiting coupling cases decreases towards higher J states, which is expressed as reduced Zeeman energy splitting which is expected to cause reduced magnetic deflection. For a graphical representation of the Hund's coupling cases see [60, 119]. Cluster Landé factors, are presented as part of the outlook in chapter 6.

3.2 Modelling of the pulsed Stern-Gerlach deflection

In order to achieve successful deflection measurements with our pulsed Stern-Gerlach setup, it is important to synchronise the relative time delays between magnetic field pulse and

laser. The optimisation of deflector timings for a given molecular beam velocity is achieved with a two dimensional space-time model. Further characterisation and verification of experimental deflection results are carried out by comparison of experimental results with molecular dynamics simulations of deflected particles. In the following sections, we present the models used to characterise the pulsed Stern-Gerlach deflection.

3.2.1 2D Space-Time Model

Our Stern-Gerlach deflector consists of a series of three electromagnets (see section 2.3.1), which are pulsed with their individual trigger timings t_1 , t_2 and t_3 . In order to achieve sufficient magnetic deflection of paramagnetic clusters, the electromagnetic trigger timings relative to the laser timing t_L have to be synchronised. Molecular beams generated via continuous supersonic expansions (see section 2.1.1) at all points along their propagation axis exhibit the characteristic cluster velocity distribution. In order to fully sample this parameter space we choose a method inspired by ray tracing. We employ a 2D space-time model where the position along the central axis of the molecular beam (y -coordinates) and the time axis (t -coordinates) are considered. In space this model uses y -coordinates corresponding to the dimensions of the electromagnets ($y_1 - y_3$) and ionisation region y_L . In time the model uses the duration of a square wave pulse ($300 \mu\text{s}$ starting at each trigger timing: t_1, t_2, t_3) and the timing of the ionisation laser pulse t_L . A graphical representation of the 2D space-time model is shown in Fig. 3.2.1.

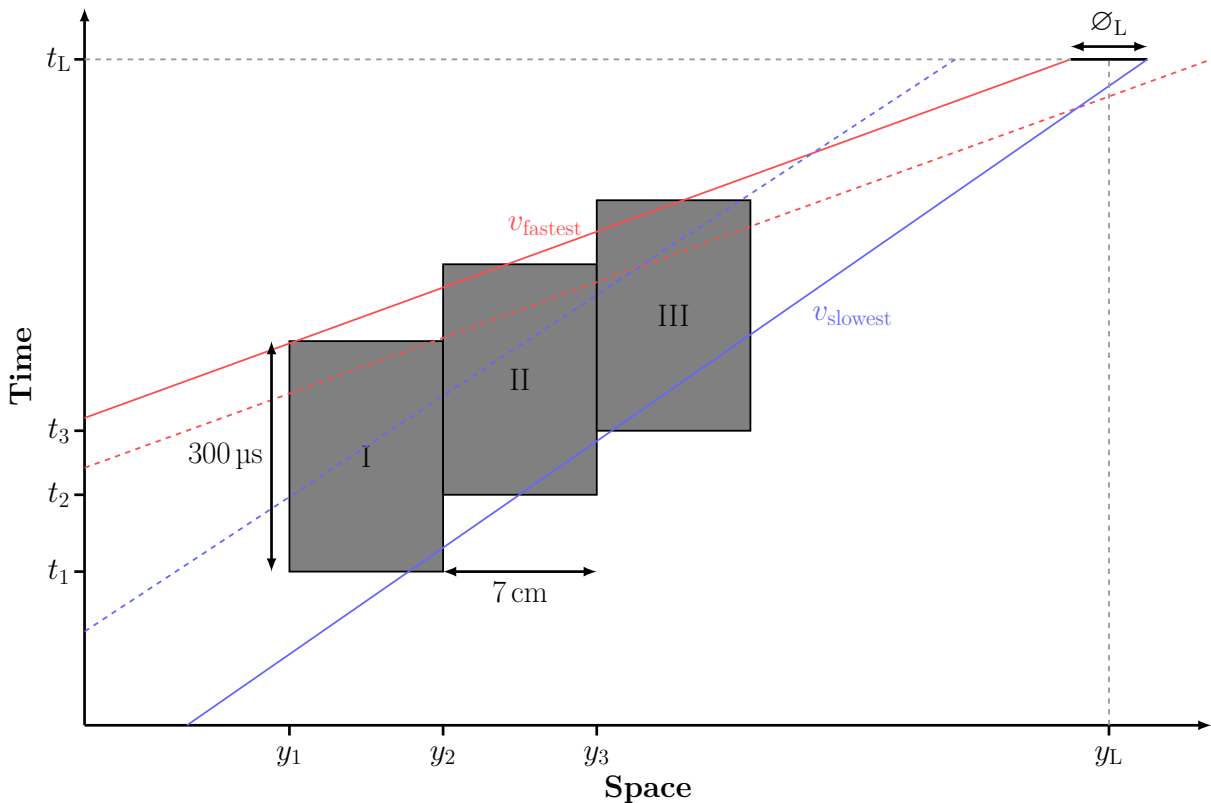


Fig. 3.2.1: Graphical representation of a 2D space-time model to optimise $\gamma_d(t_1, t_2, t_3)$ for maximal possible deflection. See text for further details.

The final parameter is a threshold value, which is used to decide if a particle was deflected or not. A particle is considered to be deflected if the time it spends in the magnetic field is above this threshold. In our model the magnetic pulse is simplified as a box (magnet length: 7 cm \times on-time: 300 μ s) and the ionisation volume is represented by a 1D line (\varnothing_L) located at the ionisation time. Cluster trajectories are represented as straight lines in this plane, with a slope depending on their inverse velocity. A part of the rays will intersect with the magnetic field pulse boxes, as a function of their slopes and ionisation coordinate. These intersections reflect the interaction time with the magnetic field. Finally, the results are scaled with a experimentally determined velocity distribution. This converts the uniform set of trajectories into realistic intensities and facilitates the computation of γ_d . A global optimisation algorithm was used to calculate $\gamma_d(t_1, t_2, t_3)$ with a scatter-search mechanism together with a sequential quadratic programming method for the refinement stage.

In the case of a pulsed supersonic expansion, the rays of cluster trajectories are additionally defined by their time of birth which corresponds to the opening time of the EL-valve t_{EL} . The relative time of valve and laser Δt_{L-EL} defines the observable velocities (see Fig. 2.1.3b). With experimentally determined velocity distributions (see section 2.3.2) we are able to calculate at which time each ray enters the electromagnets. By regarding the limiting cases of $v_{fastest}$ reaching the beginning ($y_L - 0.5 \cdot \varnothing_L$) and $v_{slowest}$ reaching the end ($y_L + 0.5 \cdot \varnothing_L$) of the ionisation region, we determine the limiting time window $\Delta t_{E,i}$ ($i = 1, 2, 3$) at the entrance of each electromagnet (y_1, y_2, y_3).

The optimal deflector trigger timings are obtained by overlaying the limiting time window and magnetic field pulse symmetrically in time.

$$t_i = t_{E,\min,i} - \left(300 \mu\text{s} - \frac{\Delta t_{E,i}}{2} \right) \quad \text{with} \quad i = 1, 2, 3 \quad (3.2.1)$$

Here, $t_{E,\min,i}$ is the earliest entering time at each coil, defined by the slowest velocity reaching the end of the ionization region. Evaluating velocity dependent deflector timings allows us to focus the magnetic field pulses on specific velocity components and thus retrieve velocity dependent deflection data, as are presented in chapter 5.

3.2.2 Molecular Dynamics Model

In order to predict the performance of the deflector and verify experimental magnetic deflection results, we choose a molecular dynamics (MD) approach which simulates the cluster trajectories from deflector entry up to the ionisation region. Newton's equations of motion are numerically integrated with the Verlet algorithm [120]. In the given model the cluster beam is defined by the initial coordinates (x, y, z) and momentum \mathbf{p}_i of each particle, where the mass of the particle corresponds to the cluster mass of interest. The initial particle coordinates are defined as a Gaussian beam profile, where the y -coordinates are defined by the y -position of the entrance skimmer and x, z -coordinates are defined by the diameter of

the entrance skimmer. The initial velocities in the molecular beam direction (y -direction) are randomly sampled from experimentally determined cluster velocity distributions (see section 2.3.2). The corresponding initial velocities in x - and z -direction are retrieved from the molecular beam divergence angle (0.17°) and the velocity component in y -direction. In order to achieve nearly continuous sampling of initial parameters, we modelled $10^5 - 10^6$ particles to achieve sufficient statistics. The experimental dimensions of the deflector, flight distances, skimmer diameters and positions, and the ionisation region are defined in our MD model (see section 2.3.1).

The inhomogeneous magnetic field of the deflector with its magnetic field gradients $\partial B/\partial x$ and $\partial B/\partial z$ are obtained from two dimensional COMSOL simulations of the deflector cross section at a DC current of 1000 A (see Fig. 2.3.3). The gradients of the Zeeman potential define the force field \mathbf{F} acting on $m_S = \pm 1/2$ particles (neglecting contributions from other angular momenta).

$$V_{\text{Zeeman}} = \frac{\mu_B g_s}{\hbar} \nabla (\mathbf{S} \cdot \mathbf{B}) \quad (3.2.2)$$

$$\mathbf{F} = \nabla (\boldsymbol{\mu}_0 \cdot \mathbf{B}) = -\frac{\mu_B g_s}{\hbar} \nabla (\mathbf{S} \cdot \mathbf{B}) \quad (3.2.3)$$

The magnetic field gradient in the z -direction causes a deflecting force in either the positive or negative z -direction, resulting in a diverging beam of $m_S = \pm 1/2$ particles. In the center of the flight channel ($x = 0$), $\partial B/\partial z$ is approximately constant. The gradient in x -direction causes one spin component to diverge while it focuses the other spin component. Since the deflector is operated in a pulsed manner the force field only acts during the on-time of the magnetic field pulses. In the experiment, the on-time of the magnetic field is defined by the electromagnetic trigger timings t_1 , t_2 and t_3 and the time dependent magnetic field profiles (see Fig. 2.3.7). The magnetic field pulses were measured for various peak currents and are used as an input parameter for the MD simulations. I_d specific scaling factors f_B of the force field are determined in relation to the integrated magnetic field pulse profile at 1000 A. These scaling factors are shown in Fig. 3.2.2.

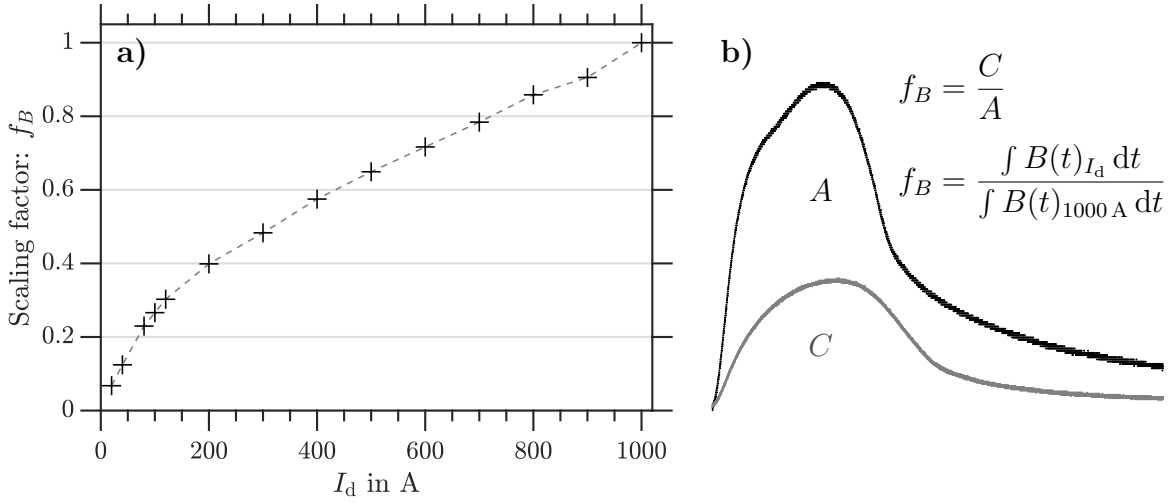


Fig. 3.2.2: (a) I_d specific scaling factor f_B of the force field. (b) Integrated magnetic field pulses $B(t)$ at $I_d = 1000$ A (A) and at $I_d < 1000$ A (C) to retrieve f_B . See Fig. 2.3.7 in chapter 2 for absolute magnetic field pulses.

Additional magnetic field measurements at the end of each metal bridge showed approximately 0.2 of the peak pulses inside the deflector flight channel. The force field in the epoxy layers is therefore defined to be $0.2 \cdot f_B$ of the current specific scaling factors of the electromagnetic coils. Each electromagnet is thus divided into three magnetic field scaling sections along the molecular beam axis. In total the deflector is simulated with nine different scaling zones Z1 – Z9, as shown in Fig. 3.2.3.

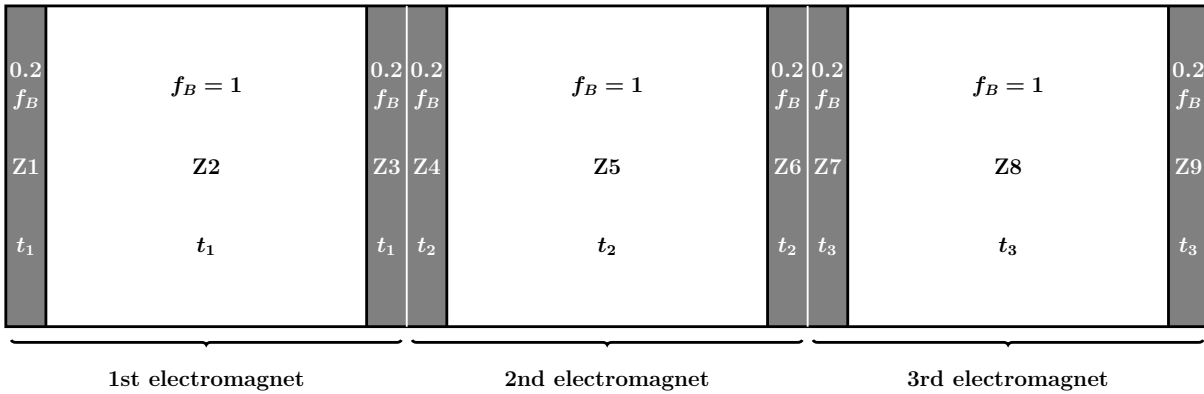


Fig. 3.2.3: The deflector as defined in our MD simulations is composed of nine zones Z1 – Z9. Current specific scaling factors f_B and deflector trigger timings t_1 , t_2 and t_3 are given for each deflector zone.

In the experiment, not all particle trajectories will reach the ionisation region. With that in mind, the following conditions are implemented into our simulations. Particles which collide with the deflector walls are considered as ‘lost’. Only particles that are in the ionisation region (Gaussian laser beam profile of 4.8 mm FWHM) at time t_L can be detected.

The MD simulation output consists of x, y, z -coordinates and corresponding momenta p_x, p_y, p_z for particles of spin states $-1/2, 0$ and $+1/2$. Since the calculations are carried

out for the three spin states, the relative signal θ_{rel} at the ionisation region is calculated by following equation.

$$\theta_{\text{rel}} = \frac{\theta_{+1/2} + \theta_{-1/2}}{2\theta_{S=0}} \quad (3.2.4)$$

$$\gamma_{\text{d}} = 1 - \theta_{\text{rel}} = 1 - \frac{\theta_{+1/2} + \theta_{-1/2}}{2\theta_{S=0}} \quad (3.2.5)$$

where $\theta_{+1/2}$, $\theta_{-1/2}$ and $\theta_{S=0}$ are the number of particles of each individual spin state which are ionised at t_{L} . Simulations of trajectories without magnetic field $B = 0$ are equivalent to $S = 0$ trajectories. Therefore, $\theta_{S=0}$ represents the particle trajectories when the deflector is switched off. Varying the deflector timing t_{d} relative to the laser timing t_{L} and evaluating θ_{rel} for each timing, leads to a relative signal dip (see for example Fig. 3.2.4 and 3.2.5) with a distinct minimum. The MD simulations are compared to experimental deflection measurements, to support the characterisation of sodium-doped solvent clusters in their magnetic properties.

We further introduce an additional (optional) scaling factor in order to account for possible intracuster spin relaxation effects. We choose to scale the magnetic moment with an exponential decay, defined by the interaction time with the magnetic field t_{m} and a characteristic relaxation time τ .

$$\mu_{\text{eff}} = \mu_0 \cdot \exp\left(-\frac{t_{\text{m}}}{\tau}\right)$$

$$\mathbf{F} = \nabla (\mu_{\text{eff}} \cdot \mathbf{B})$$

By sampling various values of τ and comparing simulations to experimental deflection results, we estimate characteristic spin relaxation times τ of the investigated clusters. With modelled effective magnetic moments μ_{eff} we are able to compare the clusters with respect to their deflection behaviour. These results are presented in chapter 6.

As an additional simulation step, the particles reaching the ionization region at t_{L} , corresponding to the output parameters of the MD simulation, are translated into input files for SIMION. The software package SIMION 8.0 is used to simulate the trajectories of the photoions in the electrostatic extraction field under VMI conditions ($V_{\text{R}} = 8000 \text{ V}$, $V_{\text{E}} = 5830 \text{ V}$). Experimental VMI conditions are not exactly the same as SIMION VMI conditions, due to an offset in the spacing between the electrode plates. To determine cluster velocity distributions, photoions have to be extracted perpendicular to the molecular beam propagation axis. Hereby 2D coordinates in the detector plane are gained for each impinging photoion. From the simulated 2D position sensitive detection data, it is possible to calibrate the spatial positions into velocity coordinates (see 2.3.2). The velocities of the neutral clusters in molecular beam direction correspond to a displacement of the photoions in the detector plane. As the extraction and calibration are carried out for the

spin states $-1/2$, 0 and $+1/2$, a simulated deflector ‘off’ velocity trace is retrieved from $S = 0$ particles and a simulated deflector ‘on’ velocity trace is retrieved from the average of $m_S = +1/2$ and $m_S = -1/2$ particles. The simulated velocity traces are then compared to the experimental velocity traces. In the following, we characterise the deflection behaviour by modelling dependences on various experimental parameters.

Detection skimmer & ionisation region

The observable deflection of $m_S = \pm 1/2$ particles depends on the detection skimmer size and its y -position. These dependencies are especially pronounced for low I_d with small molecular beam divergence in the z -direction. In order to achieve significant deflection, the detection skimmer size has to be smaller than the average spread in z -direction of the molecular beam in the xz -plane of the detection skimmer. Fig. 3.2.4a shows the relative signal θ_{rel} transmitted through various detection skimmers as a function of t_d at $I_d = 100$ A. For large skimmer diameters $\varnothing_{\text{skim}} = 6.0$ mm approximately 80% of particles pass the skimmer. Decreasing the detection skimmer size significantly improves the resolvable deflection. Increasing the deflector current to $I_d = 700$ A (see Fig. 3.2.4b), causes the transmitted signal to be less sensitive to the selecting skimmer size, since the average beam divergence is larger than $\varnothing_{\text{skim}}$. In our experimental setup, we choose to work with $\varnothing_{\text{skim}} = 2.0$ mm (red diamonds in Fig. 3.2.4), as sufficient deflection is achievable for all sampled deflector currents. Furthermore, alignment of the molecular beam is readily achievable at at skimmer size of 2 mm.

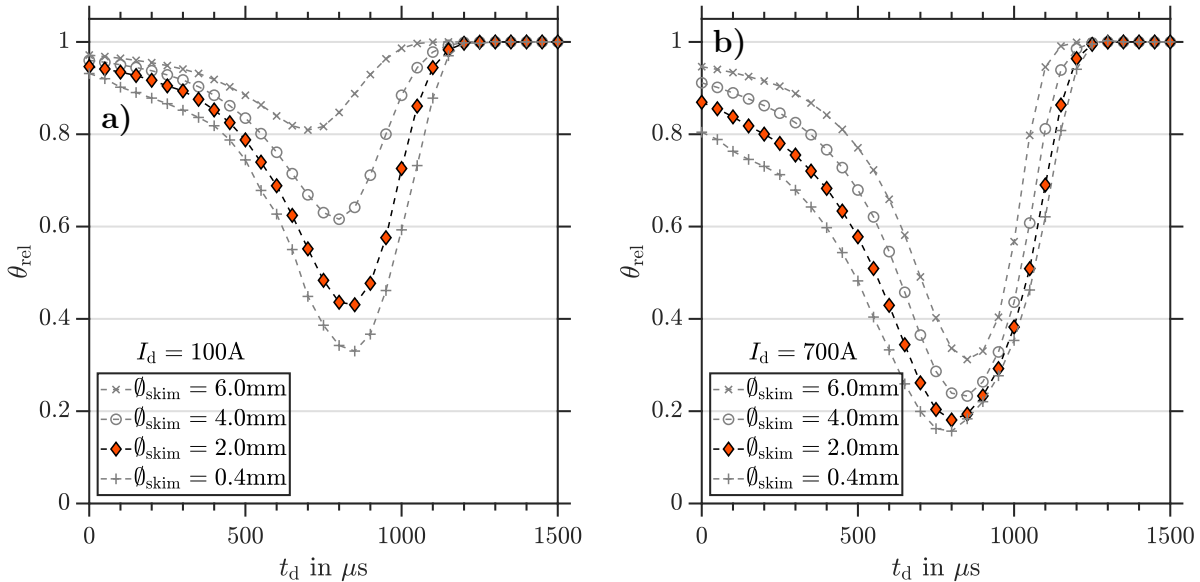


Fig. 3.2.4: MD simulations of particles with the mass of NaNH_3 with their relative signal θ_{rel} as a function of the deflector timing t_d . θ_{rel} of particles traversing the detection skimmer for various diameters $\varnothing_{\text{skim}}$ at (a) $I_d = 100$ A and (b) $I_d = 700$ A.

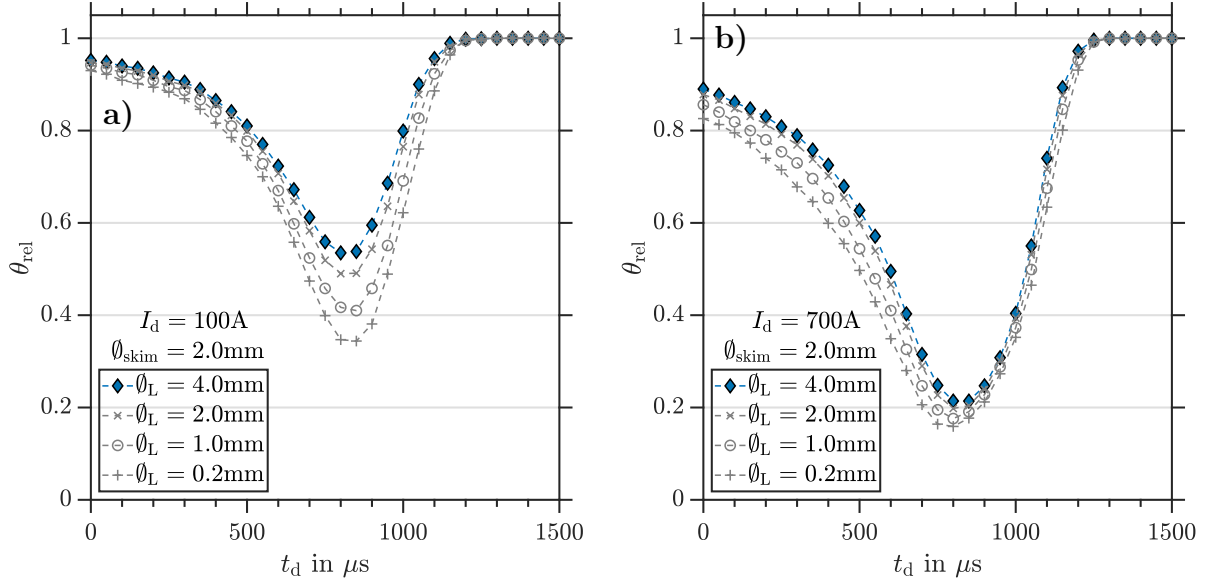


Fig. 3.2.5: MD simulations of particles with the mass of NaNH_3 with their relative signal θ_{rel} as a function of the deflector timing t_d . θ_{rel} of particles ionised for various laser beam diameters \varnothing_L with $\varnothing_{\text{skim}} = 2.0$ mm at (a) $I_d = 100$ A and (b) $I_d = 700$ A.

After traversing the detection skimmer the particles continue to the ionisation region, which is defined by the laser diameter \varnothing_L . The size of the ionisation region further defines the measurable deflection. Due to the remaining cluster beam divergence after the detection skimmer, θ_{rel} decreases with smaller laser beam diameters. This effect is more pronounced for low deflector currents shown in Fig. 3.2.5a, since weaker magnetic fields induce less beam divergence. The spread in z -direction in the ionisation region, defines the quality of θ_{rel} as a function of the laser beam diameter. With increasing I_d , this effect becomes negligible small, since θ_{rel} is mainly defined by the size of the detection skimmer, as can be concluded by comparing θ_{rel} with $\varnothing_{\text{skim}} = 2.0$ mm (red diamonds in Fig. 3.2.4b) to the relative signals in Fig. 3.2.5b. All further deflection measurements and simulations were carried out with $\varnothing_L = 4.8$ mm.

Zeeman force & cluster mass

With given detection skimmer size ($\varnothing_{\text{skim}} = 2.0$ mm) and laser beam size ($\varnothing_L = 4.8$ mm) we further investigate how the Zeeman force and cluster mass effect γ_d . The force field in the deflector is scaled by the I_d specific factor f_B , as previously discussed (see Fig. 3.2.2). Increasing the force field causes a stronger acceleration in z -direction for a given particle mass. In our experimental setup this is represented by an increase of γ_d as a function of I_d , summarised in Fig. 3.2.6a for particles with the mass of $\text{Na}(\text{NH}_3)_n$ ($n = 1 - 4$) and a molecular beam velocity distribution shown in Fig. 3.2.6b.

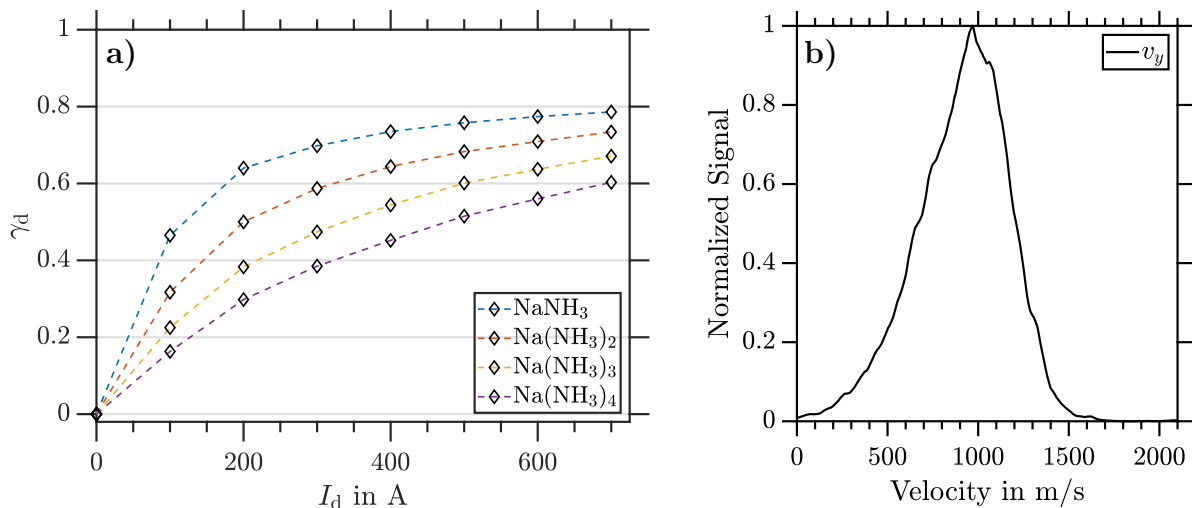


Fig. 3.2.6: (a) Deflection ratio γ_d as a function of the deflector current I_d for particle masses of $\text{Na}(\text{NH}_3)_n$ ($n = 1 - 4$). (b) Experimental molecular beam velocity distribution v_y used as MD simulation input.

The average force acting on a $m_s = \pm 1/2$ particle depends on I_d . Therefore, increasing the particle mass for a given I_d causes a deceleration in z -direction and subsequently a decrease in γ_d .

Velocity distributions

Reasonable deflection ratios with our pulsed Stern-Gerlach setup are achievable if the time delay between t_d and t_L reflects the flight time from the deflector to the ionisation region, which is defined by the experimental distance and the molecular beam velocities. As previously described (see section 3.2.1), optimised deflector trigger timings t_1 , t_2 and t_3 are set to achieve highest possible deflection for a given velocity distribution. Ideally, the magnetic field pulses should interact with the full velocity distribution in order to achieve highest possible deflection. In the experiment some velocity distributions are so broad that a suitable overlap of the magnetic field pulses and velocity distribution is not achievable. After traversing the pulsed magnetic fields residual signal remains from particles at the slow and fast end of broad velocity distributions.

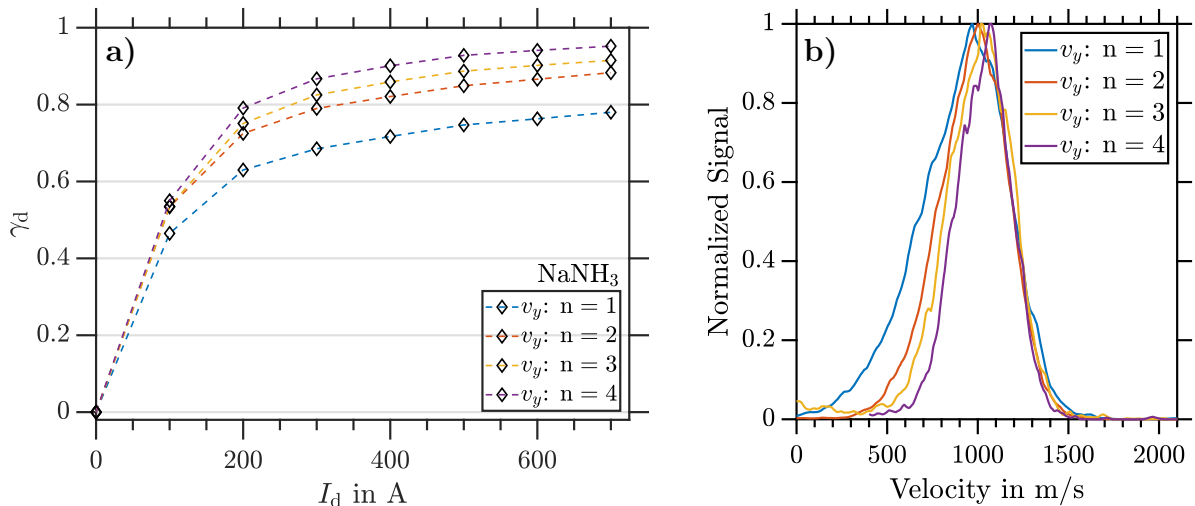


Fig. 3.2.7: (a) Deflection ratio γ_d as a function of the deflector current I_d for particle mass of NaNH_3 with various velocity distributions. (b) Experimental molecular beam velocity distributions v_y of $\text{Na}(\text{NH}_3)_n$ ($n = 1 - 4$) used as MD simulation input.

MD simulations with experimental velocity distributions of $\text{Na}(\text{NH}_3)_n$ ($n = 1 - 4$) shown in Fig. 3.2.7b and the particle mass of NaNH_3 exhibit an increase of γ_d with decreasing FWHM of the velocity distribution. These results indicate that nearly 100% deflection is achievable for narrow velocity distributions ($\text{FWHM} \leq 350$ m/s) with $v_y \leq 1000$ m/s and $I_d = 700$ A.

Individual coil contribution

Each electromagnetic coil generates a similar magnetic field gradient, hence $m_s = \pm 1/2$ particles experience the same force field while traversing each coil. Nevertheless, each coil does not contribute equally to the overall deflection (see Fig. 3.2.8). Varying the deflector delay for each coil individually results in a relative signal dip with distinct minima for each coil, shown in Fig. 3.2.8a. The minimal relative signal decreases from 3rd coil: $\theta_{\text{rel}} = 0.60$, 2nd coil: $\theta_{\text{rel}} = 0.55$ to 1st coil $\theta_{\text{rel}} = 0.50$. This trend is explained by the experimental distances along the molecular beam axis. Since, the 3rd coil is closest to the detection skimmer deflected particles exhibit the smallest spread in z -direction in the skimmer plane, compared to the 2nd and 1st coil. Optimal deflection conditions are achieved if all three coils are operated with optimised deflector delays t_1 , t_2 , t_3 (see section 3.2.1) to ensure the longest possible interaction times of the sampled velocities with the magnetic field pulses. The relative signal dip with all coils is shown in Fig. 3.2.8a, with a minimum of $\theta_{\text{rel}} = 0.20$.

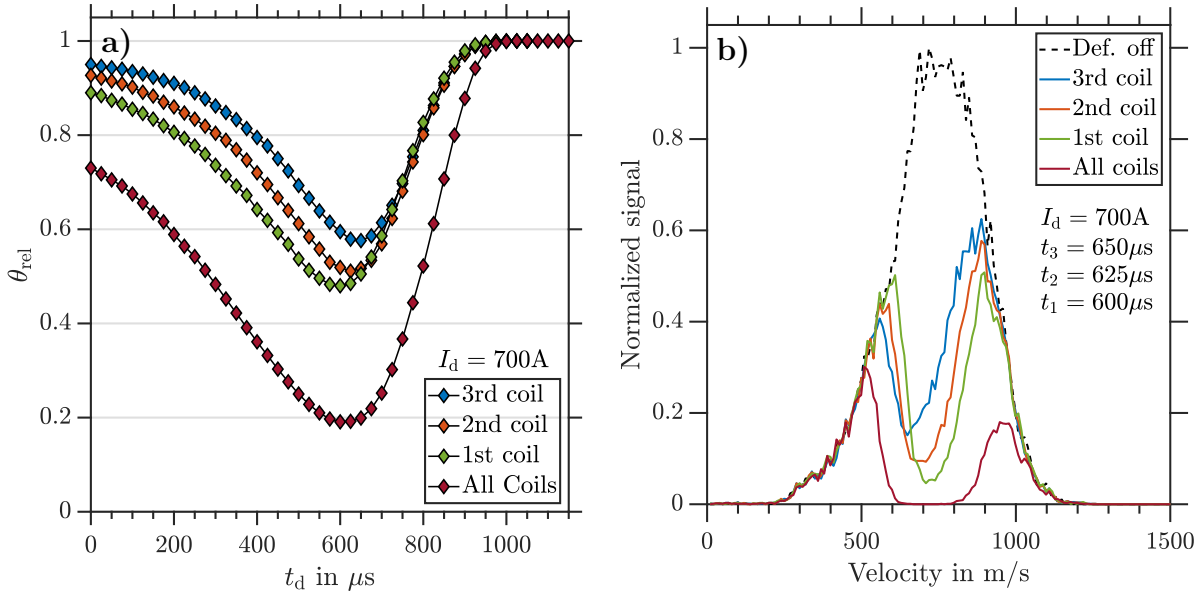


Fig. 3.2.8: (a) MD simulations of particles with the mass of NaDME with their relative signal θ_{rel} as a function of the deflector timing t_d . The coils of the deflector were pulsed individually (1st, 2nd, or 3rd) and together (all coils) with $I_d = 700\text{ A}$. (b) Corresponding velocity traces obtained from simulations at $t_d = 600\ \mu\text{s}$.

Simulated velocity traces for the deflection by each individual coil and all coils together are shown in Fig. 3.2.8b with deflector delays at minimal θ_{rel} . The velocity dependent deflection profiles demonstrate that the experimental velocity distribution of NaDME is too broad to be fully deflected by the magnetic field pulse of each coil or all three coils together. These simulations show that 100% deflection is achievable for the velocities 600 – 800 m/s. This finding shows that overall deflection can be improved by either narrowing the velocity distribution or broadening the magnetic field pulses in time. The simulations suggest that further enhancement of magnetic deflection is achievable by increasing the deflector length as well as the distance between deflector and detection skimmer.

Effective magnetic moment

As is described above, we introduce an exponential scaling factor of the magnetic moment μ_0 to account for possible intracluster spin relaxation effects. With this approach spin relaxation processes are characterised by the relaxation time τ of an exponential decay, which essentially causes a reduced effective magnetic moment μ_{eff} . Fast relaxation processes are described by small τ values, a significant reduction of the magnetic moment and observable deflection. Fig. 3.2.9a shows the dependence of θ_{rel} on t_d for various τ values. Since the cluster beam passes the deflector in approximately $200\ \mu\text{s}$, characteristic spin relaxation times are sampled with shorter times.

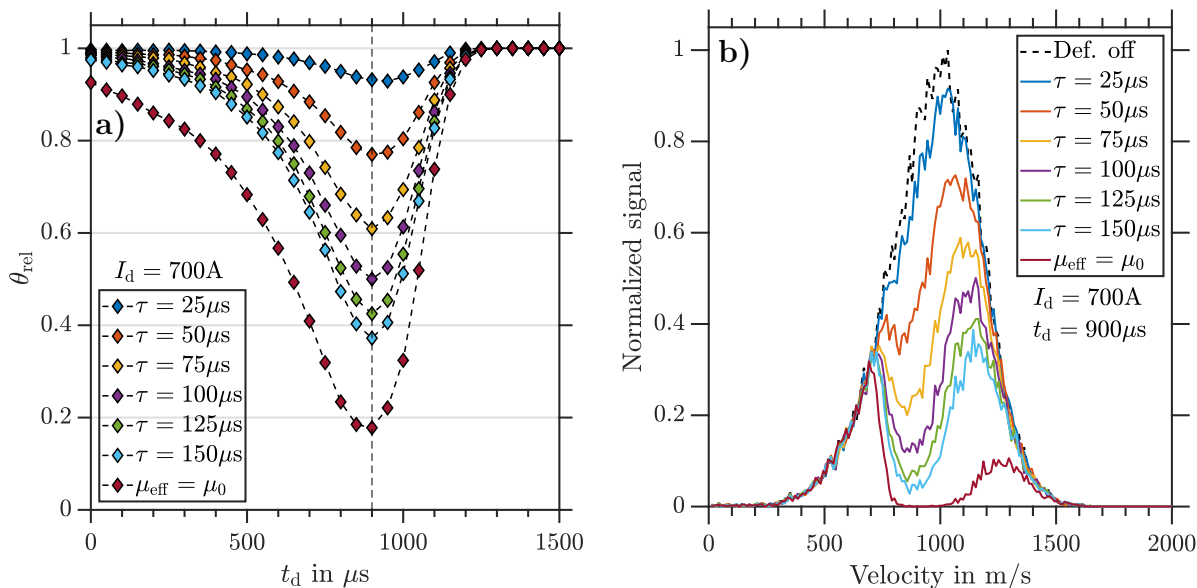


Fig. 3.2.9: (a) MD simulations of particles with the mass of $\text{Na}(\text{NH}_3)_2$ with their relative signal θ_{rel} as a function of the deflector timing t_d with various characteristic spin relaxation times τ and $I_d = 700\text{A}$. (b) Corresponding velocity traces obtained from simulations at $t_d = 900\mu\text{s}$ (dashed line in (a)).

The corresponding simulated velocity dependent deflection traces at minimal θ_{rel} ($t_d = 900\mu\text{s}$, indicated as dashed line in (a)) are shown in Fig. 3.2.9b and are compared to the deflector ‘off’ simulation. The velocity trace with $\tau = 25\mu\text{s}$ exhibits the least deviation from the deflector ‘off’ trace. As τ increases, the deviations from the deflector ‘off’ trace increase and approach the free $m_s = \pm 1/2$ case, where $\mu_{\text{eff}} = \mu_0$.

3.3 Angle-resolved photoelectron spectroscopy

Photoelectron velocity map imaging (VMI) was used to investigate the electronic properties of alkali metal doped solvent clusters. With this technique we determine angle-resolved photoelectron spectra. Measuring the kinetic energies and photoelectron angular distributions (PAD) as a function of different cluster size distributions, allows us to determine cluster size-dependent trends in ionisation energies and electronic structures. The following explanation of angle-resolved photoelectron spectroscopy has been adapted from [101, 121].

3.3.1 Photoelectron angular distribution

The photoelectron angular distribution (PAD) is given by the photoelectron intensity $I(\theta, \phi)$ as a function of the spatial emission direction, defined by θ polar angle and ϕ azimuthal angle. Quantum mechanically the electron probability distribution is described by the square of the electron wave function Ψ_e . The photoelectron intensity is thus fully

described by the wave function of the emitted electron.

$$I(\theta, \phi) = \Psi_e^* \Psi_e \quad (3.3.1)$$

Where the photoelectron wavefunction can be expressed as a superposition of initial and final state harmonic functions Y_{lm} ,

$$\Psi_e = \sum_{lm} c_{lm} e^{i\delta_l} Y_{lm}(\theta, \phi) \quad (3.3.2)$$

where c_{lm} are linear coefficients containing radial and angular information of initial and final states, as well as properties of the ionising radiation. The orbital angular momentum quantum number is given by l and its projection by m . The phase shifts δ_l reflects the interference between the partial waves. The phase shifts arise from time delays in the formation of various partial waves, which depend on the interaction with the scattering potential. With this we find the following expression for the photoelectron intensity

$$\begin{aligned} I(\theta, \phi) &= \sum_{lm} \sum_{l'm'} c_{lm}^* c_{l'm'} e^{i(\delta_l - \delta_{l'})} Y_{lm}^*(\theta, \phi) Y_{l'm'}(\theta, \phi), \\ &= \sum_{LM} B_{LM} Y_{LM}(\theta, \phi). \end{aligned} \quad (3.3.3)$$

The coefficients B_{LM} contain information regarding the individual contributions of each partial wave and their interferences with every other partial wave. For closed-shell atomic systems, when an electron is ejected from an orbital where l is a good quantum number, only two partial waves with $l \pm 1$ contribute to the photoelectron wavefunction. This arises from the selection rule $\Delta l = \pm 1$ for allowed electronic transitions during a single-photon process.

In molecular systems, l is no longer a good quantum number since the initial state is not described in terms of a single l value. The photoelectron wavefunction therefore is composed of more than two partial waves. In the case of a general PAD an infinite number of spherical harmonics results in a complete and correct description of photoelectron wavefunctions [35].

In the case of single-photon ionisation with linearly polarised light of an isotropic ensemble of gas-phase molecules an analytic solution for $I(\theta, \phi)$ can be found [32]. Equal population of magnetic sub levels $m = -l, \dots, l$ is assumed and only partial waves with $l = l_i \pm 1$ can contribute to the photoelectron wavefunction.

$$I(\theta) = \frac{\sigma_{\text{tot}}}{4\pi} \left(1 + \frac{\beta}{2} (3 \cos^2(\theta) - 1) \right) \quad (3.3.4)$$

where σ_{tot} is the total ionisation cross section, θ the angle between the photoelectron momentum vector \mathbf{k} and the electric field polarisation vector \mathbf{E} of the laser light and $\frac{1}{2}(3 \cos^2 \theta - 1)$ is the 2nd order Legendre polynomial. The parameter β is constrained to

values between $-1 \leq \beta \leq +2$ and a full description of the PAD is given by its value. Fig. 3.3.1 shows PADs for $\beta = -1, 2$ and $\beta = 0$.

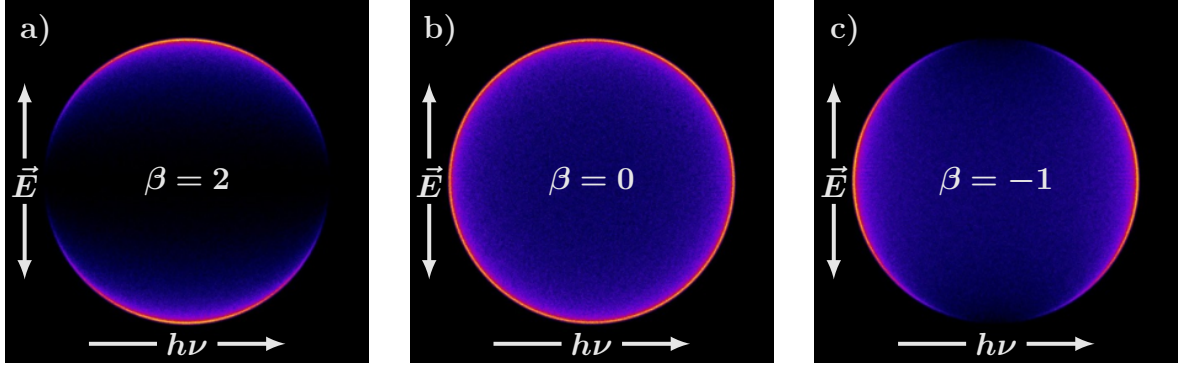


Fig. 3.3.1: Calculated photoangular distributions $I(\theta)$ obtained from the 2nd order Legendre polynomial for (a) $\beta = 2$, (b) $\beta = 0$ and (c) $\beta = -1$. The light propagation axis and electric polarisation vector are indicated as white arrows.

In the case of $\beta = 2$ the PAD is characterised by a $\cos^2(\theta)$ term where photoelectrons are ejected preferentially parallel to the light polarisation axis \mathbf{E} (see Fig. 3.3.1a). This case is described by the photoionisation of an atomic s -orbital with $l_i = 0$. Due to the selection rule $l = l_i + 1 = 1$ the photoelectron wavefunction is merely composed of a p -wave corresponding to $I(\theta) \propto \cos^2(\theta)$. An isotropic distribution with $I(\theta) = \text{const.}$ shown in Fig. 3.3.1b is described by $\beta = 0$ and is the case for an ionisation process with no angular preference in photoemission. In the case of $\beta = -1$, the PAD is described by a $\sin^2(\theta)$ term which indicates that photoelectrons are ejected mainly perpendicular to the light polarisation axis (see Fig. 3.3.1). Intermediate β -parameters resemble linear combinations of the mentioned cases. Where the resulting β value depends on the contributing partial waves with their relative intensities (given by radial matrix elements $\sigma_{l\pm 1}$) as well as their interference (given by the relative phase shifts $\delta_{l\pm 1}$). Where the β -parameter is given by the Cooper-Zare formula [32].

$$\beta = \frac{l(l-1)\sigma_{l-1}^2 + (l+1)(l+2)\sigma_{l+1}^2 - 6l(l+1)\sigma_{l-1}\sigma_{l+1}\cos(\delta_{l+1} - \delta_{l-1})}{(2l+1)(l\sigma_{l-1}^2 + (l+1)\sigma_{l+1}^2)} \quad (3.3.5)$$

3.3.2 Velocity map imaging of photoelectrons

In this section we will focus on the description of photoelectron imaging, whereas the imaging of photoions was previously described in section 2.3.2. Velocity map imaging [82] is an imaging technique to obtain 3D kinetic energy distributions of photoions (I^+) and photoelectrons (e^-). I^+ and e^- are generated via photoionisation with sufficient energy $h\nu$ in a ionisation point. Isoenergetic photoelectrons reside on a spherical surface in velocity space. The electron velocity $v_e \propto \sqrt{E_{\text{kin}}}$ defines the radius of the spherical surface and the intensity distribution follows the PAD described above. In position space

the radius of the corresponding sphere is furthermore defined by the time delay between ionisation and detection Δt . By extracting the photoelectrons with tailored electrical fields, 3D electron velocities distributions are projected onto a 2D detector plane. The resulting projection exhibits a circular geometry, where the radius contains the information of electron velocities and the 2D angular intensity distribution reflects the PAD.

In experimental reality ideal ionisation in a single point is not achievable. Instead ionisation occurs in a finite volume, defined by the cross section of laser beam and molecular beam, which causes an uncertainty of the spherical surface in position space. In order to correct for this finite irregularities, electrostatic focusing with unique electrical field gradients is applied [82]. This allows to map electrons with the same initial velocity vector to the same position in the detector plane, irrespective of their birth positions. With this technique a 2D velocity map image is generated from the projection of the initial 3D distribution.

3.3.3 Image reconstruction

Single photoionisation with linearly polarised light causes a cylindrical symmetry of the PAD, hence it is possible to reconstruct the full 3D velocity distribution from the measured 2D velocity map image. In order to reconstruct the 3D information it is required that the light polarisation axis (electric field component) is parallel to the detection plane. Mathematical inversion methods to obtain the full 3D distribution are described as follows.

Abel transformation

The 3D electron distribution of a Newton sphere can be given in Cartesian coordinates $I(x, y, z)$, where the origin is defined by the ionisation point, y is the axis of cylindrical symmetry corresponding to the polarisation vector of the light and z is the extraction direction towards the imaging detector (xy -plane). The 2D projection of the 3D distribution is expressed by [122]

$$p(x, y) = \int_{-\infty}^{+\infty} I(x, y, z) dz \quad (3.3.6)$$

A single line of the projection with a constant value of $y = y_0$ is expressed as

$$p(x, y_0) = \int_{-\infty}^{+\infty} I(x, z) dz = 2 \int_0^{\infty} s(x, z) dz. \quad (3.3.7)$$

Where $s(x, z) = I(x, z, y_0)$ is a cross-section through the 3D distribution perpendicular to the symmetry axis at $y = y_0$. In cylindrical symmetry the single line projection can be expressed in polar coordinates by variable substitution $r^2 = x^2 + y^2$.

$$p(x, y_0) = 2 \int_x^{\infty} \frac{s(r)r}{\sqrt{r^2 - x^2}} dr \quad (3.3.8)$$

This operation is known as Abel transform. With the use of an inverse Abel transform it

is possible to obtain $s(r)$ from the 2D projection $p(x, y_0)$ given by

$$s(r) = \frac{1}{\pi} \int_r^\infty \frac{dp(x, y_0)}{dx} \cdot \frac{1}{\sqrt{x^2 - r^2}} dx. \quad (3.3.9)$$

This approach allows to obtain the 3D distribution slice by slice from infinitesimal lines. In practice solving the inverse Abel transform analytically involves two problems. Firstly, the singularity $r^2 = x^2$ keeps the integral from converging and secondly the derivative in the integrand amplifies noise. Several different algorithms, as onion peeling [123, 124], backtracking algorithms [125, 126], fitting a set of basis functions to an image [127, 99] and maximum entropy methods [100, 128] were developed to circumvent these problems. The applied approaches within this work are discussed in further details.

Polar basis set expansion algorithms

The basis set expansion algorithm (BASEX) [127] method takes the experimental projection data and expands it over a set of basis functions. Garcia *et al.* [99] used polar symmetry adapted basis sets (*p*BASEX), consisting of functions f_{kl} where the radial part is described by a Gaussian function.

$$f_{kl}(r, \theta) = \exp\left(-\frac{(r - r_k)^2}{\sigma}\right) \cdot P_l(\cos(\theta)) \quad (3.3.10)$$

where the Gaussian peak has a width of σ and is centred at r_k and the angular dependence is given by Legendre polynomials $P_l(\cos(\theta))$. By expressing the basis set function $f_{kl}(r, \theta)$ as a linear expansion, the 3D distribution is expressed by

$$I(r, \theta) = \sum_{k=0}^{k_{\max}} \sum_{l=0}^{l_{\max}} c_{kl} f_{kl}(r, \theta). \quad (3.3.11)$$

here the value of k_{\max} has to be large enough in order to sample the full radius of the experimental image. For single photon ionisation processes with linearly polarised light the sum over l reduces to $l = 0$ and $l_{\max} = 2$. Via Abel transformation of the basis functions f_{kl} , a set of basis functions g_{kl} are obtained which reflect the 2D projection of the 3D distribution.

$$g_{kl}(r', \theta') = 2 \int_x^\infty \frac{f_{kl}(r, \theta) r}{\sqrt{r^2 - x^2}} dr \quad (3.3.12)$$

By linear expansion of the 2D set of basis functions g_{kl} , an expression is found which reflects an experimentally measured image.

$$p(r', \theta') = \sum_{k=0}^{k_{\max}} \sum_l c_{kl} g_{kl}(r', \theta') \quad (3.3.13)$$

The coefficients c_{kl} are subsequently determined via fitting of $p(r', \theta')$ to an experimental image. With obtained coefficients c_{kl} and the initial set of basis functions f_{kl} of the 3D

distribution, the initial 3D velocity distribution is reproduced. In order to obtain the kinetic energy distributions it is sufficient to calculate the radial part with $l = 0$.

$$I(r) = r^2 \sum_{k=0}^{k_{\max}} c_{k,0} f_{k,0} \quad (3.3.14)$$

The β parameter trace of the 2nd order Legendre polynomial is given by the ratio

$$\beta(r) = \frac{\sum_k c_{k,2} \cdot f_{k,0}}{\sum_k c_{k,0} \cdot f_{k,0}}. \quad (3.3.15)$$

Maximum entropy methods

The other method used in this work to reconstruct velocity map images is Maximum Entropy Velocity Image Reconstruction (MEVIR), developed by B. Dick [100]. The method is not based on Abel inversion instead it uses an iterative approach. In a first step the reconstructed image ('map') of a 3D distribution is simulated. In a second step the corresponding 2D projection is obtained via Abel transform, which is then compared to the experimental data in the last step. The initial reconstructed image is fitted via a least-square method until agreement is found with the experimental image. The algorithm finds several maps F which describe the experimental image reasonable well. In order to find the most likely image, a further criterion is introduced. The approach finds the image with least information content which corresponds to a maximum in entropy S . Which for a strictly positive map is given by

$$S = - \sum_{J=1}^{N_F} F_J \ln \frac{F_J}{e B_J}. \quad (3.3.16)$$

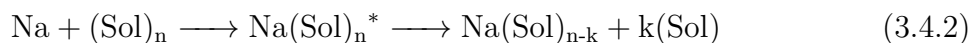
Where the index J runs over all the pixel values N_F of the simulated image F which has been fit to the data and B_J is an element of the default reference image. The negative of S holds the information content in the map F , where a maximum entropy map contains the least information necessary to still reproduce the experimental 3D distribution. The speed distribution and β parameter trace are obtained by projection of the maximum entropy map onto Legendre polynomials.

$$Q_l(r) = r^2 (2l + 1) \int_0^\pi P^S(r, \theta) P_l(\cos(\theta)) \sin(\theta) d\theta \quad (3.3.17)$$

with the Legendre polynomial order l and the maximum entropy map F transformed to spherical coordinates $P^S(r, \theta)$. The speed distribution is once more retrieved from the $l = 0$ Legendre polynomial $Q_0(r)$. For single photon ionisation processes with linearly polarised light the PAD is described by $\beta(r) = Q_2(r)/Q_0(r)$.

3.4 Momentum transfer of alkali metal-doping

The experimental technique of alkali metal-doping is presented in section 2.1.2. It is pointed out that an inelastic collision between a cluster and alkali metal atom causes a part of the total kinetic energy to be converted to internal energies of the collision complex. The sticking probability of an alkali metal atom is determined by the energy redistribution into internal degrees of freedom. Forysinski *et. al* [97] theoretically showed that the capture cross sections of sodium and acetic acid are cluster size-dependent. The average capture cross sections were calculated with a Langevin model [129], assuming long-range interaction potentials by isotropic dispersion and induction terms. It was furthermore shown that sodium-doped acetic acid monomer and dimer clusters formed upon collisions, dissociate within picoseconds ($\sim 10 \times 10^{-12}$ s). For the larger trimer and tetramer energy stabilisation is achieved via evaporation of one or two acetic acid monomer units. For small clusters with insufficient degrees of freedom adequate collision energy redistribution is not possible and dissociation of the collision complex becomes favourable, given by



Redistribution of internal excess energy can be achieved by evaporation of either sodium (equation 3.4.1) or one or more monomer units (equation 3.4.2). The collision energy can furthermore stabilise via intramolecular vibrational energy redistribution (IVR) under the formation of the sodium-doped species. The collision probability between the alkali metal and cluster are said to follow Poisson distributions [94, 95],

$$P_m = \exp(-\langle m \rangle) \frac{\langle m \rangle^m}{m!} \quad (3.4.3)$$

here P_m is the probability of m collisions between a cluster and alkali metal atoms, with the average number of collisions $\langle m \rangle$. Although it is pointed out that the simple Poisson collision probabilities describe the resulting cluster size distributions with an estimated accuracy of 30% [94]. In addition, Fárník *et al.* [130] report capture cross sections of several gas molecules on Ar_N clusters in which they show that the Poisson distributions result in too small capture cross sections inconsistent with the determined cluster size distributions of Ar_N . In contrast, capture cross section obtained from velocity measurements support their simulations.

The number of picked up sodium atoms K along the collision length L with sodium vapour as an ideal gas at a pressure p is expressed as

$$K = \frac{p}{k_B T_{\text{oven}}} \sigma_c L, \quad (3.4.4)$$

where σ_c is the pickup collision cross section. The cross section of the sodium doping

process is velocity-dependent and is expressed as a velocity corrected cross section σ_0

$$\sigma_c = \sigma_0 F(x) \quad (3.4.5)$$

where $F(x)$ is the velocity-dependent correction factor obtained from kinetic gas theory [131, 132] of the possible form

$$F(x) = \frac{1}{\sqrt{\pi}} x^{-1} \exp(-x^2) + (2 + x^{-2}) \operatorname{erf}(x). \quad (3.4.6)$$

With $x = v_{i,\text{Sol}}/v_{p,\text{Na}}$ being defined as the ratio of the initial cluster velocity $v_{i,\text{Sol}}$ and the most probable sodium velocity $v_{p,\text{Na}}$ and where $\operatorname{erf}(x)$ is the Gauss error function

$$\operatorname{erf}(x) = \frac{2}{\sqrt{\pi}} \int_0^x \exp(-y^2) dy. \quad (3.4.7)$$

The most probable velocity of alkali metal vapour $v_{p,\text{Na}}$ of a three dimensional Maxwell-Boltzmann distribution is given by

$$v_{p,\text{Na}} = \sqrt{\frac{2k_B T_{\text{oven}}}{m_{\text{Na}}}}. \quad (3.4.8)$$

Liang and Kresin [133] derive an exact expression for the average kinetic energy of the collision process. Their approach is based on kinetic gas theory [134, 135, 136] for inelastic collisions of a particle beam with a Maxwell-Boltzmann gas. The main idea of their work is to determine an expression for the number of collisions per time unit N_m as well as an expression for the amount of kinetic energy delivered by the collisions per time unit Φ_t . These analytically obtained expressions represent the collision rate, respectively the kinetic energy flux. Dividing the kinetic energy flux by the collision rate results in an expression which describes the average amount of kinetic energy deposited into the particle by one molecular collision.

$$\langle E_t \rangle = k_B T_{\text{oven}} \cdot \frac{\mu}{m_{\text{Na}}} \cdot \frac{\Theta(x)}{\Psi(x)} \quad (3.4.9)$$

where μ is the reduced mass of the collision partners and $\Theta(x)$ and $\Psi(x)$ are velocity-dependent corrections of similar form as $F(x)$. The function Ψ is given by

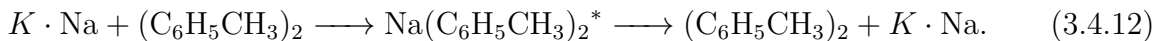
$$\Psi(x) = x \exp(-x^2) + \sqrt{\pi} \left(\frac{1}{2} + x^2 \right) \operatorname{erf}(x), \quad (3.4.10)$$

and the function Θ is expressed as

$$\Theta(x) = x \left(\frac{5}{2} + x^2 \right) \exp(-x^2) + \sqrt{\pi} \left(\frac{3}{4} + 3x^2 + x^4 \right) \operatorname{erf}(x). \quad (3.4.11)$$

We here present the non-sticky collisions between a molecular beam of toluene dimer $(\text{C}_6\text{H}_5\text{CH}_3)_2$ cluster and sodium atoms. We shortly discuss experimental possibilities to apply the theoretical approach developed by Liang and Kresin [133].

The non-sticky collisions of $(\text{C}_6\text{H}_5\text{CH}_3)_2$ with sodium are described by



where contributions of fragmentation processes of larger clusters $n > 2$ are excluded. The final velocity $v_{f,\text{Tol}2}$ of toluene dimer clusters can be expressed by conservation of momentum

$$K \cdot m_{\text{Na}} \cdot v_{i,\text{Na}} + m_{\text{Tol}2} \cdot v_{i,\text{Tol}2} = m_{\text{Tol}2} \cdot v_{f,\text{Tol}2} + K m_{\text{Na}} \cdot v_{f,\text{Na}}$$

$$v_{f,\text{Tol}2} = v_{i,\text{Tol}2} + K \cdot \frac{m_{\text{Na}}}{m_{\text{Tol}2}} \cdot (v_{i,\text{Na}} - v_{f,\text{Na}}) \quad (3.4.13)$$

with the masses for sodium m_{Na} and $(\text{C}_6\text{H}_5\text{CH}_3)_2$ $m_{\text{Tol}2}$, the initial molecular beam velocity $v_{i,\text{Tol}2}$, the velocity distribution of the sodium vapour $v_{i,\text{Na}}$, the number of picked up sodium atoms K and an isotropic velocity distribution of the dissociation process $v_{f,\text{Na}}$. In our experiments the molecular beam is defined by a small acceptance angle (0.17°), we therefore assume that observable velocities result from sodium collisions parallel and antiparallel to the molecular beam direction. The initial sodium velocity can be described by a Maxwell-Boltzmann distribution (1D, 2D and 3D at $T_{\text{oven}} = 210^\circ\text{C}$) shown in Fig. 3.4.1. Negative sodium velocities represent the possibility of antiparallel collisions with the molecular beam, whereas positive sodium velocities account for parallel collisions.

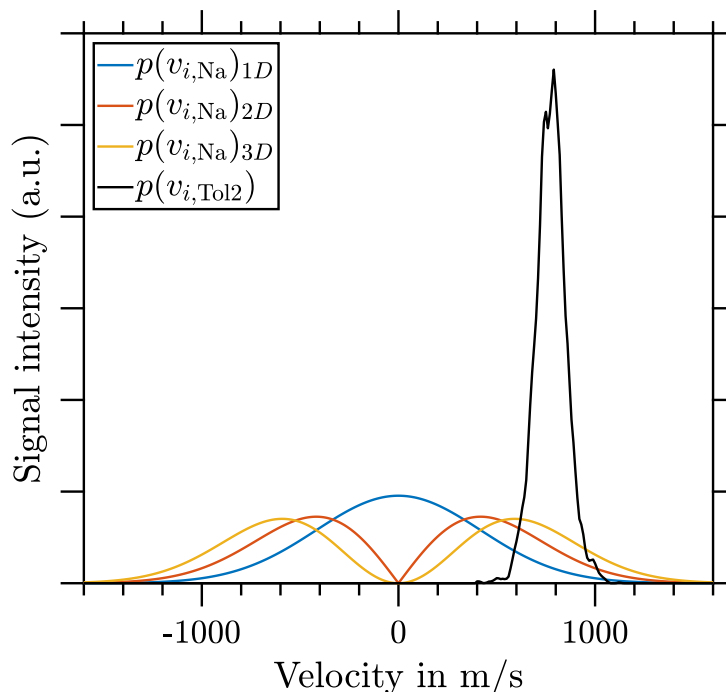


Fig. 3.4.1: Initial velocity distributions of 1D, 2D and 3D Maxwell-Boltzmann sodium gas at $T_{\text{oven}} = 210^\circ\text{C}$ as well as the initial molecular beam velocity distribution of $(\text{C}_6\text{H}_5\text{CH}_3)_2$ (black line), all distributions are normalised to their area.

Molecular beam velocity measurements of $(\text{C}_6\text{H}_5\text{CH}_3)_2$ with sodium collisions show a

distinct velocity shift towards slower velocities (see Fig. 2.1.5). Calculating $v_{f,\text{ToI}2}$ via equation 3.4.13, with the initial velocity distributions of the toluene dimer cluster and possible sodium vapour velocity distributions shown in Fig. 3.4.1 as well as a velocity independent collision cross section $\sigma_c = \sigma_0$, do not reproduce the experimentally observed velocity shift.

Applying equation 3.4.9 and evaluating the average kinetic energy $\langle E_t \rangle$ per collision reveals velocity shifts towards slower velocities although in a too large extent, not observed in the experiment. Hereby it is unclear in which form the correction factors Ψ and Θ apply, since the sodium velocity distribution may deviate from the proposed Maxwell-Boltzmann distribution and show effusive character. We suggest photoion VMI measurements (see section 2.3.2) of bare sodium atoms to determine the sodium velocity distribution in molecular beam direction. Measuring velocity distributions of *e.g.* toluene clusters as a function of sodium oven temperature is a promising experimental technique to study the kinetic energy transfer of the impinging sodium atoms. Revisiting the theoretical approach by Liang and Kresin [133] with additional corrections for dispersion interaction collision cross sections is an applicable approach to support the proposed experimental sodium collision studies.

Chapter 4

Magnetic deflection of neutral sodium-doped ammonia clusters

Results presented in this chapter have been previously published and are included in its entirety with minor modifications to the format of text, tables and figures.

Title: Magnetic deflection of neutral sodium-doped ammonia clusters.

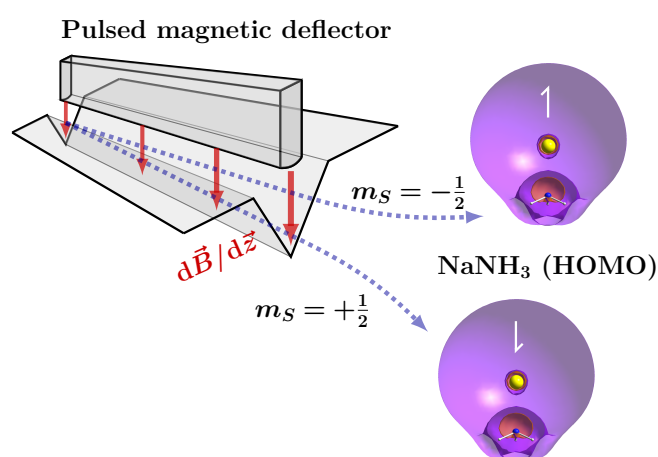
Authors: J. V. Barnes, M. Beck, S. Hartweg, A. Luski, B. L. Yoder, J. Narevicius, E. Narevicius and R. Signorell.

Citation: *Phys. Chem. Chem. Phys.*, 2021, **23**, 846.

Doi: 10.1039/d0cp04647g

Reprinted with the permission from *Phys. Chem. Chem. Phys.*, 2021, **23**, 846.

Copyright ©2021 Royal Society of Chemistry.



Abstract: We describe the setup and the performance of a new pulsed Stern-Gerlach deflector and present results for small sodium-doped ammonia clusters $\text{Na}(\text{NH}_3)_n$ ($n = 1-4$) in a molecular beam. NaNH_3 shows the expected deflection of a spin 1/2 system, while all larger clusters show much smaller deflections. Experimental deflection ratios are compared

with the values calculated from molecular dynamics simulations. The comparison reveals that intracluster spin relaxation in NaNH_3 takes place on a time scale significantly longer than $200 \mu\text{s}$. Assuming that intracluster relaxation is the cause of the reduced deflection, relaxation times seem to be on the order of $200 \mu\text{s}$ for all larger clusters $\text{Na}(\text{NH}_3)_n$ ($n = 2 - 4$). Our work is a first attempt to understand the magnetic properties of isolated, weakly-bound clusters with relevance to the variety of diamagnetic and paramagnetic species expected in solvated electron systems.

4.1 Introduction

The discovery of concentration-dependent colours of alkali metal-ammonia solutions in the early 19th century by Sir Humphry Davy and later reported by W. Weyl [3] sparked a large series of experimental and theoretical works on excess electrons in alkali metal ammonia solutions [5] (and references therein). In dilute blue coloured solutions, a variety of diamagnetic and paramagnetic species may exist (solvated electrons, electron-cation pairs, solvated metal atoms and bipolarons) [5, 6, 7, 8] In bulk solutions the paramagnetic species have been investigated via electron spin resonance (ESR) [137] and nuclear magnetic resonance (NMR) spectroscopy [138] (and references therein). Neutral sodium-doped ammonia clusters $\text{Na}(\text{NH}_3)_n$ have previously served as model systems to study the electronic properties of the ‘ammoniated’ electron via photoion spectroscopy, photoelectron spectroscopy and *ab initio* methods [17, 18, 19, 20, 21, 22, 25, 23, 26, 1, 2, 24, 27] (and references therein). Photoion spectroscopy has revealed that the ion appearance energy of $\text{Na}(\text{NH}_3)_n$ decreases systematically with increasing number of solvent molecules [23] (and references therein). Various effects such as increasing delocalization of the $3s$ electron with increasing cluster size, surface and bulk localization of the electron, closing of solvation shells and cluster symmetry can contribute to the decrease in the ion appearance energy and the ionization (binding) energy. From $n = 1$ to 4, for example, a substantial decrease of $\sim 1.4 \text{ eV}$ was observed. A similar trend for the ionization (binding) energy was later found in photoelectron studies and in high-level *ab initio* calculations [1, 2, 24]. Experiments and calculations for the smaller clusters are consistent with surface electrons (compared to internally solvated electrons), which essentially can be described as an unpaired electron of Na that is perturbed by the solvent molecules [1, 2, 24]. These studies also reveal many structural isomers for a given cluster size. An intriguing result of the high-level *ab initio* study by Gunina and Krylov [24] concerns the electronic properties. The study found that the hydrogen-bond network of the NH_3 solvent molecules contributes significantly to the overall electronic properties, such as the dipole moment. Angle resolved photoelectron spectroscopy provides experimental access to the photoelectron anisotropy (photoelectron anisotropy parameter β) and thus to the orbital character of the unpaired electron. Experimental and calculation results [1, 2] show that the lowest electronic states of small clusters have high s -character and thus large β values. The β values decrease with

increasing cluster size, except for highly symmetric clusters (*e.g.* $n = 4$; magic number for the photoelectron anisotropy). Generally, the decrease in β is accompanied by an increase in the electric dipole moment. Effective polarizabilities of $\text{Na}(\text{NH}_3)_n$ were determined from electric deflection studies [139]. Yet, detailed knowledge of the magnetic properties of the solvated electron in free clusters is still not established. To the best of our knowledge, we present the first study on the magnetic properties of small ($n = 1 - 4$) sodium-doped ammonia clusters $\text{Na}(\text{NH}_3)_n$ investigated via Stern-Gerlach deflection.

The original Stern-Gerlach experiment was designed to determine the magnetic moment of isolated silver atoms [56], later various other isolated atoms [57], several molecules with a nonzero spin S [140, 63, 64, 61, 62, 141, 142, 143, 144, 145, 146] and metallic and bi-metallic clusters [147, 69, 148, 70, 149, 150, 71, 151, 107, 72, 104, 152, 153] were investigated with Stern-Gerlach setups (except for ref. [152]). For molecular systems and metal clusters, additional degrees of freedom like vibrations and rotations are accessible compared with atomic systems. It has been shown that the overall molecular rotations can induce Zeeman-like sublevels [61, 62]. Several groups [65, 66, 67] gave theoretical explanations of why transitions between Zeeman-like sublevels can occur and how Stern-Gerlach deflection experiments could be influenced by so called intramolecular spin relaxation (ISR) and its intracluster analog. Amirav and Navon provided experimental evidence of ISR effects in isolated molecules [63, 64]. In their deflection studies on the molecular beams of paramagnetic molecules and stable organic radicals, they observed smaller-than predicted deflection magnitudes and incomplete spin refocusing involving two Stern-Gerlach magnets. These two experimental results were interpreted as ISR processes occurring on faster time scales than the interaction time with the magnetic field. In one case, however, this interpretation was disputed [62]. Later, various groups investigated the magnetic properties of free Fe_m , Co_m , and Ni_m clusters ($m = 10 - 1000$) via Stern-Gerlach deflection [69, 70, 71, 72]. Hereby, one-sided deflection toward high field instead of symmetric magnetic deflection was observed. This asymmetric deflection behaviour was interpreted as being due to rapid ISR [66] occurring among the perturbed, spinrotation induced Zeeman sublevels. Studies on one-dimensional metal-organic sandwich clusters [73, 74, 75, 76] show similar one-sided deflection in the high-field direction, indicating that intracluster spin relaxation occurs within the complexes as they traverse the magnetic field. In recent studies, Schäfer and co-workers investigated spin relaxation processes via spin refocusing of paramagnetic superatoms with two Stern-Gerlach magnets [78, 79].

Here, we present a new setup for a pulsed Stern-Gerlach experiment, characterize its performance and study the magnetic properties of neutral sodium-doped ammonia clusters, which can be seen as solvated electron precursors. An overview of previous Stern-Gerlach setups is provided in ref. [154] along with a description of a new strong permanent magnet gradient deflector and its comparison with commonly employed electromagnets. Similar to the experiments of various groups highlighted above, we investigate the deflection magnitude in relation to a predicted (from a molecular dynamics (MD) approach) deflection

magnitude. With this we aim to probe the cluster size-dependent magnetic properties of neutral $\text{Na}(\text{NH}_3)_n$ ($n = 1 - 4$) clusters. Studying the size-dependent magnetic properties of sodium-doped ammonia clusters will lead to a better understanding of the involved paramagnetic species in bulk sodium ammonia solutions. In the present study, we focus on the interpretation of cluster size-dependent intracuster relaxation times.

4.2 Methods

4.2.1 Experimental setup

Fig. 4.2.1 shows the experimental setup for the current study of the size-dependent magnetic properties of neutral sodium-doped ammonia clusters $\text{Na}(\text{NH}_3)_n$ ($n = 1 - 4$). It consists of four chambers (A-D) which are separated by skimmers, in order to produce a well-defined molecular beam along with differential pumping (Fig. 4.2.1a). For the detection of ion kinetic energies, we use velocity map imaging (VMI) [82]. Mass spectra were produced by collecting time-of-flight (TOF) signals using the same ion optics as that in the case of VMI.

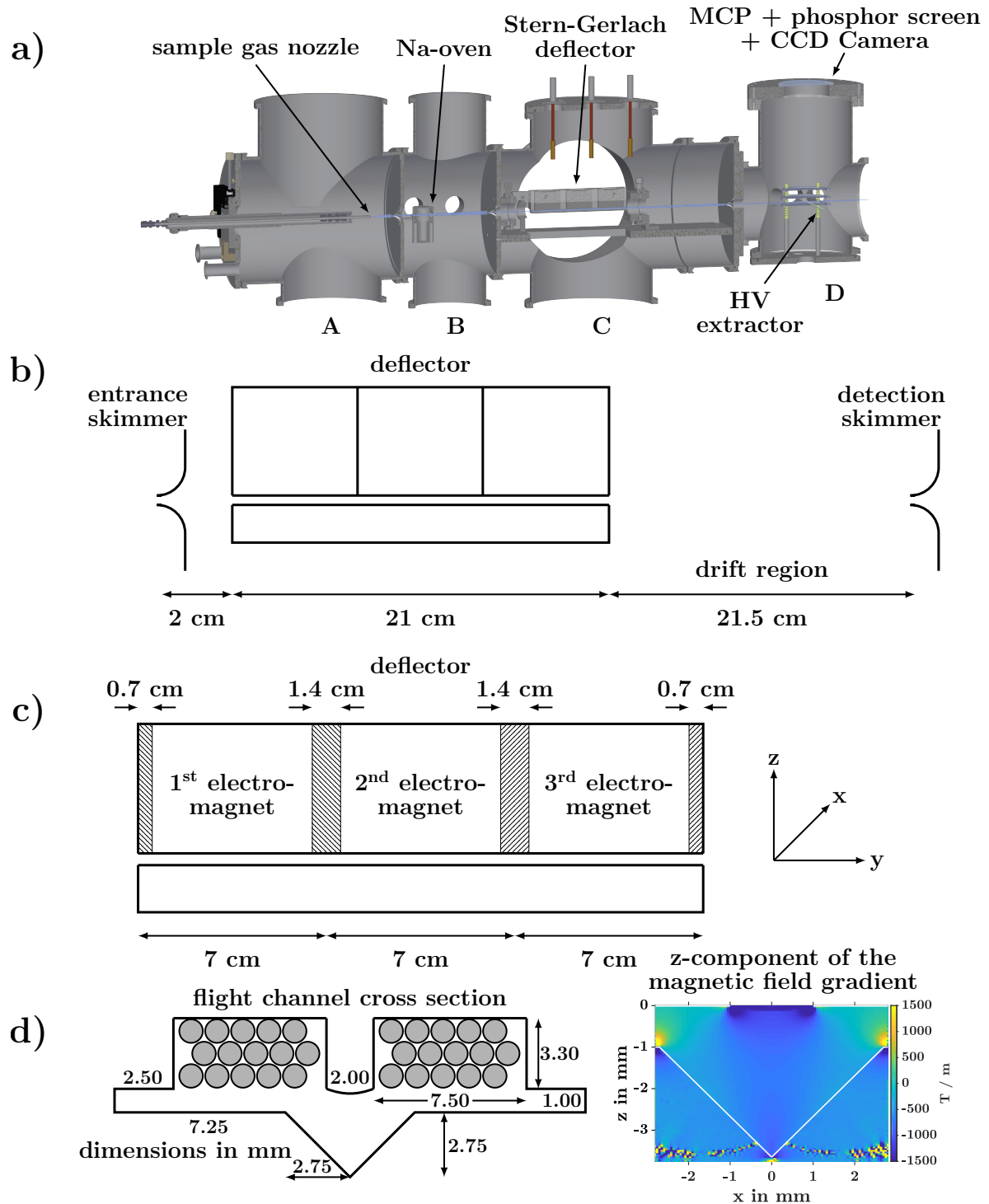


Fig. 4.2.1: (a) Sketch of the experimental setup consisting of the source chamber (A), the Na-oven chamber (B), the deflection chamber (C) and the ionization detection chamber (D). See text for details. (b) Side view with dimensions along the molecular beam propagation axis. (c) Side view of the deflector consisting of three electromagnets with relevant dimensions and the axis system (right). Shaded areas correspond to epoxy parts. (d) Cross section of the deflector flight channel and calculated z -component of the magnetic field gradient. A detailed description of the mechanical and electronic design is given in sections 4.6.1 and 4.6.2 of the supplementary information.

Cluster formation and sodium doping process.

Ammonia clusters are formed in vacuum in the source chamber (A) by continuous neat supersonic expansion (stagnation pressure: ~ 6 bar) through a temperature controlled ($T_{\text{nozzle}} = 115^\circ\text{C}$) nozzle (nominal orifice diameter: $35\ \mu\text{m}$). During operation, the chamber pressure is typically maintained below $\sim 10 \times 10^{-4}$ mbar. After passing through the source chamber, the cluster beam enters the Na-oven chamber (B) through a 2 mm diameter skimmer. Sodium doped ammonia clusters are formed via collisions with Na atoms inside the oven [25, 155, 92]. The Na vapour pressure is controlled by the oven temperature ($T_{\text{oven}} = 195^\circ\text{C}$). A typical working pressure of $\sim 4 \times 10^{-6}$ mbar is maintained in the oven chamber.

Pulsed Stern-Gerlach deflection.

After the doping process, the cluster beam enters the deflection chamber (C) through a 1.5 mm diameter skimmer. The dimensions, parallel to the molecular beam propagation (y -axis), of the deflection chamber are shown in Fig. 4.2.1b and c. Furthermore, the cross section of the flight channel and the magnetic field gradient in the z -direction are displayed in Fig. 4.2.1d. The magnetic force in the z -direction causes deflection of paramagnetic clusters. The diverging paramagnetic cluster beam is separated from the non-diverging diamagnetic cluster beam by a 2 mm diameter detection skimmer, placed 21.5 cm after the exit of the deflector. The deflector is operated at repetition rates between 1 and 5 Hz and typical chamber pressures of $\sim 1 \times 10^{-7}$ mbar. The mechanical and electronic design of the deflector are discussed in detail in sections 4.6.1 and 4.6.2 of the of the supplementary information. The performance of the deflector was tested for an effusive Na atom beam (section 4.6.3, of the supplementary information).

Ionization by UV laser light and VMI detection.

Once the clusters traverse the detection skimmer and reach the centre of the extraction zone, the clusters are ionized and then detected. Single photon ionization of sodium-doped ammonia clusters was achieved using light from a pulsed (20 Hz) nanosecond (~ 7 ns) 266 nm (4.66 eV) Nd:YAG laser (Quantel Ultra). For single photon ionization of bare sodium atoms, pulsed (20 Hz) nanosecond (~ 7 ns) 212 nm (5.85 eV) laser light generated by tripling the output of a dye laser was used [156]. The propagation direction and the polarization vector lie in a plane parallel to the ion detector. Two-dimensional (2D) VMI experiments on the photoelectrons/ ions formed upon VUV ionization of sodium-doped ammonia clusters were carried out with perpendicular extraction (see Fig. 4.2.1a). In this configuration, the molecular beam axis and the TOF axis are perpendicular. This arrangement allows the determination of velocity distributions along the molecular beam propagation axis, which is discussed in detail in section 4.2.2.

Upon ionization, the ions are accelerated by a Wiley-McLaren type extractor optimized

for either TOF conditions or VMI conditions (0 to 15 kV). The ionization region is located between the repeller and the extractor plate. The extraction region and a 20 cm field-free drift region are shielded by two concentric mu-metal cylinders. The position sensitive detector is composed of a pair of 40 mm diameter microchannel plates (MCPs) in a chevron stack which are coupled to a phosphor screen (Photonis USA, Inc.; APD), followed by a charge coupled device (CCD) camera. The front of the MCP assembly is kept at ground potential when the voltage on the back plate is used to ‘gate’ the detector. A high voltage switch (Behlke) is used to vary the MCP bias voltage by 500 V so that the gain is only high when the ions of interest are impinging on the detector. The luminescence of the screen is recorded by the CCD camera. Individual frames (12 bit grayscale image, 1/3 inch sensor, 1024×768 pixel) are taken for each laser shot, summed up in real time using NuAcq software [98] and saved to a computer connected to the CCD camera.

Timing sequence of a deflection measurement.

A deflection measurement consists of a series of TOF measurements. For each TOF mass spectrum the time delay between the deflector timing t_d and the timing of the ionizing laser t_L is varied. Throughout the presented work t_d was varied relative to t_L . This is shown in the upper sketch of Fig. 4.2.2.

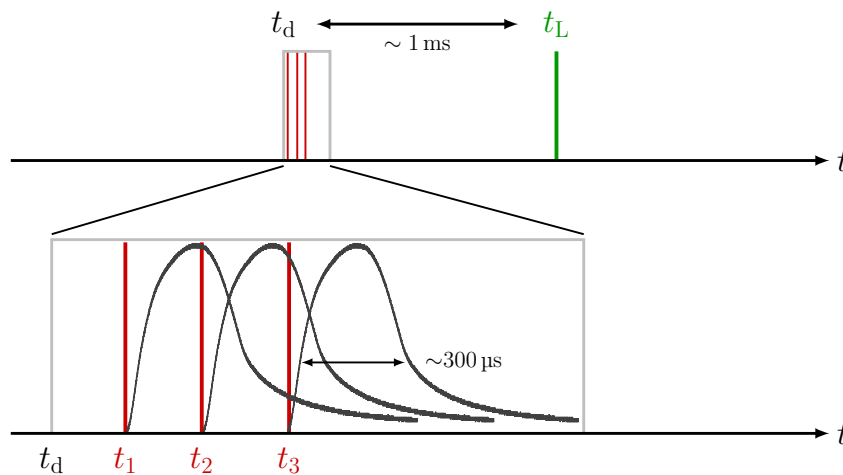


Fig. 4.2.2: Sketch of the timing sequence of a deflection measurement. The relative timing between deflection (t_d) and ionization (t_L) is varied for various TOF measurements (upper sketch). The deflector consists of three individual coils, which can be operated with different offset timings (t_1 , t_2 , t_3) relative to t_d . The lower sketch shows the experimentally measured magnetic field pulses ($I_d = 300$ A) for each coil timing, t_1 , t_2 , and t_3 .

The lower sketch of Fig. 4.2.2 shows that each individual coil can be operated with timings t_1 , t_2 , and t_3 . Throughout one deflection measurement, these coil timings are constant relative to the absolute deflector timing t_d . The relative integrated TOF mass signal γ_{rel} is defined as the ratio of the integrated TOF mass signal with the deflector switched on

and the integrated TOF mass signal with the deflector switched off.

$$\theta_{\text{rel}} = \frac{\theta_{\text{on}}}{\theta_{\text{off}}} \quad (4.2.1)$$

θ_{rel} for various t_d allows us to analyse the deflection ratio γ_d for different cluster sizes.

$$\gamma_d = 1 - \theta_{\text{rel}} = 1 - \frac{\theta_{\text{on}}}{\theta_{\text{off}}} \quad (4.2.2)$$

The optimal timings t_1 , t_2 , and t_3 (relative to t_d) were determined empirically, supported by global optimization of a simplified model. This model returns an estimate for γ_d as a function of t_1 , t_2 , and t_3 . The computational cost needed to achieve sufficient statistics using a 3D MD simulation (as used for verification, *vide infra*) would have been too high to be executing fast global optimization on an office computer. Therefore, we employed a 1D model where only the position along the central axis of the molecular beam (y coordinates) is considered. In space, this model uses the y -coordinates corresponding to the dimensions of the electromagnets and ionization region. In time, the duration of a square wave pulse (starting at each trigger time) and the timing of the ionization laser pulse act as fixed parameters. The final parameter is a threshold value, which is used to decide if a particle was deflected or not. A particle is considered to be deflected if its time spent in the magnetic field is above this threshold. This value was tuned to reproduce the deflection ratios observed in the actual experiment. To fully sample the parameter space at a low computational cost, a method inspired by ray tracing was implemented. For this, the model was represented in a 2D space-time, which is on a flat surface defined by (y, t) coordinates. On this surface, the magnetic pulse appears as a box (magnet length \times on-time) and the ionization volume can be represented by a 1D pixel array located at the ionization time. Cluster trajectories travel as straight lines over this plane, with a slope depending on their velocity. Each ray will intersect the boxes as a function of its slope and ionization pixel, and these intersections reflect the time spent in the magnetic field. If the sum of the temporal cutting ranges through the boxes is above the threshold parameter, it is deflected. Finally, the results are scaled with a simulated or measured velocity distribution. This converts the uniform set of trajectories into realistic intensities and facilitates the computation of γ_d using equation 4.2.2. The actual implementation of this model was done using MATLAB. Processing all trajectories in collective, fixed-size arrays, using a model that exclusively relies on elementary single cycle operations, the calculation of $\gamma_d(t_1, t_2, t_3)$ is sufficiently fast to be utilized within a global optimization algorithm. Relying on the built-in algorithms of MATLAB, a scatter-search mechanism was used together with a sequential quadratic programming method for the refinement stage. Two classes of solutions were found. For low fields (requiring high threshold values), the magnets are triggered sequentially, to deflect the dominant part of the velocity distribution in a joint effort. For high fields (low threshold values), the central magnet is triggered first to also deflect slow clusters, even before those fast clusters that reach the ionization

volume at the same time entered the first magnet.

4.2.2 Measured velocity distributions of $\text{Na}(\text{NH}_3)_n$

Since the deflector is operated in a pulsed manner, the coil timings t_i ($i = 1, 2, 3$) have to be synchronized with t_L . The time delay between deflection and ionization (Fig. 4.2.2) depends on the cluster size specific velocity distributions. The knowledge of individual cluster beam velocity distributions is thus crucial to optimize the deflector timings for high deflection ratios. To determine cluster velocity distributions, photoions were extracted perpendicular to the molecular beam propagation axis (Fig. 4.2.1a). The extraction field was set to optimized VMI conditions. Time-of-flight based mass gating was used to record the size selected photoion images of $\text{Na}(\text{NH}_3)_n$ ($n = 1 - 4$) shown in Fig. 4.2.3a. The velocities of the neutral clusters in the molecular beam correspond to a displacement of the photoions in the detector plane. The cluster-resolved velocities can be determined by the displacement of the image centre (white cross in Fig. 4.2.3a). The velocity v is calculated using the equation:

$$v = \left(2 \cdot C \cdot V_R \cdot r^2 / m\right)^{1/2} \quad (4.2.3)$$

where V_R is the voltage on the repeller, r is the radial position in the image, m is the cluster mass and C is a setup dependent calibration constant.

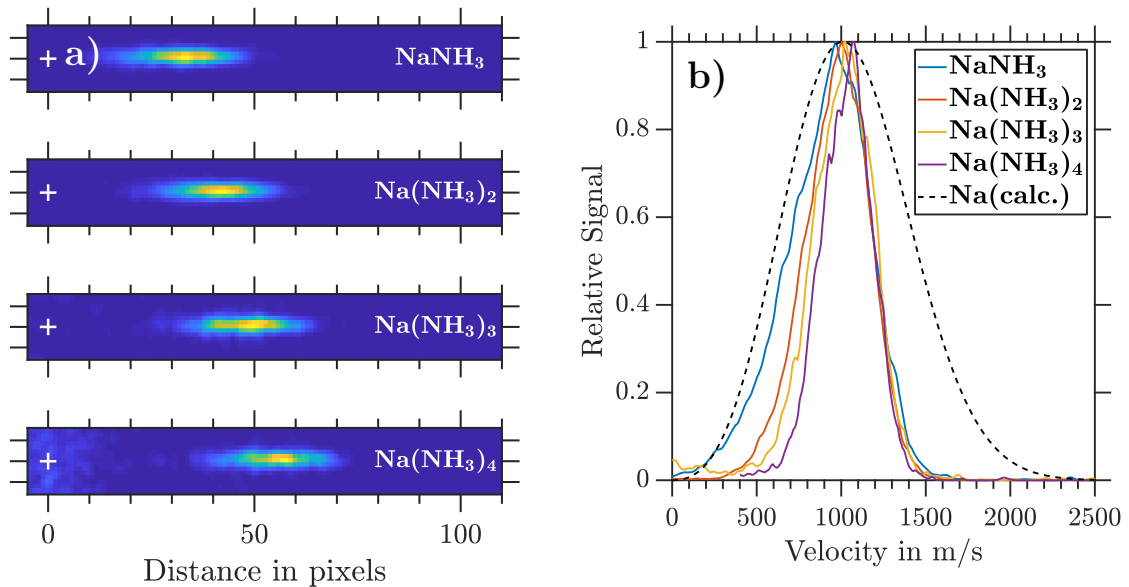


Fig. 4.2.3: (a) $\text{Na}(\text{NH}_3)_n$ ($n = 1 - 4$) ion images measured in perpendicular extraction at $V_R = 7$ kV. (b) Experimental $\text{Na}(\text{NH}_3)_n$ velocity distributions retrieved from ion images. The calculated velocity distribution for an effusive Na-beam at 265 °C is shown as a dashed line (see the supplementary information in section 4.6.3). Its distribution function is given by the convolution of a 1D Maxwell–Boltzmann distribution with an exponential transmission function.

The velocity distributions are plotted as coloured lines in Fig. 4.2.3b. The velocity distributions were retrieved by averaging over four different extraction settings ($V_R = 10$ kV, 7 kV, 5 kV and 3 kV). This is feasible because the cluster velocity distributions in the molecular beam do not depend on the extraction settings (V_R and MCP gating times). Furthermore, a calculated 1D Maxwell-Boltzmann velocity distribution for an effusive Na-beam at 265 °C convoluted with an exponential transmission function (see section 4.6.3, supplementary information) is shown as a black dashed line in Fig. 4.2.3b. The effusive Na-atoms have a centre velocity of 1000 ms^{-1} and a full width at half-maximum (FWHM) of 870 ms^{-1} . In comparison, $\text{Na}(\text{NH}_3)_4$ has a centre velocity of 1070 ms^{-1} and a FWHM of 350 ms^{-1} . The significant difference in beam velocities (magnitude and width) arises from the differences in the generation of effusive and molecular beams.

Tab. 4.2.1: Centre velocities v_c and FWHM of the measured velocity distributions of $\text{Na}(\text{NH}_3)_n$

Cluster	v_c/ms^{-1}	FWHM/ ms^{-1}
NaNH_3	970	540
$\text{Na}(\text{NH}_3)_2$	1000	445
$\text{Na}(\text{NH}_3)_3$	1020	420
$\text{Na}(\text{NH}_3)_4$	1070	350

Comparing the velocity distributions of doped ammonia clusters, two effects can be seen with increasing cluster size. Firstly, the centre velocity v_c shifts to slightly higher velocities, and secondly the FWHM decreases (Table 4.2.1). These differences can be attributed to collisions occurring between the bare clusters and sodium atoms inside the oven during the doping process. Due to momentum conservation, lighter particles deviate further from their initial molecular beam velocity than heavier particles. This explains why the velocity profiles are essentially cluster size independent on the high velocity side of the distributions (Fig. 4.2.3b). This part of the velocity distributions reflects collisions between Na and clusters with little momentum transfer, thus largely retaining the initial neat NH_3 supersonic velocity distribution.

4.2.3 Modelling of the magnetic deflection

To verify our experimental results, we chose a MD approach to simulate the cluster trajectories from the entry of the deflection chamber until ionization. For this approach, firstly, a detailed model of the cluster beam is essential. Secondly, a detailed description of the inhomogeneous magnetic field is needed. In our model we describe the cluster beam by the initial velocity and mass of each particle. The initial velocities in the y -direction are randomly sampled from the cluster size specific molecular beam velocity distribution, which is discussed in detail in section 4.2.2. The initial velocities in the x - and z -directions are calculated using their beam divergence angle and the velocity in the y -direction. The initial

particle coordinates are defined by the position and diameter of the entrance skimmer (see Fig. 4.2.1b). Hereby the skimmer position defines the y -coordinate and the diameter defines the possible x, z coordinates of the Gaussian beam profile. By sampling enough particles ($> 10^5$) a nearly continuous distribution of initial properties is achieved. The experimental dimensions described in section 4.2.1 are accounted for by our MD approach. The force caused by the inhomogeneous potential in the flight channel is defined as the negative gradient of the Zeeman potential (neglecting the contribution of the electron orbital angular momentum $L = 0$).

$$V_{\text{Zeeman}} = \frac{\mu_B g_S}{\hbar} \cdot \mathbf{S} \cdot \mathbf{B} \quad (4.2.4)$$

$$\mathbf{F} = \nabla (\boldsymbol{\mu} \cdot \mathbf{B}) = -\frac{\mu_B g_S}{\hbar} \nabla (\mathbf{S} \cdot \mathbf{B}) \quad (4.2.5)$$

where μ_B is the Bohr magneton, g_S the gyromagnetic factor of the total spin angular momentum \mathbf{S} , \mathbf{B} the magnetic field and \mathbf{F} is the force. The force field for the MD simulations is defined by the magnetic field gradients, obtained from a COMSOL simulation assuming a 2D model of the deflector cross section (see Fig. 4.2.1d) and a DC current of 1000 A. As in the experiment the force field is only applied during the on-time of the magnetic field pulses. For an accurate description of the magnetic pulse profiles, we used a Hall probe for the time-resolved measurement of the pulses inside the deflector flight channel. These magnetic pulse profiles (see Fig. 4.2.2) were measured for various peak currents and used as input for our MD simulations. Current specific scaling factors are determined in relation to the integrated magnetic field pulse profile at 1000 A. An additional magnetic field measurement showed that the induction at the end of each metal bridge is approximately 20% of the peak pulse inside the deflector flight channel. We therefore define the magnetic field magnitude in the epoxy layers to be 20% of the current specific scaling factor of the electromagnetic coils. The forces applied during the pulse are calculated using equation 4.2.5. As in the experiment, the three electromagnets can be pulsed with individual timings t_1, t_2 , and t_3 . Due to the experimental dimensions, not all particle trajectories will reach the ionization region, and consequently we introduce the following conditions to simulate the particle trajectories. Particles that collide with the deflector walls are considered ‘lost’. Only particles that are transmitted through the detection skimmer can be detected. Only particles that are in the ionization region at time t_L can be detected.

As an output, the MD simulation creates x, z -coordinates for each trajectory in the detection skimmer plane. These coordinates resemble the molecular beam cross section. In Fig. 4.2.4, the visualization of such an output (10^6 trajectories) is shown for three spin states $-1/2, 0$ and $+1/2$ for particles with the same mass as NaNH_3 .

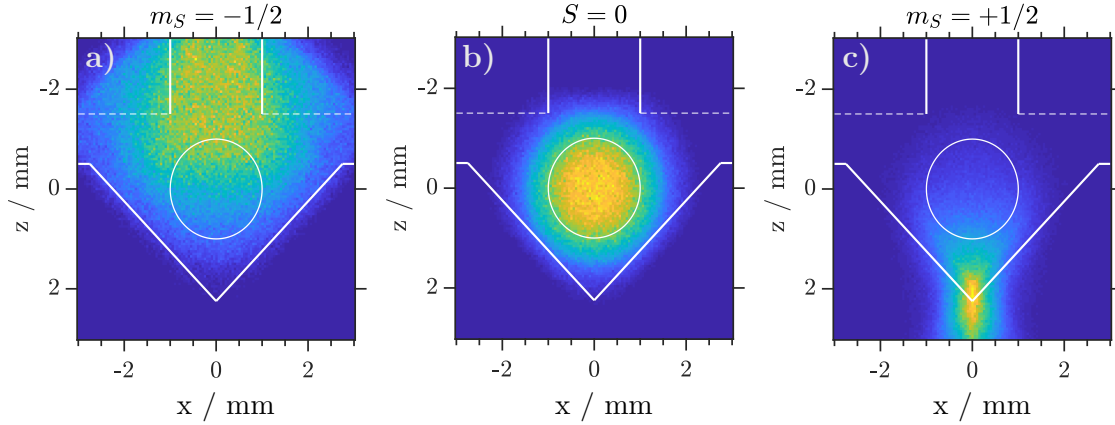


Fig. 4.2.4: MD simulations of a particle with the same mass as NaNH_3 for spin states (a) $m_S = -1/2$, (b) $S = 0$ and (c) $m_S = +1/2$. 10^6 trajectories were calculated for all simulations. The white lines indicate the cross section of the flight channel, while the white dotted lines represent the borders of the epoxy layers. The white circle represents the detection skimmer.

The magnetic field gradient in the z -direction deflects paramagnetic particles in either the positive or the negative z -direction depending on m_S . In the centre of the flight channel ($x = 0$), the field gradient along the z -axis is close to constant. The gradient in the x -direction causes one spin component to diverge (see Fig. 4.2.4a), while it focuses the other spin component (see Fig. 4.2.4c). The relative signal passing through the detection skimmer, shown as a white circle in Fig. 4.2.4, and reaching the ionization region at the same time, is calculated using the following equation:

$$\theta_{\text{rel}} = \frac{\theta_{m_S=+1/2} + \theta_{m_S=-1/2}}{2\theta_{S=0}} \quad (4.2.6)$$

where $\theta_{m_S=+1/2}$, $\theta_{m_S=-1/2}$ and $\theta_{S=0}$, respectively represent the number of trajectories of each individual spin state passing through the detection skimmer, reaching the ionization region at t_L and subsequently being ionized. Simulating trajectories without a magnetic field is equivalent to simulating trajectories for $S = 0$. Therefore, $\theta_{S=0}$ represents the ion signal when the deflector is switched off. By varying t_d with respect to t_L , relative signals can be evaluated for each time delay. This procedure generates a relative signal dip, which is compared to the experimental data.

In a further step, we simulated the trajectories reaching the ionization region. Trajectories that pass through the detection skimmer and overlap with the Gaussian laser beam profile of 4.8 mm FWHM are treated as ionized. For those ionized particles, an output file is created. It contains the spin state, ionization coordinates and velocity vectors. In addition, the output files are translated into input files for SIMION. SIMION ©8.0 [157] is used to simulate the trajectories of the generated photoions in the electrostatic extraction field and at which positions they impinge on the 2D plane of the ion detector. With this combination of simulations, we are able to simulate the full trajectories from neutral clusters entering the deflector to photoions colliding with the position-sensitive detector (see section 4.3.1).

4.3 Results

4.3.1 Coil contributions to the deflection of NaNH_3

Fig. 4.3.1 visualizes the influence of the individual coils on the deflection for the example of NaNH_3 . For that purpose, mass gated NaNH_3 photoions were extracted perpendicular to the molecular beam propagation axis and detected via VMI while operating the deflector at $I_d = 300$ A (Fig. 4.3.1a). For the experiment where all coils (‘all coils’) were used, the electromagnets were fired in an optimized $t_2 < t_1 < t_3$ sequence. Hereby, t_d was set to a timing where the highest possible deflection ratio is achievable. By operating each electromagnet separately (1st, 2nd, and 3rd coils), we aim to understand the individual deflection contribution. A further ion image was recorded when the magnetic field was turned off. These recorded ion images are shown in Fig. 4.3.1a on the same colour code intensity scale. Operating the deflector clearly reduces the ions impinging the 2D detector plane. Each coil acts on a subset of the cluster distribution and all coils acting together cause a decreased ion signal of $\theta_{\text{rel}} = 0.19$.

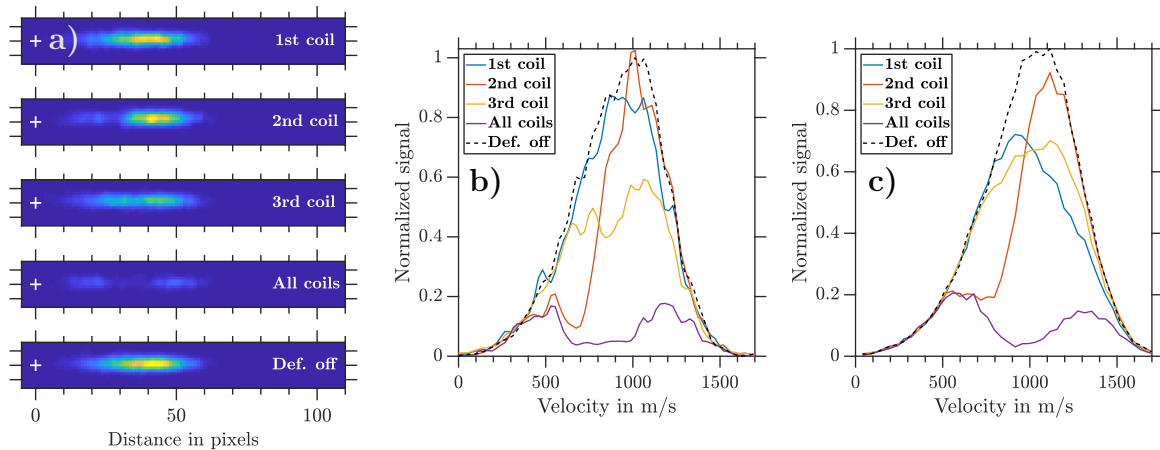


Fig. 4.3.1: (a) NaNH_3 ion images measured with $V_R = 5$ kV for different coil settings. The coils of the deflector were pulsed individually (1st, 2nd, or 3rd coil), together (all coils) with a $t_2 < t_1 < t_3$ coil sequence and $I_d = 300$ A, or not at all (Def. off). (b) Experimental NaNH_3 velocity distributions retrieved from the photoion VMIs in panel a. (c) Corresponding simulated NaNH_3 velocity distributions obtained by combining MD and SIMION simulations. The displacement coordinates on the detector were calculated and then transformed into velocity coordinates.

The retrieved experimental NaNH_3 velocity distributions for each ion image are shown in Fig. 4.3.1b. The 2nd coil (orange line), being switched on first, mainly acts on particles with slow velocities of about 500 ms^{-1} . The 1st coil (blue line) acts on particles travelling with about 1000 ms^{-1} and the 3rd coil (yellow line) acts on almost the full width of the distribution. The violet line shows all coils being fired, with residual signal remaining from particles at the fast and slow ends of the velocity distribution. These results visualize

the functioning of the pulsed deflector and clearly show how critical it is to properly set the coil timings for a given cluster velocity distribution. To achieve reasonable deflection ratios, the magnetic field pulses have to act on the full velocity distribution. If the coil timings are not set well, a certain part of the velocity distribution will not be deflected. Finding such optimal coil timings in the experiment can be challenging. Due to the repetition rate (1 – 5 Hz) of the deflector, tracking of experimental deflection signals would be prohibitively time consuming. Therefore, we decided to rely on our simplified model for global optimization of the coil timings (section 4.2.1).

Fig. 4.3.1c displays the corresponding simulated NaNH_3 velocity distributions obtained from a combination of MD simulations with SIMION simulations (section 4.2.3). The experimental and simulated data show good general agreement if all coils are operated simultaneously. Yet the experimental results for the 1st and 3rd coils are only partially verified. While the simulation overestimates the deflection ratio of the 1st coil, deflection by the 3rd coil is underestimated. The experimental and simulated deflection ratios γ_d (equation 4.2.2) of the individual coils are summarized in Table 4.3.1.

Tab. 4.3.1: Experimental and simulated deflection ratios γ_d for each individual electromagnetic coil and all coils together.

	1st coil	2nd coil	3rd coil	All coils
$\gamma_d(\text{experiment})$	0.09	0.25	0.33	0.81
$\gamma_d(\text{simulation})$	0.23	0.25	0.19	0.77

4.3.2 Deflection ratios for $\text{Na}(\text{NH}_3)_n$: Experiment vs. MD simulations

NaNH_3 .

Fig. 4.3.2a shows, as an example, the integrated relative TOF signals θ_{rel} as a function of t_d (circles) at $I_d = 300$ A with a 2σ error. The average signal intensity of the five or four (for 600 A and 700 A) late timings defines $\theta_{\text{rel}} = 1$ and their standard deviation defines the error bars (2σ) of a measurement. The minimum error of θ_{rel} for each cluster size measurement series was taken to be half of the average error determined from all of the studied deflector currents. For comparison, the results of the MD simulations are shown as diamonds. The experimental θ_{rel} decreases to a minimum of 0.31(7), which corresponds to the minimum of the MD simulation of $\theta_{\text{rel}} = 0.32$. The comparison of experimental and simulation data shows very good agreement across the sampled deflector timings t_d . This indicates that the deflection process of NaNH_3 at 300 A is correctly described by the interaction of the magnetic moment $\boldsymbol{\mu}$ and the inhomogeneous magnetic field \mathbf{B} . The same holds for larger currents (not shown). NaNH_3 TOF signals of four representative t_d (0, 4.6, 4.8 and 10.0 ms) are marked as open black circles in Fig. 4.3.2a and shown

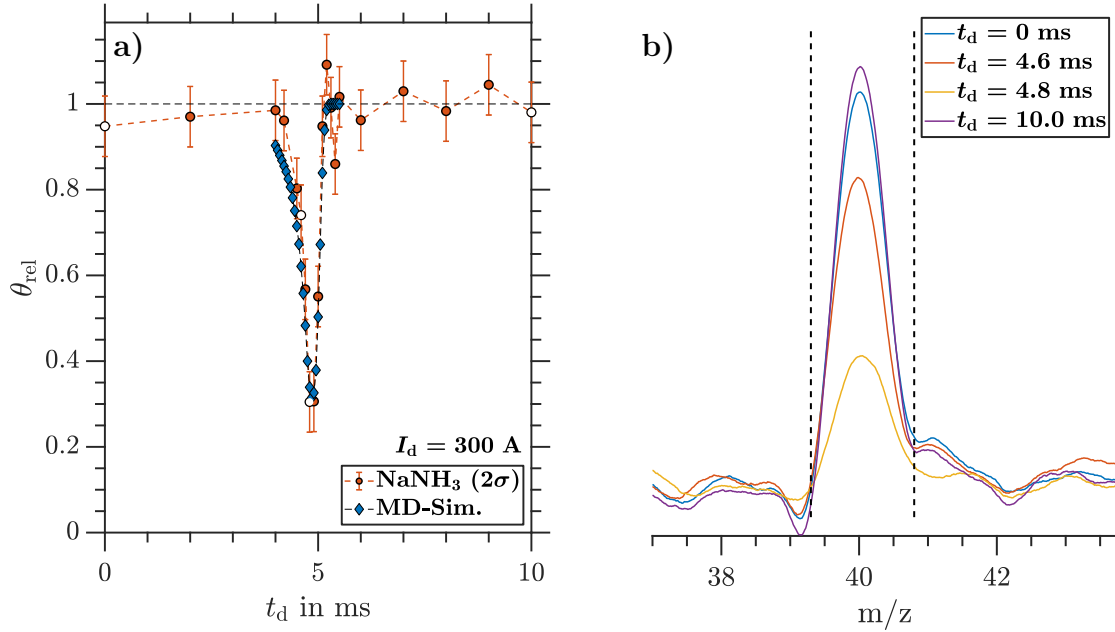


Fig. 4.3.2: (a) Relative integrated NaNH₃ TOF signal θ_{rel} (2000 shots per data point) as a function of t_d (circles with 2σ error), compared with MD simulations (diamonds). (b) NaNH₃ TOF signals for four representative t_d corresponding to the open black circles at 0, 4.6, 4.8 and 10.0 ms in panel (a). The deflector was operated at $I_d = 300$ A.

as representative TOF traces in Fig. 4.3.2b. The TOF traces are baseline subtracted, background corrected and smoothed before the signal peaks are integrated. The dashed lines indicate the integration window applied to retrieve integrated NaNH₃ TOF signals for each t_d .

By changing the integration window to larger cluster sizes, we are able to obtain equivalent data as in Fig. 4.3.2 for all cluster sizes Na(NH₃)_n ($n = 1 - 4$) from the same TOF traces. Repeating measurements and MD simulations for several magnetic field strengths by varying I_d provides the maximum γ_d (corresponding to the minima as in Fig. 4.3.2a) as a function of I_d . Fig. 4.3.3 shows the maximal γ_d as a function of I_d for NaNH₃, obtained from the experimental data (circles) and from the simulations (diamonds). With increasing magnetic field strength, the experimental γ_d increases reaching a maximum of 0.78(7) at $I_d = 700$ A.

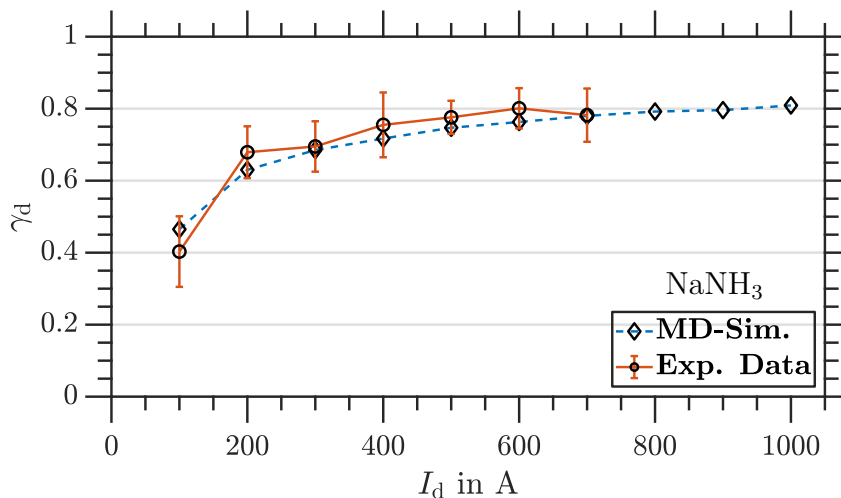


Fig. 4.3.3: Maximal γ_d as a function of I_d for NaNH_3 . Circles: experiment. The error indicates 2σ . Diamonds: MD simulation. The deflector was operated in a $t_1 < t_2 < t_3$ coil timing sequence.

For all different I_d , the experimental and simulated γ_d agree very well within error bars (2σ). Due to the fact that the applied MD approach does not take any intracluster spin relaxation (ISR) times [142, 65, 66] into account, the good agreement between experiment and simulation reveals that for NaNH_3 the intracluster spin relaxation time has to be significantly longer than the interaction time with the magnetic field gradient [63, 64] (see discussion in section 4.4). Also see Fig. A.0.1a in the appendix for additional data of maximal γ_d as a function of I_d for a $t_2 < t_1 < t_3$ coil timing sequence.

$\text{Na}(\text{NH}_3)_2$.

Fig. 4.3.4 shows equivalent data as in Fig. 4.3.3, but for $\text{Na}(\text{NH}_3)_2$. Within error bars, γ_d is larger than 0 for all experimental data points and reaches a maximal value of $\gamma_d = 0.39(8)$ at $I_d = 700$ A. In other words, deflection is observed for $\text{Na}(\text{NH}_3)_2$ for all applied magnetic field gradients.

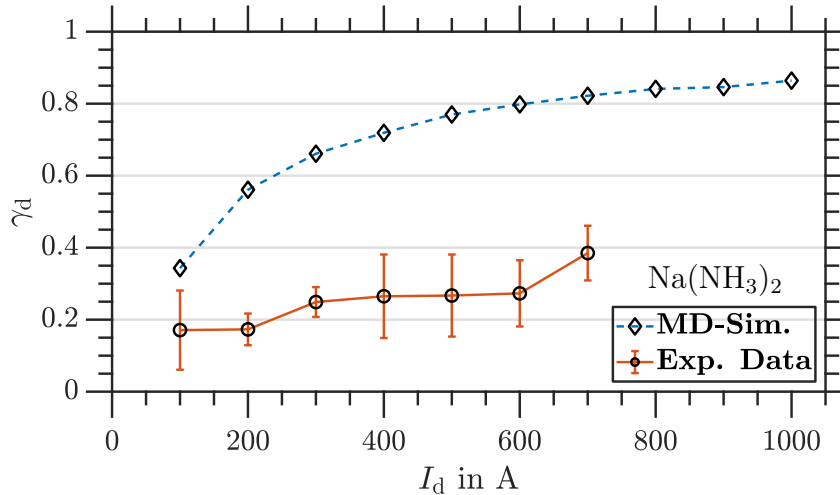


Fig. 4.3.4: Maximal γ_d as a function of I_d for $\text{Na}(\text{NH}_3)_2$. Circles: experiment. The error indicates 2σ . Diamonds: MD simulation. The deflector was operated in a $t_1 < t_2 < t_3$ coil timing sequence.

Yet an agreement with the MD simulations is not found for any applied deflector current. By increasing the cluster size, several effects have to be taken into account that influence the degree of deflection. On one hand, a higher magnetic force has to be applied to deflect a heavier particle to the same extent as a lighter particle. On the other hand, the FWHM of the velocity distribution decreases for heavier particles, which results in a higher γ_d (section 4.2.2 and section 4.6.3, supplementary information). Both of these effects are taken into account in the MD simulations. Nonetheless, the experimental results and MD simulations show crucial deviations which cannot be explained within 2σ error of each measurement. As discussed in section 4.4, a possible explanation for the discrepancies is ISR processes, [142, 65, 66] which for $\text{Na}(\text{NH}_3)_2$ would occur at the same time scale comparable to or slightly faster than the interaction time with the magnetic field gradient [63, 64]. See Fig. A.0.1b in the appendix for additional data of maximal γ_d as a function of I_d for a $t_2 < t_1 < t_3$ coil timing sequence.

$\text{Na}(\text{NH}_3)_3$ and $\text{Na}(\text{NH}_3)_4$.

Fig. 4.3.5 and 4.3.6 (circles) show that the effects observed for $\text{Na}(\text{NH}_3)_2$ become even more significant when increasing the cluster size further to $\text{Na}(\text{NH}_3)_3$ and $\text{Na}(\text{NH}_3)_4$, respectively. At a current of 300 A (panel a), $\theta_{\text{rel}} = 1$ within 2σ error for all sampled deflector timings t_d , meaning that both $\text{Na}(\text{NH}_3)_3$ and $\text{Na}(\text{NH}_3)_4$ show no clear deflection. At currents of 700 A (Fig. 4.3.5b) and 600 A (Fig. 4.3.6b), both $\text{Na}(\text{NH}_3)_3$ and $\text{Na}(\text{NH}_3)_4$ are slightly deflected, with maximal signal depletions of $\theta_{\text{rel}} = 0.77(11)$ and $\theta_{\text{rel}} = 0.79(7)$, respectively. Again, substantial deviations are found when compared with the MD simulations (diamonds). These deviations are best summarized by the maximal γ_d as a function of the current I_d (panels c in Fig. 4.3.5 and 4.3.6). Clear deflection within error bars is only achieved for the highest currents of $I_d \sim 600 - 700$ A, even though it is worth mentioning that

the average values of γ_d also lie slightly above zero for almost all other currents. For the higher currents, the MD simulations predict $\gamma_d \sim 0.7$, which is in disagreement with the experimental values of $\gamma_d \sim 0.2$.

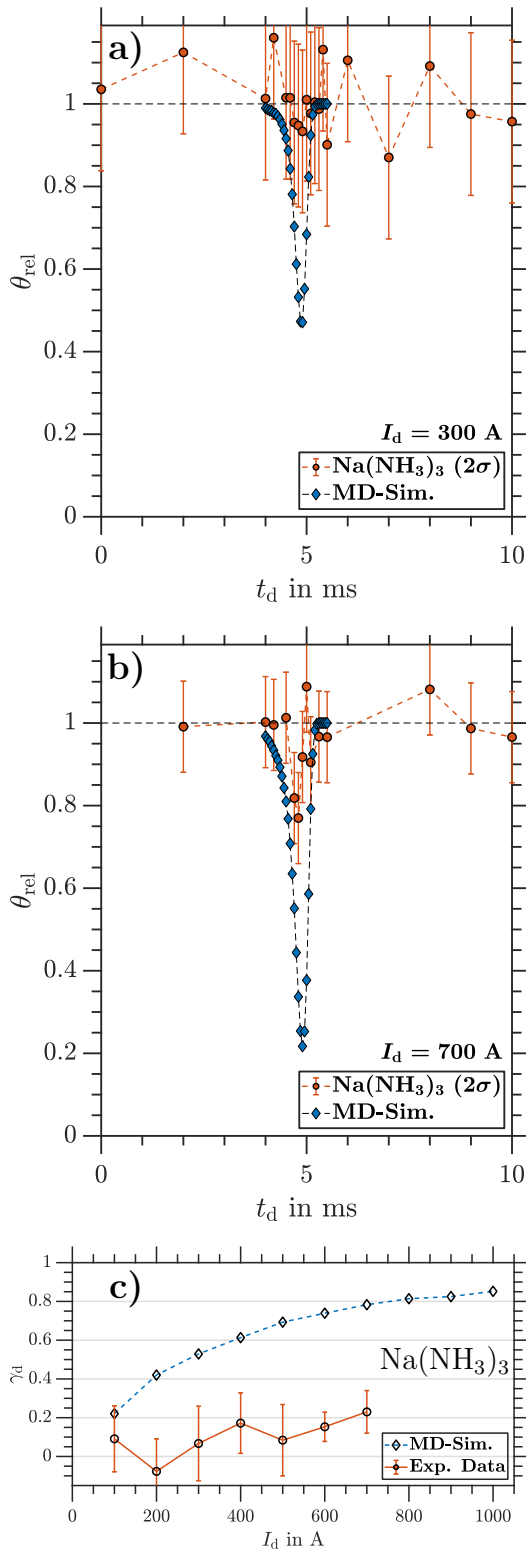


Fig. 4.3.5: θ_{rel} as a function of t_d of $\text{Na}(\text{NH}_3)_3$ recorded at (a) $I_d = 300 \text{ A}$ and (b) $I_d = 700 \text{ A}$. (c) Maximal γ_d as a function of I_d for $\text{Na}(\text{NH}_3)_3$. Circles: experiment. The error indicates 2σ . Diamonds: MD simulation.

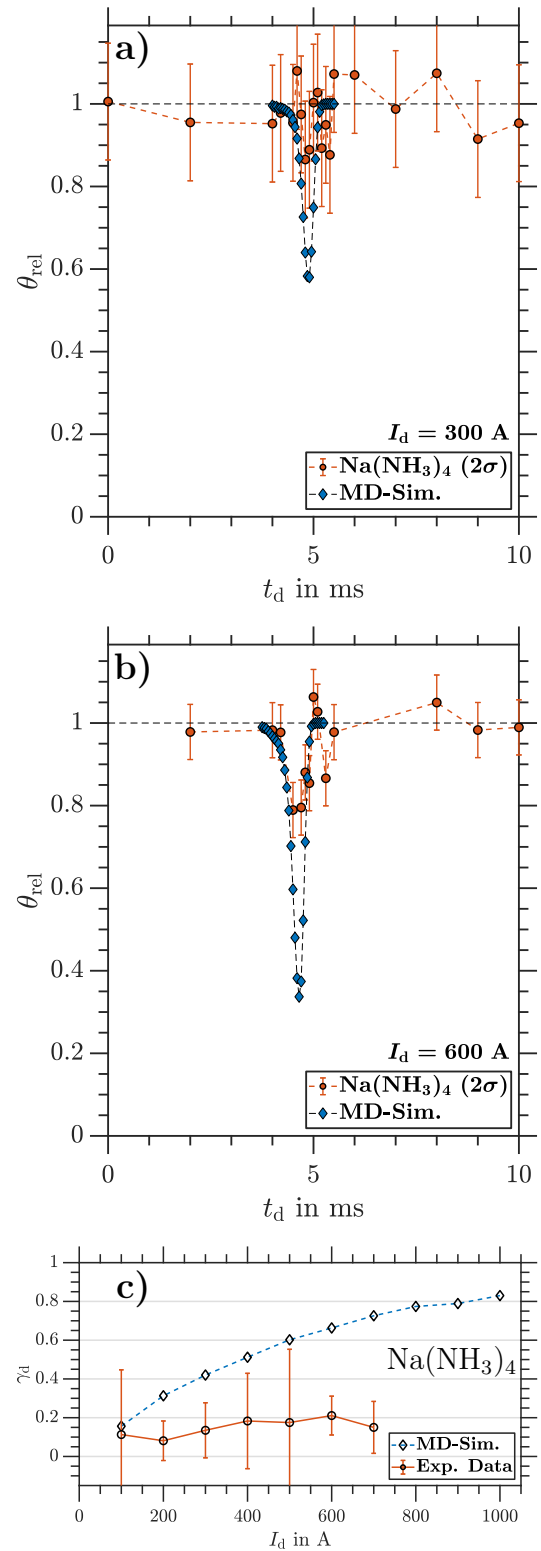


Fig. 4.3.6: θ_{rel} as a function of t_d of $\text{Na}(\text{NH}_3)_4$ recorded at (a) $I_d = 300 \text{ A}$ and (b) $I_d = 600 \text{ A}$. (c) Maximal γ_d as a function of I_d for $\text{Na}(\text{NH}_3)_4$. Circles: experiment. The error indicates 2σ . Diamonds: MD simulation.

In summary, we observe the same deflection as expected from MD simulations for the smallest cluster NaNH_3 at all currents (Fig. 4.3.3), while the larger clusters $\text{Na}(\text{NH}_3)_n$ ($n = 2 - 4$; Fig. 4.3.4 to 4.3.6) show strongly reduced deflection compared with the simulations. $\text{Na}(\text{NH}_3)_2$ experiences small but clear deflection at all currents. For $\text{Na}(\text{NH}_3)_3$ and $\text{Na}(\text{NH}_3)_4$, in contrast, clear deflection within error bars could be seen only at higher currents. For comparison, at a current of $I_d \sim 700$ A, the simulations predict γ_d values around 0.8 for all cluster sizes, while the experimentally observed deflection ratios systematically decrease from $\gamma_d \sim 0.8$ for NaNH_3 to $\gamma_d \sim 0.4$ for $\text{Na}(\text{NH}_3)_2$ to $\gamma_d \sim 0.2$ for $\text{Na}(\text{NH}_3)_3$ and $\text{Na}(\text{NH}_3)_4$. As discussed in the following section this hints that spin relaxation times decrease with increasing cluster size.

4.4 Discussion

Since the effect of increasing cluster mass is already accounted for by our MD-simulations, the reduced deflection we observe for larger clusters might at first sight be interpreted phenomenologically as an indication of a reduction in the effective magnetic moment with increasing cluster size. Such dependence of the magnetic moment on cluster size and structure was found to explain the magnetic deflection experiments of isolated bi-metal clusters. Thus, the different magnetic moments of a single magnetic impurity (Co) in non-magnetic metallic hosts of discrete size (Nb_n) have been explained within the framework of the Anderson impurity model, in terms of the increase of the local moment with increasing host band gap (HOMO-LUMO gap) [153]. Such arguments, however, are not applicable to our system of single spin 1/2 doped weakly interacting molecular clusters. The host molecules (NH_3) are closed shell with a very large HOMO-LUMO gap (liquid ammonia band gap: 7 eV) [158]. The intermolecular interaction (a few tenths of an eV) is too weak to perturb the electronic structure of the host significantly. The effect of clustering on the electronic structure of the dopant is more pronounced. According to *ab initio* calculations the HOMO-LUMO (*s-p*) gap of about 2 eV in bare Na is reduced to 1.5 eV, 0.9 eV and 0.8 eV in NaNH_3 , $\text{Na}(\text{NH}_3)_2$ and $\text{Na}(\text{NH}_3)_3$, respectively [24]. But the unpaired electron still largely retains its *s*-character. Within an earlier study of the photoelectron spectrum of the solvated electron in Na-doped ammonia clusters, we performed extensive DFT calculations on $\text{Na}(\text{NH}_3)_n$ ($n \leq 30$) [1, 2]. The *s*-character of the unpaired electron of 96% in $\text{Na}(\text{NH}_3)$ decreases only slightly to about 93% in $\text{Na}(\text{NH}_3)_4$. In all these cases the unpaired electron mainly resides on the surface of the cluster (see Fig. 4.4.1). There is some delocalization of the spin density over the NH_3 host molecules, which tends to increase with cluster size, but with 16% in $\text{Na}(\text{NH}_3)_4$ it still remains rather modest for the cluster sizes considered in the present work. It appears unlikely that any of these effects could change the magnetic moment significantly in these pure spin 1/2 systems. This leaves intracuster spin relaxation as a more plausible reason for the reduced deflection observed in our experiments.

In order to discuss our results in terms of possible intracluster spin relaxation processes, a characteristic spin relaxation time τ is compared with the cluster specific interaction time t_m with the magnetic field for two different cases. If $\tau > t_m$, the electronic spin state does not ‘flip’ when the cluster traverses the deflector setup (*i.e.* when the cluster interacts with the magnetic field) and free spin (atom-like) deflection behaviour would be observed. This matches the assumptions of our MD simulation, which, therefore, should reproduce the experimentally observed deflection ratios. This was successfully verified using a beam of Na atoms, which exhibit no spin relaxation (Fig. 4.6.1, supplementary information) during t_m . Very good agreement between the MD simulation and experimental data was observed for NaNH_3 (Fig. 4.3.3), suggesting negligible intracluster spin relaxation during t_m . In our experiment, t_m is $\sim 200 \mu\text{s}$ considering the centre velocity of NaNH_3 ($\sim 1000 \text{ms}^{-1}$) and the deflector length. Therefore, the intracluster spin relaxation time for NaNH_3 must be longer than $200 \mu\text{s}$.

If $\tau \leq t_m$, the electron spin state stochastically ‘flips’ while travelling through the magnetic field. These statistical fluctuations of the spin reduce deflection and cause a broadening of the molecular beam cross section [63, 64]. In our setup, this would result in partial deflection. Since these effects are not included in our MD model, the simulations for cases with $\tau \leq t_m$ no longer reproduce the measured deflection ratios. If $\tau \ll t_m$, γ_d values of zero are expected, while τ values on the order of t_m would result in reduced, but non-zero deflection ratios. The latter would explain our observations for $\text{Na}(\text{NH}_3)_2$ at all currents and for $\text{Na}(\text{NH}_3)_3$ and $\text{Na}(\text{NH}_3)_4$ at higher currents. With this explanation, typical intracluster relaxation times would be on the order of $200 \mu\text{s}$.

If the decrease of intracluster relaxation times in larger clusters is the reason for the observed reduced deflection, how does this size dependence come about? The electronic structure might play a role here, as both the spatial extension of the unpaired electron and its average separation from the Na core increase with cluster size [24]. Given that these effects are not dramatic we expect other contributions to be more important. A detailed theoretical description on spin relaxation processes in isolated molecules and clusters was previously given by Knickelbein [66]. In his interpretation of Stern-Gerlach experiments, intracluster/intramolecular spin relaxation (ISR) becomes more likely the higher the density of the rovibrational states. Overall rotations of molecular clusters induce Zeeman-like eigenstates in the presence of an external magnetic field. Transitions between such Zeeman sublevels may occur within the conservation laws of internal energy and total angular momentum. The free molecule or cluster can undergo intramolecular or intracluster spin relaxation processes. In such processes, the molecule or cluster serves as a ‘thermal bath’ for its own spin, especially when the system is large and the temperature is high enough to populate many intramolecular states.

In our study of sodium-doped ammonia clusters, we expect analogous Zeeman-like sublevels with possible transitions occurring between the sublevels. Yet, the weak non-covalent bonds between the sodium atom and ammonia molecules and between ammonia molecules cause

distinct differences to previously investigated free molecules [63, 64, 61, 62, 143, 144, 145, 146] and cluster systems [142, 147, 69, 148, 70, 149, 150, 71, 151, 107, 72, 104, 153, 73, 74, 75, 76, 78, 79]. They are rather floppy systems undergoing large amplitude motions with low characteristic frequencies. Many of these represent hindered internal rotations whose vibrational angular momenta provide an effective coupling mechanism to the spin of the unpaired electron. While the rovibrational dynamics of these systems are evidently highly anharmonic, a harmonic analysis of the DFT calculations for the structures shown in Fig. 4.4.1 already provides a qualitative picture. The Na–N stretching and bending harmonic wavenumbers of NaNH_3 are calculated to be 231 cm^{-1} and 323 cm^{-1} , respectively.

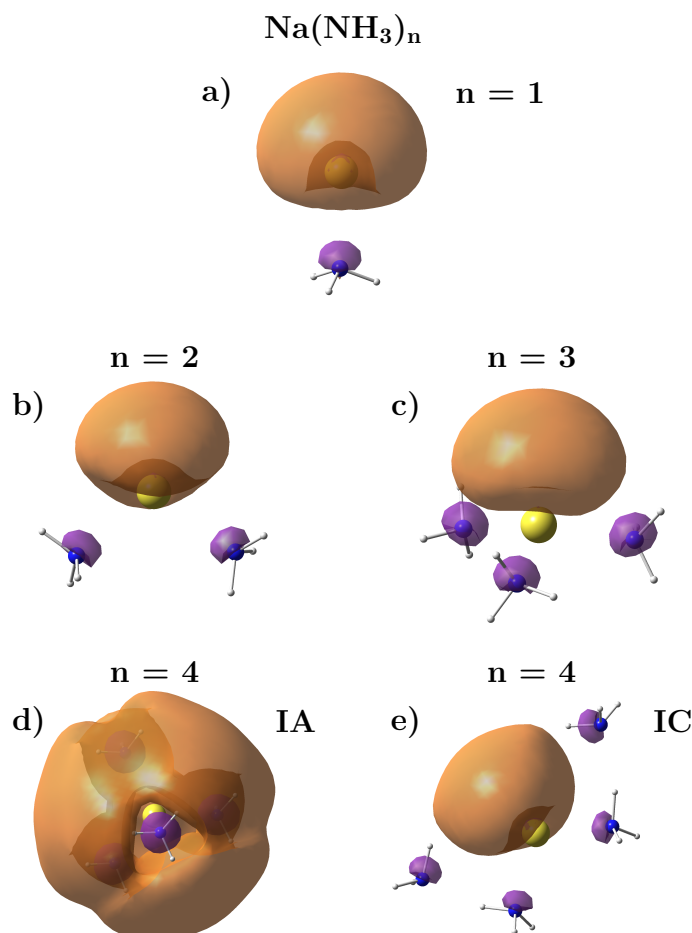


Fig. 4.4.1: Isosurfaces of the HOMOs of $\text{Na}(\text{NH}_3)_n$ clusters: (a) NaNH_3 , (b) $\text{Na}(\text{NH}_3)_2$, (c) $\text{Na}(\text{NH}_3)_3$, (d) $\text{Na}(\text{NH}_3)_4$ isomer IA with all eclipsed arrangement of NH_3 and (e) asymmetric isomer IC. (d) and (e) are adapted with permission from ref. [1] Copyright ©2015 American Chemical Society.

Considering the level of theory and experimental uncertainties, this is consistent with experimental results with values for the fundamental wavenumbers ranging from 195 cm^{-1} to 215 cm^{-1} for the stretching and 278 cm^{-1} for the bending fundamental [159, 160]. At estimated cluster temperatures in the range of $110 - 145\text{ K}$ [139], excited states of these low frequency vibrations (vibrational temperature $\sim 300\text{ K}$) are barely populated. This situation changes drastically for the larger clusters $\text{Na}(\text{NH}_3)_n$ ($n \geq 2$) [161]. Here new types of low frequency modes arise, *i.e.* internal rotation of NH_3 around the Na–N

axis and N–Na–N bending, with calculated harmonic wavenumbers of 20 cm^{-1} and 31 cm^{-1} for the NH_3 rotation and 41 cm^{-1} for the N–Na–N bending. This is consistent with a value of 25 cm^{-1} derived for the latter via ZEKE-PFI spectroscopy [160]. The corresponding vibrational temperature falls in the range between 30 K and 60 K. Compared with NaNH_3 , this leads to an abrupt increase in thermally accessible states. With each NH_3 molecule added, the number of internal modes with vibrational temperatures well below the estimated cluster temperature increases further with a corresponding exponential increase in the thermally accessible density of states.

The excited states of the NH_3 internal rotation and N–Na–N bending (hindered orbiting of NH_3 around Na) are associated with large vibrational angular momenta, which couple to the cluster’s rotational states and subsequently induce a highly perturbed Zeeman-like splitting pattern. Thus the increase of the rovibrational density of states to which the spin of the unpaired electron can couple would explain the decrease of the magnetic deflection upon the addition of NH_3 molecules to the Na-doped clusters. This density of coupling states is low for NaNH_3 translating into slow ISR. Adding a second NH_3 molecule produces a sudden increase in the density of coupling states as new types of low frequency internal motions arise. ISR accelerates accordingly and abruptly reduces the observed magnetic deflection. Adding more NH_3 molecules further enhances the effect, but does so more gradually. While we believe that this is the dominant cause for the cluster size dependence of the magnetic deflection we observe, other effects can also contribute. For example, hyperfine coupling might have to be taken into account. Furthermore, the molecular beam can contain multiple structural isomers for a given cluster size at the estimated cluster temperature. Each structural isomer would exhibit a particular Zeeman splitting pattern with possible transitions occurring between the Zeeman-like sublevels. Thereby spin relaxation would depend on the current geometry of the clusters, which might vary on the timescale of the experiment. The above phenomena would imply a marked temperature dependence of the spin relaxation process, which would be interesting to investigate in future work.

4.5 Conclusion

We have implemented a pulsed Stern-Gerlach deflection experiment to study the magnetic properties of sodium-doped ammonia clusters. The testing of the experimental setup for an effusive Na atom beam and the comparison with molecular dynamics simulations confirm the expected performance of the design. The present experimental study for $\text{Na}(\text{NH}_3)_n$ ($n = 1 - 4$) is a first attempt to understand the magnetic properties of sodium-doped ammonia clusters, which can be seen as a model system for solvated electron precursors. The combination of deflection experiments with molecular dynamics simulations provides, for the first time, insights into time-scales of intracluster spin relaxation in these small weakly-bound clusters. For NaNH_3 , we expect intracluster spin relaxation to take place on

a timescale substantially longer than 200 μs . The partial deflection that is observed for the larger clusters of $\text{Na}(\text{NH}_3)_n$ ($n = 2 - 4$) compared with molecular dynamics simulations, that do not take intracuster relaxation effects into account, suggests the relaxation times for these clusters to be in the order of 200 μs . We propose an acceleration of intracuster spin relaxation in $n > 1$ clusters as a result of Zeeman-like spin-rotation coupling. The emergence of very low frequency internal rotation modes for $n > 1$ leads to a drastic increase in the thermally accessible density of rovibrational states to which the spin can couple, which could explain the abrupt decrease of the deflection for clusters with $n > 1$. However, to obtain a more definite explanation of the observed cluster size dependence, further magnetic deflection experiments (*e.g.* spin refocusing with two Stern-Gerlach magnets) and modelling of intracuster relaxation processes should be carried out. Detailed studies of the magnetic and electronic properties of solvated electrons in clusters will lead to a better understanding of the paramagnetic and diamagnetic species in bulk alkali metal ammonia solutions.

4.6 Supplementary Information

4.6.1 Mechanical deflector design

The dimensions of the deflector and its position in the deflection chamber are shown in Fig. 4.2.1b to d. All metal body parts of the deflector are machined from magnetic steel (1080 carbon steel). As mentioned in section 4.2.1, the deflector consists of three electromagnets, each 7 cm in length, leading to an assembled deflector length of 21 cm. Each electromagnet consists of a metal body on which a coil, made from 15 turns of insulated copper wire is mounted. The cross section of the metal body with its coil is shown in Fig. 4.2.1d. The metal bridge, placed in the centre of each coil is 5.6 cm long and 2 mm wide, and acts as a pole shoe. The flight channel reaches a maximum height of 3.75 mm. The asymmetric geometry of the flight channel creates an inhomogeneous magnetic field with a strong gradient in the z -direction. The coils are set in epoxy to mechanically protect them and to increase heat conduction to the metal bodies. These bodies are mounted onto a single, liquid-cooled aluminium plate. A cooling liquid consisting of 30% glycol 70% water mixture is circulated by a closed-cycle chiller at -10°C through the aluminium plate. The deflector is mounted on two x, z -translation stages (one at each end) to allow fine alignment of the flight channel relative to the molecular beam. The detection skimmer is positioned 21.5 cm after the deflector exit to select the non-deflected species.

4.6.2 Electronic deflector design

Each electromagnet is driven by a 3-stage Pulse Forming Network (PFN) circuit designed to generate a high current square pulse of 1000 A with a pulse of 270 μs . High power thyristors are used to switch the PFN circuits, which resemble Cauer topology low-pass

filters using three capacitors and two inductors each. The PFNs are individually triggered by a delay generator (Stanford Research Systems DG535), using one channel for the master offset (t_d) and three others for the relative delays (t_1, t_2, t_3). Auxiliary signals (energy recovery and recharging sequences) are generated by a complex programmable logic device. To verify the actual performance when driving an electromagnet (of about 32 μH impedance and 75 $\text{m}\Omega$ resistance), both current pulses and resulting magnetic field pulses were measured for various charging voltages. The form of a typical magnetic field response measured in our setup (about 300 μs width) is included in Fig. 4.2.2. Charging voltage is provided from an external buffer capacitor bank, which is charged by a modified programmable power supply (TDK-lambda genesis 1000-10). With the current deflector design we are able to collect data at a repetition rate of 5 Hz when pulsing the electromagnetic coils with up to 300 A peak pulses (~ 150 V charging voltage). Working at higher currents is only feasible if the magnetic field pulse repetition rate is reduced. Operating the deflector with 700 A peak pulses (~ 350 V charging voltage) is achievable, if the repetition rate is reduced to 1 Hz. The limit in repetition rate and peak pulse currents arises from thermal loads generated in the in-vacuum coils that cannot be efficiently dissipated by our cooling method. Attempts to operate with higher thermal loads are prevented by the onset of outgassing, accompanied by a total loss of signal at about 1×10^{-4} mbar/s, which we attribute to obstruction of the flight channel. As this mechanism of signal extinction would compete with signal loss due to deflection, we choose repetition rates that keep the pressure rise in the deflector chamber below 3×10^{-8} mbar. A typical base pressure in the chamber housing the deflector is about 1×10^{-7} mbar.

The pulsed deflector design introduces several time dependent effects (time dependent field strengths, eddy currents, field fluctuations along the propagation axis). Our MD model, which includes time dependent magnetic fields (see section 4.2.3), reproduces the observed deflection of effusive Na-atoms quantitatively over the range of magnetic field strengths studied (see section 4.6.3, and also Fig. 4.3.3 for NaNH_3). A magnetic deflector being operated in a pulsed manner becomes very favourable when coupled to a photoelectron spectrometer with velocity map imaging (VMI) detection. The VMI detection of photoelectrons is very sensitive to external magnetic fields. With a pulsed magnetic field, it is easier to reduce such interfering magnetic fields and measure an undistorted photoelectron image. In addition, a pulsed deflector reduces the thermal load produced in the electromagnetic coils, which facilitates miniaturization and in-vacuum placement of the complete electromagnetic setup.

4.6.3 Deflection of effusive Na atoms

To test the performance of the deflector, we attempted to deflect sodium atoms in an effusive beam, produced by heating the sodium oven to 265 $^\circ\text{C}$. Photoionization was performed with a 212 nm laser pulse and sodium ions were detected via TOF mass spectrometry. Fig. 4.6.1 shows the relative sodium TOF signal plotted as a function of t_d (circles) at

$I_d = 400$ A (Fig. 4.6.1a) and $I_d = 800$ A (Fig. 4.6.1b) peak current. For comparison, the results of the MD-simulations (see section 4.2.3) are shown as diamonds. The experimental relative intensities and the MD simulations show good general agreement within 2σ of the former. The standard deviation σ was determined from the four latest timings (Fig. 4.6.1a), when $\theta_{\text{rel}} = 1$ and the field is switched on after the detected clusters have already passed the deflector. For these initial measurements and MD simulations, the individual coils were switched on simultaneously, $t_1 = t_2 = t_3$. For $I_d = 400$ A, the relative signal decreases to a minimum of approximately $\theta_{\text{rel}} = 0.5$. By increasing the current to 800 A (Fig. 4.6.1b), a stronger depletion of $\theta_{\text{rel}} = 0.3$ can be observed. This trend is reproduced by the MD-simulations. For our MD approach, we choose to describe the effusive sodium velocity distribution as a 1D Maxwell-Boltzmann distribution at 265 °C convoluted with a transmission function. This transmission function emulates residual gas in the deflector channel, which preferentially transmits the higher velocities contained in the initial velocity distribution leaving the sodium oven. The transmission is mathematically described by $T(v) = 1 - \exp(-bv^2)$ where b is a fit parameter which is proportional to an effective channel pressure. The remaining signal deviations of experimental data and MD simulation may be due to inaccuracies in the modelling of the effusive sodium velocity distribution.

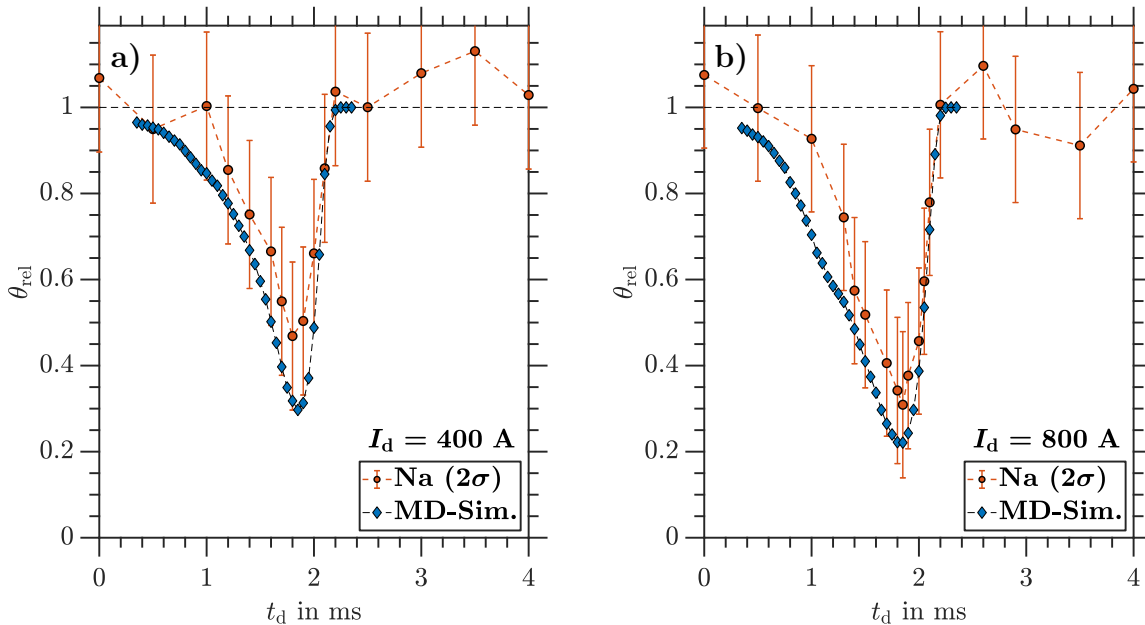


Fig. 4.6.1: Circles: relative integrated TOF signal (750 shots per data point) of Na atoms as a function of t_d . The error bars indicate an uncertainty of 2σ ; Diamonds: MD-simulations. Examples are shown for two different electromagnet currents (a) $I_d = 400$ A and (b) $I_d = 800$ A.

For light Na atoms (23 amu) deflected at these high currents, one might expect a largely reduced signal $\theta_{\text{rel}} \approx 0$. This can neither be seen in the experiment nor in the MD-simulation. The reason for this limited deflection is the broad velocity distribution (FWHM = 870 ms^{-1}) of the effusive sodium atoms (see Fig. 4.2.3b) in conjunction with the pulsed operation of the deflector. Considering the path from the deflector to the

ionization volume, the flight time differences among the particles being ionized are larger than the operation time of the deflector. Therefore, only a timing-dependent fraction of the ionized particles had been exposed to the magnetic field. The amount of deflected particles can be increased by either lengthening the magnetic field pulse in time or by narrowing the velocity distribution. These two different approaches are discussed in section 4.3.1.

Chapter 5

Magnetic deflection of neutral $\text{Na}(\text{H}_2\text{O})_n$, $\text{Na}(\text{MeOH})_n$ and $\text{Na}(\text{DME})_n$ clusters

5.1 Introduction

In the previously presented study (see chapter 4 and published in ref. [93]), we probed the magnetic properties of sodium-doped ammonia clusters $\text{Na}(\text{NH}_3)_n$ ($n = 1-4$) in a molecular beam via Stern-Gerlach deflection. By investigating the magnetic deflection as a function of cluster size n , the goal was to understand if the magnetic moment μ_0 of Na as a free $m_S = \pm 1/2$ system is perturbed by NH_3 molecules. It was shown that the cluster's effective magnet moment decreases with increasing cluster size. These results were interpreted due to a decrease of intracuster spin relaxation time with increasing cluster size. As has been discussed by Knickelbein [66] and Xu *et al.* [68], intracuster spin relaxation effects are a result of thermally accessible rovibrational states coupling to the spin and allow for spin flip processes (see chapter 3). Various groups [69, 70, 71, 72, 73, 74, 75, 76, 78, 79, 80] observed one-sided deflection behaviour which has been explained by the asymmetric topology of the Zeeman diagram with increasing energy [68]. This is simply because there is a lower energy bound but not an upper one (see Fig. 5.1.1). The observed magnetic deflection is a result of the average slope of interacting adiabatic Zeeman-like states within the experimental magnetic field range B_{exp} while traversing the deflector. The observable magnetic properties are defined by the density of adiabatic states within the Zeeman energy range ΔE_{Zeeman} . Note that the topology of such a Zeeman diagram is independent of temperature, whereas the population of the rovibrational states is defined by the cluster temperature. By sampling various sodium-doped clusters $\text{Na}(\text{H}_2\text{O})_n$ ($n = 1-4$), $\text{Na}(\text{MeOH})_n$ ($n = 1-4$) and $\text{Na}(\text{DME})_n$ ($n = 1-3$), we aim to vary the density of Zeeman-like states within ΔE_{Zeeman} , hence we aim to understand how the state density effects the overall deflection. The magnetic deflection results for these clusters are presented in the following sections and are compared in chapter 6 to the previously

presented results of $\text{Na}(\text{NH}_3)_n$ ($n = 1 - 4$) (see chapter 4).

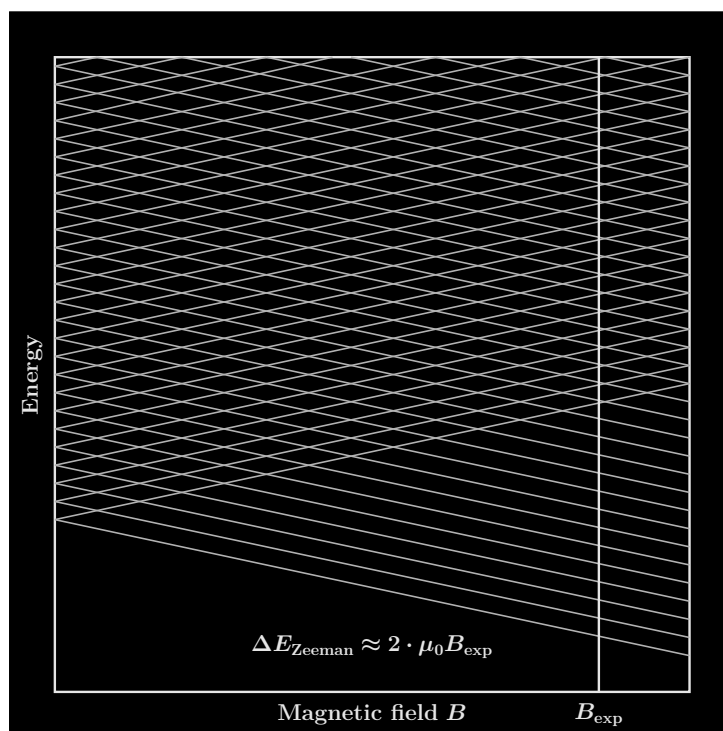


Fig. 5.1.1: Schematic Zeeman diagram of diabatic Zeeman-like levels where μ_0 corresponds to the slope of a Zeeman-like state.

5.2 Experimental & Computational Methods

The experimental setup to study size-dependent magnetic properties of neutral sodium-doped solvent clusters $\text{Na}(\text{H}_2\text{O})_n$ ($n = 1 - 4$), $\text{Na}(\text{MeOH})_n$ ($n = 1 - 4$) and $\text{Na}(\text{DME})_n$ ($n = 1 - 3$) has been described in chapter 2. Molecular clusters presented in this chapter were generated via supersonic expansion of either neat gas or mixtures into vacuum (see section 2.1.1). The cluster formation conditions of the individual substances are summarized in the following table.

Tab. 5.2.1: Experimental conditions for the generation of water, methanol and dimethyl ether clusters via supersonic expansion.

Supersonic expansion type	gas / gas mixture	p_{stag} in bar	d_{nozzle} in μm	T_{nozzle}	T_{bubbler} in $^{\circ}\text{C}$	T_{oven}
pulsed seeded	He/ H_2O	8	150	140	105	195
pulsed seeded	$\text{N}_2/\text{H}_2\text{O}$	6	150	160	145	195
continuous neat	MeOH	1.3	50	100	70	230
continuous neat	DME	3.5	55	10	-	195

Subsequent formation of sodium-doped solvent clusters occurs via collisions with sodium atoms inside the temperature controlled oven (see section 2.1.2). See Tab. 5.2.1 for

Na-oven temperatures used throughout the presented work. The newly formed sodium-doped clusters reach the centre of the extraction zone and are ionized using light from a pulsed (20 Hz) nanosecond (~ 7 ns) 266 nm (4.66 eV) Nd:YAG laser and the photoions are detected, either via time-of-flight (TOF) mass spectrometry (see section 2.3.3) or velocity map imaging (VMI) (see section 2.3.2). The experimental settings for both detection modes used throughout this chapter are given in Tab. 5.2.2.

Tab. 5.2.2: Experimental conditions for the detection of photoions via TOF mass spectrometry or VMI, all applied electrostatic potentials are given in V.

Detection mode	V_R	V_E	V_{MCP}		V_A
			high	low	
TOF	8000	6520	2200		3000
VMI	8000	5630	2000	1500	6000

The following sections showcase the experimental deflection results of Na(H₂O)_n ($n = 1 - 4$), Na(MeOH)_n ($n = 1 - 4$) and Na(DME)_n ($n = 1 - 3$) clusters. We compare the magnetic deflection results presented of this chapter to the experimental results of Na(NH₃)_n clusters (presented in chapter 4 and published in [93]) and discuss the presented deflection results in chapter 6.

5.3 Results for Na(H₂O)_n clusters

The previously presented results for Na(NH₃)_n clusters showed that the deflection ratio decreases with increasing cluster size and deviates significantly from that of an analogous $m_s = \pm 1/2$ system for cluster sizes $n = 2 - 4$. Can we expect similar cluster size-dependent deflection trends for H₂O as a solvent? We will show results and attempt to explain the size dependence for sodium-doped water clusters Na(H₂O)_n ($n = 1 - 4$). The results for Na(H₂O)_n focus on deflection measurements based on photoion VMI (see section 2.3.2).

5.3.1 Magnetic deflection of NaH₂O

As previously described in chapter 2, Na(H₂O)_n clusters were generated via pulsed (EL-valve) supersonic expansion and subsequent sodium doping. Hereby the relative time delay $\Delta t_{L-EL} = t_L - t_{EL}$ of the laser timing (t_L) and the EL-valve timing (t_{EL}), defines the observable particles reaching the ionization region simultaneously. Thus, corresponding measured velocity distributions dependent on Δt_{L-EL} . Fig. 5.3.1a shows the NaH₂O velocity distributions (obtained from VMIs) for deflector ‘off’ and deflector ‘on’ each with 2σ error recorded at $I_d = 700$ A and $\Delta t_{L-EL} = 0.70$ ms. For the sampled velocity distribution with $v_c \approx 2000$ m/s a maximal deflection of $\gamma_d = 0.66(10)$ is achieved (Fig. 5.3.1b). Agreement within 2σ error compared to the simulated deflection data is valid across the sampled

velocity distribution. Fig. 5.3.1b summarises the maximal experimental γ_d values, for all sampled I_d . Deflection ($\gamma_d > 0$) is observed for $I_d \geq 200$ A which agrees with the MD simulations for each sampled deflector current (within 2σ). We find that experimental deflection is systematically higher than the simulations. We suspect additional collisions of the molecular beam with background gas molecules (out-gassing from the deflector) while the deflector is switched on, to be a plausible reason for the systematic deviations. The additional signal depletion contributes to measured deflection due to the comparison to deflector ‘off’ measurements. However within errors, the results suggest that the deflection process of NaH_2O is described by $m_S = \pm 1/2$ particles during the interaction with the magnetic field t_m . In addition we probe slower velocity distributions by increasing $\Delta t_{\text{L-EL}}$, in order to exclude possible spin relaxation processes during t_m .

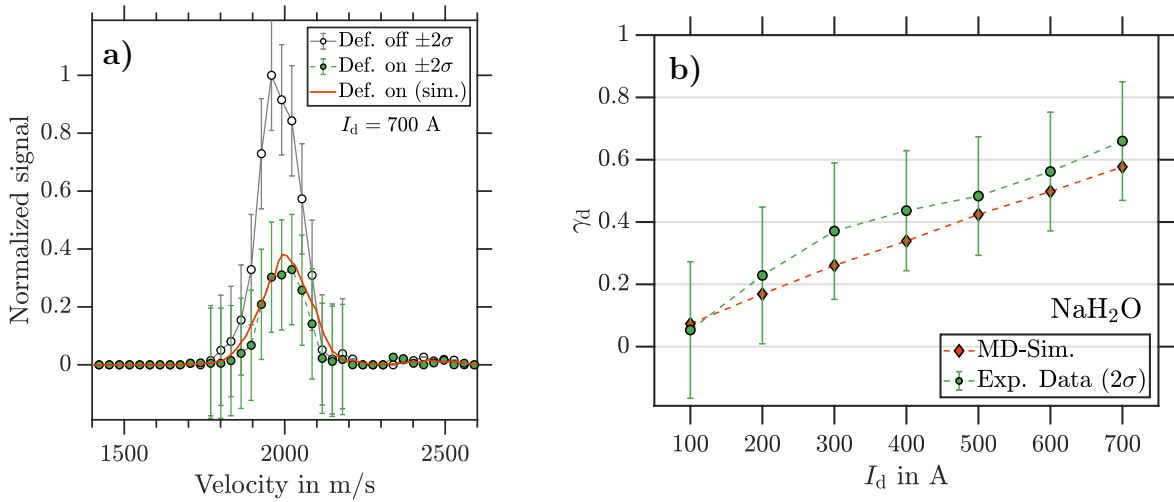


Fig. 5.3.1: (a) Experimental NaH_2O velocity distribution retrieved from photoion VMI (10 000 shots per VMI) for deflector ‘off’ (black circles with 2σ) and deflector ‘on’ (green dots with 2σ), with $I_d = 700$ A and $\Delta t_{\text{L-EL}} = 0.70$ ms. The corresponding simulated NaH_2O velocity distribution for $m_S = \pm 1/2$ are shown as red trace. (b) Maximal γ_d as a function of I_d for NaH_2O .

Fig. 5.3.2 displays velocity distributions for deflector ‘off’ and deflector ‘on’ with an operating deflector current of 500 A and the relative time delays $\Delta t_{\text{L-EL}} = 1.30$ ms, 0.80 ms and 0.70 ms. Mechanical recoils of the EL-valve’s plunger [91] cause the valve to open multiple times per trigger pulse and the formation of multiple gas pulses. This effect is shown at $\Delta t_{\text{L-EL}} = 1.30$ ms with four distinct gas pulses in a velocity range of 1100 – 1800 m/s for the deflector ‘off’ measurement. We take advantage of this mechanical characteristic, as this allows us to probe magnetic deflection over a broad velocity range by simply varying the relative time delay $\Delta t_{\text{L-EL}}$. Sampling faster velocities requires shorter relative time delays, as the particles of interest need less time to reach the ionization region. This is illustrated for $\Delta t_{\text{L-EL}} = 0.80$ ms (Fig. 5.3.2 mid panel) with velocities 1500 – 2300 m/s. The fastest particles (1800 – 2500 m/s) are sampled at $\Delta t_{\text{L-EL}} = 0.70$ ms (Fig. 5.3.2 bottom panel), these particles represent the ‘fast end’ of the velocity distribution of NaH_2O . The appendix A shows further deflection data at different time delays $\Delta t_{\text{L-EL}}$

and $I_d = 100 - 600$ A.

For $m_S = \pm 1/2$ particles, deflection is expected to increase with decreasing velocity, since the particles experience the Zeeman force for a longer time while traversing the deflector. This velocity dependence would manifest itself as an increase of γ_d . Clear evidence of this trend can be seen in Fig. 5.3.2 (top panel) for the deflector ‘on’ trace which exhibits nearly full deflection ($\theta_{\text{rel}} \approx 0$) for velocities < 1500 m/s and residual signals for velocities > 1600 m/s. The fastest sampled velocities (~ 2300 m/s) of NaH₂O show an increase in their residual signal upto $\theta_{\text{rel}} \approx 0.7$. The simulated VMI data for $m_S = \pm 1/2$ particles, reproduces the experimental velocity dependent deflection data, across the full velocity range (1100 – 2300 m/s).

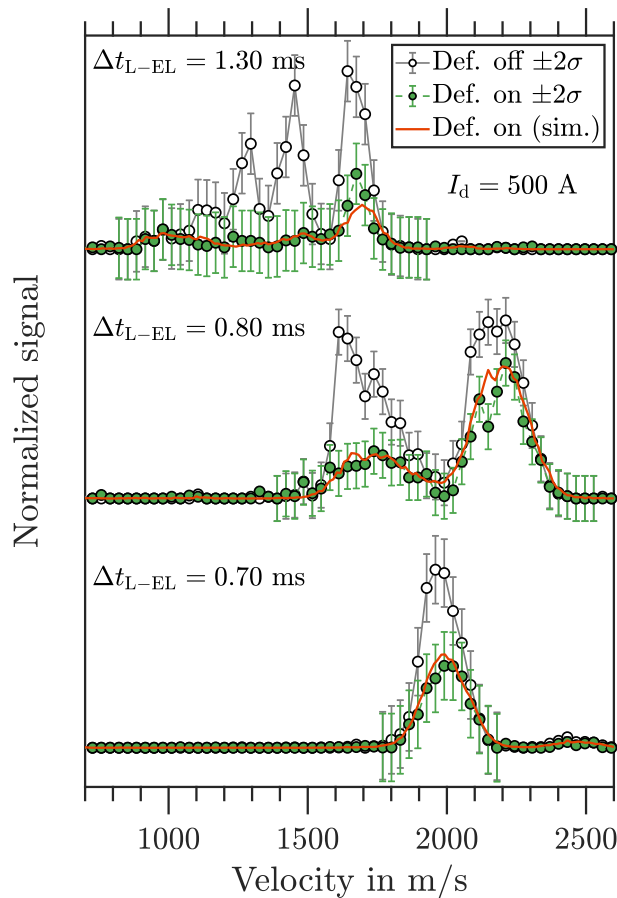


Fig. 5.3.2: Experimental NaH₂O velocity distributions retrieved from photoion VMIs (10 000 shots per VMI) for deflector ‘off’ (black circles with 2σ) and deflector ‘on’ (green dots with 2σ), with $I_d = 500$ A and the corresponding time delays: $\Delta t_{L-EL} = 1.30$ ms (top panel), 0.80 ms (mid panel) and 0.70 ms (bottom panel). The corresponding simulated NaH₂O velocity distributions for $m_S = \pm 1/2$ are shown as red traces.

The magnetic deflection results of NaH₂O, suggest that the Zeeman force acting on the cluster is described by the interaction of the unperturbed magnetic moment μ_0 of a spin $1/2$ system with the magnetic field \mathbf{B} . Furthermore, it can be stated that possible spin relaxation processes must occur on longer time scales than that of the experiment. Similar deflection behavior is observed for NaNH₃, which is discussed in chapter 4. The cluster

systems $\text{Na}(\text{NH}_3)_n$ show reduced deflection with increasing cluster size. This raises the question, if $\text{Na}(\text{H}_2\text{O})_n$ ($n > 1$) clusters exhibit similar trends with increasing cluster size n ?

5.3.2 Magnetic deflection of $\text{Na}(\text{H}_2\text{O})_{2-4}$

The deflection results for the highest possible magnetic field gradient ($I_d = 700$ A) and slowest achievable velocity distributions ($\sim 800 - 1500$ m/s) are shown in Fig. 5.3.3 for the clusters (a) $\text{Na}(\text{H}_2\text{O})_2$, (b) $\text{Na}(\text{H}_2\text{O})_3$ and (c) $\text{Na}(\text{H}_2\text{O})_4$, which are promising experimental conditions for deflection measurements. Nevertheless, deflection is not observed across the sampled velocity distributions. The obtained simulations however predict full deflection ($\theta_{\text{rel}} = 0$) for velocities < 1100 m/s. These significant deviations of experiment and simulation demonstrate that the investigated clusters do not interact with the magnetic field as $m_S = \pm 1/2$ particles. The results for $\text{Na}(\text{H}_2\text{O})_2$, $\text{Na}(\text{H}_2\text{O})_3$ and $\text{Na}(\text{H}_2\text{O})_4$ assume that possible spin relaxation processes take place on significantly faster time scales than the experiment. Additional deflection measurements at lower deflector currents are given in the appendix A.

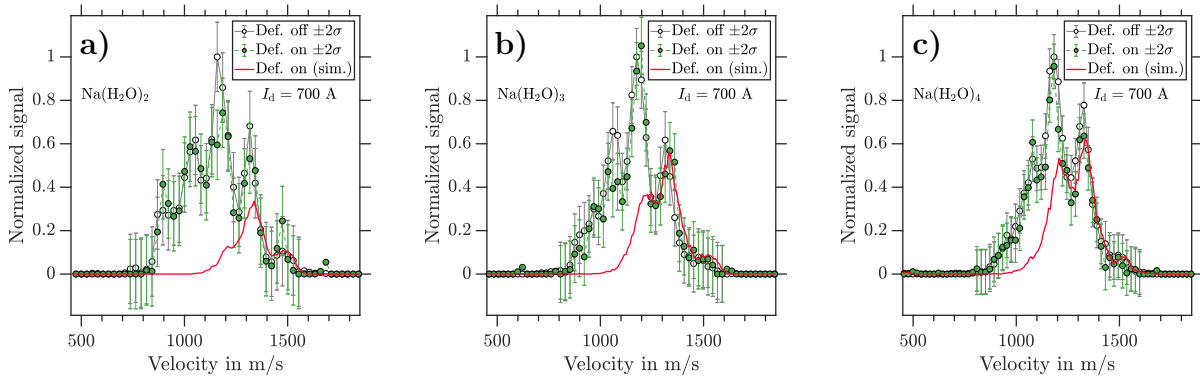


Fig. 5.3.3: Experimental velocity distributions of (a) $\text{Na}(\text{H}_2\text{O})_2$, (b) $\text{Na}(\text{H}_2\text{O})_3$ and (c) $\text{Na}(\text{H}_2\text{O})_3$ retrieved from photoion VMIs (10 000 shots per VMI) for deflector ‘off’ (black circles with 2σ) and deflector ‘on’ (green dots with 2σ), with $I_d = 700$ A and $\Delta t_{\text{L-EL}} = 1.40$ ms. The corresponding simulated $\text{Na}(\text{H}_2\text{O})_n$ ($n = 2 - 4$) velocity distributions for $m_S = \pm 1/2$ are shown as red traces.

5.4 Results for $\text{Na}(\text{MeOH})_n$ clusters

5.4.1 Magnetic deflection of NaMeOH

Fig. 5.4.1a displays velocity calibrated photoion VMIs of NaMeOH for deflector ‘off’ and deflector ‘on’ measurements at $I_d = 700$ A. NaMeOH exhibits deflection with an overall residual signal $\theta_{\text{rel}} = 0.5(1)$, and minimal relative signals ($\theta_{\text{rel}} = 0.2(1)$) in the velocity range $800 - 1100$ m/s. Although NaMeOH exhibits clear deflection, it is to a lesser extent than the simulations predict for a $m_S = \pm 1/2$ system. Fig. 5.4.1b depicts the deflection

ratio as a function of deflector current, where significant partial deflection is observed for $I_d > 500$ A. Once more the MD simulations are not in agreement with experimental observations. Similar to the other partially deflecting sodium-doped solvent clusters, we suggest that these deviations can be explained by ISR processes occurring on timescales similar or faster than the experiment. Additional deflection data at lower deflector currents are given in the appendix A.

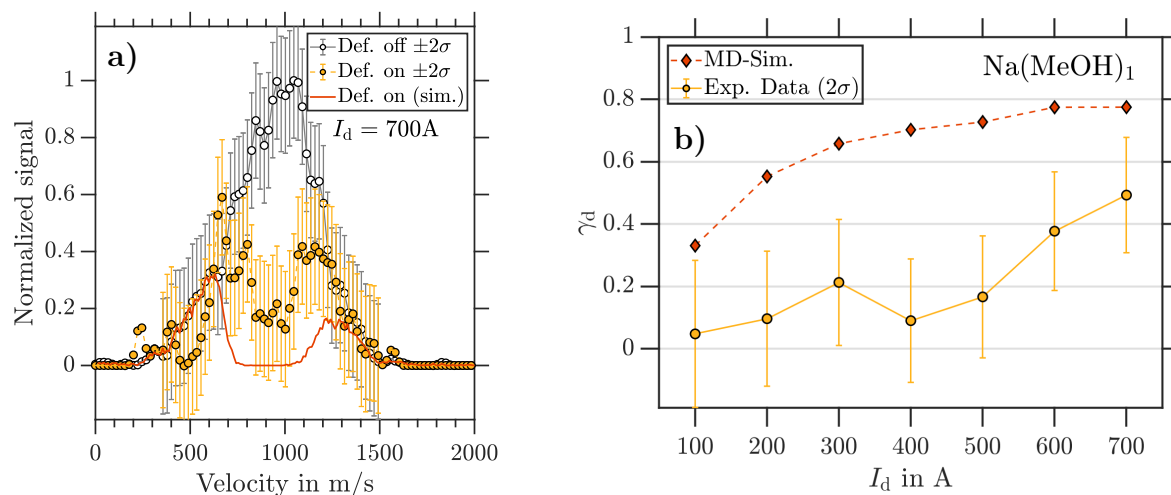


Fig. 5.4.1: (a) Experimental NaMeOH velocity distribution retrieved from photoion VMI (10 000 shots per VMI) for deflector ‘off’ (black circles with 2σ) and deflector ‘on’ (yellow dots with 2σ), with $I_d = 700$ A. The corresponding simulated NaMeOH velocity distribution for $m_S = \pm 1/2$ are shown as red trace. (b) Maximal γ_d as a function of I_d for NaMeOH.

As has been described for $\text{Na}(\text{NH}_3)_n$ and $\text{Na}(\text{H}_2\text{O})_n$ an increase in cluster size n causes a significant depletion of the experimentally observed deflection. This suggests similar cluster size-dependent deflection behaviour for $\text{Na}(\text{MeOH})_n$ with $n > 1$.

5.4.2 Magnetic deflection of $\text{Na}(\text{MeOH})_{2-4}$

The deflection results for $I_d = 700$ A are shown in Fig. 5.4.2 for the clusters (a) $\text{Na}(\text{MeOH})_2$, (b) $\text{Na}(\text{MeOH})_3$ and (c) $\text{Na}(\text{MeOH})_4$. Neither of these clusters exhibit deflection across their sampled velocity distributions. The deflector ‘off’ trace and deflector ‘on’ trace coincide within experimental error. The obtained simulations however predict deflection for all three cluster sizes. These deviations of experiment and simulation again suggest that the magnetic properties of the investigated clusters are not described by the magnetic moment of $m_S = \pm 1/2$ particles. See A in the appendix for further deflection data at lower I_d .

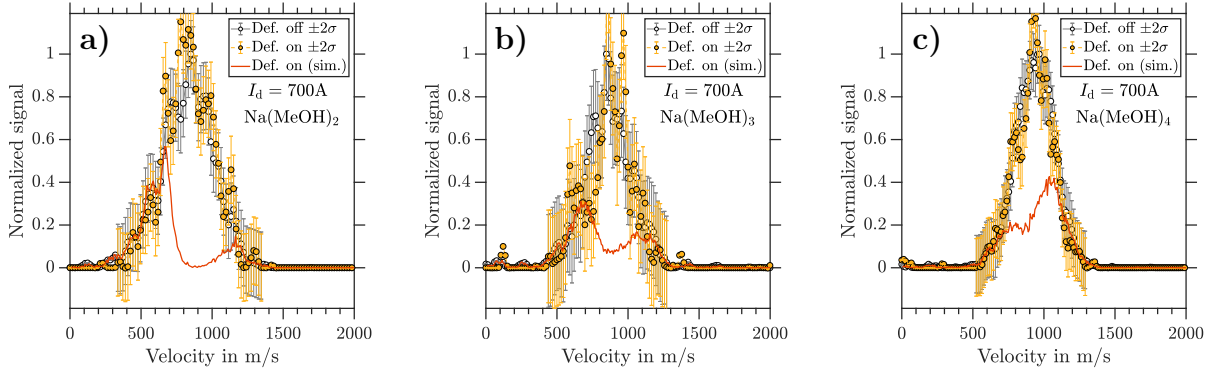


Fig. 5.4.2: Experimental velocity distributions of (a) $\text{Na}(\text{MeOH})_2$, (b) $\text{Na}(\text{MeOH})_3$ and (c) $\text{Na}(\text{MeOH})_3$ retrieved from photoion VMIs (10 000 shots per VMI) for deflector ‘off’ (black circles with 2σ) and deflector ‘on’ (yellow dots with 2σ), with $I_d = 700$ A. The corresponding simulated $\text{Na}(\text{MeOH})_n$ ($n = 2 - 4$) velocity distributions for $m_S = \pm 1/2$ are shown as red traces.

The presented results can be explained by ISR processes taking place on significantly faster timescales than the experiment. In order to discuss possible ISR processes of partially and non-deflecting clusters, we analyse thermally accessible rovibrational states as a function of cluster size n , as is discussed in chapter 6.

5.5 Results for $\text{Na}(\text{DME})_n$ clusters

5.5.1 Magnetic deflection of NaDME

Fig. 5.5.1a depicts the relative integrated TOF signals θ_{rel} of NaDME as a function of t_d at $I_d = 700$ A. The average signal intensity of the five latest timings is taken to be $\theta_{\text{rel}} = 1$ and their standard deviation define the error bars. θ_{min} is defined as the average of the three minimal θ_{rel} values (at $t_d = 1.35$ ms, 1.40 ms and 1.45 ms) which results in a value of 0.56(12), the corresponding maximal γ_d value is shown in Fig. 5.5.1b. Magnetic deflection is observed at $I_d > 100$ A which increases towards larger deflector currents and reaches a maximum of $\gamma_d = 0.44(12)$. Despite the observed deflection, an agreement with the simulations is not found within experimental errors at any of the sampled deflector currents. Deflection measurements at lower currents are shown in the appendix A.

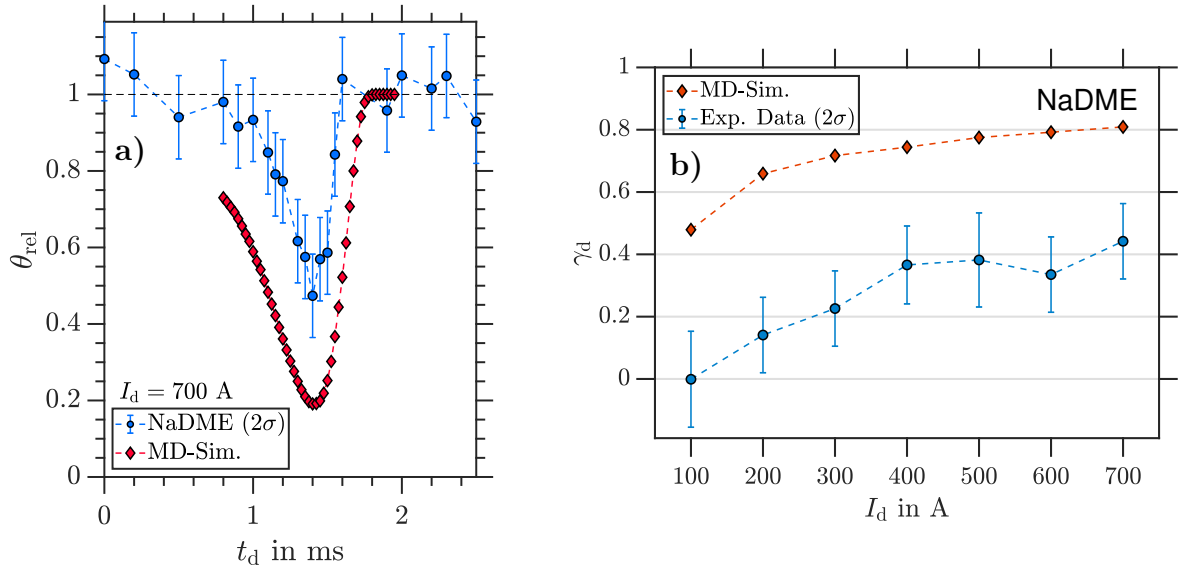


Fig. 5.5.1: (a) Relative integrated NaDME signal θ_{rel} (2000 shots per data point) as a function of t_d (blue dots with 2σ), compared with MD simulations (red diamonds). (b) Maximal γ_d as a function of I_d for NaDME.

The observed deflection behaviour is designated as partial magnetic deflection and attributed to a reduced magnetic moment when compared to μ_0 of a spin 1/2 system. Additional velocity resolved photoion VMIs for deflector ‘off’ and deflector ‘on’ measurements are shown in Fig. 5.5.2.

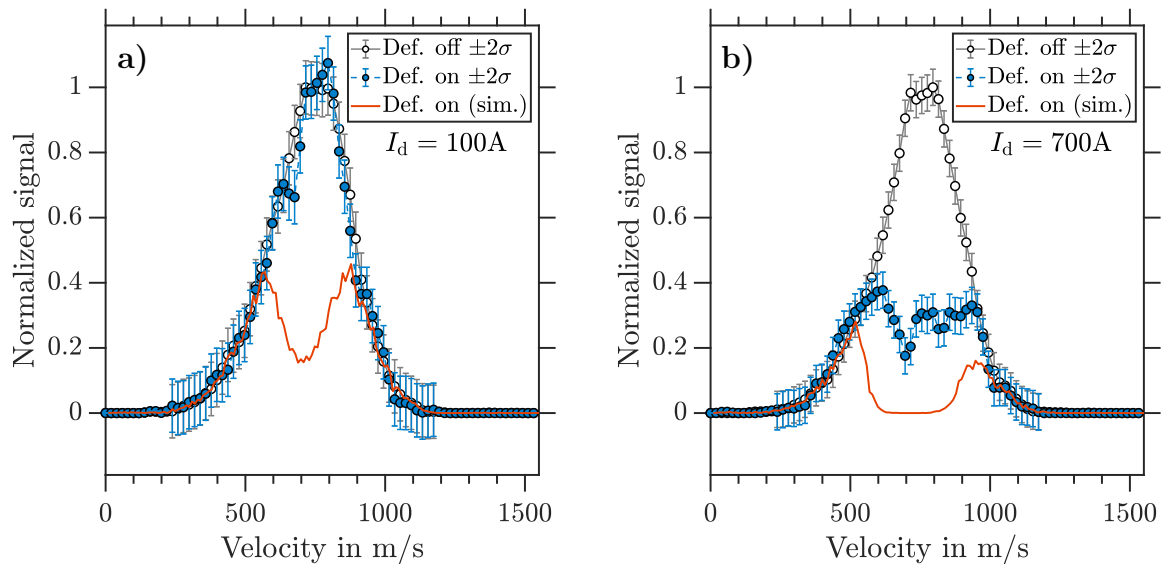


Fig. 5.5.2: Experimental NaDME velocity distributions retrieved from photoion VMIs (10000 shots per VMI) for deflector ‘off’ (whites dots with 2σ) and deflector ‘on’ (blue dots with 2σ), with (a) $I_d = 100$ A and (b) $I_d = 700$ A. The corresponding simulated NaDME velocity distributions for $m_S = \pm 1/2$ are shown as red traces.

At $I_d = 100$ A (see Fig. 5.5.2a), the deflector ‘off’ and ‘on’ signal coincide across the full velocity distribution. The simulated data shows clear deflection with a relative signal

of $\theta_{\text{rel}} = 0.52$ for the full velocity distribution. Residual signals are present for slower (~ 600 m/s) and faster (~ 900 m/s) velocities of ~ 0.40 and a minimum of ~ 0.20 for velocities (~ 800 m/s). These residuals and the minima arise from coil timing optimization for the given velocity distribution (see section 3.2.1 for an explanation). The corresponding simulations do not represent the experimental deflection data at $I_d = 100$ A.

Increasing the deflector current to $I_d = 700$ A (see Fig. 5.5.2b) causes an increase in deflection, characterised by $\theta_{\text{rel}} = 0.49(5)$ for the full deflector ‘on’ signal. The corresponding simulated data exhibits full deflection ($\theta_{\text{rel}} = 0$) at the center velocities $600 - 900$ m/s and incomplete deflection ($\theta_{\text{rel}} \approx 0.20$) for the slower ≤ 600 m/s and faster ≥ 900 m/s particles. However, this behaviour does not explain the experimental observations. The significant deviations are reasoned by possible ISR processes which for NaDME have to occur at similar or faster timescales than the interaction time with the magnetic field and are suggested to cause a reduction of the cluster’s magnetic moment.

5.5.2 Magnetic deflection of $\text{Na}(\text{DME})_2$

Magnetic deflection data of $\text{Na}(\text{DME})_2$, based on TOF and VMI measurements are presented in the following. The relative cluster signal θ_{rel} as a function of t_d shows reduced relative signals for various deflector timings shown in Fig. 5.5.3a. The relative signal instabilities are however too high to state significant magnetic deflection of $\text{Na}(\text{DME})_2$ at $I_d = 700$ A. The MD simulations in contrast predict minimal relative signal of $\theta_{\text{rel}} \approx 0.2$. These deviations between experiment and simulation are more pronounced for $\text{Na}(\text{DME})_2$ when compared to NaDME. The large discrepancies are observed at all sampled I_d with no experimental deflection ($\gamma_d = 0$) and simulations which predict deflection ratios of $\gamma_d \approx 0.3$ (see Fig. 5.5.3b).

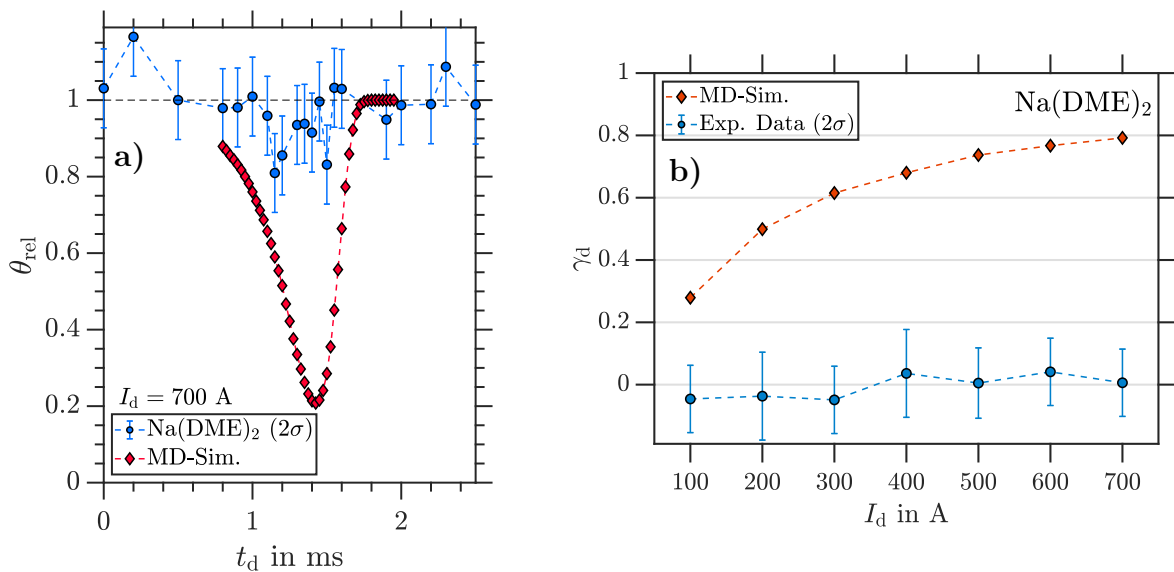


Fig. 5.5.3: (a) Relative integrated $\text{Na}(\text{DME})_2$ signal θ_{rel} (2000 shots per data point) as a function of t_d (blue dots with 2σ), compared with MD simulations (red diamonds). (b) Maximal γ_d as a function of I_d for $\text{Na}(\text{DME})_2$.

Deflection measurements of higher data quality, based on photoion VMIs for $\text{Na}(\text{DME})_2$ are shown in Fig. 5.5.4. The velocity dependent deflection data at $I_d = 100$ A exhibits no observable deflection (see Fig. 5.5.4a). Although increasing the deflector current to $I_d = 700$ A reveals slight deflection with $\theta_{\text{rel}} = 0.82(7)$ for the full velocity distribution (see Fig. 5.5.4b). Additional deflection data at lower deflector currents is shown in the appendix A.

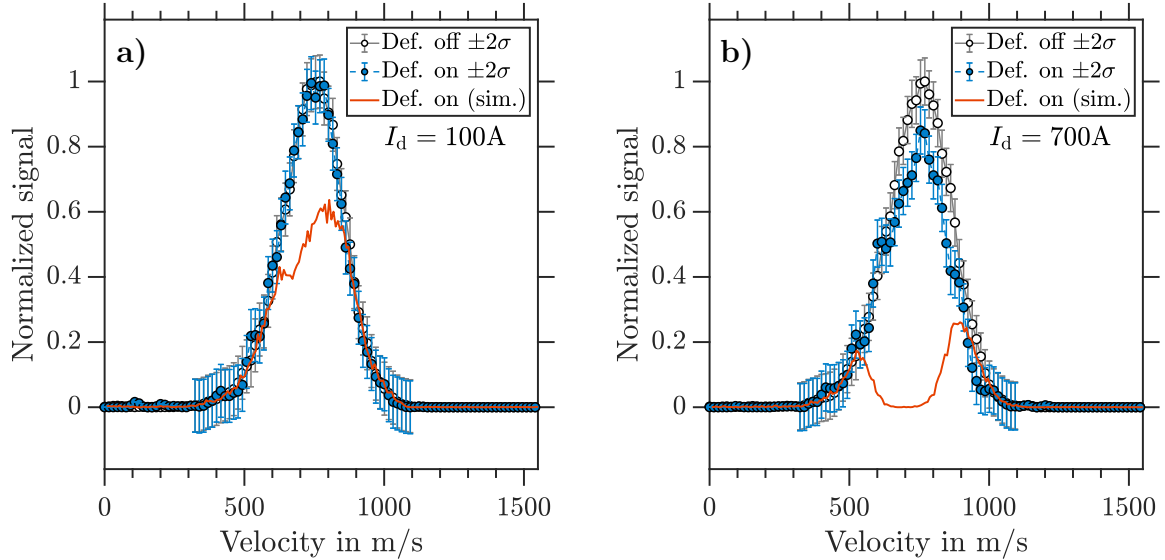


Fig. 5.5.4: Experimental $\text{Na}(\text{DME})_2$ velocity distributions retrieved from photoion VMIs (10000 shots per VMI) for deflector ‘off’ (whites dots with 2σ) and deflector ‘on’ (blue dots with 2σ), with (a) $I_d = 100$ A and (b) $I_d = 700$ A. The corresponding simulated $\text{Na}(\text{DME})_2$ velocity distributions for $m_S = \pm 1/2$ are shown as red traces.

Once more we find that the reduced deflection of $\text{Na}(\text{DME})_2$ is not described by the free spin 1/2 Zeeman interaction. Possible explanations for reduced magnetic deflection are discussed in the following chapter 6 within terms of possible ISR processes governed by spin-rotational coupled Zeeman levels.

5.5.3 Magnetic deflection of $\text{Na}(\text{DME})_3$

The magnetic deflection results of $\text{Na}(\text{DME})_3$ clusters, analogous to those of NaDME and $\text{Na}(\text{DME})_2$, are shown in Fig. 5.5.5 and Fig. 5.5.6.

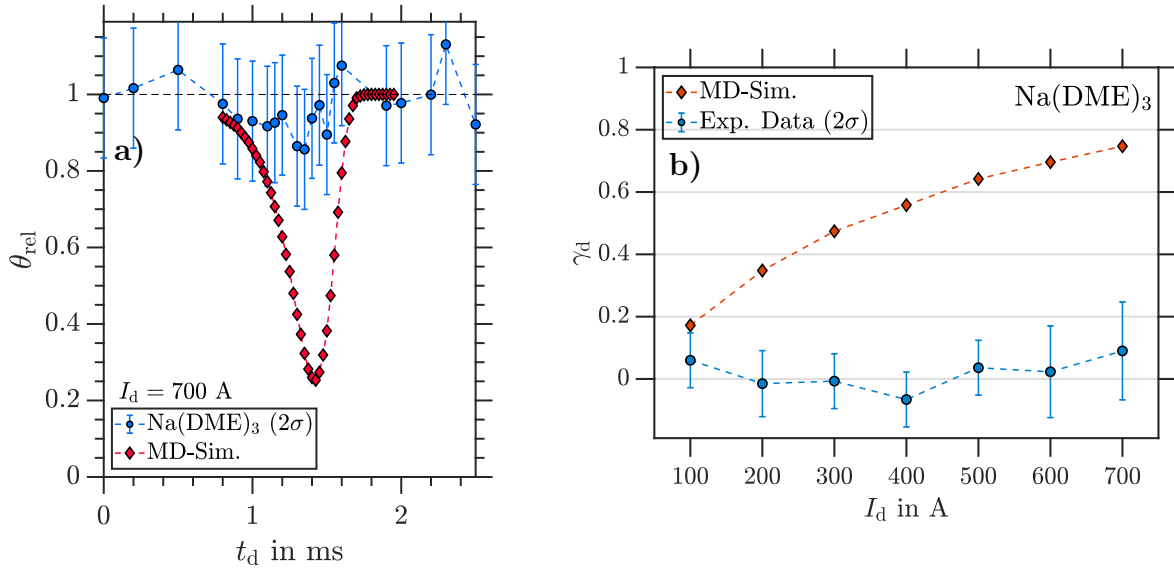


Fig. 5.5.5: (a) Relative integrated $\text{Na}(\text{DME})_3$ signal θ_{rel} (2000 shots per data point) as a function of t_d (blue dots with 2σ), compared with MD simulations (red diamonds). (b) Maximal γ_d as a function of I_d for $\text{Na}(\text{DME})_3$. Blue dots: experiment with 2σ error. Red diamonds: MD simulation.

Deflection measurements at the highest deflector current of 700 A (see Fig. 5.5.5a) reveal non deflected character for all sampled deflector delays t_d . This furthermore holds for all other sampled deflector currents with $\gamma_d = 0$ (see Fig. 5.5.5b). Once more substantial deviations are found when compared to the MD simulations. Photoion VMIs, at $I_d = 100$ A (see Fig 5.5.6) confirm the absence of deflection for $\text{Na}(\text{DME})_3$. At 700 A in the region of the center velocities ($v_c = 650 - 850$ m/s) minor deflection may be suspected, although the experimental errors are too large in order to state distinct deflection. Despite the inconclusive results we classify $\text{Na}(\text{DME})_3$ as non-deflected.

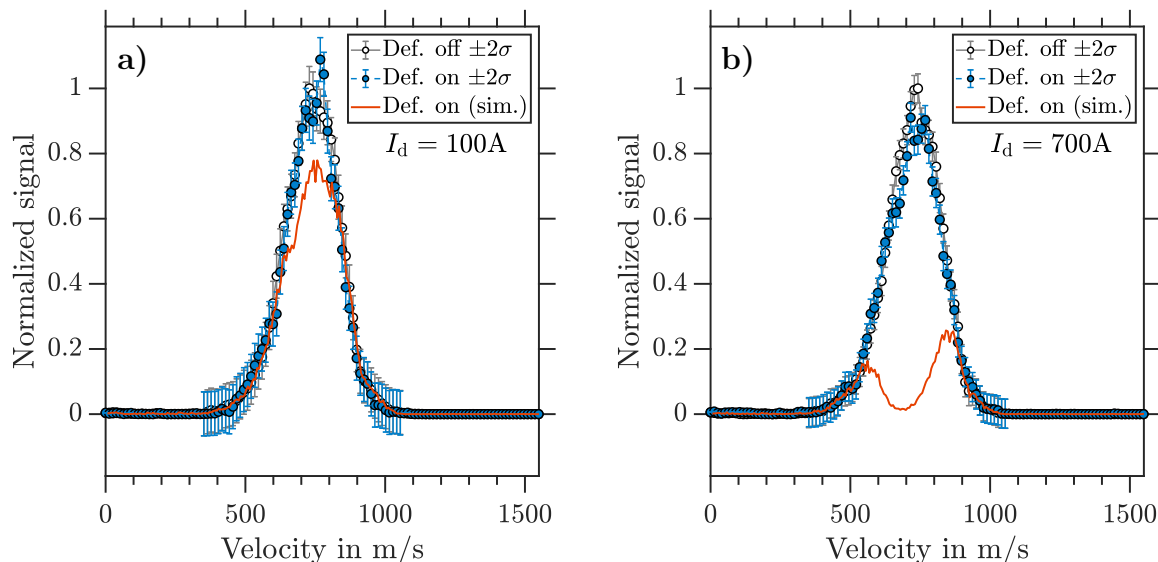


Fig. 5.5.6: Experimental $\text{Na}(\text{DME})_3$ velocity distributions retrieved from photoion VMIs (10000 shots per VMI) for deflector ‘off’ (whites dots with 2σ) and deflector ‘on’ (blue dots with 2σ), with (a) $I_d = 100$ A and (b) $I_d = 700$ A. The corresponding simulated $\text{Na}(\text{DME})_3$ velocity distributions for $m_S = \pm 1/2$ are shown as red traces.

The simulated signal in contrast reduces to $\theta_{\text{rel}} = 0.25$ and as in the case of the previous clusters with reduced deflection, we find that the deflection process is not described by the interaction of μ_0 of $m_S = \pm 1/2$ particles with the inhomogeneous magnetic field. The discrepancies between experiment and simulation, found for $\text{Na}(\text{DME})_n$ ($n = 1 - 3$) clusters are discussed in chapter 6.

5.6 Summary

The cluster size-dependent magnetic properties of neutral $\text{Na}(\text{H}_2\text{O})_n$ ($n = 1-4$), $\text{Na}(\text{MeOH})_n$ ($n = 1 - 4$) and $\text{Na}(\text{DME})_n$ ($n = 1 - 3$) clusters were studied using a pulsed Stern-Gerlach-type magnet. The detection of photoions via mass spectrometry and velocity map imaging allowed us to retrieve mass and velocity dependent deflection data. Comparing the experimental data to simulations based on the magnetic deflection of $m_S = \pm 1/2$ particles lead to the following classification of the investigated clusters.

In the case of water as the solvent molecule, deflection was measured for NaH_2O clusters at all applied deflector currents. Each experimental data set could be reproduced by the simulations within experimental errors. Therefore it was concluded that NaH_2O clusters deflect as an unperturbed $m_S = \pm 1/2$ system within our experiments. For all larger investigated clusters $\text{Na}(\text{H}_2\text{O})_n$ ($n = 2 - 4$) deflection was not measurable at any applied deflector current, these findings differ from predictions of the simulations, as corresponding $m_S = \pm 1/2$ particles should show deflection. This indicates that an effective cluster magnetic moment is cluster size-dependent.

NaMeOH partial deflection was measured at deflector currents $I_d > 500$ A and an agree-

ment with the predictions of $m_S = \pm 1/2$ was not observed. The rovibrational state density is expected to be high enough to reduce the effective magnetic moment which leads to partial deflection. Increasing the cluster size $\text{Na}(\text{MeOH})_n$ $n = 2 - 4$ leads to no measurable deflection at all applied deflector currents, again these results disagree with the simulations for free spin $1/2$ particles. We suggest that additional thermally accessible rovibrational modes cause a further reduction of an effective magnetic moment.

NaDME clusters showed significant deflection for the applied deflector currents $I_d > 100$ A, yet an agreement with the simulations was not found, thus NaDME is designated as partially deflecting. For $\text{Na}(\text{DME})_2$ clusters, only slight deflection was observed for the VMI measurement at the highest possible deflector current ($I_d = 700$ A). We therefore, conclude that the $\text{Na}(\text{DME})_2$ cluster exhibits partial deflection. The cluster $\text{Na}(\text{DME})_3$ did not show distinct deflection for any of the probed deflector currents, and therefore the cluster was classified as non-deflecting. The magnetic properties of $\text{Na}(\text{DME})_n$ ($n = 1 - 3$) clusters are highly dependent on the cluster size, as a clear reduction of the deflection could be observed with increasing cluster size. One DME molecule was already sufficient to perturb μ_0 such that the observable deflection was reduced from that of a spin $1/2$ system.

It was reasoned that clusters which show deflection behaviour of $m_S = \pm 1/2$ particles exhibit spin relaxation times which are slower than the timescale of the experiment. For clusters with reduced deflection, possible spin relaxation effects must take place on a similar or shorter time scale than that of the experiment. The likelihood of such spin relaxation effects are expected to depend on the density of thermally accessible rovibrational states. An approach for the estimation of the populated rovibrational state density is given in the following chapter. With this approach we aim to compare the different sodium-doped clusters in their thermally accessible rovibrational state densities and elaborate their relative experimental deflection trends.

Chapter 6

Comparison of $\text{Na}(\text{H}_2\text{O})_n$, $\text{Na}(\text{NH}_3)_n$, $\text{Na}(\text{MeOH})_n$ and $\text{Na}(\text{DME})_n$

With the pulsed Stern-Gerlach deflection setup (described in section 2.3.1) we studied the deflection behaviour of $\text{Na}(\text{NH}_3)_n$ (see chapter 4), $\text{Na}(\text{H}_2\text{O})_n$, $\text{Na}(\text{MeOH})_n$ and $\text{Na}(\text{DME})_n$ (see chapter 5). These experimental studies are a first attempt to understand the paramagnetic properties of sodium-doped clusters, which can be seen as solvated electron precursor systems. With the combination of experimental deflection and simulations, insight into timescales of intracuster spin relaxation (ISR) effects is gained. The reduced deflection with increasing cluster size can be interpreted as a reduction in the effective magnetic moment μ_{eff} . For a cluster size-dependent discussion in terms of possible ISR processes, a characteristic spin relaxation time τ is compared with the cluster specific magnetic field interaction time t_m . If $\tau \leq t_m$, intracuster spin relaxation processes can occur within the experimental time frame and partial or no deflection would be observed. Possible ISR processes are described in chapter 3, where electron spin state transitions with $\Delta m_S = 1$ are discussed. These spin flip transitions cause statistical changes of the trajectories through the deflector which would result in a spatial broadening of the molecular beam. On average, these changes can be described by a reduced effective magnetic moment μ_{eff} . An approach to model μ_{eff} from their corresponding characteristic relaxation time τ is given in section 6.2. MD simulations for $m_S = \pm 1/2$ particles (μ_0) no longer predict the measured deflection for cases where $\tau \lesssim t_m$. For $\tau \sim t_m$, reduced but non-zero deflection is expected. On the other hand if $\tau \ll t_m$, it is expected that deflection can not be resolved spatially and $\gamma_d = 0$.

The results suggest an acceleration of spin relaxation processes with increasing cluster size n . It is expected that thermal population of rovibrational states produce a reduction of the clusters effective magnetic moment. In a Zeeman diagram the magnetic moment reflects in the slope of the Zeeman-level. Hence, the population of rovibrational states leads to Zeeman-like states with average slopes that are reduced when compared to μ_0 of a

free $m_S = \pm 1/2$ system [68]. The average slope was discussed to be the result of adiabatic Zeeman-like states which traverse several avoided crossings [104, 68, 66]. The population of the adiabatic Zeeman-like levels is estimated by the thermal energy within the assumption of a microcanonical ensemble. By considering the population of rovibrational states in the studied clusters, we aim to gain information on possible ISR processes. In order to quantify and compare the experimental deflection results, we choose to model reduced deflection as an attenuation of the magnetic moment μ_0 . We suspect that a large attenuation of μ_0 correlates to high densities of populated Zeeman-like states. Hence, we discuss the experimental deflection trends in terms of thermally accessible rovibrational state densities based on the harmonic oscillator and rigid rotor approximations.

6.1 Summarized magnetic deflection results

Tab. 6.1.1 and Fig. 6.1.1 summarize the deflection results of $\text{Na}(\text{H}_2\text{O})_n$, $\text{Na}(\text{NH}_3)_n$, $\text{Na}(\text{MeOH})_n$ and $\text{Na}(\text{DME})_n$ clusters. The deflection behaviour of NaH_2O and NaNH_3 agree with the MD simulations based on $m_S = \pm 1/2$ particles (Fig. 6.1.1a,b). We classify these clusters as ‘fully deflected’ $\equiv \bullet$. All other clusters exhibit significant deviations between experiment and simulation. Such clusters are either classified as ‘partially deflected’ $\equiv \bullet$ with $\gamma_d > 0$ or ‘non-deflected’ $\equiv \circ$ with $\gamma_d = 0$.

Tab. 6.1.1: Summary of experimental magnetic deflection results of $\text{Na}(\text{H}_2\text{O})_n$, $\text{Na}(\text{NH}_3)_n$, $\text{Na}(\text{MeOH})_n$ and $\text{Na}(\text{DME})_n$. With minimal deflector current $I_{d,\min}$ to still achieve deflection ($\gamma_d > 0$).

n	$\text{Na}(\text{H}_2\text{O})_n$		$\text{Na}(\text{NH}_3)_n$		$\text{Na}(\text{MeOH})_n$		$\text{Na}(\text{DME})_n$	
	$I_{d,\min}$	Type	$I_{d,\min}$	Type	$I_{d,\min}$	Type	$I_{d,\min}$	Type
1	≥ 200 A	\bullet	≥ 100 A	\bullet	≥ 500 A	\bullet	≥ 200 A	\bullet
2	-	\circ	≥ 100 A	\bullet	-	\circ	≥ 700 A	\bullet
3	-	\circ	≥ 600 A	\bullet	-	\circ	-	\circ
4	-	\circ	≥ 600 A	\bullet	-	\circ	-	-

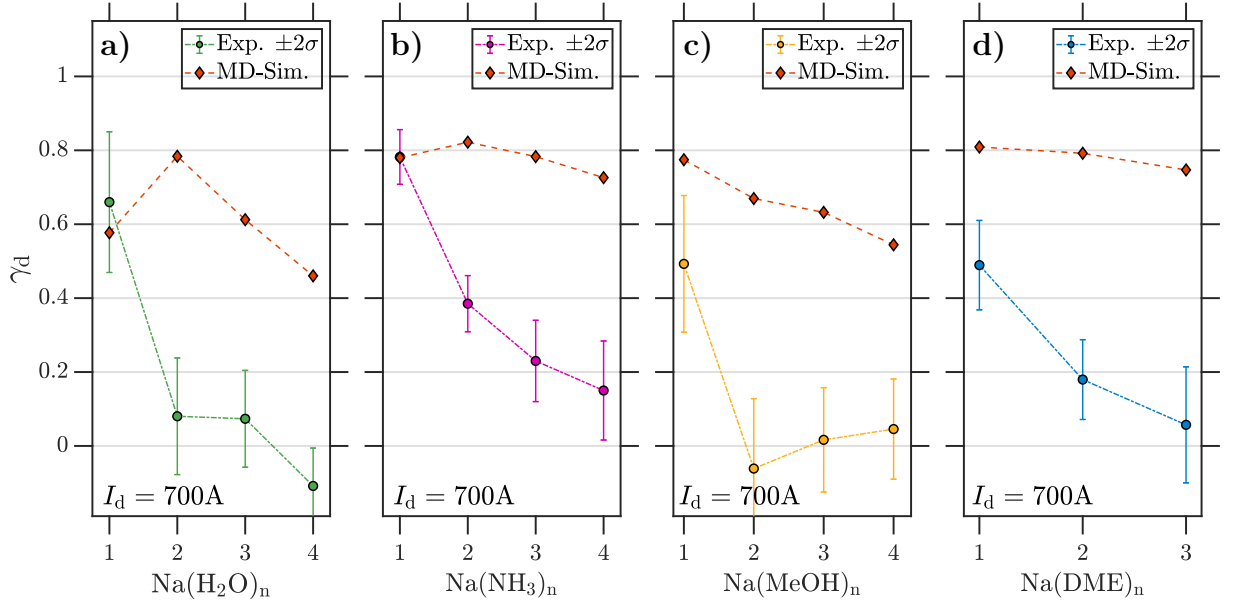


Fig. 6.1.1: γ_d at the highest possible deflector current $I_d = 700$ A for (a) $\text{Na}(\text{H}_2\text{O})_n$ (green dots), (b) $\text{Na}(\text{NH}_3)_n$ (magenta dots), (c) $\text{Na}(\text{MeOH})_n$ (yellow dots) and (d) $\text{Na}(\text{DME})_n$ (blue dots). The corresponding MD simulations for $m_S = \pm 1/2$ particles are shown as red diamonds.

In the following section an approach is introduced to account for the deviations from the $m_S = \pm 1/2$ deflection behaviour. Scaling the magnetic moment μ_0 with a characteristic attenuation factor quantifies partially deflecting clusters and we are able to rationalize relative deflection trends as a function of cluster system and size.

6.2 Modelling of an effective magnetic moment

The effective magnetic moment μ_{eff} of NaH_2O and NaNH_3 is the same as μ_0 of spin $1/2$ particles. All other clusters exhibit deflection, described by $\mu_{\text{eff}} < \mu_0$. As has been discussed in previous chapters 4 and 5, it is expected that ISR processes mediate a reduction of μ_0 . By introducing an attenuation factor a , we describe the simulated deflection process with

$$\mu_{\text{eff}} = \mu_0 \cdot a. \quad (6.2.1)$$

It has been discussed [104, 68, 66] that ISR processes are determined by the topology of the Zeeman diagram, the thermal population of spin-rotational coupled Zeeman-like levels and the magnetic field difference ΔB a cluster passes while traversing the deflector. In a precise spin relaxation model, the attenuation factor a should account for these different factors. However, an exact description considering all relevant interactions in detail is a complex task and we therefore choose a simplified model to account for spin relaxation effects. In our approach, we assume an exponential decay of μ_0 during the transit time t_m

with a characteristic relaxation time τ .

$$\mu_{\text{eff}}(t_m) = \mu_0 \cdot \exp(-t_m/\tau) \quad (6.2.2)$$

Carrying out MD simulations with μ_{eff} for various characteristic relaxation times τ (25, 50, 75, 100, 125, 150 μs) leads to reduced deviations of simulation and experiment, as shown in Fig. 6.2.1.

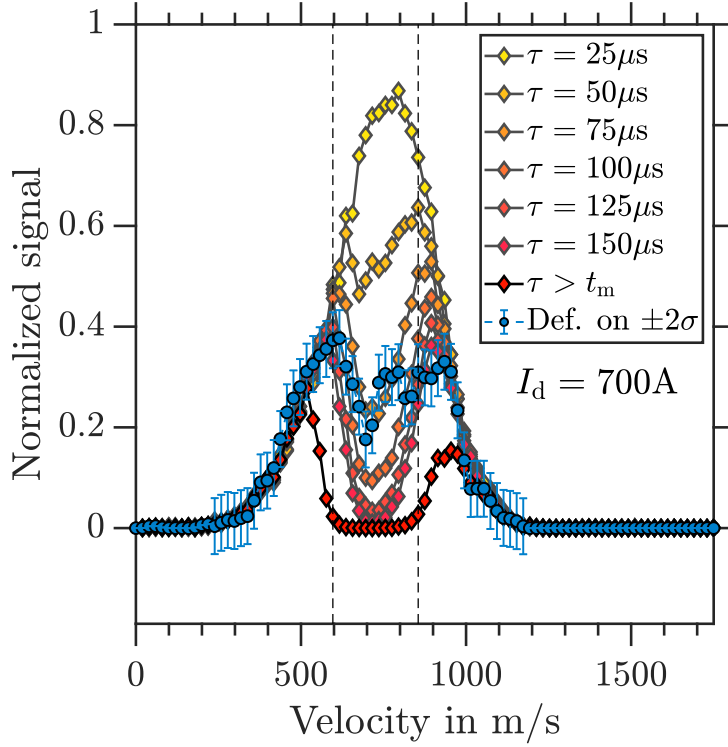


Fig. 6.2.1: Simulated deflector ‘on’ traces with various characteristic τ values (shown as diamonds) and experimental deflector ‘on’ trace of NaDME (shown as blue dots). The vertical lines indicate the region of interest used for the $\chi^2(\tau)$ fit resulting in $\tau_{\text{min}} = 105(19) \mu\text{s}$.

For each τ value the squared deviations $(\gamma_{\text{d,sim}} - \gamma_{\text{d,exp}})^2$ are evaluated by their χ^2 value, given by

$$\chi^2(\tau) = \frac{\sum_i \left((\gamma_{\text{d,sim},i} - \gamma_{\text{d,exp},i})^2 \cdot \frac{1}{\sigma_i^2} \right)}{\sum_i \frac{1}{\sigma_i^2}}. \quad (6.2.3)$$

Here σ_i is the experimental error for each sampled velocity v_i in the region of interest indicated by the vertical lines in Fig. 6.2.1. The evaluated $\chi^2(\tau)$ values are fitted quadratically as a function of τ to obtain optimal characteristic relaxation times τ_{min} where the deviations are minimal. The evaluation of τ_{min} is carried out for each deflector current individually, in order to minimize possible magnetic field dependences.

$$\text{mfit}(\tau) = \frac{(\tau - \tau_{\text{min}})^2}{c} + b, \quad (6.2.4)$$

For non-deflected clusters the fitting procedure is not applicable, we thus assume an upper limit. The results are summarized in Tab. 6.2.1.

Tab. 6.2.1: Characteristic spin relaxation times τ_{\min} obtained from quadratic fitting of $\chi^2(\tau)$ at $I_d = 700$ A. The experimental deflection behaviour is implied by the shading of the circles (full, partial and non).

	Na(H ₂ O) _n	Na(NH ₃) _n	Na(MeOH) _n	Na(DME) _n
n	τ_{\min} in μs	τ_{\min} in μs	τ_{\min} in μs	τ_{\min} in μs
1	$> t_m = 100$ ●	$> t_m = 200$ ●	112(15) ◐	105(19) ◐
2	< 25 ○	92(12) ◐	< 25 ○	34(30) ◐
3	< 25 ○	72(12) ◐	< 25 ○	< 25 ○
4	< 25 ○	62(10) ◐	< 25 ○	-

With the retrieved characteristic relaxation times τ_{\min} we determine

$$\mu_{\text{eff},i} = a_i \mu_0 \quad (6.2.5)$$

where a_i is the unitless average factor of the exponential term during the interaction time t_m , defined by the deflector length s_{def} and the molecular beam velocity v_i .

$$a_i = \frac{1}{s_{\text{def}} - 0} \cdot \int_0^{s_{\text{def}}} \exp\left(-\frac{s}{v_i \cdot \tau_{\min}}\right) ds \quad (6.2.6)$$

$$a_i = \frac{v_i \tau_{\min}}{s_{\text{def}}} \cdot \left(1 - \exp\left(-\frac{s_{\text{def}}}{v_i \tau_{\min}}\right)\right) \quad (6.2.7)$$

The determined effective magnetic moments for the partially deflecting clusters and the upper limit for the non-deflected clusters are shown in Fig. 6.2.2.

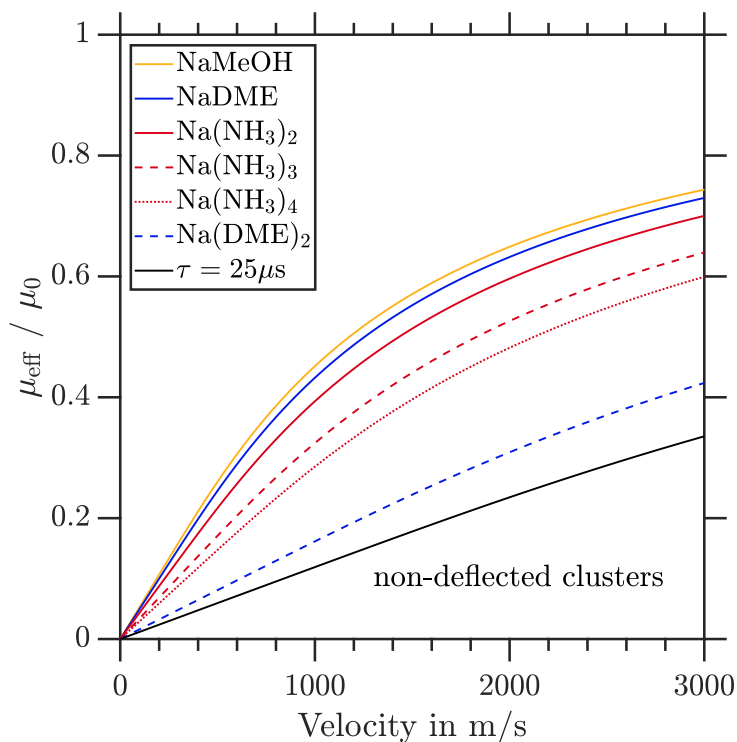


Fig. 6.2.2: Effective magnetic moment μ_{eff} as a function of molecular beam velocity for the partially deflecting clusters and limiting values for the non-deflected clusters.

NaH_2O is deflected as a spin $1/2$ system, as has been discussed in chapter 5 and is depicted in Fig. 6.1.1a with $\mu_{\text{eff}} = \mu_0$. Possible spin relaxation effects therefore have to occur on time scales longer than t_m . From measured cluster beam velocities ~ 2000 m/s, $\tau_{\text{min}} > 100 \mu\text{s}$ is determined. For water clusters with $2 \leq n \leq 4$, experimental deflection was not observed (displayed in Fig. 6.1.1a, also see chapter 5) and an upper limit of $\tau_{\text{min}}(\text{Na}(\text{H}_2\text{O})_{2-4}) < 25 \mu\text{s}$ could be estimated.

NaNH_3 exhibits spin $1/2$ deflection, which was discussed in chapter 4 and is displayed in Fig. 6.1.1b. With molecular beam velocities of ~ 1000 m/s, we infer that possible ISR processes must occur on time scales $\tau_{\text{min}}(\text{NaNH}_3) > 200 \mu\text{s}$. For larger ammonia clusters ($2 \leq n \leq 4$) magnetic deflection is less than expected from an analogues $m_S = \pm 1/2$ system and reduces with increasing cluster size. This is seen in the decrease in relaxation times $\tau_{\text{min}}(\text{Na}(\text{NH}_3)_2) = 92(12) \mu\text{s}$, $\tau_{\text{min}}(\text{Na}(\text{NH}_3)_3) = 72(12) \mu\text{s}$ and $\tau_{\text{min}}(\text{Na}(\text{NH}_3)_4) = 62(10) \mu\text{s}$.

NaMeOH exhibits partial deflection characterized by $\tau_{\text{min}} = 112(15) \mu\text{s}$. For larger $\text{Na}(\text{MeOH})_n$ clusters with $n = 2 - 4$, experimental deflection is not observed (see Fig. 6.1.1c) and an upper limit of $\tau_{\text{min}}(\text{Na}(\text{MeOH})_{2-4}) < 25 \mu\text{s}$ is given.

The reduced deflection of NaDME fitted to $\tau_{\text{min}} = 105(19) \mu\text{s}$ is shown in Fig. 6.1.1d. Larger clusters ($n = 2, 3$) are characterized by increasing attenuation of μ_{eff} . We find $\tau_{\text{min}}(\text{Na}(\text{DME})_2) = 34(30) \mu\text{s}$, (see Fig. 5.5.4b) and no deflection for $\text{Na}(\text{DME})_3$ with an upper limit of $\tau_{\text{min}}(\text{Na}(\text{DME})_3) < 25 \mu\text{s}$.

Additional deflection data for all sampled sodium clusters are given in section A of the

appendix. The interaction time with the magnetic field defined by v_i and the deflector length dictates the observable μ_{eff} within the applied model. A comparison of different μ_{eff} values is therefore only meaningful if compared at the same velocity. For a constant velocity v_i at any value (see Fig. 6.2.2) we determine the following relative experimental deflection trend:

$$\begin{aligned}
 & \underbrace{\mu_{\text{eff}}(\text{NaH}_2\text{O}) \approx \mu_{\text{eff}}(\text{NaNH}_3)}_{\text{full deflection } \bullet} & (6.2.8) \\
 & > \underbrace{\mu_{\text{eff}}(\text{NaMeOH}) > \mu_{\text{eff}}(\text{NaDME}) > \mu_{\text{eff}}(\text{Na}(\text{NH}_3)_2)}_{\text{partial deflection } \bullet} \\
 & > \underbrace{\mu_{\text{eff}}(\text{Na}(\text{NH}_3)_3) > \mu_{\text{eff}}(\text{Na}(\text{NH}_3)_4) > \mu_{\text{eff}}(\text{Na}(\text{DME})_2)}_{\text{partial deflection } \bullet} \\
 & > \underbrace{\mu_{\text{eff}}(\text{Na}(\text{H}_2\text{O})_2) \sim \mu_{\text{eff}}(\text{Na}(\text{H}_2\text{O})_3) \sim \mu_{\text{eff}}(\text{Na}(\text{H}_2\text{O})_4)}_{\text{no deflection } \circ} \\
 & \sim \underbrace{\mu_{\text{eff}}(\text{Na}(\text{MeOH})_2) \sim \mu_{\text{eff}}(\text{Na}(\text{MeOH})_3) \sim \mu_{\text{eff}}(\text{Na}(\text{MeOH})_4) \sim \mu_{\text{eff}}(\text{Na}(\text{DME})_3)}_{\text{no deflection } \circ}
 \end{aligned}$$

In the following sections of this chapter we will examine the observed deflection trend, by analyzing rovibrational energy states of various structural isomers. Harmonic frequency analysis of DFT optimized cluster geometries are carried out with the Gaussian program package [162]. In a first step, the dispersion corrected ωB97XD density functional with a 6-31+G* basis set was used to optimize cluster geometries (see Fig. B.1.1-B.1.4 of the appendix). In a second step, harmonic frequencies and rigid rotor rotational constants are evaluated for various geometric isomers. In a last step, the converged minimal energy structures are reoptimized with MP2 calculations with an aug-cc-PVDZ basis set and additional harmonic frequency calculations are carried out. From the density and thermal population of rovibrational states within their Zeeman energy splitting, their deflection trends can be rationalized.

6.3 Discussion

The Zeeman diagram of a $m_S = \pm 1/2$ system is schematically shown in Fig. 6.3.1a. In the case of $m_S = \pm 1/2$, zero field splitting (ZFS) of spin microstates can be neglected, as only one unpaired electron is present. Available rotational states increase the number of diabatic Zeeman-like levels to $(2S + 1) \cdot (2R + 1)$. If \mathbf{S} and \mathbf{R} are uncoupled degenerate, crossings are formed. However, if S and R are even weakly coupled the crossings are avoided for adiabatic states with equal total angular momentum \mathbf{J} , shown in Fig. 6.3.1c.

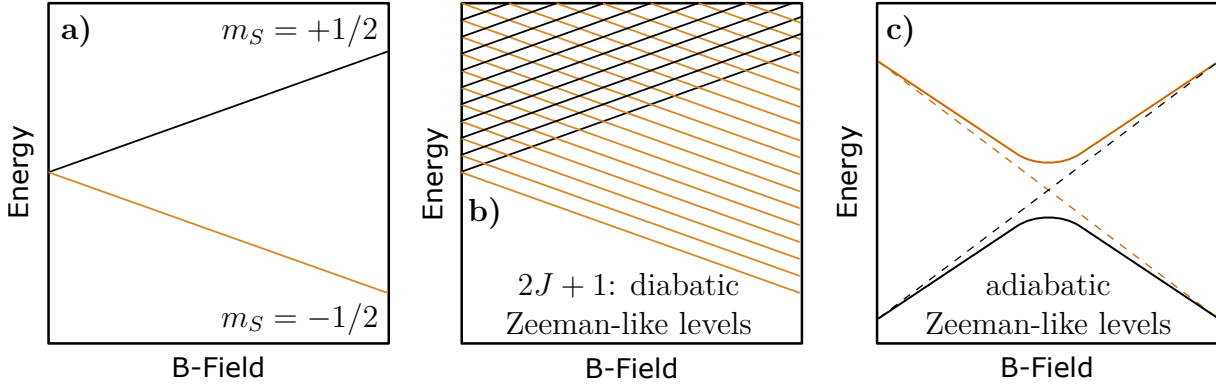


Fig. 6.3.1: Schematic Zeeman diagram of a $m_S = \pm 1/2$ cluster. (a) Spin 1/2 system without rotations, leads to $2S + 1$ Zeeman levels and symmetric SG deflection into $2S + 1$ beamlets. (b) Rotational states form $(2R + 1) \cdot (2S + 1)$ diatomic Zeeman-like levels and symmetric SG deflection into $2J + 1$ beamlets for each J level. (c) Schematic illustration of an avoided level crossing of the spin-rotational coupled adiabatic Zeeman-like states. Note that the coupling causes a spin flip process at the degeneracy point due to an avoided crossing.

Here m_S of each of the two adiabatic states reverses its sign after the avoided crossing, if the total angular momentum $\mathbf{J} = \mathbf{R} + \mathbf{S}$ is conserved. For $m_S = \pm 1/2$ systems this leads to $\Delta m_S = 1$, which only allows for spin flip processes between adiabatic Zeeman-like states with $\Delta M_R = 1$. Clusters with a higher density of populated rovibrational states are expected to undergo more spin-flip transitions and on average exhibit less deflection, when compared to clusters with lower densities of thermally accessible adiabatic Zeeman-like levels.

In order to discuss our experimental findings and relative deflection trends, we analyse the rovibrational eigenstates $E_{n,R}$. We choose to describe $E_{n,R}$ with respect to the vibrational energies of a harmonic oscillator and rotational energies of a rigid rotor.

$$E_{n,J} = \underbrace{hc \cdot \nu_0 (n + 1/2)}_{\text{harmonic vibrational term}} + \underbrace{hc \cdot B_{\text{rot}} R(R + 1)}_{\text{rigid rotor term}}$$

Where n is the vibrational quantum number, ν_0 the vibrational eigenfrequency, R the rotational quantum number and B_{rot} the rotational constant. With estimated vibrational T_{vib} and rotational T_{rot} temperatures, we express the number of thermally accessible rovibrational states in terms of the partition function. By discussing vibrational and rotational states individually we aim to understand the dominating effects of ISR processes in sodium-doped clusters. The following discussions are based on the assumption of thermally equilibrated clusters, where the population of states is described by a Maxwell-Boltzmann distribution at estimated thermal energies $k_B T$.

6.3.1 Thermally accessible vibrational states

As the temperatures of free clusters are not well defined, we consider vibrational temperatures in a range $50 \text{ K} \leq T_{\text{vib}} \leq 200 \text{ K}$ which is plausible for clusters generated via supersonic expansion [163, 164]. One way to estimate thermal cluster energies is to employ evaporative ensemble theory (EET) [139]. Essentially the theory describes a scaling law of the thermal energy $k_{\text{B}}T$ and the evaporation enthalpies per solvation molecule ΔH_{vap} for the process $\text{Na}(\text{Sol})_n \longrightarrow \text{Na}(\text{Sol})_{n-1} + \text{Sol}$.

$$\gamma = \frac{\Delta H_{\text{vap}}}{k_{\text{B}}T} \quad (6.3.1)$$

Using EET, Carrera *et al.* [139] showed that the Gspann parameter γ is nearly cluster size independent, but is dependent on the time scale of the experiment. For their experimental time scale of 1.2 ms a Gspann parameter of $\gamma = 28.3$ was determined. Since our experimental time scale 1 – 2 ms is similar, we estimate the cluster thermal energies with $\gamma = 28.3$ and calculations of ΔH_{vap} performed previously in [1]. The evaporation enthalpies and determined temperatures are summarized in Tab. 6.3.1. We suggest that the estimated average temperatures \bar{T} are close to equal to the cluster vibrational temperatures T_{vib} . These resulting temperatures $\bar{T} = T_{\text{vib}}$ are in the range of our estimation.

Tab. 6.3.1: Calculated temperatures T via equation 6.3.1 for the clusters $\text{Na}(\text{H}_2\text{O})_n$, $\text{Na}(\text{NH}_3)_n$, $\text{Na}(\text{MeOH})_n$ and $\text{Na}(\text{DME})_n$ with ΔH_{vap} taken from [1] and $\gamma = 28.3$. Values marked with * were excluded from the average quantities $\Delta \bar{H}_{\text{vap}}$ and \bar{T} .

	$\text{Na}(\text{H}_2\text{O})_n$		$\text{Na}(\text{NH}_3)_n$		$\text{Na}(\text{MeOH})_n$		$\text{Na}(\text{DME})_n$	
n	ΔH_{vap} in eV	T in K	ΔH_{vap} in eV	T in K	ΔH_{vap} in eV	T in K	ΔH_{vap} in eV	T in K
1	0.287	118	0.375	155	0.274	112	0.375	102
2	0.403	167	0.368	153	0.663*	272*	0.279	115
3	0.368	153	0.379	157	0.390	160	0.283	117
4	0.134*	56*	0.404	167	0.459	188	-	-
	$\Delta \bar{H}_{\text{vap}}$ in eV	\bar{T} in K	$\Delta \bar{H}_{\text{vap}}$ in eV	\bar{T} in K	$\Delta \bar{H}_{\text{vap}}$ in eV	\bar{T} in K	$\Delta \bar{H}_{\text{vap}}$ in eV	\bar{T} in K
	0.353	145	0.382	158	0.374	154	0.270	111

Low-frequency ground state vibrations (vibrational quantum number $n = 0$) with $\nu_n < 300 \text{ cm}^{-1}$ of the different sodium-doped clusters are shown for $\text{Na}(\text{H}_2\text{O})_n$ (Fig. 6.3.2), $\text{Na}(\text{NH}_3)_n$ (Fig. 6.3.3), $\text{Na}(\text{MeOH})_n$ (Fig. 6.3.4) and $\text{Na}(\text{DME})_n$ (Fig. 6.3.5). The population probability $p_j(T_{\text{vib}})$ of the different ground state vibrations are calculated at

approximate vibrational temperatures ($50 \leq T_{\text{vib}} \leq 200$ K). $p_j(T_{\text{vib}})$ is given by

$$p_j(T_{\text{vib}}) = \frac{\exp(-h\nu_j/k_B T_{\text{vib}})}{Q_{\text{vib}}}, \quad (6.3.2)$$

with the vibrational frequency ν_j and the vibrational partition function Q_{vib} is defined as

$$Q_{\text{vib}} = \sum_j \exp(-h\nu_j/k_B T_{\text{vib}}). \quad (6.3.3)$$

The lowest frequency vibration in the weakly bound non-covalent NaH_2O cluster is a out-of-plane wagging mode at 119 cm^{-1} . For the larger cluster $\text{Na}(\text{H}_2\text{O})_2$, further vibrations well below 200 cm^{-1} occur. The lowest vibrational frequency in $\text{Na}(\text{H}_2\text{O})_2$ is a Na–O stretching mode with 97 cm^{-1} , and additional hindered rotations of the water molecules at 109 cm^{-1} , 159 cm^{-1} and 168 cm^{-1} . For the cluster sizes $\text{Na}(\text{H}_2\text{O})_3$ (see Fig. 6.3.2e) and $\text{Na}(\text{H}_2\text{O})_4$ (see Fig. 6.3.2f), the number of low frequency vibrations increases further. $\text{Na}(\text{H}_2\text{O})_3$ exhibits a O–O bending mode at 40 cm^{-1} , two Na–O stretching modes at 62 cm^{-1} and 83 cm^{-1} as well as three further hindered internal H_2O rotations $< 200 \text{ cm}^{-1}$. NaNH_3 exhibits a Na–N stretching mode at 197 cm^{-1} and a degenerate Na–N bending mode at 276 cm^{-1} . These vibrations show populations on the order of 20% for vibrational temperatures $T_{\text{vib}} > 50$ K (see Fig. 6.3.3a). For the larger clusters $\text{Na}(\text{NH}_3)_{2-4}$, new types of low frequency modes arise, with internal rotations of NH_3 around the Na–N axis and the N–Na–N bending vibration well below 100 cm^{-1} . As for these larger clusters we predict significant relative population of their vibrational modes at estimated vibrational temperatures (see Fig. 6.3.3b,e,f).

NaMeOH exhibits a hindered rotation at 49 cm^{-1} and a wagging mode at 94 cm^{-1} . The O–Na stretching mode exhibit a frequency of 180 cm^{-1} . In the temperature range $50 \text{ K} \leq T_{\text{vib}} \leq 200 \text{ K}$ (see Fig. 6.3.4a) we expect significant population of these vibrational modes. For $\text{Na}(\text{MeOH})_2$ additional accessible vibrational modes with energies well below 200 cm^{-1} are introduced by the addition of a second MeOH molecule (see Fig. 6.3.4b). For $\text{Na}(\text{MeOH})_3$ (see Fig. 6.3.4e) and $\text{Na}(\text{MeOH})_4$ (see Fig. 6.3.4f) further thermally accessible intermolecular vibrational modes are established.

The weak non-covalent bonds between the sodium atom and dimethyl ether molecules and between the dimethyl ether molecules themselves cause large amplitude motions with characteristic low frequencies. For NaDME , hindered rotations are present with calculated vibrational energies of 51 cm^{-1} and 89 cm^{-1} and the Na–O stretching mode with 143 cm^{-1} (seen in Fig. 6.3.5a). For the larger cluster sizes $n = 2, 3$ additional types of low frequency modes arise with DME–DME wagging and bending modes $< 120 \text{ cm}^{-1}$ (seen in 6.3.5c). For $T_{\text{vib}} = 50$ K, the ground vibrational states and higher modes with $< 100 \text{ cm}^{-1}$ are especially highly populated. At higher estimated vibrational temperatures, population become more equal and contributions also from high frequency vibrations to the clusters populated rovibrational states are predicted. Generally, we observe the qualitative trend that an increase in cluster size leads to the population of more vibrational modes. The

population of vibrational modes can in principle influence ISR processes by the change in rotational energies and by possible coupling to vibrational angular momentum.

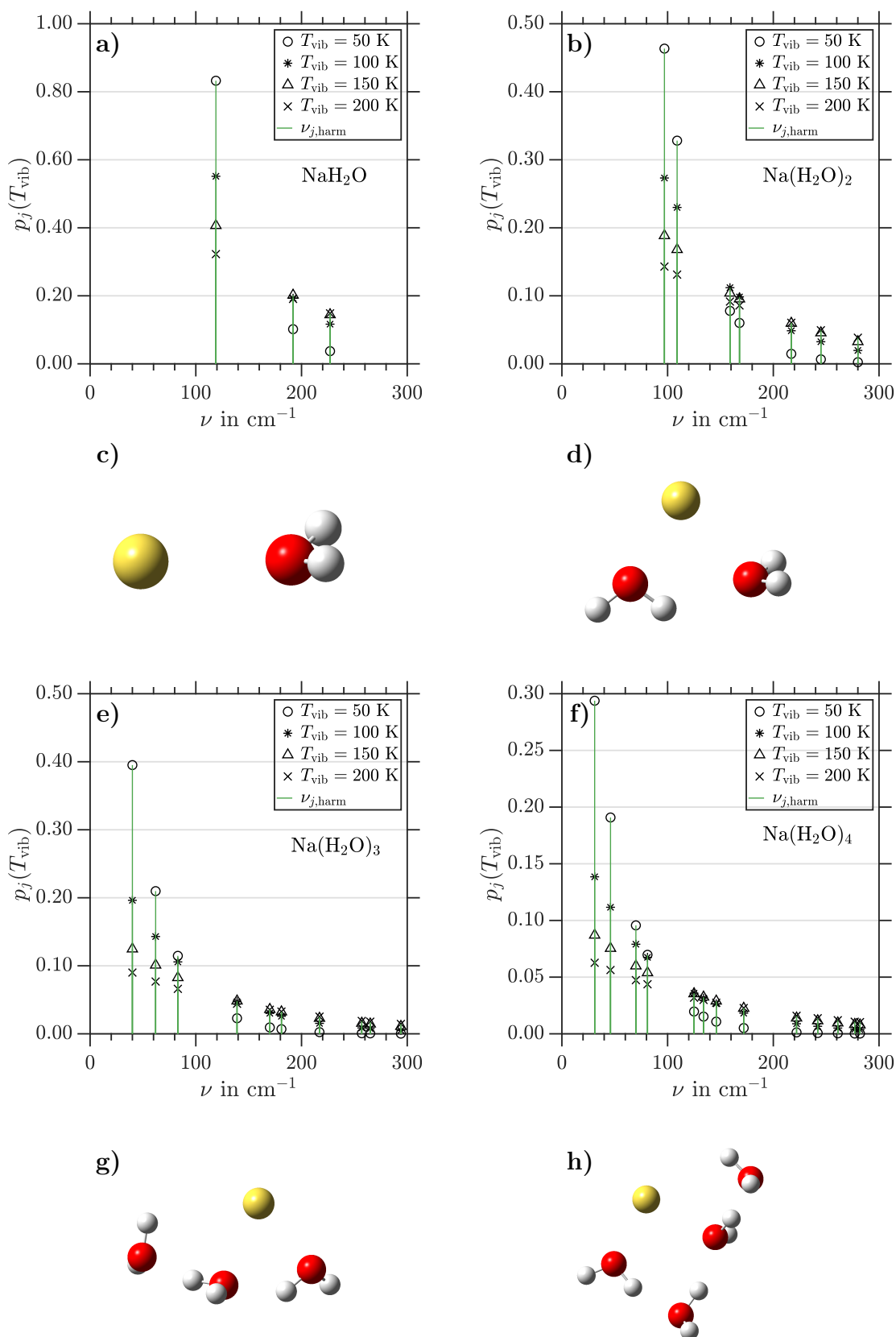


Fig. 6.3.2: Calculated harmonic frequencies (MP2/aug-cc-PVDZ) for $\text{Na}(\text{H}_2\text{O})_n$ clusters are shown as green vertical lines for (a) NaH_2O , (b) $\text{Na}(\text{H}_2\text{O})_2$, (e) $\text{Na}(\text{H}_2\text{O})_3$ and (f) $\text{Na}(\text{H}_2\text{O})_4$ with $\nu_n < 300 \text{ cm}^{-1}$. The population probabilities $p_j(T_{\text{vib}})$ are plotted for ν_j and estimated vibrational temperatures T_{vib} . Corresponding optimized cluster geometries are shown in (c) NaH_2O , (d) $\text{Na}(\text{H}_2\text{O})_2$, (g) $\text{Na}(\text{H}_2\text{O})_3$ and (h) $\text{Na}(\text{H}_2\text{O})_4$.

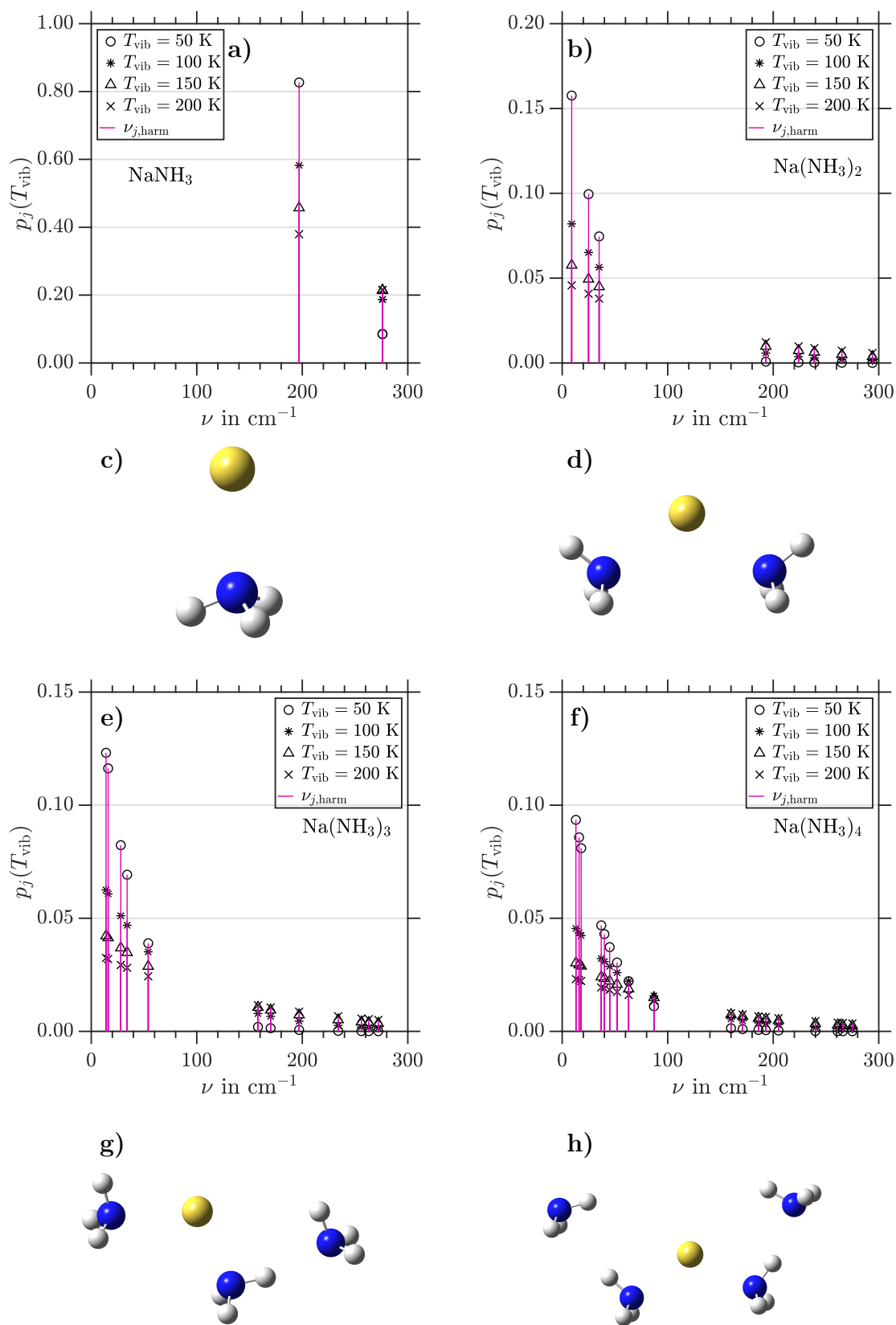


Fig. 6.3.3: Calculated harmonic frequencies (MP2/aug-cc-PVDZ) for Na(NH₃)_n clusters are shown as magenta vertical lines for (a) NaNH₃, (b) Na(NH₃)₂, (e) Na(NH₃)₃ and (f) Na(NH₃)₄ with $\nu_n < 300 \text{ cm}^{-1}$. The population probabilities $p_j(T_{\text{vib}})$ are plotted for ν_j and estimated vibrational temperatures T_{vib} . Corresponding optimized cluster geometries are shown in (c) NaNH₃, (d) Na(NH₃)₂, (g) Na(NH₃)₃ and (h) Na(NH₃)₄.

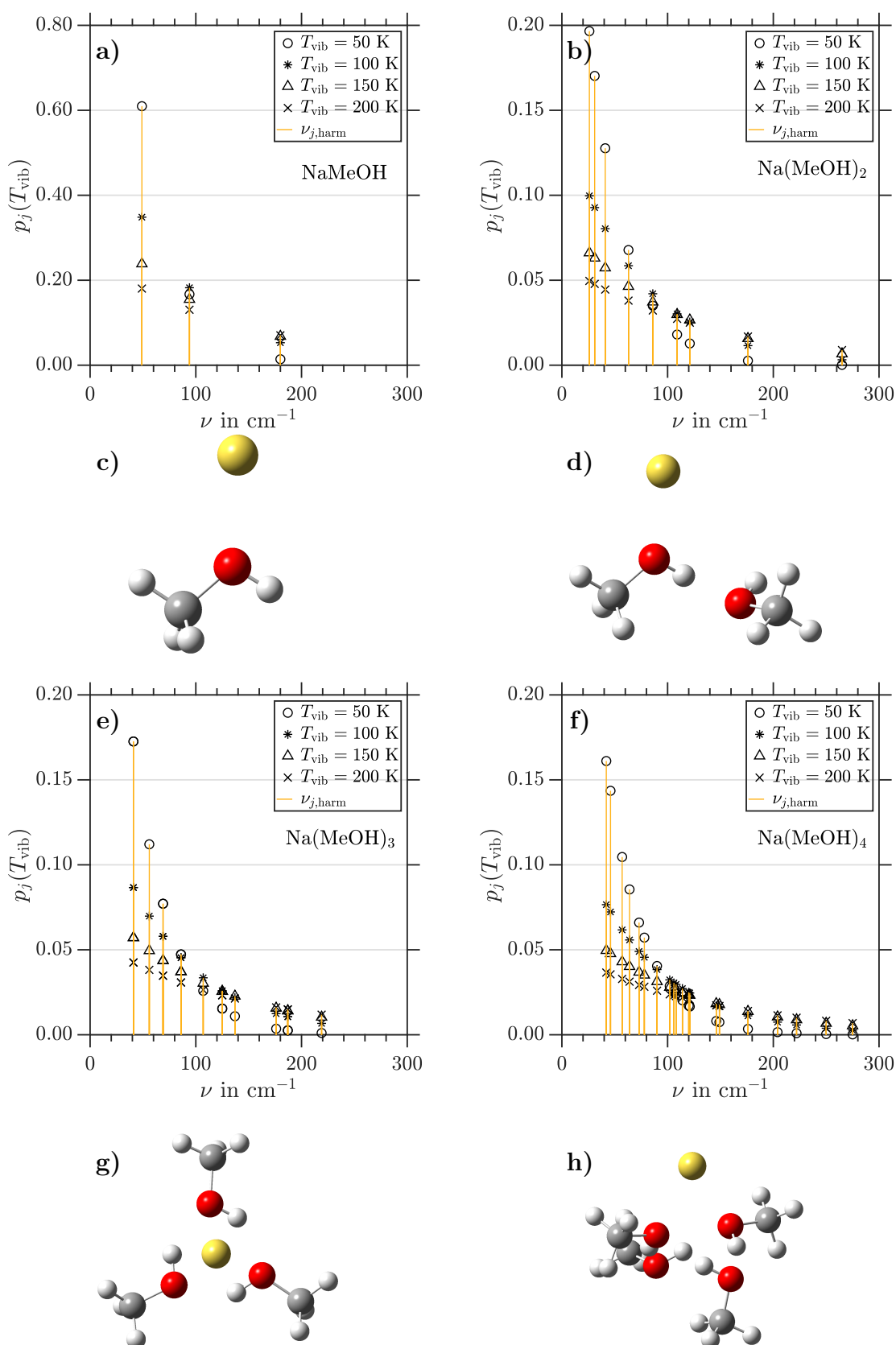


Fig. 6.3.4: Calculated harmonic frequencies (MP2/aug-cc-PVDZ) for $\text{Na}(\text{MeOH})_n$ clusters are shown as yellow vertical lines for (a) NaMeOH, (b) $\text{Na}(\text{MeOH})_2$, (e) $\text{Na}(\text{MeOH})_3$ and (f) $\text{Na}(\text{MeOH})_4$ with $\nu_n < 300 \text{ cm}^{-1}$. The population probabilities $p_j(T_{\text{vib}})$ are plotted for ν_j and estimated vibrational temperatures T_{vib} . Corresponding optimized cluster geometries are shown in (c) NaMeOH, (d) $\text{Na}(\text{MeOH})_2$, (g) $\text{Na}(\text{MeOH})_3$ and (h) $\text{Na}(\text{MeOH})_4$.

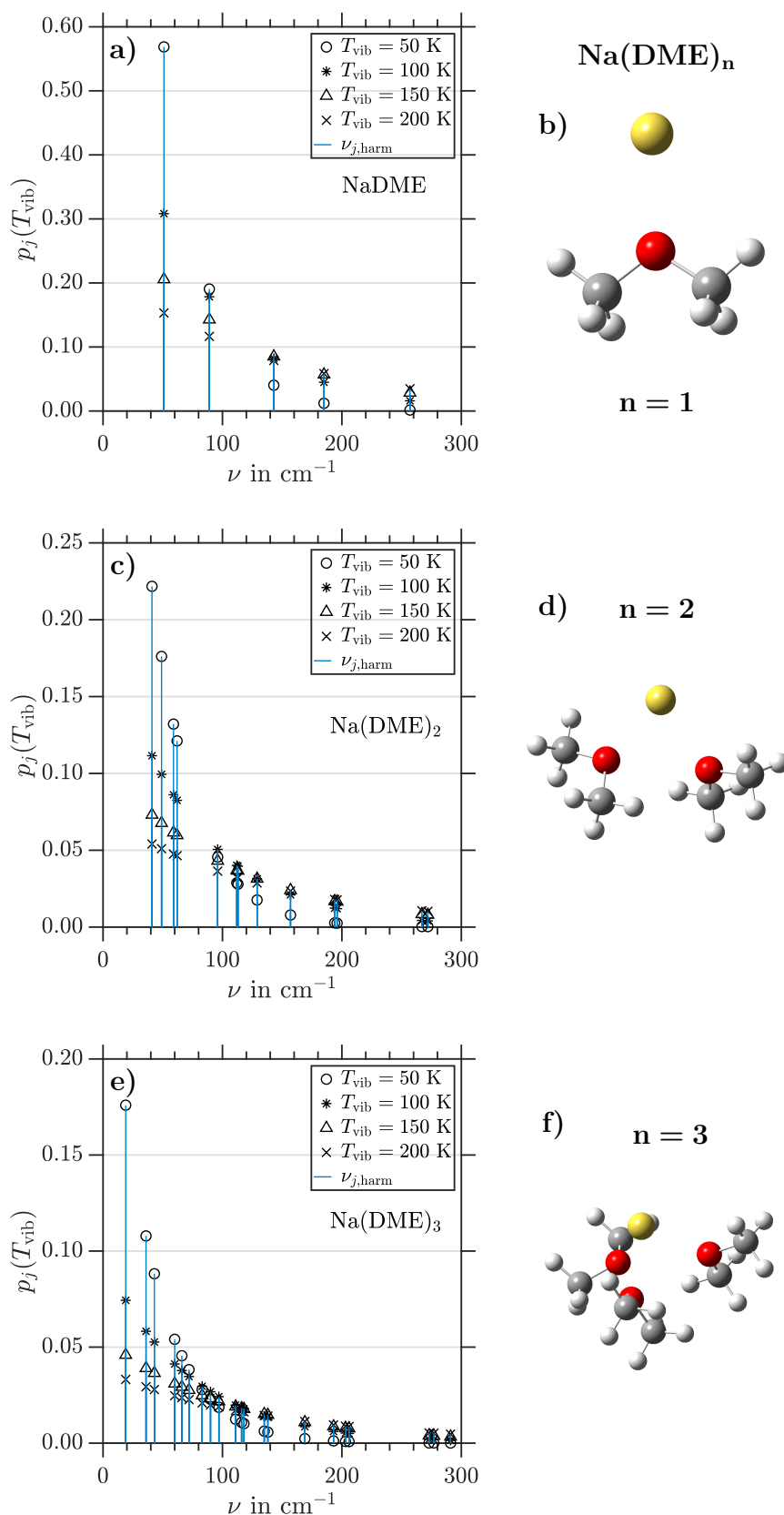


Fig. 6.3.5: Calculated harmonic frequencies (MP2/aug-cc-PVDZ) for Na(DME)_n clusters are shown as blue vertical lines for (a) NaDME , (c) Na(DME)_2 and (e) Na(DME)_3 with $\nu_n < 300 \text{ cm}^{-1}$. The population probabilities $p_j(T_{\text{vib}})$ are plotted for ν_j and estimated vibrational temperatures T_{vib} . Corresponding optimized cluster geometries are shown in (b) NaDME , (d) Na(DME)_2 and (f) Na(DME)_3 .

In the case of **S** and **R** coupled adiabatic Zeeman-like levels, states with $m_S = \pm 1/2$ contributions are able to traverse avoided crossings if neighbouring states with $\Delta M_R = 1$ exhibit an energy difference smaller than the Zeeman energy splitting. In our experiments, we estimate the maximal Zeeman energy splitting to be $\Delta E_{\text{Zeeman}} = 2\mu_B B_{\text{max}} \approx 5.6 \text{ cm}^{-1}$, where μ_B is the Bohr magneton and $B_{\text{max}} = 6 \text{ T}$. We use the maximal energy splitting for a spin 1/2 system as an upper limit for all other investigated clusters. Harmonic frequency calculations of the investigated clusters and their structural isomers (see section B.1 of the appendix) show that the differences in vibrational energies of thermal accessible modes are on average larger than the Zeeman energy splitting.

$$\Delta E_{\text{vib},j} = h(\nu_{j+1} - \nu_j) > \Delta E_{\text{Zeeman}} \quad (6.3.4)$$

In contrast, we find that the rotational energy differences, approximated by $\Delta E_{\text{rot}} = 2 \langle B \rangle_{\text{rot}}$ with the average rotational constant $\langle B \rangle_{\text{rot}} = (A_{\text{rot}} + B_{\text{rot}} + C_{\text{rot}})/3$ (see Tab. 6.3.2-6.3.5), are significantly smaller than ΔE_{Zeeman} . Thus, a large number of avoided crossings among these states is to be expected. We find that the number of avoided crossings a cluster traverses are governed by the density of rotational energy levels and are rather independent of the populated vibrational mode. In some cases the differences in thermally accessible vibrational energies are within the Zeeman energy splitting. In section 6.3.3 we describe a model which also accounts for overlapping vibrations and evaluate their contribution to conceivable avoided crossings within ΔE_{Zeeman} . We first discuss the contributions of avoided crossings in terms of rotational states, under the assumption of no additional contributions from vibrational states.

6.3.2 Average number of rotational states within ΔE_{Zeeman}

In an attempt to understand our experimental findings, we represent the average number of rotational eigenstates within ΔE_{Zeeman} by the rotational partition function (Q_{rot}). Q_{rot} represents the average number of populated states. Hence, Q_{rot} divided by the average rotational energy $k_B T_{\text{rot}}$ and multiplied by ΔE_{Zeeman} corresponds to the average number of states within ΔE_{Zeeman} . Since $k_B T_{\text{rot}}$ and ΔE_{Zeeman} are assumed to be constant, we use Q_{rot} directly in the following. Our analysis is based upon DFT optimized cluster with various isomers ($\omega\text{B97XD}/6\text{-31+G}^*$). In the high temperature approximation the rotational partition function of a non-linear rotor is expressed by

$$Q_{\text{rot}} = \frac{\sqrt{\pi}}{\sigma_{\text{sym}}} \left(\frac{k_B T_{\text{rot}}}{hc} \right)^{3/2} (A_{\text{rot}} B_{\text{rot}} C_{\text{rot}})^{-1/2}, \quad (6.3.5)$$

where σ_{sym} is the symmetry number, T_{rot} the rotational temperature and A_{rot} , B_{rot} , C_{rot} are the rotational constants of the rigid rotor. Rotational constants obtained from quantum chemical calculations are given in Tab. 6.3.2 – 6.3.5. The cluster structures of various isomers are shown in section B.1 of the appendix. Since the rotational temperatures of free

clusters are not well defined, we assume a temperature range $10 \text{ K} \leq T_{\text{rot}} \leq 50 \text{ K}$. This is reasoned by the comparison of the vibrational and rotational energy transfer cross sections σ_{vib} and σ_{rot} , which follow the order $\sigma_{\text{vib}} \ll \sigma_{\text{rot}}$ [165, 166]. In an adiabatic expansion the differences in effective energy transfer lead to $T_{\text{rot}} < T_{\text{vib}}$. Fuchs *et al.* [164] determined $T_{\text{rot}} < T_{\text{vib}}$ with $5 \text{ K} \leq T_{\text{rot}} \leq 20 \text{ K}$ for small metal clusters generated in a supersonic expansion at a nozzle temperature of 16 K. In our experiments, nozzle temperatures are significantly higher ($10^\circ\text{C} \leq T_{\text{nozzle}} \leq 150^\circ\text{C}$) and additional collisions with sodium atoms in the oven are expected to affect the cluster temperatures. Although unclear by how much this influences the cluster temperatures. A rotational temperature range $10 \text{ K} \leq T_{\text{rot}} \leq 50 \text{ K}$ seems a generous range to account for all collisions.

With estimated rotational temperatures ($10 \text{ K} \leq T_{\text{rot}} \leq 50 \text{ K}$) and obtained rigid rotor constants (see Tab. 6.3.2 – 6.3.5), we determine the rotational partition functions Q_{rot} via equation 6.3.5. The results are shown in Fig. 6.3.6. Q_{rot} is here used as an estimator for the number of rotational states within ΔE_{Zeeman} and thus for the number of spin flip processes, which should reflect the average deflection behaviour. These arguments imply that an increase in thermally accessible density of rotational states should coincide with a reduction in deflection [79, 80, 78, 77, 104, 68].

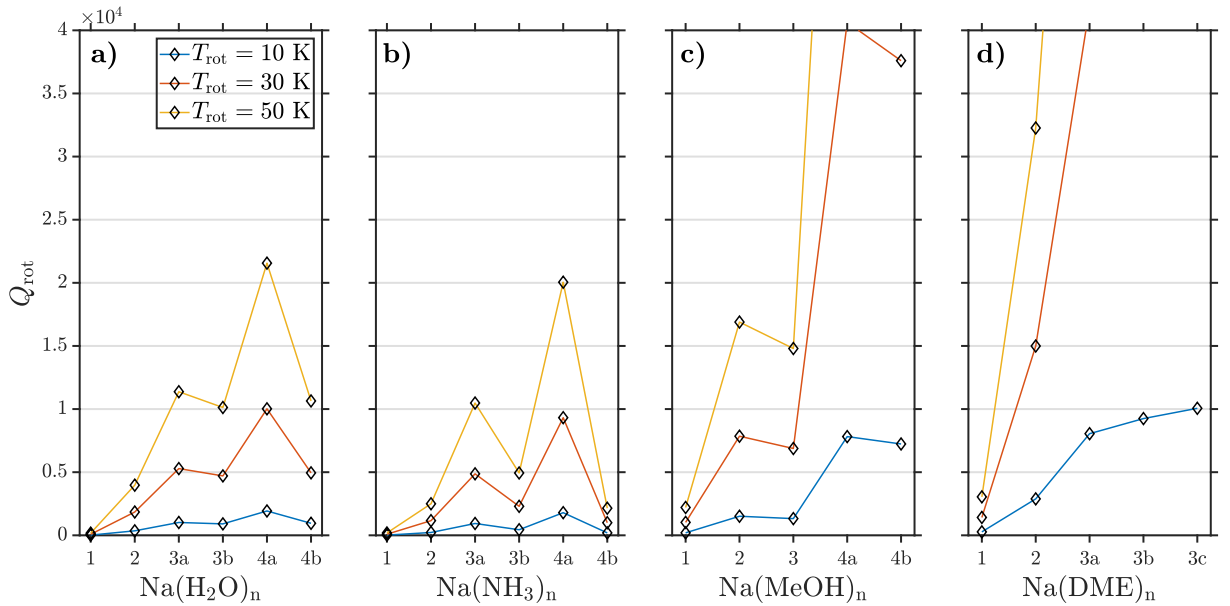


Fig. 6.3.6: Rotational partition function Q_{rot} obtained from asymmetric rigid rotors of DFT optimized cluster structures of: (a) $\text{Na}(\text{H}_2\text{O})_n$, (b) $\text{Na}(\text{NH}_3)_n$, (c) $\text{Na}(\text{MeOH})_n$ and (d) $\text{Na}(\text{DME})_n$.

The comparison of the cluster systems in Q_{rot} shows minimal values for NaH_2O and NaNH_3 in the temperature range $10 \text{ K} \leq T_{\text{rot}} \leq 50 \text{ K}$, and a rotational state population that is weakly-dependent on rotational temperature. This lets one expect effective magnetic moments similar to μ_0 . The experimental $m_S = \pm 1/2$ deflection behaviour confirms these expectations. NaMeOH and NaDME show a gradual increase of Q_{rot} with temperature and the relative deflection trend $\mu_{\text{eff}}(\text{NaMeOH}) > \mu_{\text{eff}}(\text{NaDME})$ is confirmed by the slightly higher Q_{rot} values for the latter.

Previous estimations of thermal temperature (see Tab. 6.3.1) showed that $\text{Na}(\text{DME})_n$ clusters are expected to be colder. It is reasonable to expect similar relative differences in rotational temperatures. With $T_{\text{rot}}(\text{Na}(\text{NH}_3)_n) \geq T_{\text{rot}}(\text{Na}(\text{DME})_n)$ we estimate fewer rotational states for NaDME than for $\text{Na}(\text{NH}_3)_2$ and confirm the experimental observation $\mu_{\text{eff}}(\text{NaDME}) > \mu_{\text{eff}}(\text{Na}(\text{NH}_3)_2)$. Slight deflection of $\text{Na}(\text{DME})_2$ is explained by likely colder rotational temperatures ($T_{\text{rot}} \approx 10$ K) with $Q_{\text{rot}} \approx 2500$. Whereas $\text{Na}(\text{MeOH})_2$ shows an increase of rotational states ($Q_{\text{rot}} \gtrsim 5000$) at $T_{\text{rot}} > 30$ K, which would explain the non-deflected character. For $\text{Na}(\text{H}_2\text{O})_2$ the trend is too indistinct in order to truly support the absence of deflection in the given temperature range.

The larger clusters $\text{Na}(\text{H}_2\text{O})_{3,4}$, $\text{Na}(\text{MeOH})_{3,4}$ and $\text{Na}(\text{DME})_3$ with various isomers, show enhanced rotational state population. The comparison suggests that these non-deflected clusters are characterized by $Q_{\text{rot}} \gtrsim 5000$. Non-deflection for water clusters seems ambiguous when only comparing Q_{rot} . A higher rotational temperature might be an explanation, or other contributions than spin-rotational couplings.

Q_{rot} is substantially different for the structural isomers of $\text{Na}(\text{NH}_3)_{3,4}$. The relative energy difference of 83 meV between 3a and 3b at $\bar{T} = 158$ K suggest a nearly sole population of 3b. The experimental observation of partial deflection for $\text{Na}(\text{NH}_3)_3$ supports the indication of a strong population of 3b with $Q_{\text{rot}} < 5000$. Similar arguments hold for $\text{Na}(\text{NH}_3)_4$ which shows partial deflection and can be explained by preferential population of the tetrahedral isomer 4b with significantly lower Q_{rot} . Previous work of our group [1] found $n = 4$ as magic number for the photoelectron anisotropy in sodium-doped ammonia clusters. This independent experiment supports the idea that deflection of $\text{Na}(\text{NH}_3)_4$ as a highly symmetric tetrahedral structure with substantially lower Q_{rot} is measured. For the T_d structure $\sigma_{\text{sym}} = 12$, less symmetric isomers with lower σ_{sym} (IB in [1]) would cause an increase in Q_{rot} and may lead to reduced deflection. This hints at the possibility of cluster symmetry selective deflection measurements. A combination of magnetic deflection and angle-resolved photoelectron spectroscopy would be a promising experiment to identify orbital angular contributions. In such an experiment, magnetic deflection of highly symmetric cluster structures could be demonstrated as a decrease in β parameter of the recorded photoelectron VMI (see section 3.3).

In general we find appropriate agreement of experimental deflection trends and relative differences in the population of rotational states. So far we suggest that ISR effects in sodium-doped clusters are strongly influenced by the density of thermally accessible rotational states. The most significant deviations of experiment and model are possibly due to differences in cluster rotational temperatures, with proposed order being $T_{\text{rot}}(\text{Na}(\text{DME})_n) < T_{\text{rot}}(\text{Na}(\text{NH}_3)_n) < T_{\text{rot}}(\text{Na}(\text{MeOH})_n) < T_{\text{rot}}(\text{Na}(\text{H}_2\text{O})_n)$. Although, influences from other contributions than spin-rotational coupling cannot be excluded. In the following sections we discuss further dependences which may influence the magnetic properties of sodium-doped solvent clusters.

Tab. 6.3.2: $\text{Na}(\text{H}_2\text{O})_n$: Rotational constants of DFT optimized cluster structures ($\omega\text{B97XD}/6\text{-}31\text{+G}^*$) with their point group (PG), symmetry number σ_{sym} and energy difference between structural isomers ΔE_{iso} . The experimental deflection behaviour indicated by the shading of the circles in the first column (full, partial, and non).

$\text{Na}(\text{H}_2\text{O})_n$	PG	σ_{sym}	A_{rot} in m^{-1}	B_{rot} in m^{-1}	C_{rot} in m^{-1}	ΔE_{iso} in meV
1 ●	C_{2v}	2	1394.3	28.3	27.9	-
2 ○	C_s	1	28.9	22.5	12.9	-
3a	C_1	1	19.0	8.3	6.5	+64
3b ○	C_s	1	13.4	12.3	7.9	0
4a ○	C_1	1	10.5	6.1	4.5	0
4b	C_{2v}	2	11.7	6.1	4.0	+107

Tab. 6.3.3: $\text{Na}(\text{NH}_3)_n$: Rotational constants of DFT optimized cluster structures ($\omega\text{B97XD}/6\text{-}31\text{+G}^*$) with their point group (PG), symmetry number σ_{sym} and energy difference between structural isomers ΔE_{iso} . The experimental deflection behaviour indicated by the shading of the circles in the first column (full, partial, and non).

$\text{Na}(\text{NH}_3)_n$	PG	σ_{sym}	A_{rot} in m^{-1}	B_{rot} in m^{-1}	C_{rot} in m^{-1}	ΔE_{iso} in meV
1 ●	C_{3v}	3	625.0	26.1	26.1	-
2 ●	C_{2v}	2	44.6	12.1	9.8	-
3a	C_1	1	65.0	4.6	4.1	+83
3b ●	C_3	3	10.6	10.2	5.6	0
4a	C_{2v}	2	13.3	2.7	2.3	+235
4b ●	T_d	12	6.3	5.6	5.6	0

Tab. 6.3.4: $\text{Na}(\text{MeOH})_n$: Rotational constants of DFT optimized cluster structures ($\omega\text{B97XD}/6\text{-}31\text{+G}^*$) with their point group (PG), symmetry number σ_{sym} and energy difference between structural isomers ΔE_{iso} . The experimental deflection behaviour indicated by the shading of the circles in the first column (full, partial, and non).

$\text{Na}(\text{MeOH})_n$	PG	σ_{sym}	A_{rot} in m^{-1}	B_{rot} in m^{-1}	C_{rot} in m^{-1}	ΔE_{iso} in meV
1 ●	C_s	1	156.7	13.6	12.8	-
2 ○	C_1	1	14.8	6.5	4.8	-
3 ○	C_1	3	4.7	4.6	3.1	-
4a	C_1	1	3.9	2.2	2.0	+351
4b ○	C_1	1	3.0	2.7	2.5	0

Tab. 6.3.5: Na(DME)_n: Rotational constants of DFT optimized cluster structures (ω B97XD/6-31+G*) with their point group (PG), symmetry number σ_{sym} and energy difference between structural isomers ΔE_{iso} . The experimental deflection behaviour indicated by the shading of the circles in the first column (full, partial, and non).

Na(DME) _n	PG	σ_{sym}	A_{rot} in m^{-1}	B_{rot} in m^{-1}	C_{rot} in m^{-1}	ΔE_{iso} in meV
1 ●	C_{2v}	2	33.2	11.9	9.0	-
2 ●	C_1	1	10.5	3.7	3.2	-
3a ○	C_1	1	3.2	2.8	1.8	0
3b	C_1	1	3.7	2.1	1.6	+79
3c	C_1	1	3.8	1.9	1.4	+113

6.3.3 Average number of rovibrational states within ΔE_{Zeeman}

We here describe a simplified model in order to analyse rovibrational states which may contribute to the deflection behaviour. Additional contributions of rovibrational states to the number of avoided crossings are possible if several thermally accessible vibrational states exist within ΔE_{Zeeman} . In order to account for these possible contributions, we introduce an additional vibrational temperature dependent scaling factor $G_{\text{vib}}(T_{\text{vib}})$. The scaling factor is based on the following considerations. In the case of vibrational modes separated large enough in energy, described by $\Delta E_{\text{vib},i} > \Delta E_{\text{Zeeman}}$ (see equation 6.3.4) $G_{\text{vib}} = 1$, since no additional avoided crossings are gained. For degenerate vibrational states with $\Delta E_{\text{vib},i} = 0$, we assume G_{vib} to be equal to the vibrational degeneracy, since the harmonic oscillator model is defined by independent vibrations. For an intermediate case with vibrational energy differences between $0 < \Delta E_{\text{vib},i} < \Delta E_{\text{Zeeman}}$, $G_{\text{vib},i}$ is described by

$$G_{\text{vib},i} = \frac{\Delta E_{\text{Zeeman}} - \Delta E_{\text{vib},i}}{\Delta E_{\text{Zeeman}}} + 1. \quad (6.3.6)$$

The scaling factors are evaluated in an energy interval $< k_B T_{\text{vib}}$ given by estimated vibrational temperatures $50 \text{ K} \leq T_{\text{vib}} \leq 200 \text{ K}$. Averaging the scaling factors over the vibrational energy interval with $T_{\text{vib}} = 50 \text{ K}$ and $T_{\text{vib}} = 200 \text{ K}$, leads to the results shown in Fig. 6.3.7 and 6.3.8.

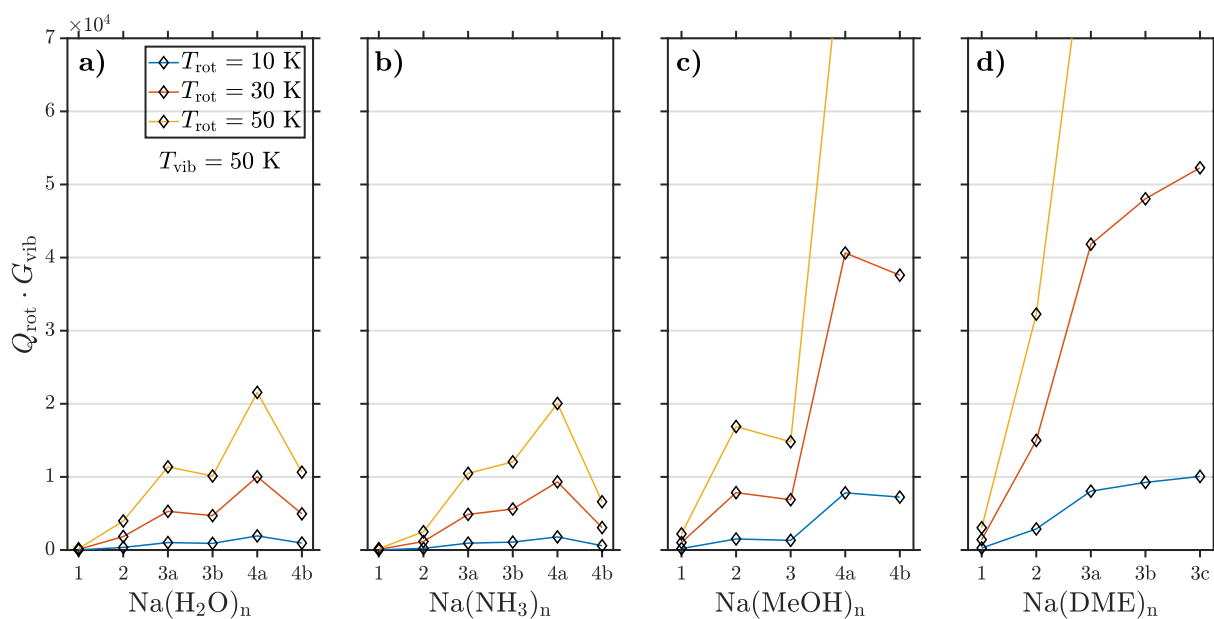


Fig. 6.3.7: Rotational partition function Q_{rot} scaled with G_{vib} at $T_{\text{vib}} = 50$ K, which estimates the number of rovibrational states within ΔE_{Zeeman} . The analysis of rovibrational states is based on the harmonic oscillator and asymmetric rigid rotor of DFT optimized cluster structures of: (a) $\text{Na}(\text{H}_2\text{O})_n$, (b) $\text{Na}(\text{NH}_3)_n$, (c) $\text{Na}(\text{MeOH})_n$ and (d) $\text{Na}(\text{DME})_n$.

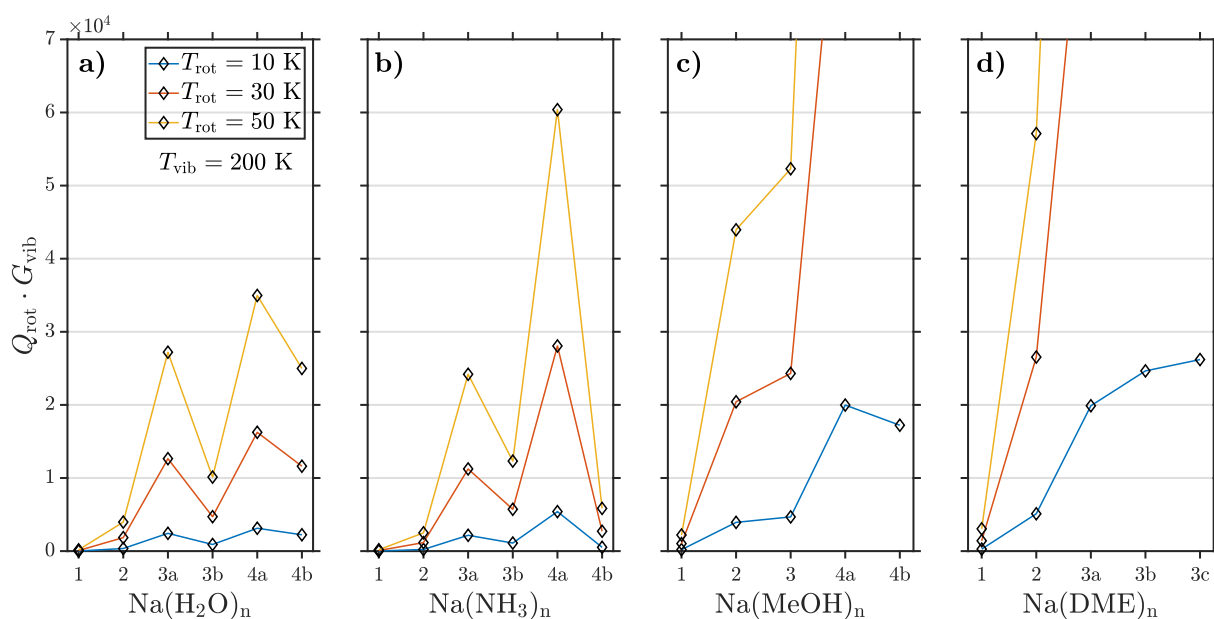


Fig. 6.3.8: Rotational partition function Q_{rot} scaled with G_{vib} at $T_{\text{vib}} = 200$ K, which estimates the number of rovibrational states within ΔE_{Zeeman} . The analysis of rovibrational states is based on the harmonic oscillator and asymmetric rigid rotor of DFT optimized cluster structures of: (a) $\text{Na}(\text{H}_2\text{O})_n$, (b) $\text{Na}(\text{NH}_3)_n$, (c) $\text{Na}(\text{MeOH})_n$ and (d) $\text{Na}(\text{DME})_n$.

The relative trends of $Q_{\text{rot}} \cdot G_{\text{vib}}$ for both vibrational temperatures are similar to the relative trends discussed in section 6.3.2. These findings confirm that the average deflection behaviour is anticipated to be governed by the density of thermally accessible rotational states with similar influences by the vibrational density of states. We show that the

deflection behaviour of NaH₂O, Na(H₂O)₂, Na(H₂O)_{3b}, NaNH₃, Na(NH₃)₂, NaMeOH and NaDME are likely to be insensitive of vibrational excitation at given temperatures, as the vibrational energies are separated larger than the Zeeman splitting. The comparison of Fig. 6.3.6 with Fig. 6.3.7 and 6.3.8 reveals a weak dependence on vibrational temperature for the partially deflecting clusters Na(NH₃)_{3b} and Na(NH₃)_{4b} as well as a more pronounced dependency for Na(H₂O)_{4b}, Na(MeOH)₂₋₄ and Na(DME)_{2,3}.

These results suggest that the magnetic properties of fully and partially deflecting clusters are primarily governed by the population of rotational states. In contrast, slightly and non-deflected clusters exhibit a non-negligible dependence on vibrational temperature. These interpretations let us suggest that ISR times are governed by the rovibrational state density within ΔE_{Zeeman} . With several vibrational levels populated within ΔE_{Zeeman} , we suggest an acceleration of spin relaxation effects, which we observe experimentally as non-deflected clusters.

It should be noted that low frequency vibrations are commonly known to exhibit significant anharmonicity. Therefore a harmonic oscillator model is likely not a good approximation for the fundamental vibrational energies and even worse for overtones. This might cause significant differences in vibrational level density within ΔE_{Zeeman} , since an anharmonic potential allows for higher state densities with increasing potential energy. Additionally, one should also consider the dependence of the rotational constants on the vibrational state and possible couplings to vibrational angular momenta. These mentioned points could further affect the magnetic deflection behaviour, due to reasons discussed above. The previous discussion of magnetic deflection trends are based on the avoided crossings model [104, 68], where we estimated that the molecular Landé factor g_J is similar to $g_S = 2.00232$ of the free electron, and contributions of the orbital angular momentum Landé factor g_L were neglected. In the following we give an outlook on possible refinements for the interpretation of SG deflection results.

6.4 Outlook

First of all we propose an expansion of the harmonic oscillator and rigid rotor model for a more precise description of the rovibrational energy states $E_{n,R}$.

$$\begin{aligned}
 E_{n,R} = & \underbrace{hc \cdot \nu_0 (n + 1/2)}_{\text{harmonic vibrational term}} - \underbrace{hc \cdot \nu_0 \chi (n + 1/2)^2}_{\text{anharmonic vibrational term}} + \underbrace{hc \cdot BR(R + 1)}_{\text{rigid rotor term}} \\
 & - \underbrace{hc \cdot DR^2 (R + 1)^2}_{\text{centrifugal distortion term}} - \underbrace{hc \cdot \alpha (n + 1/2) R (R + 1)}_{\text{Coriolis term}}
 \end{aligned} \tag{6.4.1}$$

Further terms of $E_{n,R}$ describe the vibrational anharmonicity (χ : anharmonicity constant), the centrifugal distortion (D : centrifugal distortion constant) and the coupling term of vibration and rotation (α : vibration-rotation coupling constant).

Our results and discussions on sodium-doped clusters indicated that the topology of the Zeeman diagram is dominated by spin-rotational coupled Zeeman-like eigenstates. Each Zeeman state is described by its total angular momentum \mathbf{J} and the corresponding Landé factor g_J . Theoretical work on the molecular Zeeman effect and expressions of the molecular Landé factor have been carried out by various groups [58, 59, 115, 60, 103]. Solanki and Berdyugina [60] give an overview on ensuing experimental and theoretical work done on the molecular Zeeman effect in diatomic molecules. In their work the theory of the Zeeman effect for diatomic molecules in the limiting Hund's cases (a) and (b) are evaluated. In Hund's coupling case (a), the angular momenta, of electron orbital and spin are coupled to the internuclear axis and interact very weakly with the rotational angular momentum. While in Hund's case (b) the electron orbital angular momentum is coupled to the internuclear axis and the spin is decoupled or very weakly coupled to the molecular axis [118]. Solanki and Berdyugina [60] furthermore developed a numerical approach for the intermediate coupling case (a-b). Yurchenko *et al.* provide a program DUO [167] based on the theoretical work of Solanki [60] which computes Landé factors of open shell diatomic molecules from the direct solutions of the nuclear motion Schrödinger equation. Since our investigated cluster systems are polyatomic with $N_{\text{atom}} > 4$, one would expect significant absolute errors in similar evaluation of g_J values. Sears [108] summarizes methods to calculate g_J values of polyatomic asymmetric-top free radicals. We expect the relative differences in g_J lead to further insight on additional effects of ISR processes in sodium-doped clusters. We present a preliminary qualitative discussion of g_J assuming a Hund's coupling case (b) representation, with the sole justification that spin-orbit coupling is likely weak. In Hund's coupling case (a) a proportionality $g_J \propto 1/J(J+1)$ is found (see chapter 3), leading to a comparable reduction of g_J towards larger J states. The corresponding expression of the diatomic Landé factor for Hund's case (b) is given by Solanki [60]

$$g_J = \frac{g_L}{2J(J+1)} \cdot \left(\frac{\Lambda^2 [J(J+1) + R(R+1) - S(S+1)]}{R(R+1)} \right) + \frac{g_S}{2J(J+1)} [J(J+1) - R(R+1) + S(S+1)] \quad (6.4.2)$$

where Λ is the projection of electron orbital angular momentum on the molecular axis. Previous work in our group [1] showed experimental evidence for high s -character ($\sim 95\%$) of the unpaired electron HOMO via photoelectron VMI. Therefore we assume $\Lambda \approx 0$ and g_J simplifies to

$$g_J = \frac{g_S}{2J(J+1)} [J(J+1) - R(R+1) + S(S+1)]. \quad (6.4.3)$$

Describing the population of J states with a probability function p_J results in an average

Landé factor $\langle g_J \rangle$ characteristic for each cluster.

$$\langle g_J \rangle = g_J \cdot p_J \quad (6.4.4)$$

It has to be shown if p_J can be approximated by the population of rotational states at zero field. The effective magnetic moment μ_{eff} has been previously described as an attenuation of μ_0 (see section 6.2), governed by ISR processes invoked by traversing several avoided crossings. In a similar manner, we find an expression for μ_{eff} which results from quenching of the free electron Landé factor g_S due to spin-rotational coupling.

$$\mu_{\text{eff}} = \frac{\langle g_J \rangle}{g_S} \quad (6.4.5)$$

Population of highly excited rotational states leads to a significant decrease in g_J and as a consequence Zeeman-like levels with decreased energy splitting. The Zeeman states depict a decrease in slope towards higher angular momentum states \mathbf{J} . Xu *et al.* discussed similar dependences towards higher energy Zeeman states, although discussed with a different underlying mechanism, respectively the avoided crossing model. It was discussed that the effective magnetic moment in sodium-doped solvent clusters is dominated by spin-rotational couplings, which are likely the cause for avoided crossings and a reduced characteristic Landé factor. However, further experimental and theoretical work needs to be carried out to express their contributions to the attenuation of the magnetic moment. In particular, well defined vibrational T_{vib} and rotational T_{rot} temperatures are of great interest to improve the interpretations of magnetic deflection trends. The influence of thermal population of states, expressed by their population function p_J , may be studied in deflection experiments as a function of temperature. Deflection measurements with spatial resolution is an established experimental technique to obtain the deflected beam profile. Characterising the deflected beam profile (*e.g.* asymmetric deflection to one side [78, 168, 104, 77]) lead to insight on the deflection mechanism and gave guidance to the avoided crossing model. In the near future, we aim to measure deflection via spatial map imaging [82] and resolve the deflection in magnetic field gradient direction. With the spatial information we would gain insight if possible spin flip processes occur during the deflection process.

Further contributions as spin-orbit couplings and hyperfine couplings to nuclear spins, may perturb the Zeeman-like levels and influence the deflection behaviour. Fuchs *et al.* [81] showed in double magnetic deflection experiments that nuclear spins diminish the electron spin coherence. Methods to calculate the cluster Zeeman effect with further angular momenta contributions have been reviewed by Jansen and Merkt [103], as well as summarised by Sears [108]. Previous work of Berdyugina and Kuzmychov [169] showed that the energy level structure of CrH molecule in the presence of a magnetic field, determined via quantum chemical calculations allowed to predict the magnetic deflection behaviour. Similar approaches seem feasible for small clusters *e.g.* NaNH₃ and NaH₂O, however for

larger systems calculations may already be too demanding. Calculating the Zeeman energy structure for small sodium-doped clusters is of interest, to evaluate other angular momenta contributions.

6.5 Summary

The magnetic deflection behaviour of $\text{Na}(\text{H}_2\text{O})_n$ ($n = 1 - 4$), $\text{Na}(\text{NH}_3)_n$ ($n = 1 - 4$), $\text{Na}(\text{MeOH})_n$ ($n = 1 - 4$) and $\text{Na}(\text{DME})_n$ ($n = 1 - 3$) clusters was characterised. Reduced magnetic deflection was modelled by the attenuation of the magnetic moment μ_0 of a $m_S = \pm 1/2$ system. With this approach we are able to retrieve characteristic spin relaxation times τ . The experimental deflection trends were discussed in terms of thermally accessible rovibrational states and cluster Landé factors g_J with the goal being to identify the dominating factors for intracluster spin relaxation. In our approach we estimated the cluster thermal energies with the help of evaporative ensemble theory and calculated vaporization enthalpies. The rovibrational states were analyzed with the harmonic oscillator and rigid rotor model of optimized cluster geometries. With the applied models we showed that the fully deflecting $m_S = \pm 1/2$ character of NaH_2O and NaNH_3 is due to them exhibiting a low number of populated rovibrational states. For all other sodium-doped clusters reduced deflection was attributed to an increased population of rovibrational states. The results show that the magnetic deflection behaviour is dominated by the thermal population of rotational states. We discuss that spin-rotational couplings allow for avoided crossings and a reduction of the cluster Landé factor g_J , which seems likely to be the cause for reduced deflection.

Chapter 7

How solvated dielectrons and their electron transfer mediated decay govern the ionization dynamics of metal-ammonia solutions

We here present a first summary of unpublished results, contributions of my work are restricted to the experimental measurements.

Title: How solvated dielectrons and their electron transfer mediated decay govern the ionization dynamics of metal-ammonia solutions.

Authors: S. Hartweg, J. V. Barnes, B. L. Yoder, G. Garcia, L. Nahon, E. Miliordos and R. Signorell.

Citation: Manuscript in progress.

7.1 Introduction

Solvated electrons in solutions of alkali metals in liquid ammonia and other amines are widely used as strong reducing agents in chemical synthesis and proof to be difficult to replace although their use, especially at large industrial scales is expensive and challenging [170]. The first observations and descriptions of solvated electrons in these systems go back to Sir Humphry Davy and Weyl [5, 3], long before the discovery of the Birch reduction [12]. The concentration dependent properties of alkali ammonia solutions are of scientific interest since these early times, but our molecular level understanding of the involved species and processes remains superficial and fragmentary [5]. At low concentrations alkali ammonia solutions behave like normal electrolytes consisting of solvated electrons and alkali counterions. At increasing concentrations interactions between solvated electrons as well as between solvated electrons and counterions amplify. The solvated electrons form

spin-paired solvated dielectrons, before at very high concentrations a transition to a metallic liquid phase occurs, accompanied by a change of colour from deep blue to bronze gold. How well the solvated electrons and solvated dielectrons are separated from the alkali counterions in which concentration range, remains unclear, since experimental access to such details in liquid solutions are still a challenge in itself. Recent photoelectron spectroscopy studies addressed the concentration dependent properties in sodium ammonia nanodroplets [54] and liquid bulk solutions [55], without finding a clear photoelectron signature to distinguish solvated electrons from dielectrons. Bulk solutions were presumably studied only in the spin-pairing concentration range, while cluster studies could not distinguish the two species. In clusters of ammonia and other solvents, finite size effects in electron solvation due to the limited system size have been studied [1, 2, 23, 24]. Also the relaxation dynamics of solvated electrons in small sodium-doped ammonia clusters have been studied after near infra-red excitation to *p*-type electron solvation orbitals [161]. While the spin-pairing of solvated electrons has been observed experimentally by magnetic measurements early on [171], the most insights we have today into the structure and electronic properties of these dielectrons originates from theoretical studies [5, 172, 173]. Some of the properties of alkali solutions in ammonia and other amines as well as the solvated electrons they contain are certainly unique to these systems. This concerns for example the stability and high concentrations of solvated electrons that can be produced in sodium ammonia solutions, while other neutral bulk systems rather know solvated electrons as transient species after optical excitation. Nevertheless, the study of alkali-doped solvent clusters provided already valuable insights for other electron solvation systems, including those in aqueous solutions, which are much discussed recently for their importance in radiation chemistry and radiation damage processes.

Here we present a VUV photoelectron-photoion-coincidence study, obtaining cluster size-resolved photoelectron spectra of small sodium ammonia clusters containing solvated electrons. Our experimental results in combination with *ab initio* calculations reveal three distinct ionization pathways of the single solvated electron leading to the electronic ground state of the cationic cluster. Each pathway is dominant in a certain photon energy range. One of these pathways proceeds via the formation of spin-paired solvated dielectrons, which are produced by photoexcitation of an electron from the ammonia valence shell to the electron solvation orbital. While solvated dielectrons in ammonia bulk solutions and clusters are metastable on an hour timescale these transient dielectrons in the vicinity of the ammonia valence shell vacancy decay on a presumably ultrafast timescale via a special form of electron transfer mediated decay (ETMD) [48, 49, 50, 51].

7.2 Experimental Methods

The experimental setup used here is a permanent endstation comprising the molecular beam chamber Saphirs and the double imaging photoelectron-photoion-coincidence-spectrometer

Delicious III [47, 46] on the VUV beamline DESIRS [96] of the synchrotron SOLEIL in St. Aubin, France and has been described elsewhere. To produce ammonia clusters, neat ammonia was expanded at 2.5 – 3.5 bar stagnation pressure through a pinhole nozzle with a diameter of 25 μm . The first wall and skimmer between the Saphirs molecular beam chamber and the differential pumping chamber was removed in order to accommodate the sodium-oven used to dope the ammonia clusters. The resistively heated sodium-oven was mounted in between the pinhole nozzle and the skimmer separating the molecular beam chamber from the spectrometer chamber. The doped clusters entered the spectrometer through a skimmer of 1 mm diameter and were ionized by monochromatized synchrotron radiation propagating perpendicular to the molecular beam direction and spectrometer axis. Higher harmonics of the synchrotron radiation were efficiently removed by the gas filter upstream from the monochromator operated with xenon. For measurements at 5.5 eV, we additionally used a MgF_2 window to remove the second harmonic, which for this photon energy lies below the ionization potential of xenon. After photoionization, photoelectron and photoions were detected in coincidence on the dedicated imaging detectors of the Delicious III spectrometer. After subtraction of the false coincidence background and photoelectron signals were filtered according to the ion mass to obtain mass-selected photoelectron velocity map images. Additional background suppression was achieved by selecting only the central part of the molecular beam using in the photoion image. Mass-selected photoelectron images were subsequently smoothed using Gaussian convolution filters before reconstruction of the photoelectron kinetic energy and angular distributions using the pBasex algorithm [99].

7.3 Computational Methods

The geometric and electronic structure of sodium complexes with up to six ammonia molecules are investigated with Møller-Plesset second order perturbation theory (MP2) and coupled-clusters with single, double and perturbatively connected triple excitations (CCSD(T)). The correlation consistent basis sets aug-cc-pVDZ and aug-cc-pVTZ are employed for this study. The general notation $[\text{Na}, n\text{NH}_3]$ ($n = 1 - 6$) is used to denote these complexes. When all n ammonia molecules coordinate to sodium the $\text{Na}(\text{NH}_3)_n$ notation is used, while when m of them are in the second solvation shell we use the notation $\text{Na}(\text{NH}_3)_{n-m}(\text{NH}_3)_m$. MP2 geometry optimizations and harmonic frequencies for ground states were calculated with Gaussian16 [174], while MP2 and CCSD(T) calculations for the excited states were done with MOLPRO 2021 [175]. The presented quantum chemical calculations were performed by Prof. Evangelos Miliordos.

7.4 Results & Discussion

The experimental setup used for double imaging photoelectron-photoion-coincidence-spectroscopy at the VUV beamline DESIRS of Soleil Synchrotron has been described previously [47, 46] and details about experimental and computational parameters and procedures are given in the corresponding method sections. Fig. 7.4.1a shows photoelectron spectra (PES) for selected cluster species obtained at different photon energies (for the full data sets see section 7.5). The electron binding energy (eBE) scale is calculated by the difference of the photon energy and the detected kinetic energy of the photoelectrons, $\text{eBE} = h\nu - E_{\text{kin}}$. Examples for typical velocity map images prior to Abel inversion [99] are shown in Fig. 7.4.1b. The photoelectron spectra and images in Fig. 7.4.1 reveal a characteristic trend with increasing photon energy independent of cluster size. At low photon energies (5.5 eV), the spectra are dominated by a single low-binding energy feature, while they are dominated by a single high-binding energy band at high photon energy (9.9 eV). For intermediate photon energies (6.2 – 8.0 eV), the spectra show a very broad binding energy distribution with a maximum close to zero kinetic energy in addition to the sharp low-binding energy feature.

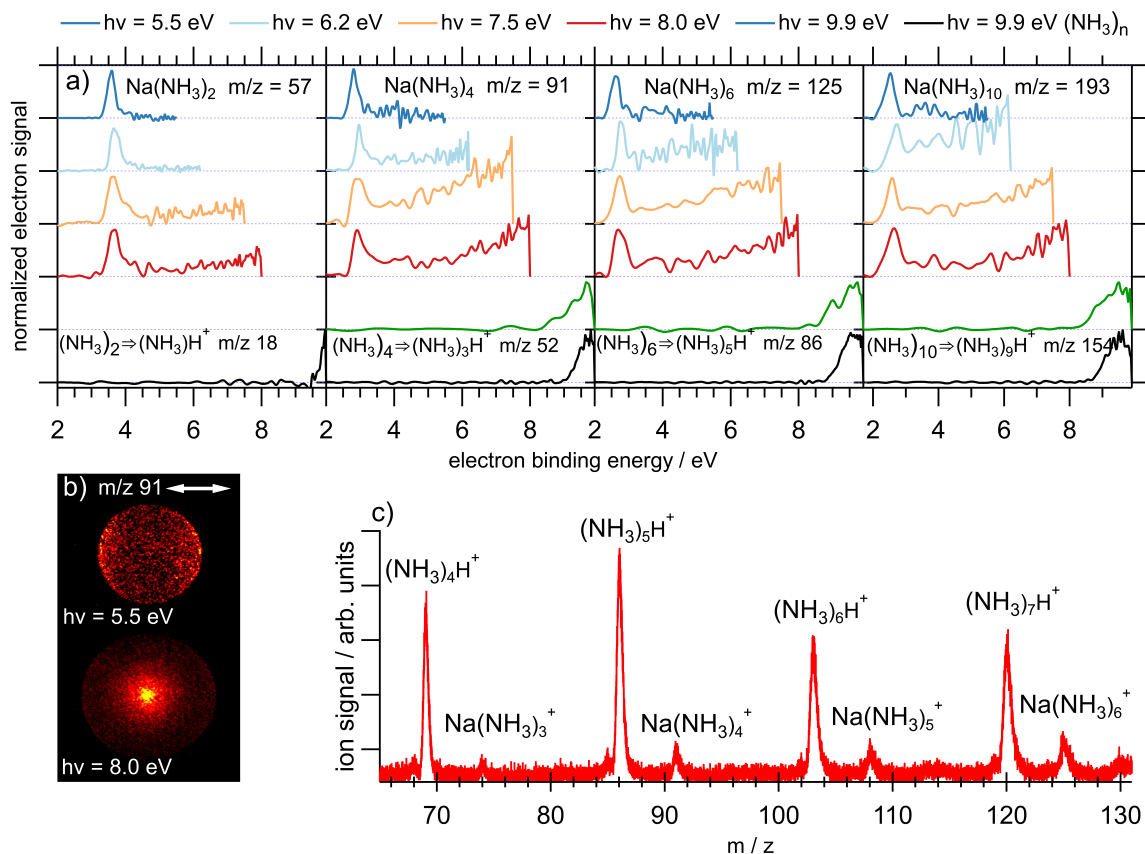


Fig. 7.4.1: (a) Selection of photoelectron spectra: $\text{Na}(\text{NH}_3)_n$ ($n = 2, 4, 6, 10$) at various photon energies $h\nu$ (coloured lines). Data for the photoionization of pure ammonia clusters $(\text{NH}_3)_n$ ($n = 2, 4, 6, 10$) are shown as black lines. (b) Unreconstructed velocity map images for $\text{Na}(\text{NH}_3)_6$, highlighting the increase of isotropic low energy electrons over the anisotropic fast photoelectrons with increasing photon energy. (c) Mass spectrum recorded at 9.9 eV showing protonated ammonia cluster ions arising from direct ionization of pure ammonia clusters, and non-protonated cluster ions containing a sodium atom. The inset shows a mass spectrum recorded at 6.2 eV.

The single sharp feature at low binding energy observed in the PES for photon energies below 9.9 eV corresponds to the direct photoionization of the weakly bound solvated electron [54, 2, 23, 161] (and references therein). The process is schematically depicted in Fig. 7.4.2a and can be seen as a non-resonant transition from the electronic ground state 2X of the neutral cluster and the electronic ground state $^1x^+$ of the cationic cluster. The involved electron solvation orbital ϕ_{solv} is depicted in Fig. 7.4.2d for $\text{Na}(\text{NH}_3)_4$. The binding energy of the solvated electrons in these clusters depends on their cluster size and shifts from 4.4 eV for NaNH_3 to about 2.5 eV for $\text{Na}(\text{NH}_3)_{n \geq 10}$, which is in agreement with our *ab initio* calculations and previous studies [1, 2, 24]. For a comparison to the computational results and previous measurements see the supplementary information in section 7.5. The removal of the solvated electron in these systems is considered very soft, such that only minor nuclear rearrangement follows, and no chemical reactions are

triggered [23]. At 9.9 eV photon energy the appearance of the spectra changes drastically and shows only electrons bound by more than 8 eV. These electron signals correspond to the direct ionization from cluster orbitals derived from the highest occupied molecular orbital (HOMO) of the ammonia molecule. The cluster cations formed by these non-resonant ionizing transitions are in the first electronically excited state $^1a^+$. In the isolated ammonia molecules this HOMO corresponds to a nitrogen lone pair orbital. In clusters of n ammonia molecules (with or without alkali atoms) these individual molecular orbitals interact and form n cluster orbitals ϕ_L . This means, albeit we depict the $^1a^+$ as a single discrete state, the spectral band consists of n very similar states. The energetically highest of the four orbitals ϕ_L for a cluster $\text{Na}(\text{NH}_3)_4$ is depicted in Fig. 7.4.2e. This photoelectron band shows a strong similarity to the signals arising from direct ionization of pure ammonia clusters, shown in black in Fig. 7.4.1a, which further corroborates the assignment. Also, the similarity highlights that the presence of the sodium counter ion and the solvated electron do not strongly affect the electronic structure of the ammonia solvent molecules. This is especially true for clusters containing more than four ammonia molecules. For fewer ammonia molecules the effect of the sodium counter ion on the hydrogen bond network is strongest and consequently the mixing of molecular orbitals and the electronic structure is affected. At this photon energy no signals corresponding to the direct ionization of the solvated electrons can be detected, which we explain by the dominating cross sections for ionization from the ammonia lone pair orbital. Despite the similarity in the appearance of the PES of pure ammonia clusters and sodium-doped ammonia clusters at 9.9 eV photon energy, there is a substantial difference in the fate of the corresponding photoions. In pure ammonia clusters photoionization produces a radical photoion $\text{NH}_3^{\bullet+}$ solvated within the hydrogen-bonded cluster. This radical ion subsequently receives a hydrogen transfer from a neighbouring ammonia molecule, creating an ammonium cation NH_4^+ and a neutral NH_2^{\bullet} radical. The latter is lost from the cluster, giving rise to $(\text{NH}_3)_n\text{H}^+$ peaks in the mass spectrum in Fig. 7.4.1c [176, 177, 178]. Note that the formation of non-protonated ammonia cluster cations can be observed as a minor channel in Fig. 7.4.2c. The same hydrogen transfer pathway followed by the loss of a neutral radical is well known from other hydrogen-bonded clusters including water [176, 179, 180, 181, 182, 183, 184]. Ammonia clusters containing a single sodium atom on the contrary do not show protonated cluster ions in the mass spectrum (see Fig. 7.4.1c), although the photoionization process removes an electron from the same ammonia lone pair orbital. For the smallest sodium-doped ammonia clusters containing less than four ammonia molecules one can explain this difference by the absence of a real hydrogen-bond network, since up to four ammonia molecules can coordinate to the sodium counterion. For larger clusters, with up to ten ammonia molecules one would, however, certainly expect the hydrogen transfer reaction to occur. The absence of protonated cluster ions containing sodium atoms from the mass spectrum suggests the dominance of an alternative relaxation channel. This is surprising given the ultrafast timescales on which these hydrogen transfer reactions typically occur.

The simple possibility to quench the hydrogen transfer reaction is the repopulation of the lone pair orbital from which the photoionization process removed an electron. Such a relaxation channel, schematically shown in Fig. 7.4.2c, can be realized by the relaxation of the solvated electron into the ammonia lone pair vacancy, thus relaxing the cluster to the cationic ground state $^1x^+$ and quenching the driving force of the hydrogen transfer reaction. It remains unclear from our experiments, if this relaxation occurs via a radiation less internal conversion process or radiative via the emission of a photon. In order to dominate the competing hydrogen transfer reaction, the relaxation of the solvated electron into the ammonia lone pair vacancy should occur at least on a similar timescale, which suggests a radiation less internal conversion process. Similar relaxation processes have been observed for excited solvated electron states in these systems [161]. Another mechanism, by which the presence of a solvated electron quenches the hydrogen transfer reaction, without filling the valence shell vacancy driving the reaction seems unlikely. Note that this observed relaxation process, comprising the relaxation of a solvated electron into a lower lying singly occupied orbital is closely related to the first step of the Birch reduction, in which an initially solvated electron attaches to an unoccupied molecular orbital. The time-resolved study of sodium-doped clusters seems therefore to offer a straight-forward way to study the fundamental dynamics of such reactions of high relevance for chemical synthesis.

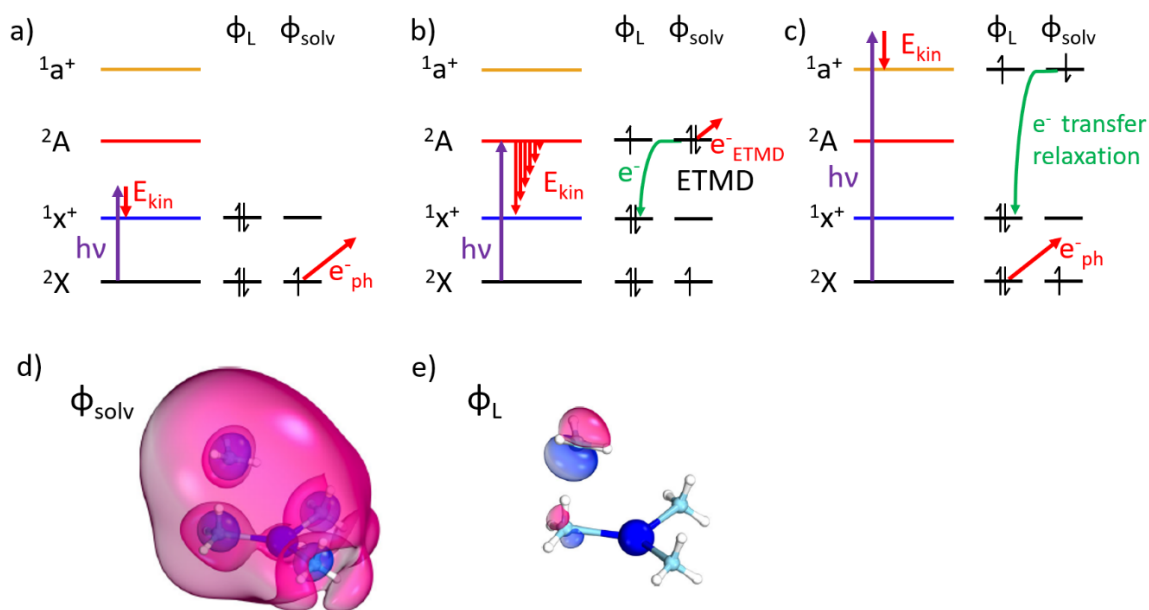


Fig. 7.4.2: Schematic energy level diagrams including electron configurations of sodium-doped ammonia clusters. Arrows in panels (a)-(c) show the different observed ionization mechanisms and the involved orbitals, *i.e.* the electron solvation orbital ϕ_{solv} and one of the ammonia lone pair orbitals ϕ_L are depicted in panels (d) and (e), respectively. The violet arrows indicate excitation with a photon energy $h\nu$, the red arrows indicate the emission of an electron with kinetic energy E_{kin} and the green arrows indicate electron transfer reactions between the orbitals. (a) Direct ionization to the cationic ground state, corresponding to the removal of the solvated electron from ϕ_{solv} . (b) Excitation of the neutral $2A$ state, followed by autoionization to the ionic ground state via ETMD.

In the intermediate photon energy range (6.2 – 8.0 eV) the PES for all cluster sizes show an additional broad feature extending from the sharp direct ionization band of the solvated electron ϕ_{solv} to the highest measured binding energy for each photon energy. This feature with a maximum signal at zero electron kinetic energy can also be observed in the photoelectron images displayed in Fig. 7.4.1b for $\text{Na}(\text{NH}_3)_4$. These broad low-kinetic-energy features can only be produced by an autoionization process occurring after a resonant excitation to a neutral excited state. This becomes clear, considering the electronic structure of the sodium-doped ammonia clusters. The first electronic orbital below the electron solvation orbital is the ammonia lone pair, corresponding to an electron binding energy ~ 8 eV. In between these two orbitals, there are no electrons that could be removed in a direct ionization process. Autoionization is energetically accessible since already the photon energy of 6.2 eV lies between 1.8 and 3.7 eV (depending on the cluster size) above the ionization potential. The lowest electronically excited states of solvated electrons in sodium-doped clusters have been studied previously experimentally [161] and theoretically [24, 185, 186]. These excited states are also known as Rydberg excitations of the solvated electron, converging to its ionization limit (2.5 – 4.4 eV depending on the cluster size). Above this Rydberg series and its associated ionization limit our calculations

at the MP2 and CCSD(T) levels of theory reveal a series of states, which we denote 2A . The lowest of these states lies between 6.1 and 6.9 eV above the ground state of the clusters depending on the cluster size. These states are characterized by a doubly occupied electron solvation orbital ϕ_{solv} (Fig. 7.4.2d), and a vacancy in one of the ammonia lone pair HOMO orbitals ϕ_{L} . The excitation has therefore a charge transfer character, nominally transferring an electron from an ammonia lone pair into the electron solvation orbital, thus creating a spin-paired solvated dielectron. While this solvated dielectron is presumably very similar to solvated dielectrons in alkali ammonia bulk solutions, in this case it is destabilized by the vicinity of the low-lying ammonia lone pair vacancy, such that the cluster can relax by autoionization. In this autoionization process, constituting a peculiar case of ETMD, one of the electrons in the solvated electron pair relaxes into the ammonia lone pair vacancy. The electron transfer relaxation is similar to the one described above (Fig. 7.4.2c), while the other electron is emitted from the cluster. This ETMD process is shown schematically in Fig. 7.4.2b. To our knowledge this is the first time that such a non-local autoionization process is observed for solvated electrons and constitutes evidence of the electron correlation within a solvated electron pair.

Nevertheless, there is the possibility for an alternative relaxation pathway potentially avoiding autoionization. For vertical excitation reaching the 2A state in a saddle point, geometry optimized structure of the 2A state reveal a cluster geometry energetically below the cationic ground state (see Fig. 7.4.3). In this minimum energy structure of the 2A state, a solvated electron pair conceptually forms a σ -bond between an ammonia dimer cation $(\text{NH}_3)_2^+$ and a sodium cation solvated by a few ammonia molecules $\text{Na}(\text{NH}_3)_{n-2}^+$ (see Fig. 7.5.5). In this relaxed geometry, the autoionization process described above is no longer possible because the cationic state lies energetically above the 2A state, as depicted in Fig. 7.4.3. Because the performed experiment is neither sensitive to the timescales of the autoionization process nor to any neutral reaction products, it remains unclear if any clusters undergo complete nuclear relaxation to reach the minimum structure of the 2A state. Furthermore, it remains unclear where along the nuclear relaxation pathway the ETMD process occurs. The shape of the ETMD electron signal could in principal be exploited to obtain information on where along the relaxation coordinate autoionization occurs. ETMD occurring close to the vertical geometry would create high kinetic energy electrons, close to the sharp direct ionization feature, whereas low kinetic energy electrons would be emitted by ETMD close to the conical intersection. This picture however neglects the possibility of the system to undergo ETMD to vibrationally excited cationic states, which would also lower the observed electron kinetic energies. These vibrationally hot cations are indeed favoured by the Franck-Condon overlap between vertically excited 2A state and the cationic ground state ${}^1x^+$.

Note that the computational results in Fig. 7.4.3 show the 2A state as a single sharp state. It is however important to keep in mind that the number of ammonia lone pair orbitals that can participate in this type of excitation is equal to the number of ammonia

molecules in a given cluster. This gives rise to a band of 2A state excitations with slightly different excitation energies. The saddle points of these 2A states at the vertical geometry ascertains furthermore a broad Franck-Condon region of low frequency vibrational modes that transforms the n discrete excitation energies to a potentially structured broad band. In summary this strongly relaxes the strict resonance conditions and allows efficient excitation of the 2A band over a wide photon energy range ~ 2.5 eV below the ionization energy. Inducing the removal of an electron from the ammonia lone pair orbital, which is characterised by a dominating autoionization photoelectron signal in the given photon energy range. Similar excitations are expected to be observed in photon energy ranges of 2.5 eV below the ionization energies corresponding to the other ammonia molecular orbitals.

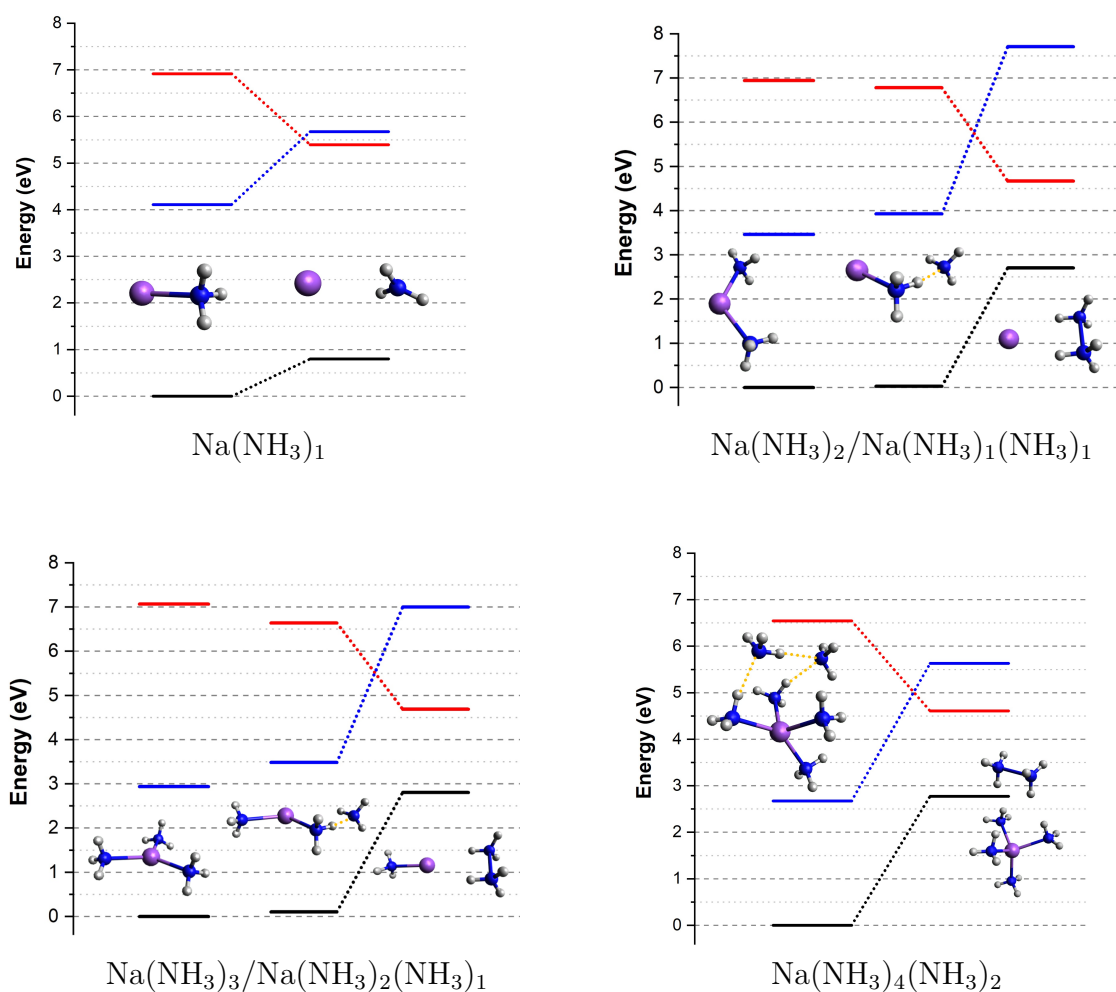


Fig. 7.4.3: Energy diagrams for selected $[\text{Na}, n\text{NH}_3]$ species with $n = 1, 2, 3, 6$. Black and red lines correspond to the 2X and 2A states of the neutral species, respectively, and blue lines pertain to ${}^1x^+$. The structures correspond to 2X (left) and 2A (rightmost) of the neutral species. The vertical excitation creates an electronically excited cluster at a saddle point on the potential energy surface.

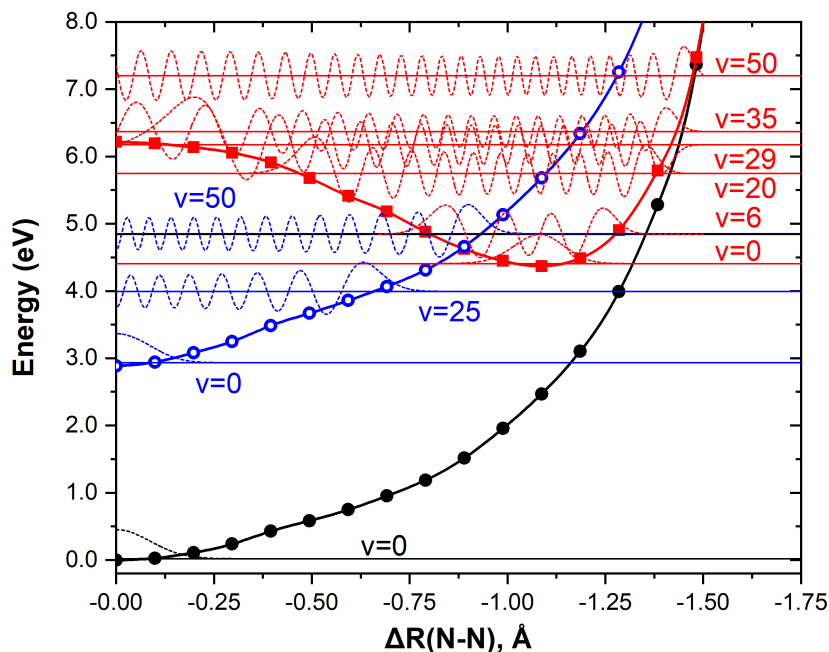


Fig. 7.4.4: Potential energy profile for the path from the geometry of 2X of $\text{Na}(\text{NH}_3)_4(\text{NH}_3)_2$ ($\Delta R = 0.0 \text{ \AA}$) to structure of the 2A state, $\Delta R = -1.1 \text{ \AA}$ (see Fig. 7.4.3). Selected vibrational levels and wavefunctions are included. The high vibrational density of states at the saddle point makes these transitions highly efficient. The excited state can relax toward a geometry best described as a ammonia dimer cation $(\text{NH}_3)_2^+$ bound by a solvated electron pair to a smaller sodium-doped ammonia cluster cation $\text{Na}(\text{NH}_3)_{n-2}^+$.

The non-local Coulombic decay processes, intermolecular (or interatomic) Coulombic decay (ICD) [187] and ETMD [188] have been first predicted theoretically before being observed experimentally [48, 189]. Until today, such processes have been observed in several sample systems, which in some aspects are comparable to the analogous process in sodium-doped ammonia clusters. Examples for these previous observations include the ETMD of alkali dimers and earth alkaline clusters attached to liquid helium nanodroplets [49, 50, 190, 191], and in aqueous solutions [192, 193]. Also in liquid bulk ammonia non-local Coulombic decay processes have been observed. Note that ICD processes can also have a substantial electron transfer contribution [194, 195]. Of these examples, the ETMD of alkali dimers attached to superfluid liquid helium droplets most closely resembles the ETMD process we described above. In these experiments and calculations, a helium droplet or atom is ionized, and in a subsequent ETMD process an electron from the σ -bonding orbital between the two covalently bound alkali atoms fills the $1s$ vacancy of the helium atom, while the second electron from the σ -bond is emitted. The fundamental difference from those previously reported ETMD processes is the delocalized nature of the solvated electron pairs undergoing ETMD in sodium ammonia clusters. These solvated electron pairs are not localized on one species as in the case of a covalently bound alkali dimer attached to an electrophobic helium droplet but delocalized over the complete system (see Fig. 7.4.2d).

This delocalization and the resulting orbital overlap between the solvated electron pair and the ammonia lone pair orbital make the electron transfer more of an electron localization process. This sudden localization, occurring when one of the solvated electrons relaxes to fill the ammonia lone pair vacancy resembles an Auger-Meitner decay. Although the ETMD process observed here requires only 6.2 eV of excitation energy. This low excitation energy is an additional major difference to previously described nonlocal Coulombic decay processes, which typically require significantly higher excitation energies to access inner valence or even core shells. The orbitals that are involved in the excitation of transient solvated dielectrons and their subsequent electron transfer mediated decay are the two highest occupied valence orbitals, as is described above. Sodium-doped clusters therefore promise to be a valuable model system to study ICD and ETMD processes at low excitation energies.

Fig. 7.4.5 shows the relative yield of ETMD as a function of the number of solvent molecules as well as for different photon energies. Only for clusters containing less than three ammonia molecules we observe a cluster size dependence. We assume that the observed cluster size dependence of the ETMD yield does not reflect a cluster size dependence of the ETMD process itself but is rather caused by the excitation cross section to the 2A state. For small clusters with a low number of ammonia lone pair orbitals contributing to the band of 2A states and reduced vibrational state density, the cross section becomes more dependent on the photon energy. Therefore, it is plausible that the used discrete narrow-band photon energies do not efficiently excite the 2A state for all small cluster sizes. For larger clusters, the band of possible 2A state excitations broadens considerably due to the increasing amounts of ammonia lone pair orbitals and a higher vibrational density of states. The data in Fig. 7.4.5 neither show a significant cluster size dependence of the excitation cross section of the 2A state nor for the ETMD efficiency. The cluster size independent ETMD signature suggests that similar excitations of solvated dielectrons may also be possible for larger clusters and sodium ammonia bulk solutions. Increasing numbers of solvation shells around the sodium counter ion will stabilize the cationic states, also in the geometry of the 2A state. We assume that the existence of the crossing between the cationic state and the solvated dielectron state affects the shape of the kinetic energy distribution of the ETMD electrons and the time scales of the process. It seems likely that ETMD will remain the dominant relaxation pathway of solvated electron pairs in the vicinity of an ammonia lone pair vacancy in large clusters and liquid bulk ammonia.

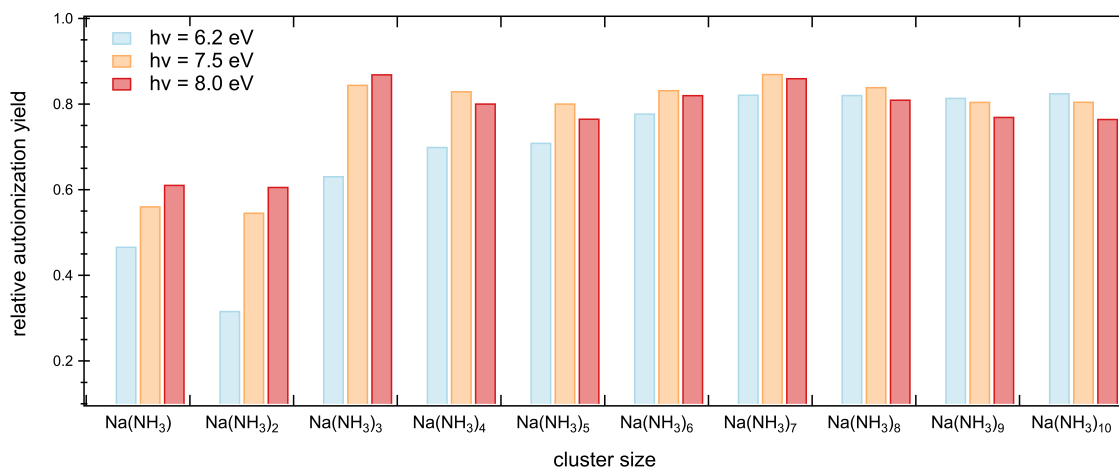


Fig. 7.4.5: Relative branching ratios for electron solvation mediated decay as a function of photon energy and cluster size.

Additional calculations for solvated electrons in pure anionic ammonia clusters $(\text{NH}_3)_n^-$ find very similar excited 2A states. Analogous to the ETMD of the 2A states in neutral sodium-doped clusters, the 2A states in anionic ammonia clusters can emit one electron to produce neutral ammonia clusters in their electronic ground state. This computational result raises the suspicion that the observed and calculated 2A state excitations of solvated dielectrons and their subsequent electron transfer mediated decay is a general feature of solvated electron systems. In the case of neutral ammonia clusters our calculations indicate that a single solvated electron can be excited with photon energies comparable to the 2A state excitation. This single solvated electron can however not undergo ETMD, but will eventually recombine with the ammonia lone pair vacancy. Further calculations for solvated electrons in sodium-doped and pure clusters of water and methanol confirm the assumption that the excitation of solvated dielectrons by electron transfer excitation from solvent molecules to an already existing solvated electron are likely to occur in all cluster or bulk systems hosting solvated electrons. The existing singly occupied electron solvation orbital thereby acts as an extended delocalized electron acceptor orbital, energetically lying just below the vacuum level. Electron transfer reactions from molecular orbitals of solute or solvent molecules to this electron solvation orbitals can be excited in a photon energy window located below each separate ionization threshold. The width of these windows is given by the binding energy of the solvated electron and can therefore differ for various solvent systems. In many bulk solvents, solvated electrons are not stable over long timescales, but can be excited as transient species and decay subsequently over various recombination processes. The orbital vacancy, created in the electron transfer excitations, is likely to destabilise the system which facilitates ETMD of the solvated electron pairs as a dominant decay channel, as soon as the 2A state excitation energy is higher than the binding energy of the solvated electron. The electron kinetic energy distributions measured in the scope of this work for small sodium-doped clusters have a maximum near zero kinetic energy. ETMD provides a pathway for solvated electrons with close to zero kinetic energy to gain momentum and travel through the solvent before becoming

solvated again or recombining. This UV light-induced-ETMD process is a simple way to generate high yields of dielectrons and detect them even in the presence of single solvated electrons. Processes like ICD and ETMD have been discussed as possible sources of low kinetic energy electrons that are of importance in radiation chemistry processes. In this perspective, the above described ETMD process offers a possibility to extend the distance these electrons can travel in a solvent and affect the electron kinetic energy distributions.

7.5 Supplementary Information

7.5.1 Time-of-flight mass spectra

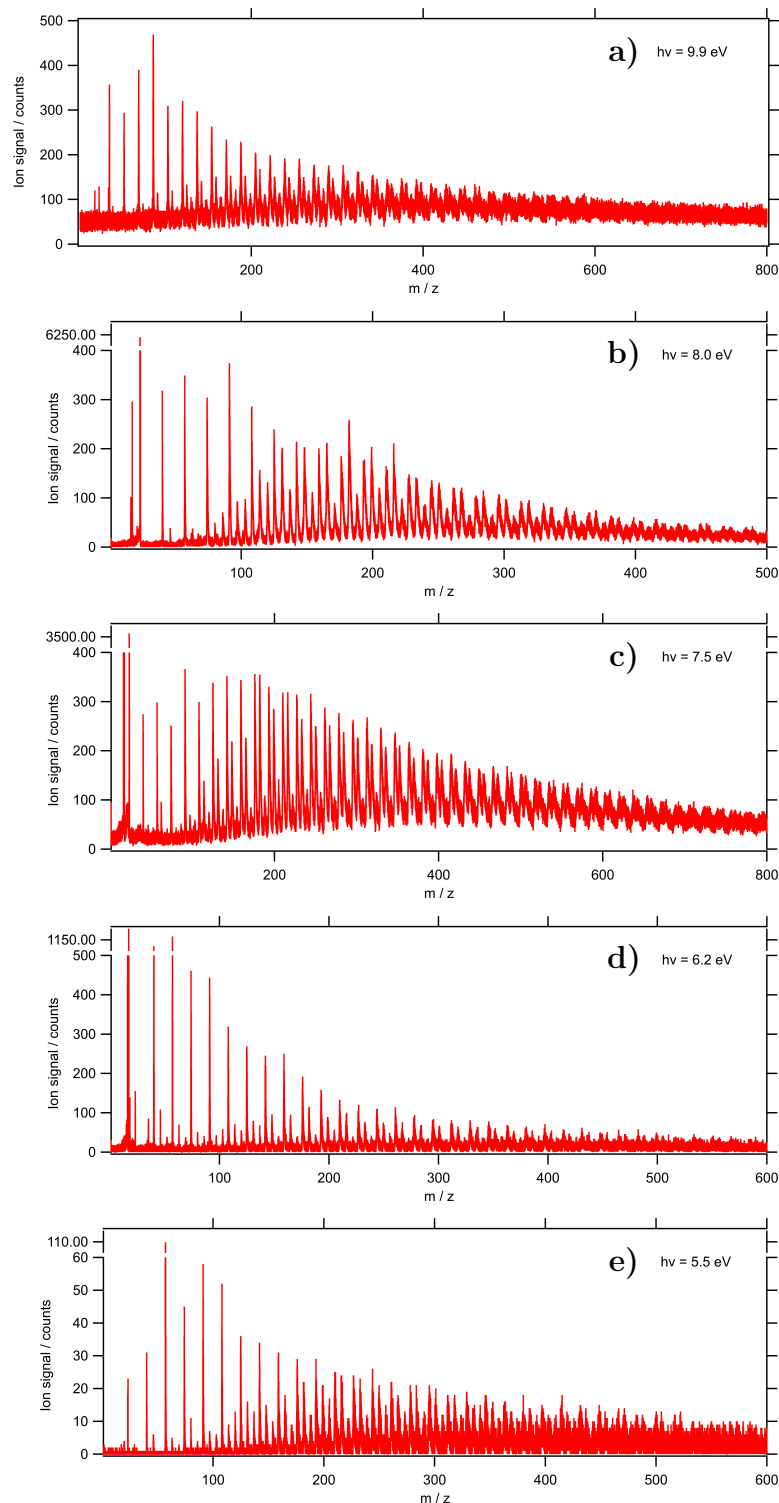


Fig. 7.5.1: Mass spectra of cluster size distributions detected at different photon energies (a-e). Differences between the size distributions are mainly due to different experimental conditions. The most intense peaks in the mass spectrum at 9.9 eV (a) are pure ammonia clusters, which are not detectable at lower photon energies. For mass spectra between 8.0 eV (b) and 5.5 eV (e) photon energy, the most intense peaks correspond to $\text{Na}(\text{NH}_3)_n$.

7.5.2 Electron binding energies and photoelectron spectra

Fig. 7.5.2-7.5.4 show all photoelectron spectra evaluated in the scope of this study. Black vertical lines indicate the electron binding energies for the smallest sodium-doped ammonia clusters determined in a previous study [2]. In the right panel of Fig. 7.5.2 we additionally indicate calculated electron binding energies at the highest level of theory applied for each cluster size. Multiple green vertical dashed lines for a single cluster size correspond to energetically higher lying conformers of the clusters. The most stable conformer for each cluster size shows the lowest electron binding energy, and the higher lying conformer contain less ammonia molecules coordinated to the ammonia (see Fig. 7.5.5). These measurements, calculations and previous measurements [2], show good agreement. The recorded spectra at 5.5 eV and 6.2 eV photon energy show slightly better resolution than the measurements at 7.5 eV and 8.0 eV photon energy due to the lower electron kinetic energies. The energy axis is calibrated relative to the binding energy of the bare sodium atom. The fact that the sodium peak appears at very low kinetic energies at 5.5 eV photon energy and is almost not detectable at 6.2 eV due to the Cooper minimum of sodium at this photon energy, makes the calibration less reliable. For 7.5 eV and 8.0 eV the combination of a more reliable energy calibration and a slight decreased resolution leads to binding energy peak positions equivalent to previously reported values.

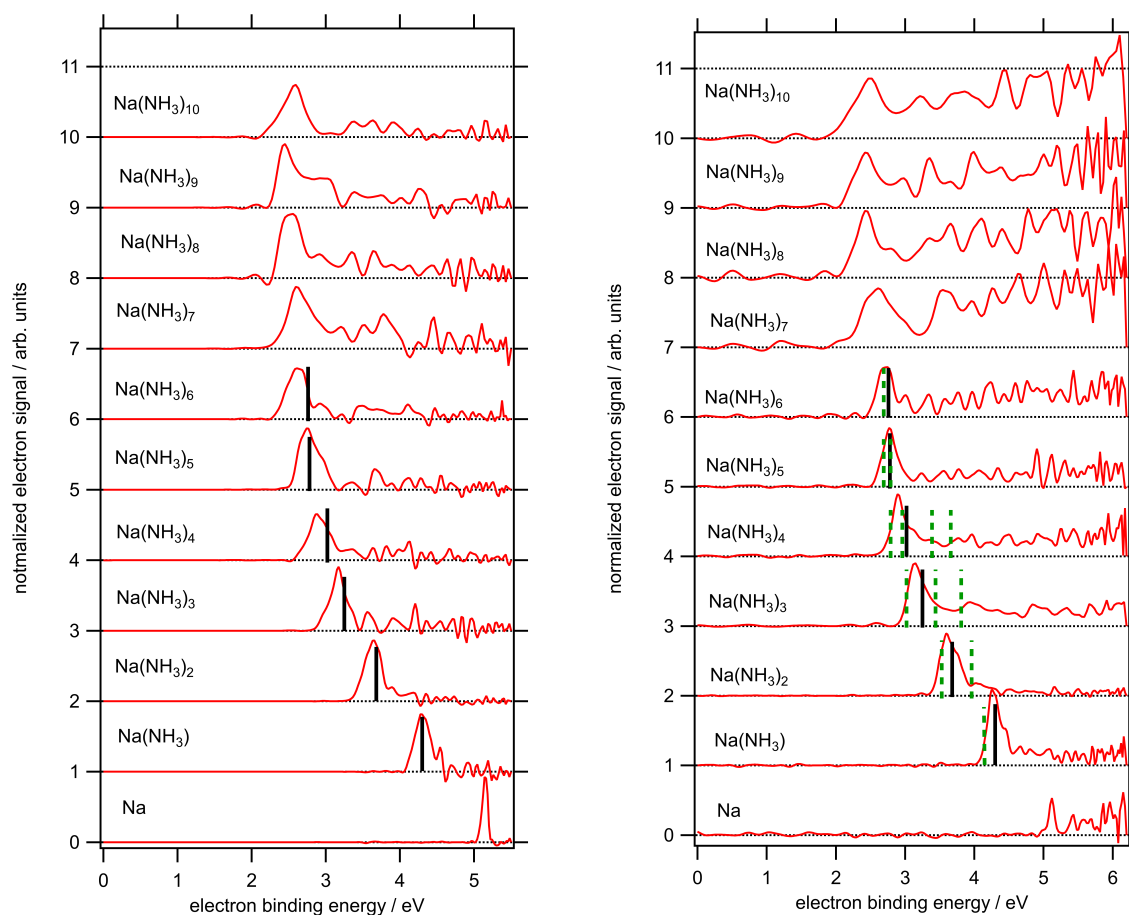


Fig. 7.5.2: Photoelectron spectra of ammonia clusters with $n = 0 - 10$ ammonia molecules doped with a single sodium atom. Data recorded at photon energies of 5.5 eV (left panel) and 6.2 eV (right panel). The black vertical lines indicate electron binding energies determined by West *et al.* [2]. Green dashed vertical lines indicate calculated electron binding energies from this work.

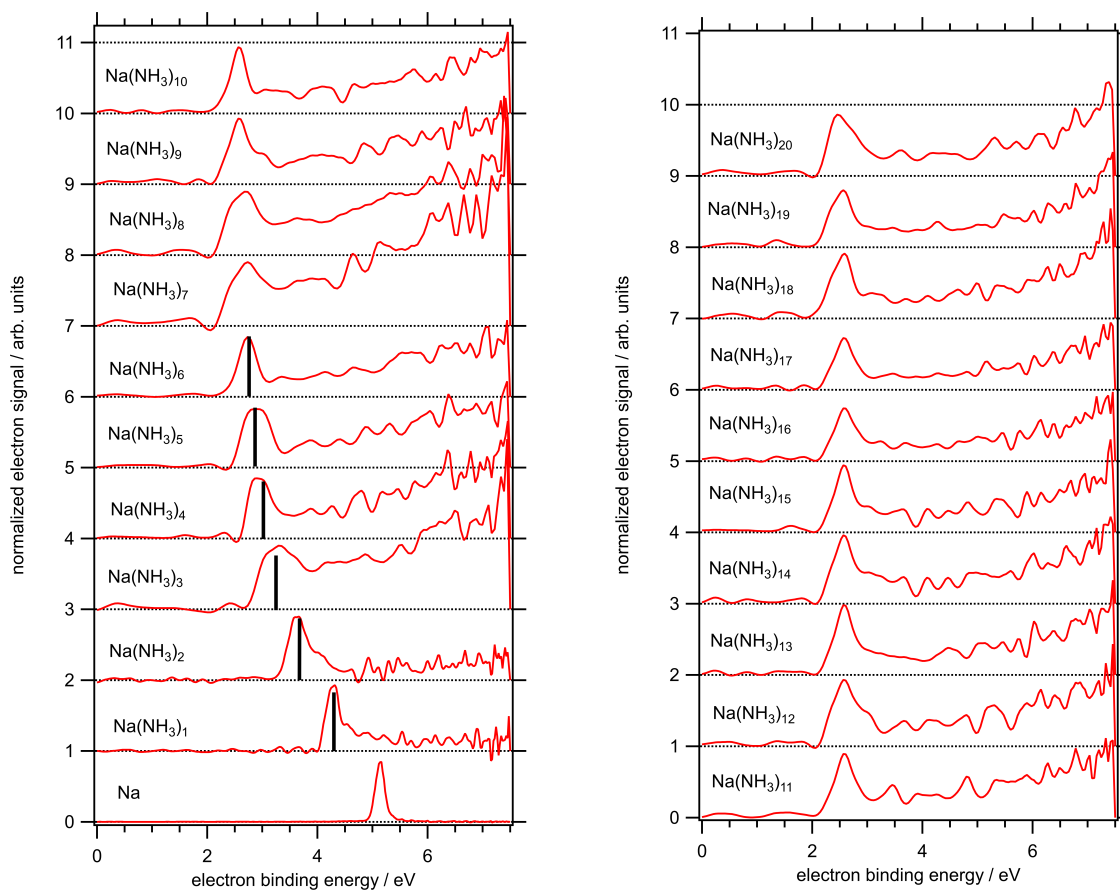


Fig. 7.5.3: Photoelectron spectra of ammonia clusters with $n = 0 - 10$ (left panel) and $n = 11 - 20$ (right panel) ammonia molecules doped with a single (red) sodium atom. Data recorded at 7.5 eV photon energy. The black vertical lines indicate electron binding energies determined by West *et al.* [2].

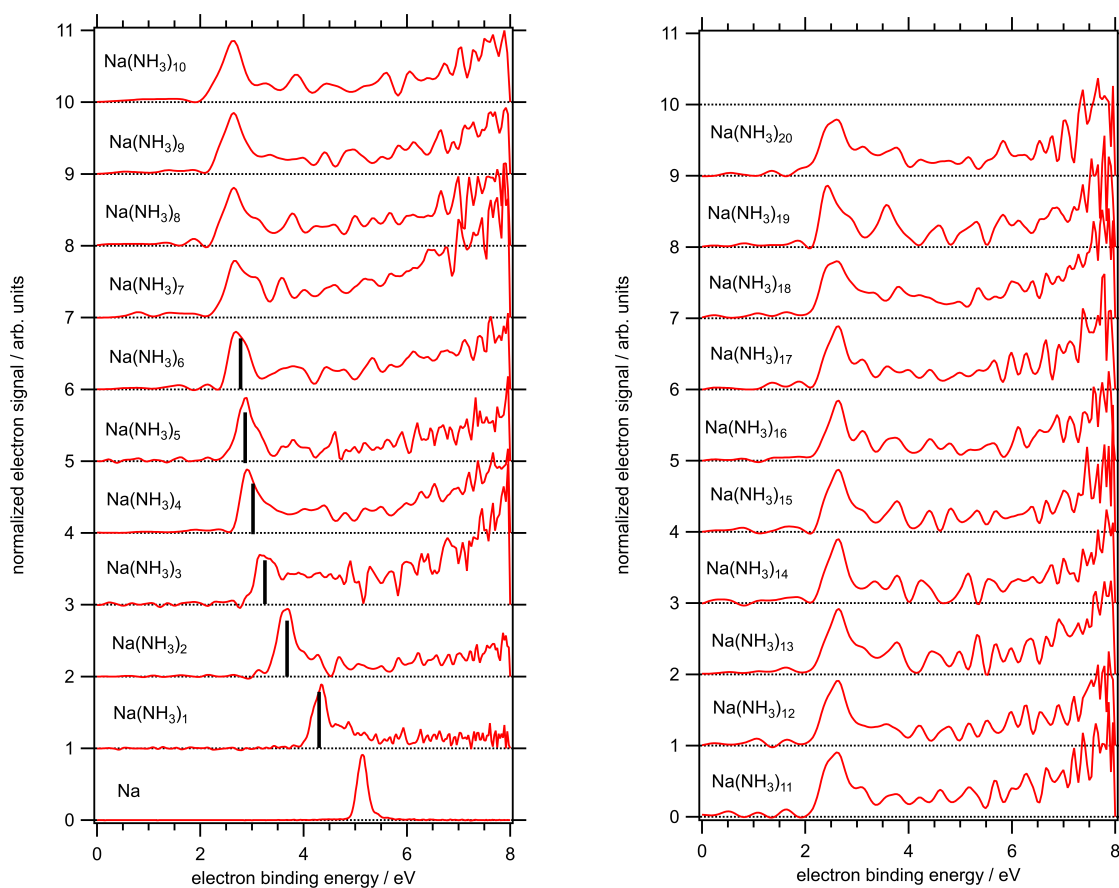


Fig. 7.5.4: Photoelectron spectra of ammonia clusters with $n = 0 - 10$ (left panel) and $n = 11 - 20$ (right panel) ammonia molecules doped with a single (red) sodium atom. Data recorded at 8.0 eV photon energy. The black vertical lines indicate electron binding energies determined by West *et al.* [2].

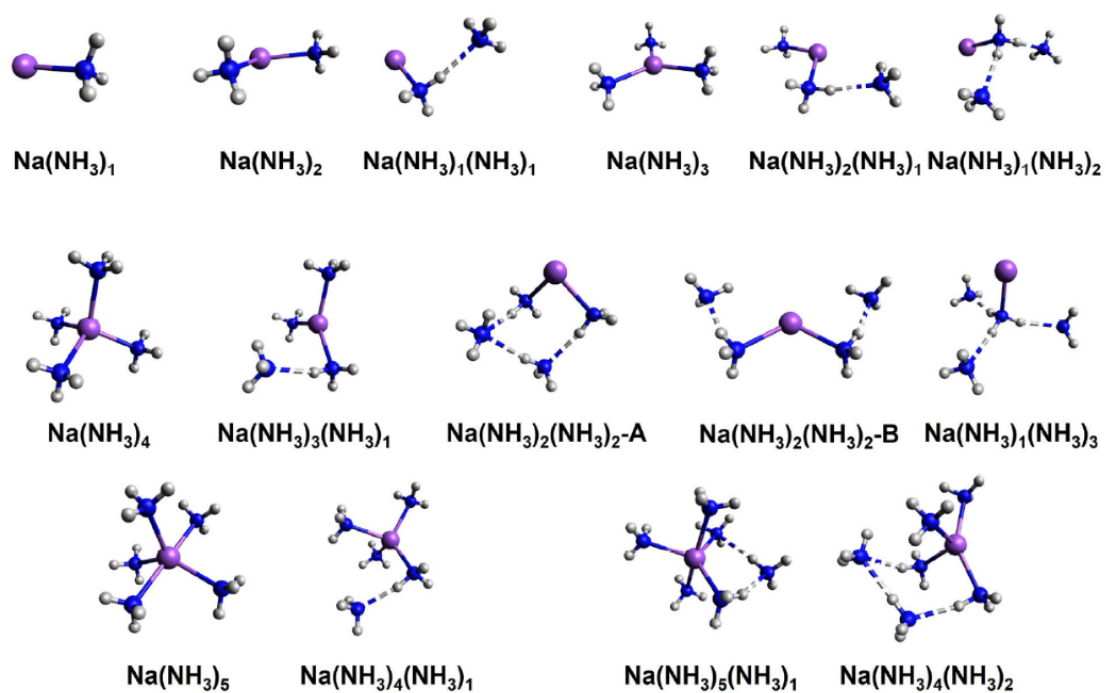


Fig. 7.5.5: All sodium-doped ammonia cluster conformers for which electron binding energies were calculated.

Chapter 8

Magic numbers for the photoelectron anisotropy in Li-doped dimethyl ether clusters

Results presented in this chapter have been previously published and are included in its entirety with minor modifications to the format of text, tables and figures.

Title: Magic numbers for the photoelectron anisotropy in Li-doped dimethyl ether clusters.

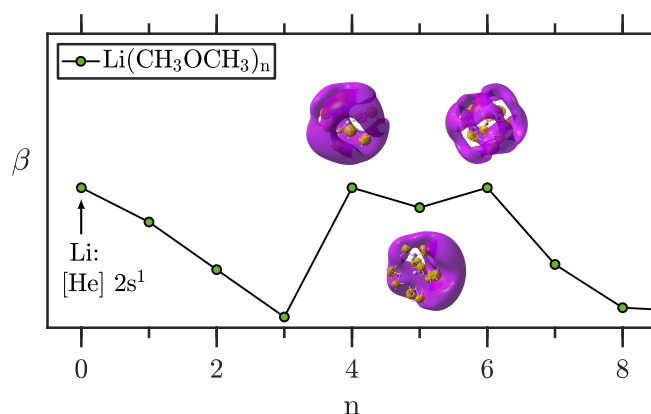
Authors: J. V. Barnes, B. L. Yoder and R. Signorell.

Citation: *J. Phys. Chem. A*, 2019, **123**, 2379.

Doi: 10.1021/acs.jpca.8b12262

Reprinted with the permission from *J. Phys. Chem. A*, 2019, **123**, 2379.

Copyright ©2019 American Chemical Society.



Abstract: Photoelectron velocity map imaging of $\text{Li}(\text{CH}_3\text{OCH}_3)_n$ clusters ($1 \leq n \leq 175$) is used to search for magic numbers related to the photoelectron anisotropy. Comparison with density functional calculations reveals magic numbers at $n = 4, 5,$ and 6 , resulting from the symmetric charge distribution with high s -character of the highest occupied molecular orbital. Since each of these three cluster sizes correspond to the completion of a

first coordination shell, they can be considered as “isomeric motifs of the first coordination shell”. Differences in the photoelectron anisotropy, the vertical ionization energies and the enthalpies of vaporization between $\text{Li}(\text{CH}_3\text{OCH}_3)_n$ and $\text{Na}(\text{CH}_3\text{OCH}_3)_n$ can be rationalized in terms of differences in their solvation shells, atomic ionization energies, polarizabilities, metal-oxygen bonds, ligand-ligand interactions and by cooperative effects.

8.1 Introduction

Magic numbers play a central role in cluster science (see, *e.g.*, references [196, 197, 198, 199, 200, 201, 202, 23, 5, 1, 24, 203]). Usually, these magic numbers are related to the high stability of clusters of certain sizes. By contrast, reports on magic numbers related to photoelectron anisotropy are comparatively sparse [1, 24, 52, 53]. This is because measurements of photoelectron angular distributions (PADs) of clusters are not so common and the modeling of cluster PADs is demanding [200, 1, 24, 52, 53, 204, 205, 34, 206, 207, 208, 26, 31, 30, 2, 41, 42, 43, 33, 44]. Typically, a prerequisite for the observation of magic numbers in the photoelectron anisotropy is a high cluster symmetry that results in orbitals with high fractional *s*-character [1, 52, 53, 2].

In our recent studies [1, 2], we reported the first observation of magic numbers in the photoelectron anisotropy of solvated electrons in Na-doped clusters of dimethyl ether, ammonia, methanol, and water. The studies have revealed that in clusters of high symmetry the solvated electron can delocalize over extended regions, forming symmetric charge distributions of high *s*-character. However, they have also shown that the direct experimental observation of magic clusters can be hindered by several factors. An important factor is the lack of size selection for the neutral clusters under investigation. This results in PADs that are averages of several cluster sizes, making the detection of magic numbers more difficult. Furthermore, many structural isomers with similar energies can occur in these weakly bound systems, again making the observation of magic numbers less likely compared with systems that exhibit fewer structural isomers. Our calculations showed that in particular the strong hydrogen bonds in the Na-doped methanol and water clusters result in a large number of isomers. In addition, these systems tend to prefer nonsymmetric structures with the Na core and the electron pushed to one side of the cluster to minimize the perturbation of the hydrogen bond network. Given these facts, it is thus not so surprising that the clearest experimental result for a magic number cluster was found for Na-doped dimethyl ether clusters, namely, for the hexamer $\text{Na}(\text{CH}_3\text{OCH}_3)_6$, which has near O_h symmetry with an octahedral coordination of Na by the CH_3OCH_3 molecules. The lack of strong hydrogen bonding in these clusters strongly reduced the number of isomers, and in addition the hexamer was also found to be a particularly stable structure; *i.e.*, it is also a magic number cluster with respect to stability. High level quantum chemical calculations for $\text{Na}(\text{CH}_3\text{OCH}_3)_n$ and $\text{Na}(\text{NH}_3)_n$ clusters by Gunina and Krylov [24] are in agreement with our previous experimental results [1, 2] and provide

a detailed understanding of the underlying phenomena regarding the character of the electronic structure and the influence of structural fluctuations on the electronic properties. The present study focuses on magic numbers in the photoelectron anisotropy of Li-doped dimethyl ether clusters ($\text{Li}(\text{CH}_3\text{OCH}_3)_n$). Many aspects of Li-doped molecular clusters have been investigated in detail (see references [5, 209, 210, 211, 212, 213, 214, 215] and references therein) but to the best of our knowledge no angle-resolved photoelectron spectra have been reported so far. Li is smaller and less polarizable than Na, which, for example, lets one expect that the almost perfect O_h symmetry with octahedral coordination of the Na core in $\text{Na}(\text{CH}_3\text{OCH}_3)_6$ might be distorted in the Li-doped hexamer so that the magic number cluster might shift to another cluster size than the hexamer. The goal of the present work is to unravel how the substitution of the alkali metal in dimethyl ether clusters influences the energetics, structure, and magic numbers by a combination of experimental data and density functional theory (DFT) calculations.

8.2 Experiment

The experimental setup, the measurement procedures, and the data analysis are essentially identical to those used in our previous investigations of $\text{Na}(\text{CH}_3\text{OCH}_3)_n$ clusters [1, 2]. For convenience, we repeat here the main aspects as provided in the experimental part of West *et al.* [1] The experimental setup has been previously described in detail [26, 31, 30, 2, 25, 40, 97].

All measurements were performed in a velocity map imaging (VMI) [216, 82] photoelectron spectrometer, which can also function as a time-of-flight mass spectrometer. $(\text{CH}_3\text{OCH}_3)_n$ solvent clusters were generated by pulsed supersonic expansion of a $\text{He}/\text{CH}_3\text{OCH}_3$ gas mixture into vacuum. The solvent cluster size was varied from one molecule up to a maximum of approximately 175 molecules per cluster by varying the expansion conditions (backing pressure, gas composition, pressure, nozzle temperature) and oven temperature. The solvent clusters were doped with a single Li atom in a Li-oven, which was heated to a temperature of 650 K. The resulting $\text{Li}(\text{CH}_3\text{OCH}_3)_n$ clusters were ionized with a 266 nm pulse from an Nd:YAG laser (photon energy of 4.66 eV), which exclusively ionized the unpaired (solvated) electron. The cluster size distributions were determined by mass spectrometry, which through the cluster mass provides information on the number of solvent molecules n per cluster [26, 2, 25]. For small clusters ($n \leq 4$) we use the actual number of molecules n to assign a cluster size, while the cluster size distributions for large clusters are characterized by the average cluster size $\langle n \rangle$ (and sometimes in addition by the maximum cluster size n_{max}). As exemplified by the relatively high intensity of the $\text{Na}(\text{CH}_3\text{OCH}_3)_6$ mass peak in Fig. 2f of West *et al.* [1], relative intensities of clusters of different sizes in mass spectra can provide information on cluster stability (magic numbers related to cluster stability).

Information on cluster-size-dependent photoelectron angular distributions (PAD) and

photoelectron kinetic energies are retrieved from the photoelectron velocity map images after reconstruction with MEVIR [100] (note that reconstruction with pBASEX [99] provides very similar results). Experimental electron binding energy (eBE) spectra are determined from the difference between the photon energy (4.66 eV) and the recorded photoelectron kinetic energy spectrum. The experimental ionization energies IE_{\max} for different cluster sizes are determined at the maxima of the photoelectron bands using Gaussian/Lorentzian fits. It is generally assumed that the IE_{\max} lie close to the values for the calculated vertical ionization energies IE_{vert} (section 8.4). We characterize the PAD by the anisotropy parameter β [32],

$$\frac{d\sigma}{d\omega} = \frac{\sigma_{\text{tot}}}{4\pi} \left[1 + \frac{\beta}{2} (3 \cos^2 \theta - 1) \right] \quad (8.2.1)$$

$d\sigma/d\omega$ and σ_{tot} are the differential and the total photoionization cross section, respectively, and θ is the angle between the photoelectron velocity vector and the polarization axis of the incident light. The indicated experimental cluster size-dependent β -parameters are determined from an average over 11 pixels, including 5 pixels on each side of the peak maximum in the eBE spectra. As in our previous study [1], we estimate the relative uncertainty of IE_{\max} and β as a function of cluster size to be on the order of 5% in both cases. The absolute uncertainties in IE_{\max} and β are on the order of ± 0.1 eV and ± 0.1 , respectively.

8.3 DFT Calculations

The experimental results are compared with various quantities (β -parameters, vertical ionization energies IE_{vert} , enthalpies of vaporization H_{vap} , and dipole moments) obtained from calculations with the Gaussian program package [162] using the dispersion corrected ω B97XD density functional with a 6-31+G* basis set. The calculations are analogous to those for Na(CH₃OCH₃)_n clusters [1, 2], the most important aspects of which we repeat here for convenience. H_{vap} is calculated for the neutral clusters as the total dissociation energy divided by the number of solvent monomer units. It is used here to compare cluster stabilities for different cluster sizes. The calculated total dipole moment of the different neutral clusters is used as a simple but very sensitive measure of the displacement of the charge distribution. IE_{vert} are compared with the experimental IE_{\max} . IE_{vert} are obtained by subtracting the energy of the neutral cluster from the energy of the ionic cluster with the same geometry. The calculated β -parameters are determined as previously explained in detail [1] and in the Supporting Information of West *et al.* [2]. Briefly, the highest occupied molecular orbital (HOMO) is expanded in terms of atomic natural orbitals (ANOs) [217]. In order to account for the polarization of the HOMO upon solvation, we use an expanded valence shell including $2p$ functions on Li for the ANO analysis (NBO program version 3.1). The normalized angular momentum (l) character c_l^2 of the HOMO is calculated as

the sum over ANO contributions of the same l . The β -parameters are then obtained from [34]

$$\beta = \sum_l c_l^2 \beta_l \quad (8.3.1)$$

with β_l determined from the Cooper-Zare formula [32],

$$\beta_l = \frac{l(l-1)(1-R)^2 + (l+1)(l+2)R^2 - 6l(l+1)(1-R)R}{(2l+1)[l(1-R)^2 + (l+1)R^2]} \quad (8.3.2)$$

R is the relative radial dipole matrix element of the $(l+1)$ partial wave. We neglect the phase shift between outgoing partial waves. Furthermore, we provide here the results for $R = 0.5$ and for radial matrix elements that vanish at all centers except at the Li atom. We have previously shown for Na-doped clusters that the size dependence of β (not the actual values) is almost independent of the choice of the parameters (*i.e.*, other limiting cases for R and for radial matrix elements for all atomic centers) [2]. In Li-doped and Na-doped clusters, the unpaired electron largely retains the character of the Li and Na valence electron, respectively. The above-mentioned robustness with respect to the model parameters derives from precisely this special property of the unpaired electron in the clusters, and enables us to derive meaningful results from the simple approach in equation 8.3.1 and 8.3.2. Note that trends in the size dependence of calculated and experimental β -parameters can be compared, even though their actual values cannot.

8.4 Results for Li(CH₃OCH₃)_n clusters

As an example, Fig. 8.4.1 shows a photoelectron image for small Li(CH₃OCH₃)_n clusters with $n \leq 4$ together with the corresponding energy dependent β -trace (full black line) and the photoelectron spectrum (dotted red line) as a function of the eBE. For these small clusters, the different rings in the image, the different bands in the energy dependent β -trace, and the resolved bands in the photoelectron spectrum can be assigned to specific cluster sizes.

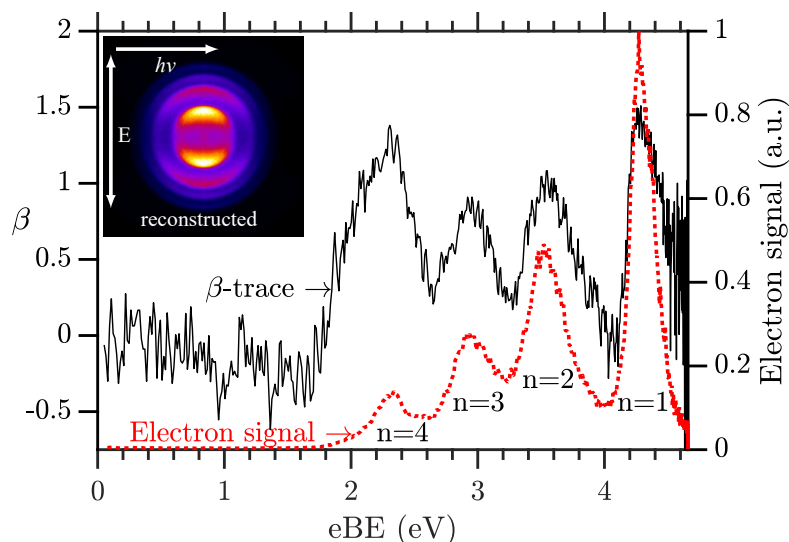


Fig. 8.4.1: Inset: reconstructed photoelectron images of $\text{Li}(\text{CH}_3\text{OCH}_3)_n$ clusters with $n = 1 - 4$ solvent molecules. Full black line: β -trace as a function of the electron binding energy (eBE). Dotted red line: Photoelectron spectrum as a function of eBE.

The image and the β -trace show that the PAD remains clearly anisotropic (large values of the β -parameters at the band maxima), while the photoelectron spectrum reveals a very strong decrease in IE_{max} by around 2 eV with increasing cluster size from $n = 1$ to $n = 4$. For Li-doped clusters, truly size-resolved data could only be obtained up to $n = 4$. As shown in Fig. 8.4.2a, the photoelectron bands of larger clusters lie too close in energy to resolve specific cluster sizes. We thus assign an average cluster size $\langle n \rangle$ to these merged bands (see bands for $\langle n \rangle = 20$ and $\langle n \rangle = 63$ in Fig. 8.4.2a). Parts b and c of Fig. 8.4.2 show representative mass spectra for the cases $n = 1 - 4$ and $\langle n \rangle = 63$, respectively. The decrease in IE_{max} with increasing cluster size is systematic but rather moderate beyond $n = 4$ (see Fig. 8.4.3g and 8.5.1b and Tab. 8.7.1 in the supplementary information 8.7). The evolution of the β -parameter with increasing cluster size is more complicated. Its value strongly decreases from $\beta = 1.4$ to $\beta = 0.8$ between $n = 1$ and $n = 3$, to peak again at $n = 4$ with a value of $\beta = 1.3$. Beyond $n = 4$ we lose cluster size resolved information. However, the fact that β stays fairly high up to $\langle n \rangle = 20$ (see Fig. 8.4.3e and 8.5.1c and Tab. 8.7.1 in the supplementary information 8.7) implies that several clusters with sizes larger than $n = 4$ must also have fairly high β -parameters. At first sight, this result appears rather surprising.

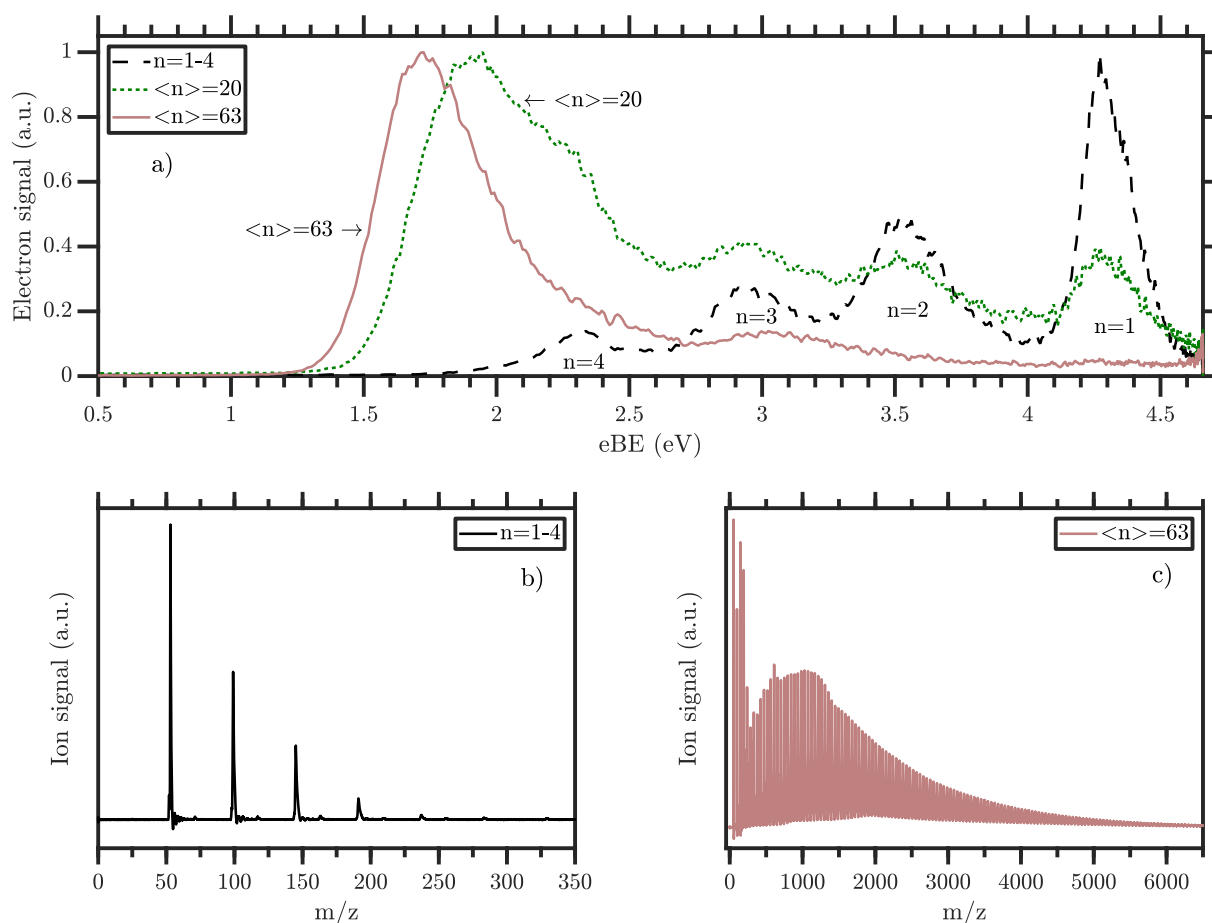


Fig. 8.4.2: (a) Photoelectron spectra of $\text{Li}(\text{CH}_3\text{OCH}_3)_n$ clusters as a function of eBE. Dashed black line: $n = 1 - 4$. Dotted green line: $\langle n \rangle = 20$. Full red line: $\langle n \rangle = 63$. (b) Mass spectrum for $n = 1 - 4$. (c) Mass spectrum for $\langle n \rangle = 63$.

To better understand this behavior, we have performed DFT calculations to obtain structures and β -parameters for clusters with up to 20 molecules (see Fig. 8.4.3 and Tab. 8.7.2 in the supplementary information 8.7). The calculated β -parameter of 2 in Fig. 8.4.3a and the isosurface of the HOMO in Fig. 8.5.2a clearly reveal the tetramer $\text{Li}(\text{CH}_3\text{OCH}_3)_4$ as a magic cluster with respect to the photoelectron anisotropy consistent with the experiment (Fig. 8.4.3e). This cluster has a highly symmetric structure with a tetrahedral coordination of the Li core by the ligands and a symmetric HOMO that is delocalized over an almost spherical shell around the cluster (Fig. 8.5.2a). As a result, this HOMO has a very high s -character (100% in the calculation), which explains the high β value. The high symmetry is also reflected in the very low dipole moment (Fig. 8.4.3d). However, H_{vap} in Fig. 8.4.3b shows that $\text{Li}(\text{CH}_3\text{OCH}_3)_4$ is not particularly stable compared with the neighboring clusters of different sizes; *i.e.*, it is not a magic cluster with respect to the stability. This is consistent with the experimental mass spectra, in which the mass signal does not peak at $n = 4$ (see example in Fig. 8.4.2c and 8.4.3f). In the case of sodium clusters we had observed a rather different behavior, with the Na-hexamer $\text{Na}(\text{CH}_3\text{OCH}_3)_6$ as a magic cluster with respect to both stability and anisotropy (see Fig. 2b, f in West *et al.* [1]). This difference between Li and Na can be rationalized by the

balance between the electronic stabilization afforded by the metal-oxygen “bonds” on one hand and the steric destabilization due to crowding of ligands on the other hand. In small Na-clusters the former dominates, while the latter gains importance in Li-clusters as a result of the much smaller atomic radius and hence shorter metal-oxygen bond (see further below and section 8.5). $\text{Li}(\text{CH}_3\text{OCH}_3)_4$ shows a highly symmetric coordination with an almost perfect LiO_4 tetrahedron. The T_d symmetry is necessarily broken by the C_2 symmetry of the ligands resulting in a number of symmetry equivalent minima. At the $\omega\text{B97XD}/6\text{-}31\text{+G}^*$ level the rotation angles around the C_3 -axes of the LiO_4 tetrahedron are virtually all equal, resulting in a highly symmetric HOMO. As a result, the dipole moment almost vanishes and β reaches its maximum value of 2. At higher levels of electronic theory the symmetry of the equilibrium structure might be further broken, resulting in the localization of the unpaired electron at one side of the (approximate) tetrahedron, a correspondingly large dipole moment, and a reduction of the calculated β . Nevertheless, one would still expect to observe tetrahedral symmetry of the HOMO in the experiment. This is a consequence of the inverse Born-Oppenheimer (or sudden) character of the unpaired electron’s wave function: very small nuclear displacements lead to a large change in the electronic wave function. Effectively, the unpaired electron will “see” a vibrationally averaged structure of the cluster. As long as the barrier between symmetry-equivalent minima remains small (as expected for small rotation angles around the C_3 -axes of the LiO_4 tetrahedron), the vibrationally averaged structure will remain tetrahedral.

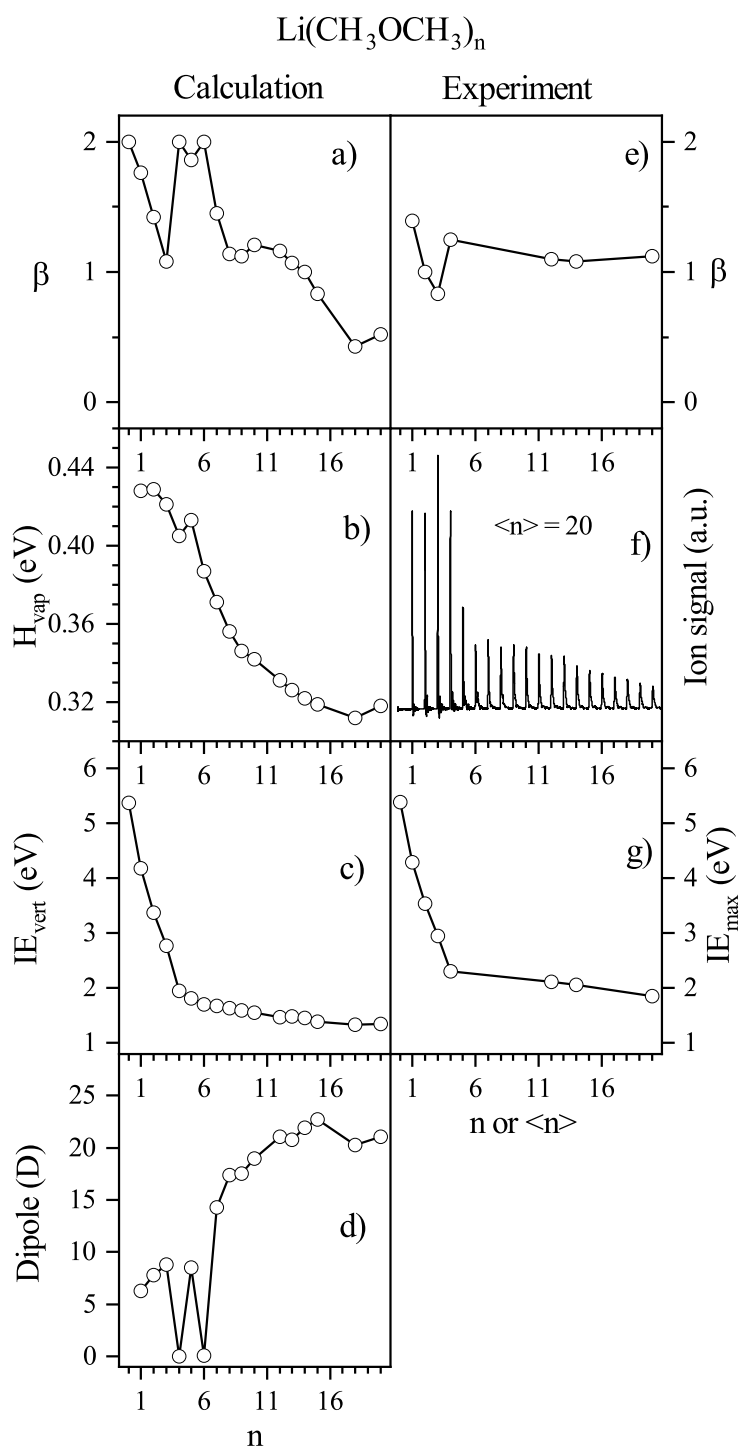


Fig. 8.4.3: Properties of $\text{Li}(\text{CH}_3\text{OCH}_3)_n$ clusters as a function of the number of solvent molecules n : (a) calculated β -parameters, (b) calculated enthalpies of vaporization H_{vap} , (c) calculated vertical ionization energies IE_{vert} , (d) calculated dipole moments, (e) experimental β -parameters, (f) representative mass spectrum for $\langle n \rangle = 20$, and (g) experimental ionization energies determined at the maximum of the photoelectron bands IE_{max} . For the calculations, the open circles connected by lines are the values for the energetically lowest isomers. For other isomers see Tab. 8.7.2 in the supplementary information.

The next two larger cluster sizes, $\text{Li}(\text{CH}_3\text{OCH}_3)_5$ and $\text{Li}(\text{CH}_3\text{OCH}_3)_6$, have similarly high

β -parameters as the tetramer (Fig. 8.4.3a). This is rather surprising and different from the Na case in West *et al.* [1]. However, it supports our hypothesis that several clusters with sizes larger than $n = 4$ and high β -parameters are the reason for the experimentally observed trend of high β -values even up to $\langle n \rangle = 20$ (Fig. 8.4.3e) because the contribution of the highly symmetric smaller cluster is high in the corresponding size distributions. The most stable pentamer has a trigonal-bipyramidal structure (Fig. 8.5.2b) and the most stable hexamer has an octahedral structure (Fig. 8.5.2c). To make space for the additional ligands in the expanded solvation shell, the Li–O distance increases. This weakening of the Li–O “bond” reduces H_{vap} . In the case of the pentamer, an axial distortion of the trigonal-bipyramidal structure counteracts this effect by reducing the unfavorable steric interaction between the ligands, so that overall H_{vap} even slightly increases compared with that for the tetramer (but still lies below that of the trimer). The crowding of ligands leads to an additional symmetry breaking in terms of the rotational angles of the three equatorial ligands around the Li–O “bonds”. The ensuing localization of the unpaired electron on one side of the pyramid is reflected in the sizable dipole moment. The dominant s -character of the HOMO (95%) is much less affected by this localization with a correspondingly small reduction of the β value. In the hexamer cluster the further lengthening of the Li–O distance is the dominant effect, such that H_{vap} decreases significantly. The octahedral structure remains intact with a highly symmetric HOMO (100% s -character) and correspondingly vanishing dipole moment and maximal β value. All these clusters correspond to the completion of a first coordination shell, so that they can be considered as “isomeric motifs of the first coordination shell”. This explains their similar values for β and IE_{vert} and their relatively high stability (high values of H_{vap}). Tab. 8.7.2 in the supplementary information 8.7 also lists data for a few isomers for $n = 5$ and 6. Isomer a of the pentamer has a tetrahedral first ligand shell with one additional molecule added in the second shell. Its β value of 1.49 is significantly lower than that for the most stable isomer because of the lower symmetry. Similarly, isomers of the hexamer with a symmetric first ligand shell and additional molecules placed in the second shell also have low β values (isomer b with a first tetrahedral shell $\beta = 1.34$ and isomer a with a first bipyramidal ligand shell $\beta = 1.44$; see Tab. 8.7.2).

The PADs of even larger clusters are still anisotropic but with β values clearly below those of $n = 4, 5,$ and 6 (Fig. 8.5.1a). These clusters are less symmetric than the smaller ones with correspondingly lower β values and larger dipoles. The less symmetric structures, typically with the Li and its electron pushed to one side of the cluster (see Fig. 8.7.1 in the supplementary information 8.7 for $n = 20$), allow the perturbation of the solvent molecules to be minimized, while keeping the unpaired electron close to the Li core and maximizing the strong favorable Li–O interactions in the first solvation shell. Tab. 8.7.2 in the supplementary information 8.7 lists the properties of some higher lying isomers. Among them are also highly symmetric isomers with high β values, such as isomer b for $n = 10$. For Li clusters, H_{vap} decreases almost continuously with increasing cluster

size (Fig. 8.4.3b). For very large clusters it has to converge to the calculated bulk value of pure (without Li) dimethyl ether of about 0.23 eV (experimental bulk value around 0.29 eV) [218]. For small clusters with one ligand shell (up to $n \sim 6$), H_{vap} is comparatively high because the strong Li–O bond dominates, partially counterbalanced by the steric interaction in the increasingly crowded ligand shell. With more ligands ($n \gtrsim 7$), the contribution of the Li–O bonds to H_{vap} is increasingly “diluted” by the much weaker ligand-ligand interaction in the outer shells and gradually converges to the bulk value. For IE_{vert} , pronounced changes are only observed until the completion of the first solvation shell at $n = 4$. The extension of the first shell in $n = 5$ and 6 retains a balance between the increase in the number of strong Li–O interactions and their weakening as a consequence of ligand crowding (bond lengthening). The further slow decrease of IE_{vert} beyond $n = 6$ can be attributed to increasing polarization effects (as the cluster’s polarizability increases with its size).

8.5 Comparison of $\text{Li}(\text{CH}_3\text{OCH}_3)_n$ and $\text{Na}(\text{CH}_3\text{OCH}_3)_n$ clusters

Fig. 8.5.1 provides a comparison of $\text{Li}(\text{CH}_3\text{OCH}_3)_n$ and $\text{Na}(\text{CH}_3\text{OCH}_3)_n$ cluster data. The behavior of H_{vap} for the Na-clusters differs pronouncedly from that of the Li-clusters (Fig. 8.5.1a). Small Na-clusters have a lower H_{vap} that increases with cluster size, while small Li-clusters have a higher H_{vap} that decreases with cluster size. The maxima for H_{vap} are reached at the hexamer of Na and at the monomer for Li. The generally lower H_{vap} for small Na-clusters can likely be attributed to the weaker Na–O bond compared with the Li–O bond. As mentioned in section 8.4, the decrease of H_{vap} is consistent with a weakening (*i.e.*, lengthening) of the Li–O bond because of the increased crowding of ligands in the first solvation shell. Given the much larger atomic radius of sodium, ligand crowding plays a less important (if any) role in small $\text{Na}(\text{CH}_3\text{OCH}_3)_n$ clusters. This would lead to the expectation of a roughly constant H_{vap} until the first solvation shell is complete at $n = 6$. The increase of H_{vap} observed instead points toward significant cooperative effects, possibly resulting in part from (weak) hydrogen bonding interactions between the ligands. For larger clusters ($n > 6$), H_{vap} decreases again, but more slowly than for Li-clusters. This is in part a trivial consequence of the smaller difference between the Na–O bond strength and the ligand-ligand interaction (the “dilution” per ligand added is less in Na- than in Li-clusters). Another contributing factor is the larger polarizability of the 3s unpaired electron of Na as compared with the polarizability of the 2s electron of Li. The former more easily deforms to adapt to its position on the cluster surface.

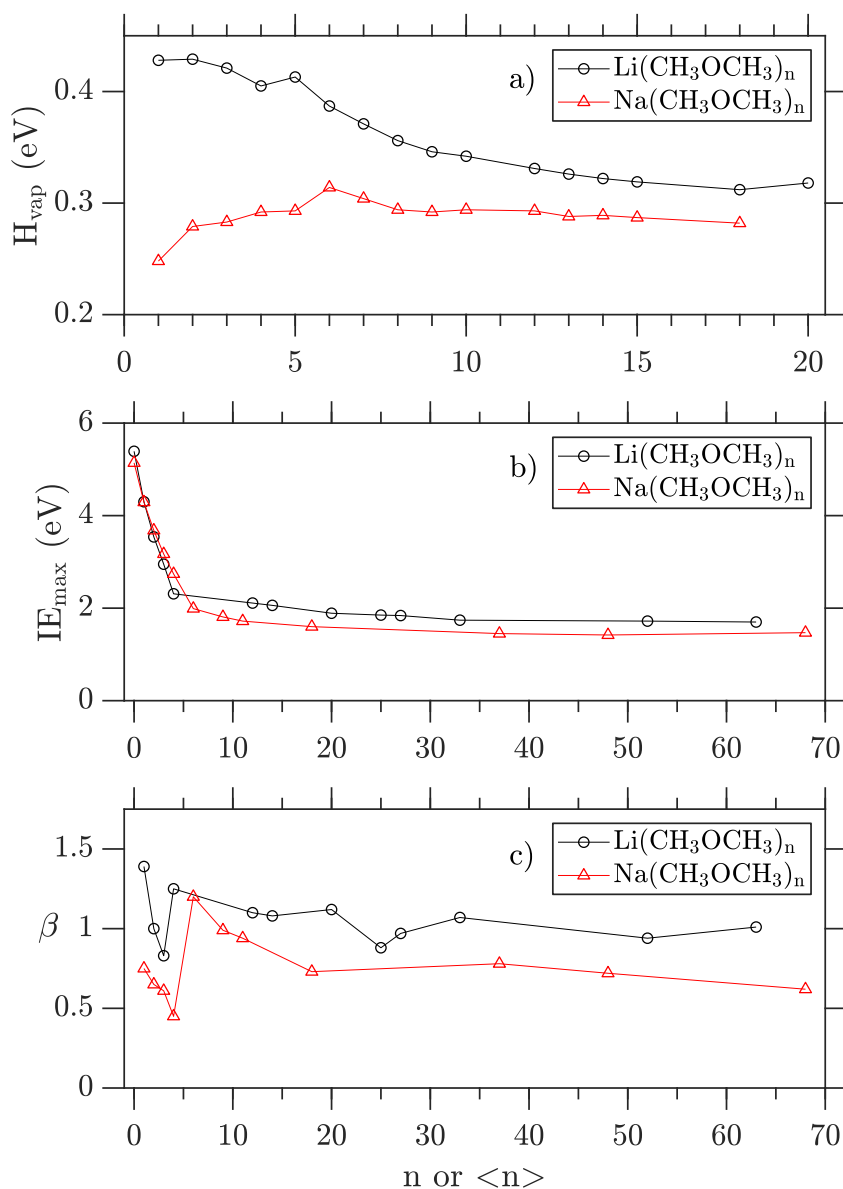


Fig. 8.5.1: Comparison of $\text{Li}(\text{CH}_3\text{OCH}_3)_n$ (open circles) and $\text{Na}(\text{CH}_3\text{OCH}_3)_n$ (open triangles) cluster data. (a) Calculated enthalpies of vaporization H_{vap} . (b) Experimental ionization energies IE_{max} . (c) Experimental β -parameters.

In contrast to the trends in H_{vap} , the trends in IE_{max} are qualitatively identical for Na- and Li-clusters (Fig. 8.5.1b). Strong decreases are only observed before the closure of the first solvation shells (at $n = 4$ for Li and $n = 6$ for Na), while for larger clusters the values of IE_{max} drop only very slowly as a result of the increasing overall polarizability of the cluster. For larger Li-clusters, the absolute values of IE_{max} observed experimentally lie systematically above those of the Na-clusters by about 0.3 eV. This difference approximately equals the difference between the ionization energies for atomic Na and Li (5.14 eV [219] and 5.39 eV [220] respectively). The unpaired (surface-solvated) electron in the cluster apparently still feels the core it belonged to. This is consistent with the results of our DFT calculations. As mentioned above, the most stable larger clusters tend to have the metal core and the electron located at one side of the cluster close to the surface. The electron is thus still close to the respective metal core, which might explain the conservation of the

shift between cluster and atomic metal.

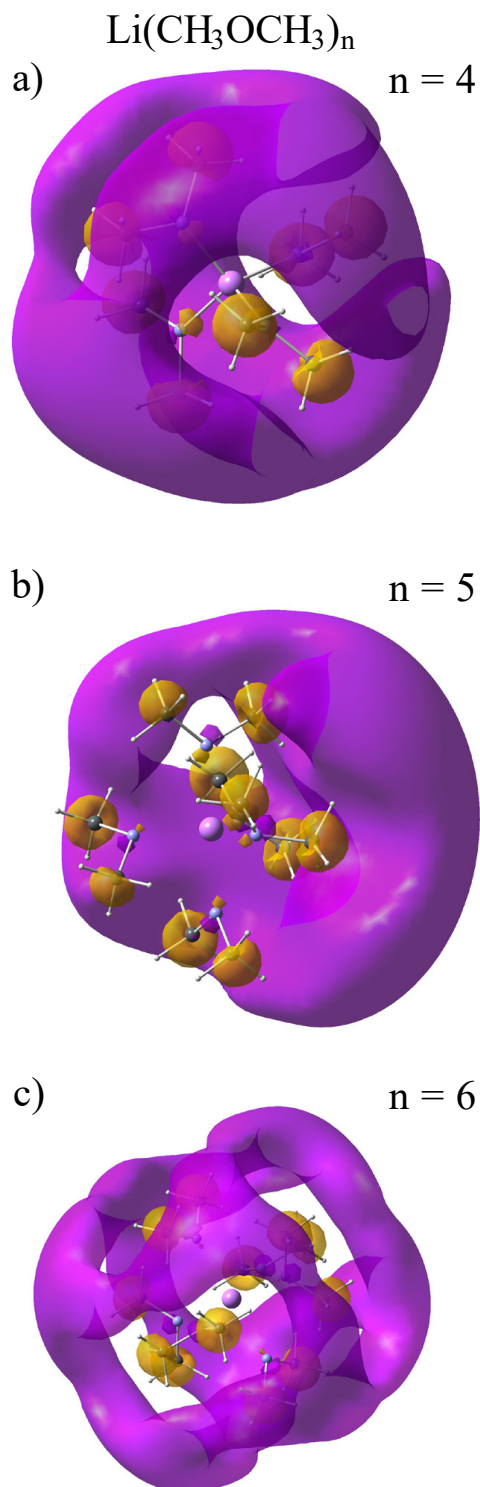


Fig. 8.5.2: Isosurfaces of the HOMO of the most stable isomers of (a) the $\text{Li}(\text{CH}_3\text{OCH}_3)_4$ cluster, (b) the $\text{Li}(\text{CH}_3\text{OCH}_3)_5$ cluster, and (c) the $\text{Li}(\text{CH}_3\text{OCH}_3)_6$ cluster. The calculated s -character of these HOMO are 100%, 95%, and 100%, respectively.

Finally, Fig. 8.5.1c compares the β -parameters for the two cases. The occurrence of magic clusters related to the anisotropy at $n = 6$ for Na-clusters and at $n = 4, 5,$ and 6 for

Li-clusters was already discussed in West *et al.* [1] and in section 8.4. Here, we additionally point out the general downshift of β of Na-clusters compared with results for Li-clusters observed experimentally for essentially all cluster sizes. This phenomenon is reproduced at least qualitatively by the DFT calculations. A lowering of β results from the polarization of the HOMO upon solvation, which gives rise to higher angular momentum components l (essentially $l = 1$) of the HOMO. A more polarizable atomic orbital is more easily distorted (polarized), *i.e.*, more easily acquires higher l components upon solvation of the atom. The lower β values of the Na clusters can thus be explained by the higher polarizability of the $3s$ electron compared with that of the $2s$ electron of Li.

8.6 Summary

This paper compares properties of neutral $\text{Li}(\text{CH}_3\text{OCH}_3)_n$ and $\text{Na}(\text{CH}_3\text{OCH}_3)_n$ clusters with a focus on magic numbers related to the photoelectron anisotropies from the highest occupied molecular orbital, *i.e.*, the solvated electron that can delocalize over extended cluster regions. In Li-doped clusters, magic numbers are observed at $n = 4, 5$, and 6 as a result of the completion of the first solvation shell. Such “isomeric motifs of the first coordination shell” were not observed for Na-doped clusters, which showed a distinct magic cluster at $n = 6$ [1]. The difference between the two alkali metals seems to arise from a balance between the electronic stabilization by the metal-oxygen bonds and the steric destabilization due to crowding of ligands. The general lowering of the β -parameters to around 0.25 for Na-clusters compared with those for Li-clusters for clusters with up to $\langle n \rangle \approx 70$ can be explained by the higher polarizability of the $3s$ compared with that of the $2s$ electron. Similarly, a general lowering of the ionization energy by approximately 0.3 eV of Na-clusters compared with results for Li-clusters is observed in the same cluster size range. It roughly matches the difference of the ionization energies of the two bare metals, which seems to be conserved in the molecular clusters. Both alkali metal clusters show a very pronounced decrease of the ionization energy by about 2 eV for small clusters before the closure of the first solvation shell. DFT calculations reveal a distinct difference between the behavior of the enthalpies of vaporization for the two metal clusters as a function of the cluster size, which can be rationalized by differences in the metal-oxygen bonds and the ligand-ligand interactions, in the polarizabilities of the $3s$ and $2s$ electrons, in the crowding of ligands, and by cooperative effects. Such cluster studies might also contribute to a better understanding of the properties of the solvated electron in the condensed phase [5, 8, 221, 222, 54, 223, 224, 225, 226, 227, 228, 229, 230].

8.7 Supplementary information

Tab. 8.7.1: Experimental Results of the reconstructed images using MEVIR. n , $\langle n \rangle$ and n_{\max} are the number of solvent molecules per cluster, the average number of solvent molecules per cluster and the maximum number of solvent molecules per cluster, respectively. IE_{\max} is the determined peak position for the individual cluster sizes in the photoelectron spectra and β the anisotropy parameter.

n	$\langle n \rangle$	n_{\max}	$IE_{\max}(\text{eV})$	β
0			5.39	-
1			4.30	1.39
2			3.54	1.00
3			2.95	0.83
4			2.31	1.25
	12	18	2.11	1.10
	14	21	2.06	1.08
	20	52	1.89	1.12
	25	63	1.85	0.88
	27	70	1.84	0.97
	33	83	1.74	1.07
	52	142	1.72	0.94
	63	175	1.70	1.01

Tab. 8.7.2: Results of the DFT calculations (ω B97XD/6-31+G*) using Gaussian 09. Enthalpies of vaporization H_{vap} , dipole moments, vertical ionization energies IE_{vert} , and β -parameters. The table has been divided into two sections in order to display it more effectively.

n	isomer	H_{vap} (eV)	dipole(D)	IE_{vert} (eV)	β
0		-	-	5.37	2.00
1		0.428	6.3	4.19	1.76
2		0.429	7.8	3.38	1.42
3		0.421	8.8	2.77	1.08
4		0.405	0.0	1.95	2.00
5		0.413	8.5	1.81	1.86
	a	0.384	13.1	1.82	1.49
6		0.387	0.1	1.70	2.00
	a	0.380	13.8	1.76	1.44
	b	0.365	15.5	1.72	1.34
7		0.371	14.3	1.68	1.45
	a	0.363	16.0	1.70	1.21
8		0.356	17.4	1.64	1.14
	a	0.353	15.9	1.62	1.29
9		0.346	17.5	1.60	1.12
	a	0.344	16.3	1.60	1.19

n = 2: bent.

n = 3: flat trigonal pyramid.

n = 4: tetrahedron.

n = 5: trigonal bipyramid. (a) n = 4 (tetrahedron) with one ligand added in the 2nd shell.

n = 6: octahedron. (a): n = 5 (trigonal bipyramid) with one ligand added in the 2nd shell.

(b) n = 4 (tetrahedron) with two ligands added in the 2nd shell.

n = 7: n = 6 (octahedron) with one ligands added in the 2nd shell. (a) n = 5 (trigonal bipyramid) with two ligands added in the 2nd shell.

n = 8: n = 5 (trigonal bipyramid) with three ligands added in the 2nd shell. (a) n = 6 (octahedron) with two ligands added in the 2nd shell.

n = 9: n = 5 (trigonal bipyramid) with four ligands added in the 2nd shell. (a) n = 6 (octahedron) with three ligands added in the 2nd shell.

Tab. 8.7.2 continued: Results of the DFT calculations (ω B97XD/6-31+G*) using Gaussian 09. Enthalpies of vaporization H_{vap} , dipole moments, vertical ionization energies IE_{vert} , and β -parameters. The table has been divided into two sections in order to display it more effectively.

n	isomer	H_{vap} (eV)	dipole(D)	IE_{vert} (eV)	β
10		0.342	17.5	1.60	1.12
	a	0.344	16.3	1.60	1.19
	b	0.344	16.3	1.60	1.19
12		0.331	21.1	1.47	1.16
	a	0.329	18.6	1.51	0.79
	b	0.322	19.2	1.49	0.91
	c	0.321	18.4	1.46	0.71
	d	0.318	18.0	1.47	0.68
	e	0.318	17.4	1.48	0.66
13		0.326	20.8	1.48	1.07
14		0.322	21.9	1.46	1.00
	a	0.318	15.0	1.50	0.77
	b	0.312	22.2	1.43	0.84
15		0.319	22.7	1.39	0.83
	a	0.318	21.1	1.45	0.90
	b	0.232	7.0	3.97	1.75
18		0.312	20.3	1.33	0.43
	a	0.308	18.5	1.38	0.38
20		0.318	21.1	1.35	0.52
	a	0.312	19.2	1.33	0.32

n = 10: n = 6 (octahedron) with four ligands added in the 2nd shell on one side (Li near the surface of the cluster). (a) similar to 10, but Li further away from the surface of the cluster. (b) n = 6 (octahedron) with four ligands distributed symmetrically in the 2nd shell (Li at the center of the cluster).

n = 12: n = 6 (octahedron) with six ligands added in the 2nd shell on one side (Li near the surface of the cluster). (a) similar to n = 12, but one ligand of the 2nd shell moved closer to the Li-side. (b) n = 10 with one ligand added on the far side and one on the near side of Li. (c) similar to n = 12b, but one ligand in the 2nd shell rearranged so that Li is more centered. (d, e) n = 10b with two ligands added in the 2nd shell, distorting the symmetry.

n = 14: n = 6 (octahedron) with eight ligands added in the 2nd and 3rd shell on one side (Li near the surface of the cluster). (a) similar to n = 12d, e with two more ligands added

in the 2nd shell, Li slightly off-center. (b) $n = 14$ with one ligand moved from the 2nd to the 3rd shell.

$n = 15$: $n = 6$ (octahedron) with nine ligands added in the 2nd and 3rd shell on one side (Li near the surface of the cluster). (a) similar to $n = 15$, but ligands in the outer shell rearranged to yield an overall flatter cluster. (b) crystalline slab (monolayer) with Li at one edge.

$n = 18$: $n = 6$ (octahedron) with twelve ligands added in the 2nd and 3rd shell to yield a compact slightly flattened cluster shape with an off center Li closer to one surface. (a) similar to $n = 18$, but more spherical in shape with Li closer to the center.

$n = 20$: $n = 18$ with two ligands added on the far side of Li. (a) $n = 18a$ with two ligands added, Li closer to the center.

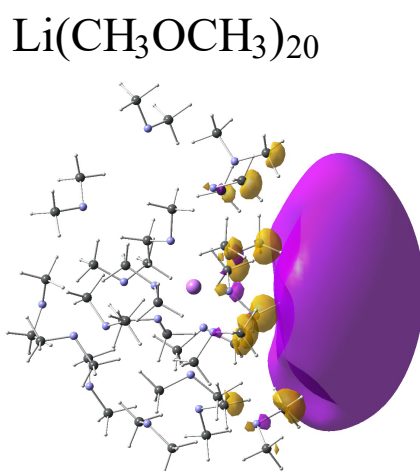


Fig. 8.7.1: Isosurface of the HOMO of the most stable isomer of the $\text{Li}(\text{CH}_3\text{OCH}_3)_{20}$ cluster.

Chapter 9

Conclusion & outlook

A pulsed Stern-Gerlach setup for the investigation of size-dependent magnetic properties of alkali-metal doped clusters has successfully been implemented into the existing velocity map imaging spectrometer (chapter 2). The performance of the deflector was characterised by the magnetic deflection of an effusive sodium atom beam as a free spin 1/2 system. The comparison to molecular dynamics simulations of the deflection process confirm the experimental performance and design. The combination of pulsed SG deflection and photoion velocity map imaging allows for the measurement of velocity dependent deflection data as a function of cluster size.

The presented SG deflection results for $\text{Na}(\text{NH}_3)_n$ ($n = 1 - 4$) (chapter 4 and published in [93]), as well as $\text{Na}(\text{H}_2\text{O})_n$ ($n = 1 - 4$), $\text{Na}(\text{MeOH})_n$ ($n = 1 - 4$) and $\text{Na}(\text{DME})_n$ ($n = 1 - 3$) (chapter 5) are first experimental studies on the magnetic properties in solvated electron precursor systems. It was observed that in general an increase in cluster size causes a significant reduction in deflection. NaNH_3 and NaH_2O in combination with molecular dynamics simulations, revealed $m_S = \pm 1/2$ deflection behaviour and for all other sampled clusters reduced deflection is observed. We thereby describe reduced deflection as an attenuation of the magnetic moment μ_0 of the free spin 1/2 systems, resulting in a characteristic cluster effective magnetic moment μ_{eff} . Effective magnetic moments are discussed in terms of thermally accessible cluster eigenstates, characterised by their total angular momentum \mathbf{J} . Each state \mathbf{J} state is in general terms composed of the orbital angular momentum \mathbf{L} , electron spin angular momentum \mathbf{S} , rotational angular momentum \mathbf{R} and nuclear spin angular momentum \mathbf{I} . Former angle-resolved photoelectron spectroscopy study of West *et. al* revealed high s -character of the highest occupied molecular orbital for the investigated solvated electron precursor systems. We expect minor contributions of the orbital angular momentum \mathbf{L} and furthermore neglect contributions of nuclear spins \mathbf{I} . In the case of sodium-doped clusters we suggest that the total angular momentum \mathbf{J} is primarily governed by \mathbf{S} and \mathbf{R} . Spin-rotational coupling leads to adiabatic Zeeman-like levels in the presence of a magnetic field. Within the avoided crossing model [68] it is assumed that a large number of thermally accessible Zeeman states leads to several spin flip processes, which on average causes reduced deflection. In addition,

the clusters Landé factor g_J is to be expressed for each populated J state via quantum chemical calculations. In the case of spin-rotational coupled systems g_J decreases towards higher J states [60] and subsequently leads to reduced average deflection. Describing the Zeeman levels with their corresponding Landé factor and possible avoided crossings between states of same total angular momentum, reflects the full Zeeman diagram and in principal contains the entire magnetic information. Experimentally observable magnetic properties can be attributed to the applied magnetic field and the thermal population of states. In our approach we discuss relative deflection trends due to differences of the Zeeman diagram governed by thermally populated rovibrational states. The comparison of populated rovibrational states at estimated vibrational $50 \text{ K} \leq T_{\text{vib}} \leq 200 \text{ K}$ and rotational $10 \text{ K} \leq T_{\text{rot}} \leq 50 \text{ K}$ temperatures confirms the observed deflections trends. We show that the deflection trend is dominated by the density of populated rotational states and suggest differences in rotational temperatures among the clusters systems, with proposed order being $T_{\text{rot}}(\text{Na}(\text{DME})_n) < T_{\text{rot}}(\text{Na}(\text{NH}_3)_n) < T_{\text{rot}}(\text{Na}(\text{MeOH})_n) < T_{\text{rot}}(\text{Na}(\text{H}_2\text{O})_n)$. We conclude that the magnetic deflection behaviour of sodium-doped clusters is dominated by the coupling of spin and rotational angular momentum, and further coupling interactions can be neglected in a first approximation. Although, additional theoretical and experimental work is to be carried out to support these suggestions. An important next step is to determine spin-rotational coupling elements via quantum chemical calculations, in order to evaluate the likelihood of diabatic crossings, as these may exhibit non-negligible differences for the sampled clusters. An experimentally promising approach is spatially resolving the deflected beam and comparing the results to molecular dynamics simulations with spin-rotational coupled cluster Landé factors. The comparison of experiment and model are likely to reveal if further angular momentum couplings show non-negligible contributions.

$\text{Li}(\text{DME})_n$ clusters ($1 \leq n \leq 175$) were studied via photoelectron velocity map imaging in order to search for magic numbers related to the photoelectron anisotropy from the highest occupied orbital (chapter 8 and published in [27]). In lithium-doped DME clusters magic numbers are found for $n = 4, 5$ and 6 which are said to be structural isomers of the first solvation shell. The high s -character of these structural isomers is reflected by an orbital angular momentum close to zero. Similar to sodium-doped clusters, one can expect that \mathbf{J} is dominated by the coupling of spin and rotational angular momenta. Rotational constants determined for $\text{Li}(\text{DME})_n$ within the rigid rotor model are systematically larger (see Tab. 9.0.1) than the sodium-doped dimethyl ether clusters. This manifests itself in a lower density of thermally populated rotational states. In case of Li-doped clusters increased deflection is expected compared to Na-doped clusters, at similar rotational temperatures and dominant angular momenta contributions of spin and rotations to \mathbf{J} .

Tab. 9.0.1: Li(DME)_n: Rotational constants of DFT optimized cluster structures (ω B97XD/6-31+G*) with their point group (PG) and symmetry number σ_{sym} .

Li(DME) _n	PG	σ_{sym}	A_{rot} in m^{-1}	B_{rot} in m^{-1}	C_{rot} in m^{-1}
1	C_{2v}	2	33.5	32.9	17.7
2	C_1	1	17.0	4.0	3.9
3	C_1	1	3.6	3.4	2.0
4	T_d	12	2.0	1.8	1.8
5	C_1	1	1.5	1.3	1.3
6	O_h	24	1.0	1.0	1.0

Measuring SG deflection of lithium-doped clusters in comparison to sodium-doped clusters, is a promising experimental approach to test our hypotheses and evaluate more subtle dependences of rotational states on the magnetic properties.

The design and development of the SG deflector was also motivated by magnetic selection of singlet and triplet states in order to probe spin pairing effects as a function of alkali metal concentration. With increasing alkali metal concentration, interactions between solvated electrons increase and solvated dielectrons may form. Recent photoelectron studies investigated the concentration dependent electronic properties of sodium-doped nanodroplets [54] and of liquid bulk solutions [55]. Neither study showed distinct features in the photoelectron spectra which would be assigned to solvated dielectrons. In chapter 7 we present a photoelectron photoion coincidence study of size resolved sodium-doped ammonia clusters. The experiments combined with *ab initio* calculations revealed one ionisation pathway which proceeds via the formation of excited state spin-paired solvated dielectrons. We assume that solvated dielectrons are generated via photoexcitation from the ammonia valence shell to the electron solvation orbital and subsequently decay under electron transfer processes. It is discussed that these electrons show significant contributions to the low kinetic energy electron signal. Yet, the experimental evidence for the formation of ground state solvated dielectrons is still uncertain. Experimental confirmation of the formation of such ground state solvated dielectrons should be in principle achievable by exploiting their differences in magnetic properties.

Bibliography

- [1] A. H. West, B. L. Yoder, D. Luckhaus, and R. Signorell. Solvated electrons in clusters: Magic numbers for the photoelectron anisotropy. *The Journal of Physical Chemistry A*, 119(50):12376–12382, 2015.
- [2] A. H. West, B. L. Yoder, D. Luckhaus, C.-M. Saak, M. Doppelbauer, and R. Signorell. Angle-resolved photoemission of solvated electrons in sodium-doped clusters. *The Journal of Physical Chemistry Letters*, 6(8):1487–1492, 2015.
- [3] W. Weyl. Über die Bildung des Ammoniums und einiger Ammoniummetalle. *Annalen der Physik*, 199(10):350–367, 1864.
- [4] C. A. Kraus. Solutions of metals in non-metallic solvents; I. general properties of solutions of metals in liquid ammonia. *Journal of the American Chemical Society*, 29(11):1557–1571, 1907.
- [5] E. Zurek, P. P. Edwards, and R. Hoffmann. A molecular perspective on lithium-ammonia solutions. *Angewandte Chemie International Edition*, 48(44):8198–8232, 2009.
- [6] J. M. Herbert and L. D. Jacobson. Structure of the aqueous electron: Assessment of one-electron pseudopotential models in comparison to experimental data and time-dependent density functional theory. *The Journal of Physical Chemistry A*, 115(50):14470–14483, 2011.
- [7] P. Voehringer. Ultrafast dynamics of electrons in ammonia. *Annual review of physical chemistry*, 66:97–118, 2015.
- [8] D. Holton and P. Edwards. Metals in non-aqueous solvents. *Chemistry in Britain*, 21:1007, 1985.
- [9] E. J. Hart and J. W. Boag. Absorption spectrum of the hydrated electron in water and in aqueous solutions. *Journal of the American Chemical Society*, 84(21):4090–4095, 1962.
- [10] J. V. Coe. Fundamental properties of bulk water from cluster ion data. *International reviews in physical chemistry*, 20(1):33–58, 2001.

- [11] B. C. Garrett, D. A. Dixon, D. M. Camaioni, D. M. Chipman, M. A. Johnson, C. D. Jonah, G. A. Kimmel, J. H. Miller, T. N. Rescigno, P. J. Rossky, et al. Role of water in electron-initiated processes and radical chemistry: Issues and scientific advances. *Chemical reviews*, 105(1):355–390, 2004.
- [12] A. J. Birch. 117. Reduction by dissolving metals. Part I. *Journal of the Chemical Society (Resumed)*, pages 430–436, 1944.
- [13] E. Alizadeh and L. Sanche. Precursors of solvated electrons in radiobiological physics and chemistry. *Chemical reviews*, 112(11):5578–5602, 2012.
- [14] E. Alizadeh, T. M. Orlando, and L. Sanche. Biomolecular damage induced by ionizing radiation: The direct and indirect effects of low-energy electrons on DNA. *Annual review of physical chemistry*, 66:379–398, 2015.
- [15] B. Abel. Hydrated interfacial ions and electrons. *Annual review of physical chemistry*, 64:533–552, 2013.
- [16] B. Abel, U. Buck, A. Sobolewski, and W. Domcke. On the nature and signatures of the solvated electron in water. *Physical Chemistry Chemical Physics*, 14(1):22–34, 2012.
- [17] I. Hertel, C. Hüglin, C. Nitsch, and C. Schulz. Photoionization of $\text{Na}(\text{NH}_3)_n$ and $\text{Na}(\text{H}_2\text{O})_n$ clusters: A step towards the liquid phase? *Physical review letters*, 67(13):1767, 1991.
- [18] C. Nitsch, C. Schulz, A. Gerber, W. Zimmermann-Edling, and I. Hertel. Photoionization studies of free sodium ammonia clusters. *Zeitschrift für Physik D Atoms, Molecules and Clusters*, 22(3):651–658, 1992.
- [19] C. Steinbach and U. Buck. Ionization potentials of large sodium doped ammonia clusters. *The Journal of chemical physics*, 122(13):134301, 2005.
- [20] I. Dauster, M. A. Suhm, U. Buck, and T. Zeuch. Experimental and theoretical study of the microsolvation of sodium atoms in methanol clusters: Differences and similarities to sodium-water and sodium-ammonia. *Physical Chemistry Chemical Physics*, 10(1):83–95, 2008.
- [21] K. Hashimoto and K. Daigoku. Ground and low-lying excited states of $\text{Na}(\text{NH}_3)_n$ and $\text{Na}(\text{H}_2\text{O})_n$ clusters: Formation and localization of solvated electron. *Chemical Physics Letters*, 469(1-3):62–67, 2009.
- [22] T. Almeida and B. C. Cabral. Ab initio approach to the electronic properties of sodium-ammonia clusters: Comparison with ammonia clusters. *The Journal of chemical physics*, 132(9):094307, 2010.

- [23] T. Zeuch and U. Buck. Sodium doped hydrogen bonded clusters: Solvated electrons and size selection. *Chemical Physics Letters*, 579:1–10, 2013.
- [24] A. O. Gunina and A. I. Krylov. Probing electronic wave functions of sodium-doped clusters: Dyson orbitals, anisotropy parameters, and ionization cross-sections. *The Journal of Physical Chemistry A*, 120(49):9841–9856, 2016.
- [25] B. L. Yoder, J. H. Litman, P. W. Forysinski, J. L. Corbett, and R. Signorell. Sizer for neutral weakly bound ultrafine aerosol particles based on sodium doping and mass spectrometric detection. *The Journal of Physical Chemistry Letters*, 2(20):2623–2628, 2011.
- [26] R. Signorell, B. L. Yoder, A. H. West, J. J. Ferreira, and C.-M. Saak. Angle-resolved valence shell photoelectron spectroscopy of neutral nanosized molecular aggregates. *Chemical Science*, 5(4):1283–1295, 2014.
- [27] J. V. Barnes, B. L. Yoder, and R. Signorell. Magic numbers for the photoelectron anisotropy in Li-doped dimethyl ether clusters. *The Journal of Physical Chemistry A*, 123(12):2379–2386, 2019.
- [28] S. Hüfner, S. Schmidt, and F. Reinert. Photoelectron spectroscopy—An overview. *Nuclear Instruments and Methods in Physics Research Section A: Accelerators, Spectrometers, Detectors and Associated Equipment*, 547(1):8–23, 2005.
- [29] T. A. Carlson. Photoelectron spectroscopy. *Annual Review of Physical Chemistry*, 26(1):211–234, 1975.
- [30] B. L. Yoder, A. H. West, B. Schläppi, E. Chasovskikh, and R. Signorell. A velocity map imaging photoelectron spectrometer for the study of ultrafine aerosols with a table-top VUV laser and Na-doping for particle sizing applied to dimethyl ether condensation. *The Journal of Chemical Physics*, 138(4):044202, 2013.
- [31] A. H. West, B. L. Yoder, and R. Signorell. Size-dependent velocity map photoelectron imaging of nanosized ammonia aerosol particles. *The Journal of Physical Chemistry A*, 117(50):13326–13335, 2013.
- [32] J. Cooper and R. N. Zare. Angular distribution of photoelectrons. *The Journal of chemical physics*, 48(2):942–943, 1968.
- [33] S. J. Peppernick, K. D. Gunaratne, and A. Castleman Jr. Superatom spectroscopy and the electronic state correlation between elements and isoelectronic molecular counterparts. *Proceedings of the National Academy of Sciences*, 107(3):975–980, 2010.

- [34] J. J. Melko and A. Castleman. Photoelectron imaging of small aluminum clusters: Quantifying $s - p$ hybridization. *Physical Chemistry Chemical Physics*, 15(9):3173–3178, 2013.
- [35] K. L. Reid. Photoelectron angular distributions. *Annual review of physical chemistry*, 54:397, 2003.
- [36] K. L. Reid. Photoelectron angular distributions: Developments in applications to isolated molecular systems. *Molecular Physics*, 110(3):131–147, 2012.
- [37] F. Filsinger, U. Erlekam, G. Von Helden, J. Küpper, and G. Meijer. Selector for structural isomers of neutral molecules. *Physical review letters*, 100(13):133003, 2008.
- [38] S. Trippel, Y.-P. Chang, S. Stern, T. Mullins, L. Holmegaard, and J. Küpper. Spatial separation of state-and size-selected neutral clusters. *Physical Review A*, 86(3):033202, 2012.
- [39] D. Horke, S. Trippel, Y.-P. Chang, S. Stern, T. Mullins, T. Kierspel, and J. Küpper. Spatial separation of molecular conformers and clusters. *JoVE (Journal of Visualized Experiments)*, (83):e51137, 2014.
- [40] J. H. Litman, B. L. Yoder, B. Schläppi, and R. Signorell. Sodium-doping as a reference to study the influence of intracluster chemistry on the fragmentation of weakly-bound clusters upon vacuum ultraviolet photoionization. *Physical Chemistry Chemical Physics*, 15(3):940–949, 2013.
- [41] C. Melania Oana and A. I. Krylov. Dyson orbitals for ionization from the ground and electronically excited states within equation-of-motion coupled-cluster formalism: Theory, implementation, and examples. *The Journal of chemical physics*, 127(23):234106, 2007.
- [42] C. M. Oana and A. I. Krylov. Cross sections and photoelectron angular distributions in photodetachment from negative ions using equation-of-motion coupled-cluster Dyson orbitals. *The Journal of chemical physics*, 131(12):124114, 2009.
- [43] Y.-I. Yamamoto, Y.-I. Suzuki, G. Tomasello, T. Horio, S. Karashima, R. Mitríc, and T. Suzuki. Time-and angle-resolved photoemission spectroscopy of hydrated electrons near a liquid water surface. *Physical review letters*, 112(18):187603, 2014.
- [44] A. Humeniuk, M. Wohlgemuth, T. Suzuki, and R. Mitríc. Time-resolved photoelectron imaging spectra from non-adiabatic molecular dynamics simulations. *The Journal of chemical physics*, 139(13):134104, 2013.
- [45] B. Brehm and E. von Puttkamer. Koinzidenzmessung von Photoionen und Photoelektronen bei Methan. *Zeitschrift für Naturforschung A*, 22(1):8–10, 1967.

- [46] X. Tang, G. A. Garcia, J.-F. Gil, and L. Nahon. Vacuum upgrade and enhanced performances of the double imaging electron/ion coincidence end-station at the vacuum ultraviolet beamline DESIRS. *Review of Scientific Instruments*, 86(12):123108, 2015.
- [47] G. Garcia, B. Cunha de Miranda, M. Tia, S. Daly, and L. Nahon. DELICIOUS III: A multipurpose double imaging particle coincidence spectrometer for gas phase vacuum ultraviolet photodynamics studies. *Review of Scientific Instruments*, 84(5):053112, 2013.
- [48] K. Sakai, S. Stoychev, T. Ouchi, I. Higuchi, M. Schöffler, T. Mazza, H. Fukuzawa, K. Nagaya, M. Yao, Y. Tamenori, et al. Electron-transfer-mediated decay and interatomic Coulombic decay from the triply ionized states in argon dimers. *Physical review letters*, 106(3):033401, 2011.
- [49] L. B. Ltaief, M. Shcherbinin, S. Mandal, S. Krishnan, R. Richter, T. Pfeifer, M. Bauer, A. Ghosh, M. Mudrich, K. Gokhberg, et al. Electron transfer mediated decay of alkali dimers attached to He nanodroplets. *Physical Chemistry Chemical Physics*, 22(16):8557–8564, 2020.
- [50] A. LaForge, V. Stumpf, K. Gokhberg, J. von Vangerow, F. Stienkemeier, N. Kryzhevoi, P. O’Keeffe, A. Ciavardini, S. Krishnan, M. Coreno, et al. Enhanced ionization of embedded clusters by electron-transfer-mediated decay in helium nanodroplets. *Physical Review Letters*, 116(20):203001, 2016.
- [51] T. Jahnke, U. Hergenhahn, B. Winter, R. Dörner, U. Frühling, P. V. Demekhin, K. Gokhberg, L. S. Cederbaum, A. Ehresmann, A. Knie, et al. Interatomic and intermolecular Coulombic decay. *Chemical reviews*, 120(20):11295–11369, 2020.
- [52] C. Bartels, C. Hock, J. Huwer, R. Kuhnen, J. Schwobel, and B. Von Issendorff. Probing the angular momentum character of the valence orbitals of free sodium nanoclusters. *Science*, 323(5919):1323–1327, 2009.
- [53] C. Bartels. *Angular distributions of photoelectrons from cold, size-selected sodium cluster anions*. PhD thesis, Universität Freiburg, 2008.
- [54] S. Hartweg, A. H. West, B. L. Yoder, and R. Signorell. Metal transition in sodium-ammonia nanodroplets. *Angewandte Chemie*, 128(40):12535–12538, 2016.
- [55] T. Buttersack, P. E. Mason, R. S. McMullen, H. C. Schewe, T. Martinek, K. Brezina, M. Crhan, A. Gomez, D. Hein, G. Wartner, et al. Photoelectron spectra of alkali metal-ammonia microjets: From blue electrolyte to bronze metal. *Science*, 368(6495):1086–1091, 2020.
- [56] W. Gerlach and O. Stern. Das magnetische Moment des Silberatoms. *Zeitschrift für Physik*, 9(1):353–355, 1922.

- [57] N. Ramsey. *Molecular beams*. Oxford University Press, 1985.
- [58] E. Hill. On the Zeeman effect in doublet band spectra. *Physical Review*, 34(12):1507, 1929.
- [59] A. Schadee. On the Zeeman effect in electronic transitions of diatomic molecules. *Journal of quantitative spectroscopy and radiative transfer*, 19(5):517–531, 1978.
- [60] S. Berdyugina and S. Solanki. The molecular Zeeman effect and diagnostics of solar and stellar magnetic fields I. Theoretical spectral patterns in the Zeeman regime. *Astronomy & Astrophysics*, 385(2):701–715, 2002.
- [61] N. Kuebler, M. Robin, J. Yang, A. Gedanken, and D. Herrick. Fully resolved Zeeman pattern in the Stern-Gerlach deflection spectrum of O_2 ($^3\Sigma_g^-, K = 1$). *Physical Review A*, 38(2):737, 1988.
- [62] A. Gedanken, N. Kuebler, M. Robin, and D. Herrick. Stern-Gerlach deflection spectra of nitrogen oxide radicals. *The Journal of chemical physics*, 90(8):3981–3993, 1989.
- [63] A. Amirav and G. Navon. Intramolecular spin relaxation in isolated molecules. *Physical Review Letters*, 47(13):906, 1981.
- [64] A. Amirav and G. Navon. Intramolecular spin relaxation probed by Stern-Gerlach experiments. *Chemical physics*, 82(3):253–267, 1983.
- [65] D. Herrick, M. Robin, and A. Gedanken. Theoretical investigation of the effects of intramolecular electron-spin relaxation on Stern-Gerlach deflections. *Chemical Physics*, 130(1-3):201–209, 1989.
- [66] M. B. Knickelbein. Spin relaxation in isolated molecules and clusters: The interpretation of Stern-Gerlach experiments. *The Journal of chemical physics*, 121(11):5281–5283, 2004.
- [67] H. Wennerström and P.-O. Westlund. The Stern-Gerlach experiment and the effects of spin relaxation. *Physical Chemistry Chemical Physics*, 14(5):1677–1684, 2012.
- [68] X. Xu, S. Yin, R. Moro, and W. A. de Heer. Distribution of magnetization of a cold ferromagnetic cluster beam. *Physical Review B*, 78(5):054430, 2008.
- [69] W. A. De Heer, P. Milani, and A. Châtelain. Spin relaxation in small free iron clusters. *Physical review letters*, 65(4):488, 1990.
- [70] J. Bucher, D. Douglass, and L. Bloomfield. Magnetic properties of free cobalt clusters. *Physical review letters*, 66(23):3052, 1991.

- [71] T. Hihara, S. Pokrant, and J. Becker. Magnetic moments and chemical bonding in isolated Bi_NCo_M clusters. *Chemical physics letters*, 294(4-5):357–362, 1998.
- [72] M. B. Knickelbein. Nickel clusters: The influence of adsorbates on magnetic moments. *The Journal of chemical physics*, 116(22):9703–9711, 2002.
- [73] K. Miyajima, A. Nakajima, S. Yabushita, M. B. Knickelbein, and K. Kaya. Ferromagnetism in one-dimensional vanadium-benzene sandwich clusters. *Journal of the American Chemical Society*, 126(41):13202–13203, 2004.
- [74] K. Miyajima, M. B. Knickelbein, and A. Nakajima. Magnetic properties of lanthanide organometallic sandwich complexes produced in a molecular beam. *Polyhedron*, 24(16-17):2341–2345, 2005.
- [75] K. Miyajima, M. Knickelbein, and A. Nakajima. Stern-Gerlach studies of organometallic sandwich clusters. *The European Physical Journal D-Atomic, Molecular, Optical and Plasma Physics*, 34(1):177–182, 2005.
- [76] K. Miyajima, S. Yabushita, M. B. Knickelbein, and A. Nakajima. Stern-Gerlach experiments of one-dimensional metal-benzene sandwich clusters: $\text{M}_n(\text{C}_6\text{H}_6)_m$ ($\text{M}=\text{Al}, \text{Sc}, \text{Ti}, \text{and V}$). *Journal of the American Chemical Society*, 129(27):8473–8480, 2007.
- [77] U. Rohrmann and R. Schäfer. Stern-Gerlach experiments on MnSn_{12} : Identification of a paramagnetic superatom and vibrationally induced spin orientation. *Physical Review Letters*, 111(13):133401, 2013.
- [78] U. Rohrmann and R. Schäfer. Stern-Gerlach experiments on Fe@Sn_{12} : Magnetic response of a Jahn-Teller distorted endohedrally doped molecular cage cluster. *The Journal of Physical Chemistry C*, 119(20):10958–10961, 2015.
- [79] T. M. Fuchs and R. Schäfer. Double Stern-Gerlach experiments on Mn@Sn_{12} : Refocusing of a paramagnetic superatom. *Physical Review A*, 98(6):063411, 2018.
- [80] T. M. Fuchs and R. Schäfer. Effect of vibrational excitation and spin-rotation coupling on Stern-Gerlach experiments: A detailed case study on GdSn_{15} as an asymmetric rotor. *Physical Review A*, 100(1):012512, 2019.
- [81] T. M. Fuchs and R. Schäfer. Influence of nuclear spins on electron spin coherence in isolated, p-doped tin clusters. *Physical Chemistry Chemical Physics*, 23(19):11334–11344, 2021.
- [82] A. T. Eppink and D. H. Parker. Velocity map imaging of ions and electrons using electrostatic lenses: Application in photoelectron and photofragment ion imaging of molecular oxygen. *Review of Scientific Instruments*, 68(9):3477–3484, 1997.

- [83] H. Pauly. *Atom, Molecule, and Cluster Beams I: Basic theory, production and detection of thermal energy beams*. Atom, Molecule, and Cluster Beams. Springer, 2000.
- [84] R. Johnston. *Atomic and Molecular Clusters*. Master's Series in Physics and Astronomy. Taylor & Francis, 2002.
- [85] R. Campargue. High intensity supersonic molecular beam apparatus. *Review of Scientific Instruments*, 35(1):111–112, 1964.
- [86] R. Campargue. Progress in overexpanded supersonic jets and skimmed molecular beams in free-jet zones of silence. *The Journal of Physical Chemistry*, 88(20):4466–4474, 1984.
- [87] O. Hagena and W. Obert. Cluster formation in expanding supersonic jets: Effect of pressure, temperature, nozzle size, and test gas. *The Journal of Chemical Physics*, 56(5):1793–1802, 1972.
- [88] E. Becker, K. Bier, and W. Henkes. Strahlen aus kondensierten Atomen und Molekülen im Hochvakuum. *Zeitschrift für Physik*, 146(3):333–338, 1956.
- [89] E. W. Becker, R. Klingelhöfer, and P. Lohse. Strahlen aus kondensiertem Wasserstoff, kondensiertem Helium und kondensiertem Stickstoff im Hochvakuum. *Zeitschrift für Naturforschung A*, 17(5):432–438, 1962.
- [90] H. Burghoff and J. Gspann. Bestimmung der mittleren Agglomeratgröße und des Restgasanteils kondensierter Molekularstrahlen durch Streuung eines K-Atomstrahls. *Zeitschrift für Naturforschung A*, 22(5):684–689, 1967.
- [91] U. Even. The Even-Lavie valve as a source for high intensity supersonic beam. *EPJ Techniques and Instrumentation*, 2(1):17, 2015.
- [92] C. Bobbert, S. Schütte, C. Steinbach, and U. Buck. Fragmentation and reliable size distributions of large ammonia and water clusters. *The European Physical Journal D-Atomic, Molecular, Optical and Plasma Physics*, 19(2):183–192, 2002.
- [93] J. V. Barnes, M. Beck, S. Hartweg, A. Luski, B. L. Yoder, J. Narevicius, E. Narevicius, and R. Signorell. Magnetic deflection of neutral sodium-doped ammonia clusters. *Physical Chemistry Chemical Physics*, 23(2):846–858, 2021.
- [94] B. Schläppi, J. J. Ferreiro, J. H. Litman, and R. Signorell. Sodium-sizer for neutral nanosized molecular aggregates: Quantitative correction of size-dependence. *International Journal of Mass Spectrometry*, 372:13–21, 2014.
- [95] S. Vongehr, T. Shao-Chun, and M. Xiang-Kang. Collision statistics of clusters: From Poisson model to Poisson mixtures. *Chinese Physics B*, 19(2):023602, 2010.

- [96] L. Nahon, N. de Oliveira, G. A. Garcia, J.-F. Gil, B. Pilette, O. Marcouillé, B. Lagarde, and F. Polack. DESIRS: A state-of-the-art VUV beamline featuring high resolution and variable polarization for spectroscopy and dichroism at SOLEIL. *Journal of synchrotron radiation*, 19(4):508–520, 2012.
- [97] P. W. Forysinski, P. Zielke, D. Luckhaus, J. Corbett, and R. Signorell. Photoionization of small sodium-doped acetic acid clusters. *The Journal of chemical physics*, 134(9):094314, 2011.
- [98] W. Li, S. D. Chambreau, S. A. Lahankar, and A. G. Suits. Megapixel ion imaging with standard video. *Review of scientific instruments*, 76(6):063106, 2005.
- [99] G. A. Garcia, L. Nahon, and I. Powis. Two-dimensional charged particle image inversion using a polar basis function expansion. *Review of Scientific Instruments*, 75(11):4989–4996, 2004.
- [100] B. Dick. Inverting ion images without Abel inversion: Maximum entropy reconstruction of velocity maps. *Physical Chemistry Chemical Physics*, 16(2):570–580, 2014.
- [101] S. Hartweg. *Electron solvation and scattering in clusters*. PhD thesis, ETH Zürich, Zürich, 2019.
- [102] W. Wiley and I. H. McLaren. Time-of-flight mass spectrometer with improved resolution. *Review of scientific instruments*, 26(12):1150–1157, 1955.
- [103] P. Jansen and F. Merkt. Manipulating beams of paramagnetic atoms and molecules using inhomogeneous magnetic fields. *Progress in Nuclear Magnetic Resonance Spectroscopy*, 120:118–148, 2020.
- [104] X. Xu, S. Yin, R. Moro, and W. A. de Heer. Magnetic moments and adiabatic magnetization of free cobalt clusters. *Physical review letters*, 95(23):237209, 2005.
- [105] G. Bertsch and K. Yabana. Cold cluster ferromagnetism. *Physical Review A*, 49(3):1930, 1994.
- [106] V. Visuthikraisee and G. Bertsch. Spin-rotation coupling in ferromagnetic clusters. *Physical Review A*, 54(6):5104, 1996.
- [107] N. Hamamoto, N. Onishi, and G. Bertsch. Magnetic properties of an ensemble of rotating ferromagnetic clusters. *Physical Review B*, 61(2):1336, 2000.
- [108] T. J. Sears. The calculation of the energy levels of an asymmetric top free radical in a magnetic field. *Computer Physics Reports*, 2(1):1–32, 1984.
- [109] R. N. Zare and W. G. Harter. Angular momentum: understanding spatial aspects in chemistry and physics. *New York*, 120, 1988.

- [110] C. Zener. Non-adiabatic crossing of energy levels. *Proceedings of the Royal Society of London. Series A, Containing Papers of a Mathematical and Physical Character*, 137(833):696–702, 1932.
- [111] S. Blundell. *Magnetism in condensed matter*, 2003.
- [112] S. Khanna and S. Linderoth. Magnetic behavior of clusters of ferromagnetic transition metals. *Physical review letters*, 67(6):742, 1991.
- [113] M. B. Knickelbein. Experimental observation of superparamagnetism in manganese clusters. *Physical review letters*, 86(23):5255, 2001.
- [114] I. M. Billas, W. A. de Heer, and A. Châtelain. Magnetic properties of small iron systems: From ferromagnetic resonance of precipitated particles in silica to Stern-Gerlach deflections in molecular beam. *Journal of non-crystalline solids*, 179:316–323, 1994.
- [115] F. Crawford. Zeeman effect in diatomic molecular spectra. *Reviews of Modern Physics*, 6(2):90, 1934.
- [116] E. Hirota. *High-resolution spectroscopy of transient molecules*, volume 40. Springer Science & Business Media, 2012.
- [117] I. Bowater, J. Brown, and A. Carrington. Microwave spectroscopy of nonlinear free radicals I. General theory and application to the Zeeman effect in HCO. *Proceedings of the Royal Society of London. A. Mathematical and Physical Sciences*, 333(1594):265–288, 1973.
- [118] G. Herzberg. *Molecular spectra and molecular structure. Vol. 1: Spectra of diatomic molecules*. New York: Van Nostrand Reinhold, 1950.
- [119] C. H. Townes and A. L. Schawlow. *Microwave spectroscopy*. Courier Corporation, 2013.
- [120] L. Verlet. Computer "experiments" on classical fluids. I. Thermodynamical properties of Lennard-Jones molecules. *Physical review*, 159(1):98, 1967.
- [121] A. H. C. West. *Photoelectron Velocity Map Imaging of Neutral Nanoscale Clusters and Aerosol Particles*. PhD thesis, ETH Zürich, Zürich, 2016.
- [122] B. J. Whitaker. *Imaging in molecular dynamics: Technology and applications*. Cambridge University Press, 2003.
- [123] S. Manzhos and H.-P. Looock. Photofragment image analysis using the onion-peeling algorithm. *Computer physics communications*, 154(1):76–87, 2003.

- [124] G. Roberts, J. Nixon, J. Lecointre, E. Wrede, and J. Verlet. Toward real-time charged-particle image reconstruction using polar onion-peeling. *Review of Scientific Instruments*, 80(5):053104, 2009.
- [125] C. Bordas, F. Paulig, H. Helm, and D. Huestis. Principle and inversion method. *Review of scientific instruments*, 67(6):2257–2268, 1996.
- [126] C. J. Dasch. One-dimensional tomography: A comparison of Abel, onion-peeling, and filtered backprojection methods. *Applied optics*, 31(8):1146–1152, 1992.
- [127] V. Dribinski, A. Ossadtchi, V. A. Mandelshtam, and H. Reisler. Reconstruction of Abel-transformable images: The Gaussian basis-set expansion Abel transform method. *Review of Scientific Instruments*, 73(7):2634–2642, 2002.
- [128] B. Dick. MELEXIR: Maximum entropy legendre expanded image reconstruction. A fast and efficient method for the analysis of velocity map imaging or photoelectron imaging data. *Physical Chemistry Chemical Physics*, 21(35):19499–19512, 2019.
- [129] M. J. Pilling and I. W. Smith. *Modern gas kinetics*. Blackwell Scientific Publications, 1987.
- [130] J. Fedor, V. Poterya, A. Pysanenko, and M. Fárnik. Cluster cross sections from pickup measurements: Are the established methods consistent? *The Journal of chemical physics*, 135(10):104305, 2011.
- [131] K. Berkling, R. Helbing, K. Kramer, H. Pauly, C. Schlier, and P. Toschek. Effektive Stoßquerschnitte bei Streuversuchen. *Zeitschrift für Physik*, 166(4):406–428, 1962.
- [132] N. C. Lang, H. Lilenfeld, and J. L. Kinsey. Velocity corrections for total scattering cross sections. *The Journal of Chemical Physics*, 55(7):3114–3115, 1971.
- [133] J. Liang and V. V. Kresin. Kinetic energy deposited into a nanodroplet, cluster, or molecule in a sticking collision with background gas. *The Journal of Chemical Physics*, 153(19):196101, 2020.
- [134] J. Jeans. *The dynamical theory of gases*. University Press, 1925.
- [135] L. B. Loeb. *The kinetic theory of gases*. Courier Corporation, 2004.
- [136] S. Chapman and T. Cowling. *The mathematical theory of non uniform gases*, cambridge mathematical library, 1970.
- [137] A. Meyer and M. van Gastel. EPR and ENDOR study of the frozen ammoniated electron at low alkali-metal concentrations. *The Journal of Physical Chemistry A*, 115(10):1939–1945, 2011.

- [138] P. P. Edwards. Magnetic resonance studies of alkali metals in nonaqueous solvents. *The Journal of Physical Chemistry*, 88(17):3772–3780, 1984.
- [139] Á. Carrera and E. Marceca. Electric deflection of middle-size ammonia clusters containing (e^- , Na^+) pairs. *The Journal of Physical Chemistry A*, 119(18):4207–4213, 2015.
- [140] D. J. Meschi and A. W. Searcy. Investigation of the magnetic moments of S_2 , Se_2 , Te_2 , Se_6 , and Se_5 by the Stern-Gerlach magnetic deflection method. *The Journal of Chemical Physics*, 51(11):5134–5138, 1969.
- [141] A. Gedanken, N. Kuebler, M. B. Robin, and D. Herrick. Magnetic deflection spectrum of vanadium tetrachloride. *Journal of the American Chemical Society*, 111(15):5568–5572, 1989.
- [142] D. Herrick, M. Robin, and A. Gedanken. Spin-rotation effects in the Stern-Gerlach deflection spectra of $^3\Sigma^-$ molecules and their complexes with argon. *Journal of Molecular Spectroscopy*, 133(1):61–81, 1989.
- [143] A. Gedanken, V. Kelner, and E. Sominksa. Stern-Gerlach deflection spectrum of chlorine dioxide. *Chemical physics letters*, 221(3-4):274–278, 1994.
- [144] A. Malakhovskii and A. Gedanken. Stern-Gerlach study of nitric oxide. *Journal of the Chemical Society, Faraday Transactions*, 92(3):329–332, 1996.
- [145] A. Malakhovskii, E. Sominska, and A. Gedanken. Magnetism in oxygen clusters. study of pure and mixed clusters of oxygen by Stern-Gerlach spectroscopy. *Journal of the Chemical Society, Faraday Transactions*, 92(8):1319–1322, 1996.
- [146] M. Alagia, V. Aquilanti, D. Ascenzi, N. Balucani, D. Cappelletti, L. Cartechini, P. Casavecchia, F. Pirani, G. Sanchini, and G. G. Volpi. Magnetic analysis of supersonic beams of atomic oxygen, nitrogen, and chlorine generated from a radio-frequency discharge. *Israel journal of chemistry*, 37(4):329–342, 1997.
- [147] D. Cox, D. Trevor, R. Whetten, E. Rohlfing, and A. Kaldor. Aluminum clusters: Magnetic properties. *The Journal of chemical physics*, 84(8):4651–4656, 1986.
- [148] P. Ballone, P. Milani, and W. de Heer. Pseudospin relaxation in ferromagnetic clusters. *Physical Review B*, 44(18):10350, 1991.
- [149] W. De Heer, P. Milani, and A. Châtelain. Magnetic properties of free alkali and transition metal clusters. *Zeitschrift für Physik D Atoms, Molecules and Clusters*, 19(4):241–245, 1991.
- [150] I. M. Billas, A. Châtelain, and W. A. de Heer. Magnetism from the atom to the bulk in iron, cobalt, and nickel clusters. *Science*, 265(5179):1682–1684, 1994.

- [151] A. Châtelain. Stern-Gerlach deflection of ferromagnetic cluster beams. *Philosophical Magazine B*, 79(9):1367–1378, 1999.
- [152] D. Dieleman, M. Tombers, L. Peters, J. Meyer, S. Peredkov, J. Jalink, M. Neeb, W. Eberhardt, T. Rasing, G. Niedner-Schatteburg, et al. Orbit and spin resolved magnetic properties of size selected $[\text{Co}_n\text{Rh}]^+$ and $[\text{Co}_n\text{Au}]^+$ nanoalloy clusters. *Physical Chemistry Chemical Physics*, 17(42):28372–28378, 2015.
- [153] A. Diaz-Bachs, L. Peters, R. Logemann, V. Chernyy, J. Bakker, M. Katsnelson, and A. Kirilyuk. Magnetic properties of Co-doped Nb clusters. *Physical Review B*, 97(13):134427, 2018.
- [154] J. Liang, T. M. Fuchs, R. Schäfer, and V. V. Kresin. Strong permanent magnet gradient deflector for Stern-Gerlach-type experiments on molecular beams. *Review of Scientific Instruments*, 91(5):053202, 2020.
- [155] S. Schütte and U. Buck. Strong fragmentation of large rare gas clusters by high energy electron impact. *International Journal of Mass Spectrometry*, 220(2):183–192, 2002.
- [156] R. Signorell, M. Goldmann, B. L. Yoder, A. Bodi, E. Chasovskikh, L. Lang, and D. Luckhaus. Nanofocusing, shadowing, and electron mean free path in the photoemission from aerosol droplets. *Chemical Physics Letters*, 658:1–6, 2016.
- [157] D. A. Dahl. SIMION for the personal computer in reflection. *International Journal of Mass Spectrometry*, 200(1-3):3–25, 2000.
- [158] T. Vogler and P. Vöhringer. Probing the band gap of liquid ammonia with femtosecond multiphoton ionization spectroscopy. *Physical Chemistry Chemical Physics*, 20(40):25657–25665, 2018.
- [159] D. A. Rodham and G. A. Blake. ZEKE-PFI spectroscopy of 1:1 complexes of sodium with water and ammonia. *Chemical physics letters*, 264(5):522–530, 1997.
- [160] X. Peng and W. Kong. Zero energy kinetic electron and mass analyzed threshold ionization spectroscopy of $\text{Na}(\text{NH}_3)_n$ ($n = 1, 2, \text{ and } 4$) complexes. *The Journal of chemical physics*, 117(20):9306–9315, 2002.
- [161] C. P. Schulz, A. Scholz, and I. V. Hertel. Ultrafast energy redistribution in photoexcited sodium-ammonia clusters. *Israel journal of chemistry*, 44(1-3):19–25, 2004.
- [162] M. Frisch, G. Trucks, H. Schlegel, G. Scuseria, M. Robb, J. Cheeseman, G. Scalmani, V. Barone, B. Mennucci, G. Petersson, et al. Gaussian, Inc., Wallingford CT. *Wallingford CT*, 2009.

- [163] D. Becker, C. W. Dierking, J. Suchan, F. Zurheide, J. Lengyel, M. Fárník, P. Slavíček, U. Buck, and T. Zeuch. Temperature evolution in IR action spectroscopy experiments with sodium doped water clusters. *Physical Chemistry Chemical Physics*, 23(13):7682–7695, 2021.
- [164] T. M. Fuchs, F. Rivic, and R. Schäfer. Determining the translational and internal temperatures of isolated metal clusters: A comprehensive approach based on molecular-beam-deflection experiments. *Physical Review A*, 104(1):012820, 2021.
- [165] I. M. Billas, J. A. Becker, and W. A. de Heer. Magnetic properties of iron clusters in a molecular beam: Resolution of a controversy. *Zeitschrift für Physik D Atoms, Molecules and Clusters*, 26(1):325–327, 1993.
- [166] J. Bucher, D. Douglass, and L. Bloomfield. Pulsed supersonic source producing clusters with an adjustable vibrational temperature. *Review of scientific instruments*, 63(12):5667–5670, 1992.
- [167] S. N. Yurchenko, L. Lodi, J. Tennyson, and A. V. Stoliarov. Duo: A general program for calculating spectra of diatomic molecules. *Computer Physics Communications*, 202:262–275, 2016.
- [168] I. M. Billas, A. Châtelain, and W. A. de Heer. Magnetism of Fe, Co and Ni clusters in molecular beams. *Journal of magnetism and magnetic materials*, 168(1-2):64–84, 1997.
- [169] O. Kuzmychov and S. Berdyugina. Paschen-Back effect in the CrH molecule and its application for magnetic field measurements on stars, brown dwarfs, and hot exoplanets. *Astronomy & Astrophysics*, 558:A120, 2013.
- [170] B. K. Peters, K. X. Rodriguez, S. H. Reisberg, S. B. Beil, D. P. Hickey, Y. Kawamata, M. Collins, J. Starr, L. Chen, S. Udyavara, et al. Scalable and safe synthetic organic electroreduction inspired by Li-ion battery chemistry. *Science*, 363(6429):838–845, 2019.
- [171] N. W. Taylor and G. N. Lewis. The paramagnetism of "odd molecules". *Proceedings of the National Academy of Sciences of the United States of America*, pages 456–457, 1925.
- [172] M. Mauksch and S. B. Tsogoeva. Spin-paired solvated electron couples in alkali-ammonia systems. *Physical Chemistry Chemical Physics*, 20(44):27740–27744, 2018.
- [173] G. J. Martyna, Z. Deng, and M. L. Klein. Quantum simulation studies of singlet and triplet bipolarons in liquid ammonia. *The Journal of chemical physics*, 98(1):555–563, 1993.

- [174] M. e. Frisch, G. Trucks, H. Schlegel, G. Scuseria, M. Robb, J. Cheeseman, G. Scalmani, V. Barone, G. Petersson, H. Nakatsuji, et al. Gaussian 16, 2016.
- [175] H.-J. Werner, P. J. Knowles, F. R. Manby, J. A. Black, K. Doll, A. Heßelmann, D. Kats, A. Köhn, T. Korona, D. A. Kreplin, et al. The Molpro quantum chemistry package. *The Journal of Chemical Physics*, 152(14):144107, 2020.
- [176] F. Dong, S. Heinbuch, J. Rocca, and E. Bernstein. Dynamics and fragmentation of van der Waals clusters: $(\text{H}_2\text{O})_n$, $(\text{CH}_3\text{OH})_n$, and $(\text{NH}_3)_n$ upon ionization by a 26.5 eV soft x-ray laser. *The Journal of chemical physics*, 124(22):224319, 2006.
- [177] B. Oostenrijk, N. Walsh, J. Laksman, E. P. Månsson, C. Grunewald, S. L. Sorensen, and M. Gisselbrecht. The role of charge and proton transfer in fragmentation of hydrogen-bonded nanosystems: The breakup of ammonia clusters upon single photon multi-ionization. *Physical Chemistry Chemical Physics*, 20(2):932–940, 2018.
- [178] S. Ceyer, P. Tiedemann, B. Mahan, and Y.-T. Lee. Energetics of gas phase proton solvation by NH_3 . *The Journal of Chemical Physics*, 70(1):14–17, 1979.
- [179] S. Hartweg, B. L. Yoder, G. A. Garcia, L. Nahon, and R. Signorell. Size-resolved photoelectron anisotropy of gas phase water clusters and predictions for liquid water. *Physical Review Letters*, 118(10):103402, 2017.
- [180] S. Hartweg, G. A. Garcia, and L. Nahon. Photoelectron spectroscopy of the water dimer reveals unpredicted vibrational structure. *The Journal of Physical Chemistry A*, 125(22):4882–4887, 2021.
- [181] B. L. Yoder, K. B. Bravaya, A. Bodi, A. H. West, B. Sztáray, and R. Signorell. Barrierless proton transfer across weak $\text{CH}\cdots\text{O}$ hydrogen bonds in dimethyl ether dimer. *The Journal of Chemical Physics*, 142(11):114303, 2015.
- [182] L. Belau, K. R. Wilson, S. R. Leone, and M. Ahmed. Vacuum ultraviolet (VUV) photoionization of small water clusters. *The Journal of Physical Chemistry A*, 111(40):10075–10083, 2007.
- [183] C. Ng, D. Trevor, P. Tiedemann, S. Ceyer, P. Kronebusch, B. Mahan, and Y.-T. Lee. Photoionization of dimeric polyatomic molecules: Proton affinities of H_2O and HF . *The Journal of Chemical Physics*, 67(9):4235–4237, 1977.
- [184] E. Kamarchik, O. Kostko, J. M. Bowman, M. Ahmed, and A. I. Krylov. Spectroscopic signatures of proton transfer dynamics in the water dimer cation. *The Journal of chemical physics*, 132(19):194311, 2010.
- [185] I. R. Ariyaratna, F. Pawłowski, J. V. Ortiz, and E. Miliordos. Aufbau principle for diffuse electrons of double-shell metal ammonia complexes: The case of $\text{M}(\text{NH}_3)$

- 4@12NH₃, M = Li, Be⁺, B²⁺. *The Journal of Physical Chemistry A*, 124(3):505–512, 2019.
- [186] I. R. Ariyarathna, F. Pawłowski, J. V. Ortiz, and E. Miliordos. Molecules mimicking atoms: Monomers and dimers of alkali metal solvated electron precursors. *Physical Chemistry Chemical Physics*, 20(37):24186–24191, 2018.
- [187] L. Cederbaum, J. Zobeley, and F. Tarantelli. Giant intermolecular decay and fragmentation of clusters. *Physical review letters*, 79(24):4778, 1997.
- [188] J. Zobeley, R. Santra, and L. S. Cederbaum. Electronic decay in weakly bound heteroclusters: Energy transfer versus electron transfer. *The Journal of Chemical Physics*, 115(11):5076–5088, 2001.
- [189] T. Jahnke, A. Czasch, M. Schöffler, S. Schössler, A. Knapp, M. Kász, J. Titze, C. Wimmer, K. Kreidi, R. Grisenti, et al. Experimental observation of interatomic Coulombic decay in neon dimers. *Physical review letters*, 93(16):163401, 2004.
- [190] A. Ghosh, L. S. Cederbaum, and K. Gokhberg. Signature of the neighbor’s quantum nuclear dynamics in the electron transfer mediated decay spectra. *Chemical Science*, 12(27):9379–9385, 2021.
- [191] A. Ghosh, L. S. Cederbaum, and K. Gokhberg. Electron transfer mediated decay in HeLi₂ cluster: Potential energy surfaces and decay widths. *The Journal of Chemical Physics*, 150(16):164309, 2019.
- [192] I. Unger, R. Seidel, S. Thürmer, M. N. Pohl, E. F. Aziz, L. S. Cederbaum, E. Muchová, P. Slavíček, B. Winter, and N. V. Kryzhevoi. Observation of electron-transfer-mediated decay in aqueous solution. *Nature chemistry*, 9(7):708–714, 2017.
- [193] M. N. Pohl, C. Richter, E. Lugovoy, R. Seidel, P. Slavicek, E. F. Aziz, B. Abel, B. Winter, and U. Hergenbahn. Sensitivity of electron transfer mediated decay to ion pairing. *The Journal of Physical Chemistry B*, 121(32):7709–7714, 2017.
- [194] J. D. Asmussen, R. Michiels, U. Bangert, N. Sisourat, M. Binz, L. Bruder, M. Danailov, M. Di Fraia, R. Feifel, L. Giannessi, et al. Time-resolved ultrafast interatomic coulombic decay in superexcited sodium-doped helium nanodroplets. *The Journal of Physical Chemistry Letters*, 13:4470–4478, 2022.
- [195] L. Ben Ltaief, M. Shcherbinin, S. Mandal, S. Krishnan, A. LaForge, R. Richter, S. Turchini, N. Zema, T. Pfeifer, E. Fasshauer, et al. Charge exchange dominates long-range interatomic coulombic decay of excited metal-doped helium nanodroplets. *The Journal of Physical Chemistry Letters*, 10(21):6904–6909, 2019.

- [196] K. Vafayi and K. Esfarjani. Abundance of nanoclusters in a molecular beam: The magic numbers for Lennard-Jones potential. *Journal of Cluster Science*, 26(2):473–490, 2015.
- [197] M. T. Coolbaugh and J. F. Garvey. Magic numbers in molecular clusters: A probe for chemical reactivity. *Chemical Society Reviews*, 21(3):163–169, 1992.
- [198] J. A. Alonso. *Structure and properties of atomic nanoclusters*. World Scientific, 2012.
- [199] H.-C. Chang, C.-C. Wu, and J.-L. Kuo. Recent advances in understanding the structures of medium-sized protonated water clusters. *International Reviews in Physical Chemistry*, 24(3-4):553–578, 2005.
- [200] R. M. Young and D. M. Neumark. Dynamics of solvated electrons in clusters. *Chemical reviews*, 112(11):5553–5577, 2012.
- [201] N. I. Hammer, J.-W. Shin, J. M. Headrick, E. G. Diken, J. R. Roscioli, G. H. Weddle, and M. A. Johnson. How do small water clusters bind an excess electron? *Science*, 306(5696):675–679, 2004.
- [202] L. Turi and P. J. Rossky. Theoretical studies of spectroscopy and dynamics of hydrated electrons. *Chemical reviews*, 112(11):5641–5674, 2012.
- [203] D. Borgis, P. J. Rossky, and L. Turi. Electronic excited state lifetimes of anionic water clusters: Dependence on charge solvation motif. *The Journal of Physical Chemistry Letters*, 8(10):2304–2309, 2017.
- [204] D. Rolles, H. Zhang, Z. Pešić, R. Bilodeau, A. Wills, E. Kukk, B. Rude, G. Ackerman, J. Bozek, R. D. Muiño, et al. Size effects in angle-resolved photoelectron spectroscopy of free rare-gas clusters. *Physical Review A*, 75(3):031201, 2007.
- [205] A. Sanov. Laboratory-frame photoelectron angular distributions in anion photodetachment: Insight into electronic structure and intermolecular interactions. *Annual review of physical chemistry*, 65:341–363, 2014.
- [206] D. Khuseynov, C. C. Blackstone, L. M. Culberson, and A. Sanov. Photoelectron angular distributions for states of any mixed character: An experiment-friendly model for atomic, molecular, and cluster anions. *The Journal of chemical physics*, 141(12):124312, 2014.
- [207] A. Kammrath, J. R. Verlet, G. B. Griffin, and D. M. Neumark. Photoelectron imaging of large anionic methanol clusters: $(\text{MeOH})_n^-$ ($n \sim 70 - 460$). *The Journal of chemical physics*, 125(17):171102, 2006.

- [208] R. M. Young, M. A. Yandell, M. Niemeyer, and D. M. Neumark. Photoelectron imaging of tetrahydrofuran cluster anions (THF). *The Journal of chemical physics*, 133(15):154312, 2010.
- [209] W. S. Hopkins, A. P. Woodham, N. M. Tonge, A. M. Ellis, and S. R. Mackenzie. Photodissociation dynamics of $\text{Li}(\text{NH}_3)_4$: A velocity map imaging study. *The Journal of Physical Chemistry Letters*, 2(3):257–261, 2011.
- [210] L. Varriale, N. M. Tonge, N. Bhalla, and A. M. Ellis. Communications: The electronic spectrum of $\text{Li}(\text{NH}_3)_4$. *The Journal of chemical physics*, 132(16):161101, 2010.
- [211] T. E. Salter and A. M. Ellis. Microsolvation of lithium in ammonia: Dissociation energies and spectroscopic parameters of small $\text{Li}(\text{NH}_3)_n$ clusters ($n = 1$ and 2) and their cations. *Chemical physics*, 332(1):132–138, 2007.
- [212] T. E. Salter, V. A. Mikhailov, C. J. Evans, and A. M. Ellis. Infrared spectroscopy of $\text{Li}(\text{NH}_3)_n$ clusters for $n = 4 - 7$. *The Journal of chemical physics*, 125(3):034302, 2006.
- [213] M. B. More, E. D. Glendening, D. Ray, D. Feller, and P. Armentrout. Cation- ether complexes in the gas phase: Bond dissociation energies and equilibrium structures of $\text{Li}^+[\text{O}(\text{CH}_3)_2]_x$, $x = 1 - 4$. *The Journal of Physical Chemistry*, 100(5):1605–1614, 1996.
- [214] B. R. Sohnlein, S. Li, J. F. Fuller, and D.-S. Yang. Pulsed-field ionization electron spectroscopy and binding energies of alkali metal-dimethyl ether and -dimethoxyethane complexes. *The Journal of chemical physics*, 123(1):014318, 2005.
- [215] R. Takasu, K. Hashimoto, and K. Fuke. Study on microscopic solvation process of Li atom in ammonia clusters: Photoionization and photoelectron spectroscopies of $\text{M}(\text{NH}_3)_n$ ($\text{M} = \text{Li}, \text{Li}^-$). *Chemical physics letters*, 258(1-2):94–100, 1996.
- [216] D. W. Chandler and P. L. Houston. Two-dimensional imaging of state-selected photodissociation products detected by multiphoton ionization. *The Journal of chemical physics*, 87(2):1445–1447, 1987.
- [217] A. E. Reed, R. B. Weinstock, and F. Weinhold. Natural population analysis. *The Journal of Chemical Physics*, 83(2):735–746, 1985.
- [218] W. Acree Jr and J. S. Chickos. Phase transition enthalpy measurements of organic and organometallic compounds. Sublimation, vaporization and fusion enthalpies from 1880 to 2010. *Journal of Physical and Chemical Reference Data*, 39(4):043101, 2010.
- [219] K. Peterson, P. Dao, R. Farley, and A. Castleman Jr. Photoionization of sodium clusters. *The Journal of chemical physics*, 80(5):1780–1785, 1984.

- [220] B. A. Bushaw, W. Nörtershäuser, G. W. Drake, and H.-J. Kluge. Ionization energy of ${}^6,7\text{Li}$ determined by triple-resonance laser spectroscopy. *Physical Review A*, 75(5):052503, 2007.
- [221] S. J. M. Thomas, P. P. Edwards, and V. L. Kuznetsov. Sir Humphry Davy: Boundless chemist, physicist, poet and man of action. *ChemPhysChem*, 9(1):59–66, 2008.
- [222] A. G. Seel, H. Swan, D. T. Bowron, J. C. Wasse, T. Weller, P. P. Edwards, C. A. Howard, and N. T. Skipper. Electron solvation and the unique liquid structure of a mixed-amine expanded metal: The saturated $\text{Li-NH}_3\text{-MeNH}_2$ system. *Angewandte Chemie*, 129(6):1583–1587, 2017.
- [223] M. P. Coons, Z.-Q. You, and J. M. Herbert. The hydrated electron at the surface of neat liquid water appears to be indistinguishable from the bulk species. *Journal of the American Chemical Society*, 138(34):10879–10886, 2016.
- [224] S. Karashima, Y. Yamamoto, and T. Suzuki. Resolving nonadiabatic dynamics of hydrated electrons using ultrafast photoemission anisotropy. *Physical Review Letters*, 116(13):137601, 2016.
- [225] D. Luckhaus, Y. Yamamoto, T. Suzuki, and R. Signorell. Genuine binding energy of the hydrated electron. *Science advances*, 3(4):e1603224, 2017.
- [226] M. H. Elkins, H. L. Williams, A. T. Shreve, and D. M. Neumark. Relaxation mechanism of the hydrated electron. *Science*, 342(6165):1496–1499, 2013.
- [227] J. Stähler, J.-C. Deinert, D. Wegkamp, S. Hagen, and M. Wolf. Real-time measurement of the vertical binding energy during the birth of a solvated electron. *Journal of the American Chemical Society*, 137(10):3520–3524, 2015.
- [228] J. W. Riley, B. Wang, J. L. Woodhouse, M. Assmann, G. A. Worth, and H. H. Fielding. Unravelling the role of an aqueous environment on the electronic structure and ionization of phenol using photoelectron spectroscopy. *The Journal of Physical Chemistry Letters*, 9(4):678–682, 2018.
- [229] J. Savolainen, F. Uhlig, S. Ahmed, P. Hamm, and P. Jungwirth. Direct observation of the collapse of the delocalized excess electron in water. *Nature chemistry*, 6(8):697–701, 2014.
- [230] G. Kumar, A. Roy, R. S. McMullen, S. Kutagulla, and S. E. Bradforth. The influence of aqueous solvent on the electronic structure and non-adiabatic dynamics of indole explored by liquid-jet photoelectron spectroscopy. *Faraday discussions*, 212:359–381, 2018.

Appendix A

Magnetic deflection results

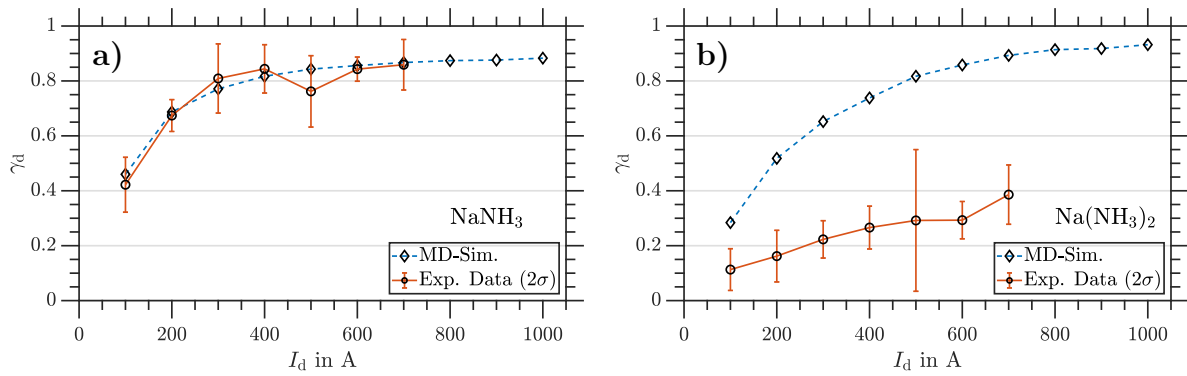


Fig. A.0.1: Maximal γ_d as a function I_d for (a) NaNH_3 and (b) $\text{Na}(\text{NH}_3)_2$. The circles represent the experiment and the diamonds the corresponding simulations. The was operated in a $t_2 < t_1 < t_3$ coil timing sequence.

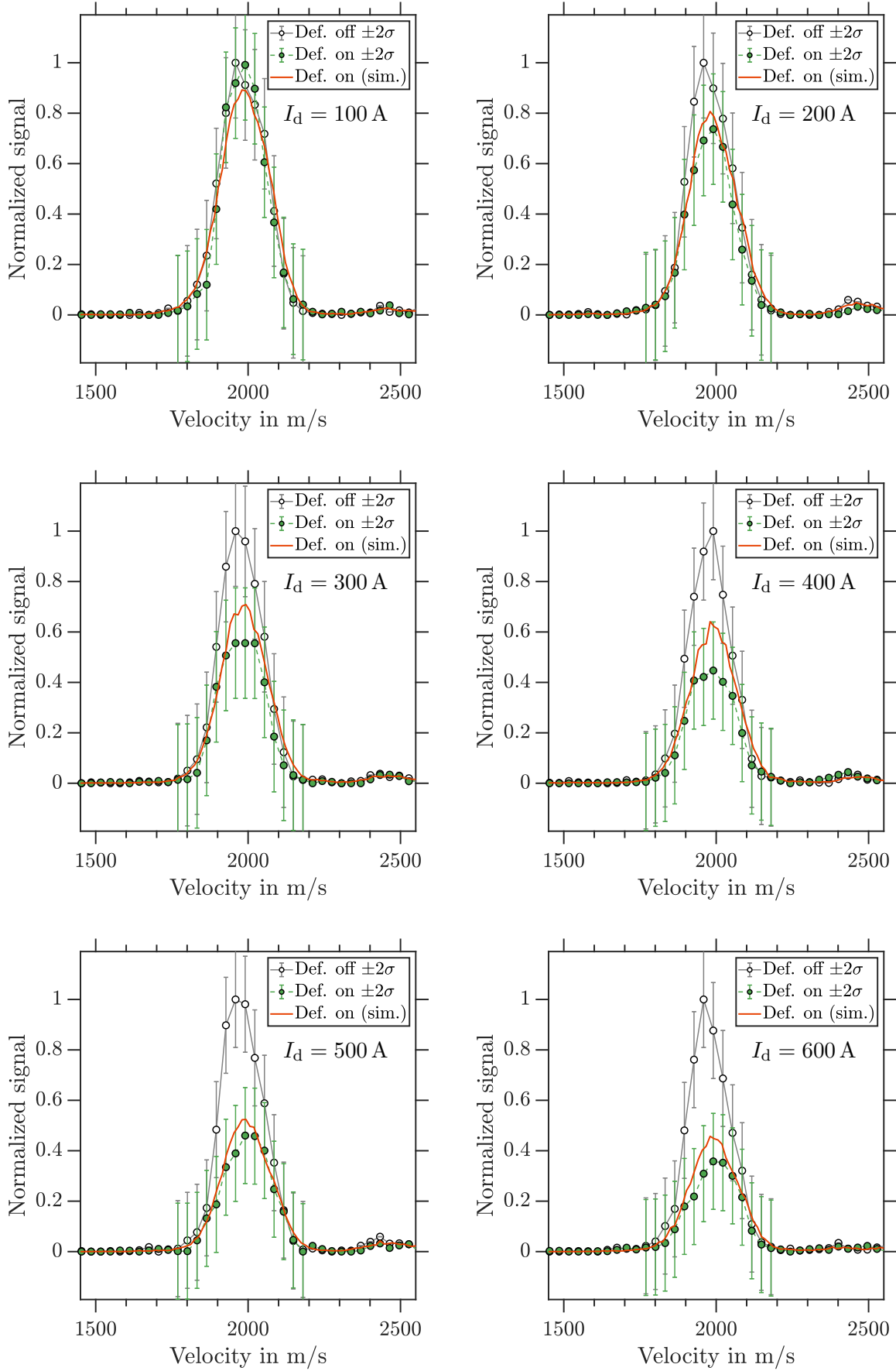


Fig. A.0.2: Photoion VMIs of NaH_2O for deflector ‘off’ and deflector ‘on’ measurements at $100 \text{ A} \leq I_d \leq 600 \text{ A}$ and $\Delta t_{\text{L-EL}} = 0.70 \text{ ms}$. The corresponding simulations for $m_S = \pm 1/2$ are shown as red traces.

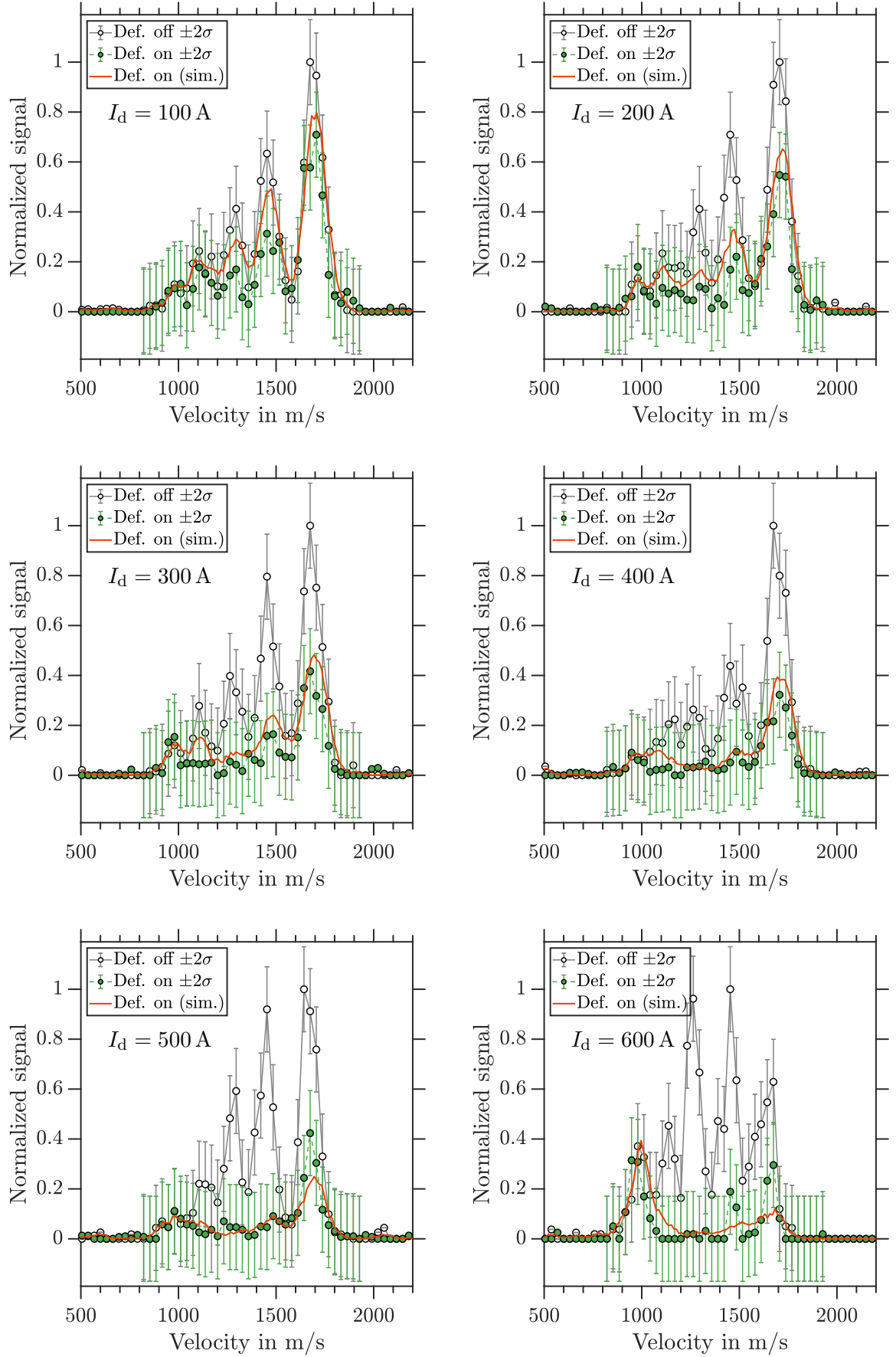


Fig. A.0.3: Photoion VMIs of NaH₂O for deflector ‘off’ and deflector ‘on’ measurements at $100 \text{ A} \leq I_d \leq 600 \text{ A}$ and $\Delta t_{L-EL} = 1.30 \text{ ms}$. The corresponding simulations for $m_S = \pm 1/2$ are shown as red traces.

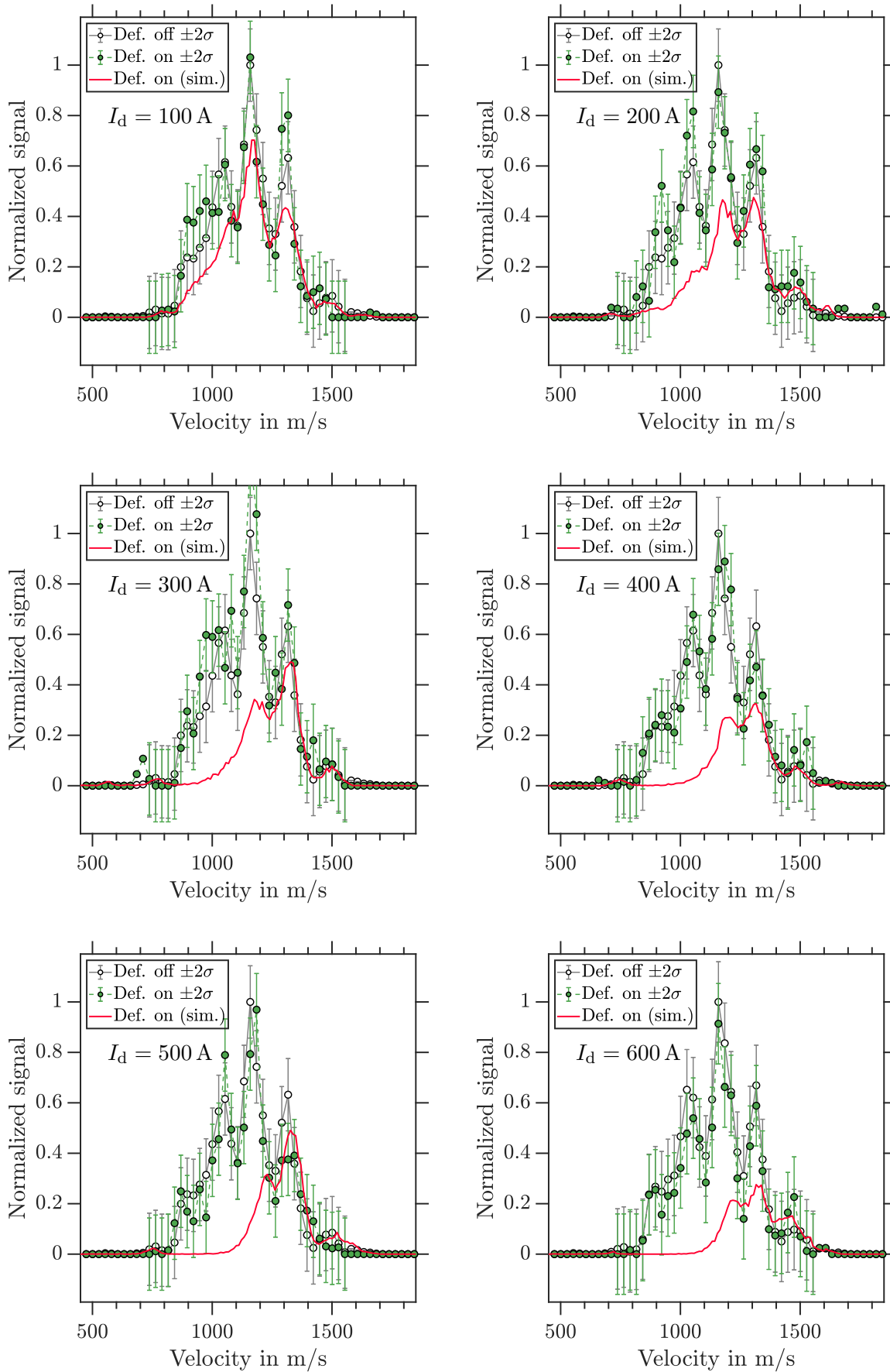


Fig. A.0.4: Photoion VMIs of Na(H₂O)₂ for deflector ‘off’ and deflector ‘on’ measurements at $100 \text{ A} \leq I_d \leq 600 \text{ A}$. The corresponding simulations for $m_S = \pm 1/2$ are shown as red traces.

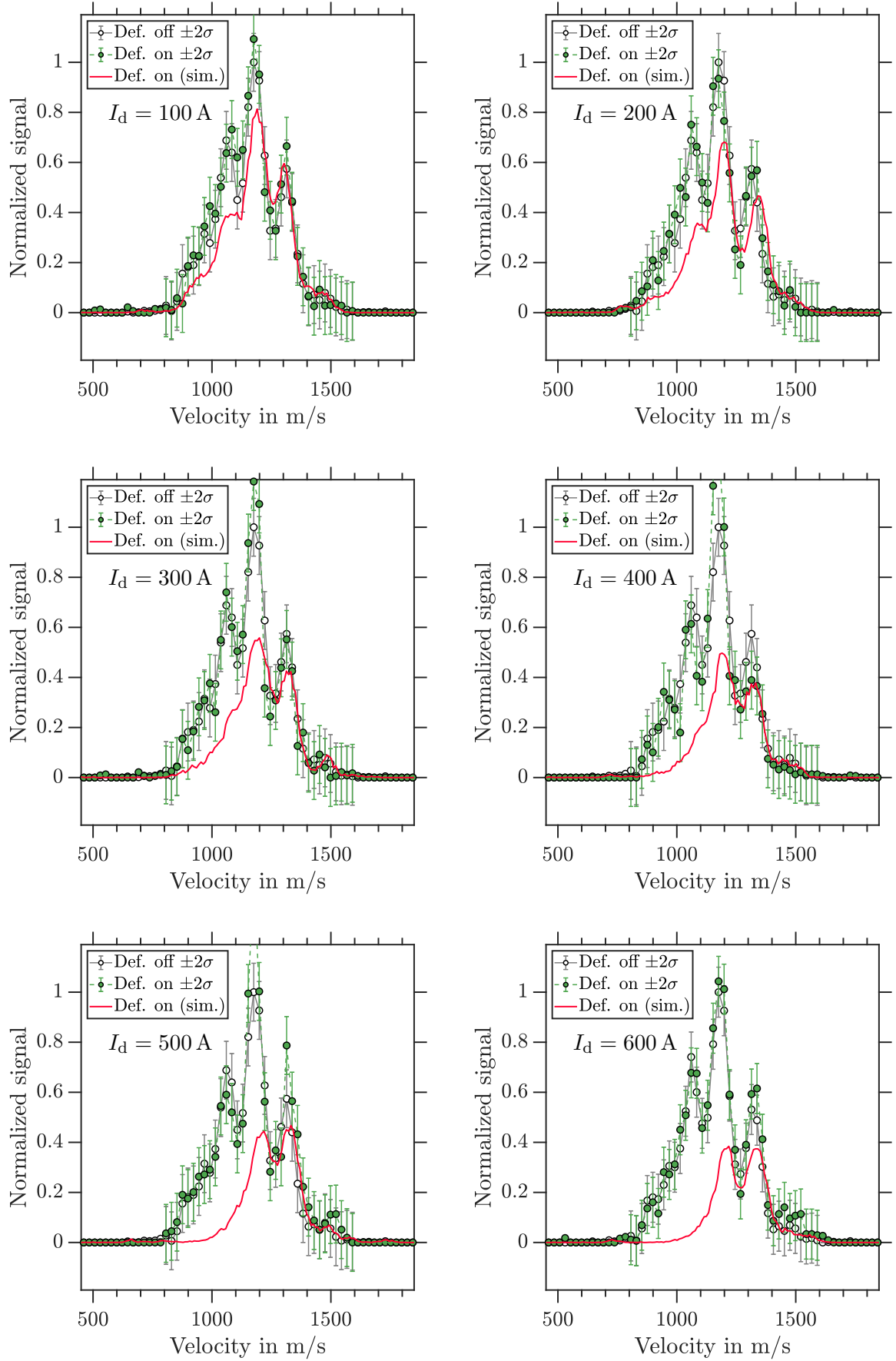


Fig. A.0.5: Photoion VMIs of $\text{Na}(\text{H}_2\text{O})_3$ for deflector ‘off’ and deflector ‘on’ measurements at $100 \text{ A} \leq I_d \leq 600 \text{ A}$. The corresponding simulations for $m_S = \pm 1/2$ are shown as red traces.

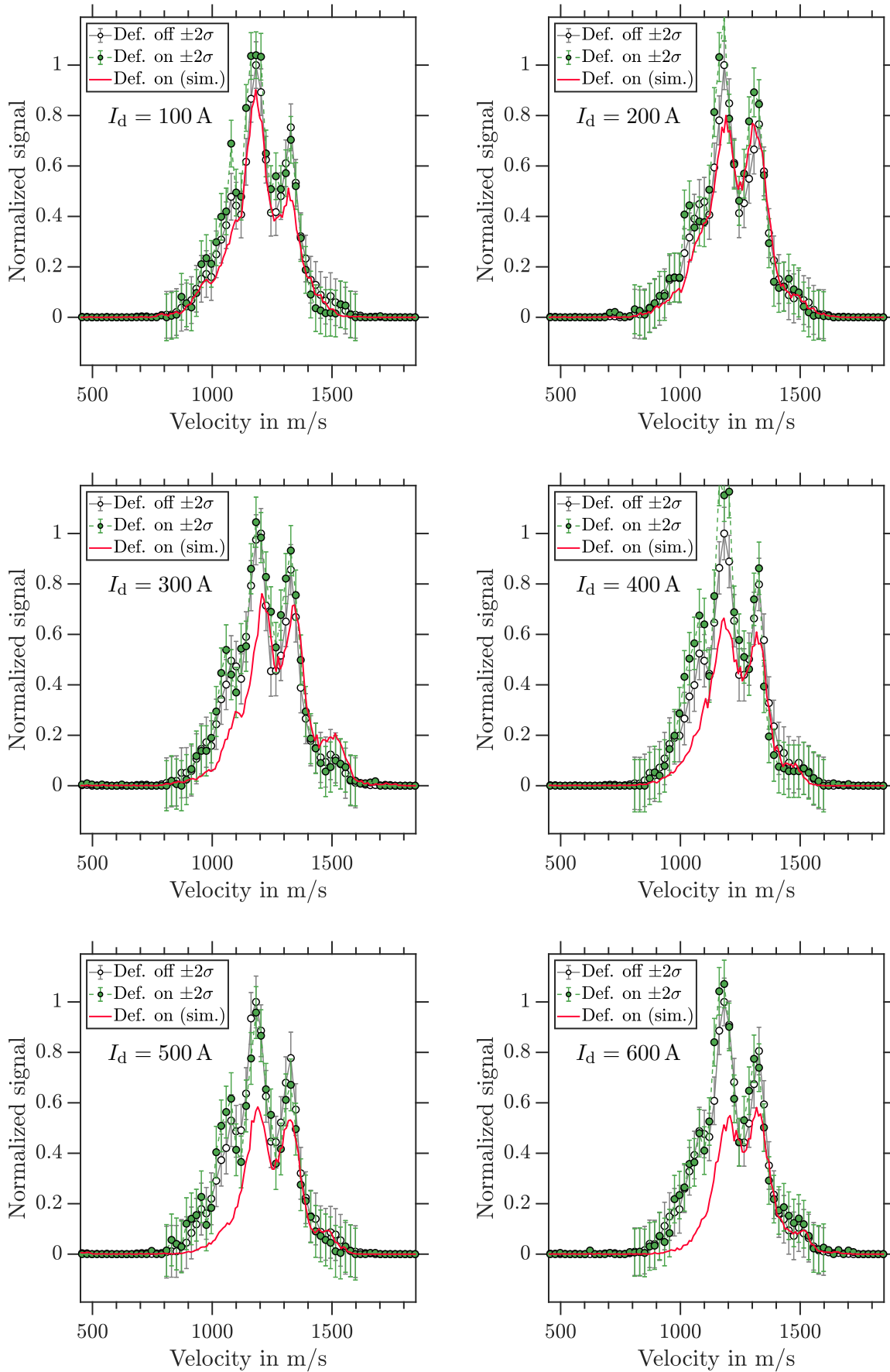


Fig. A.0.6: Photoion VMIs of $\text{Na}(\text{H}_2\text{O})_4$ for deflector ‘off’ and deflector ‘on’ measurements at $100 \text{ A} \leq I_d \leq 600 \text{ A}$. The corresponding simulations for $m_S = \pm 1/2$ are shown as red traces.

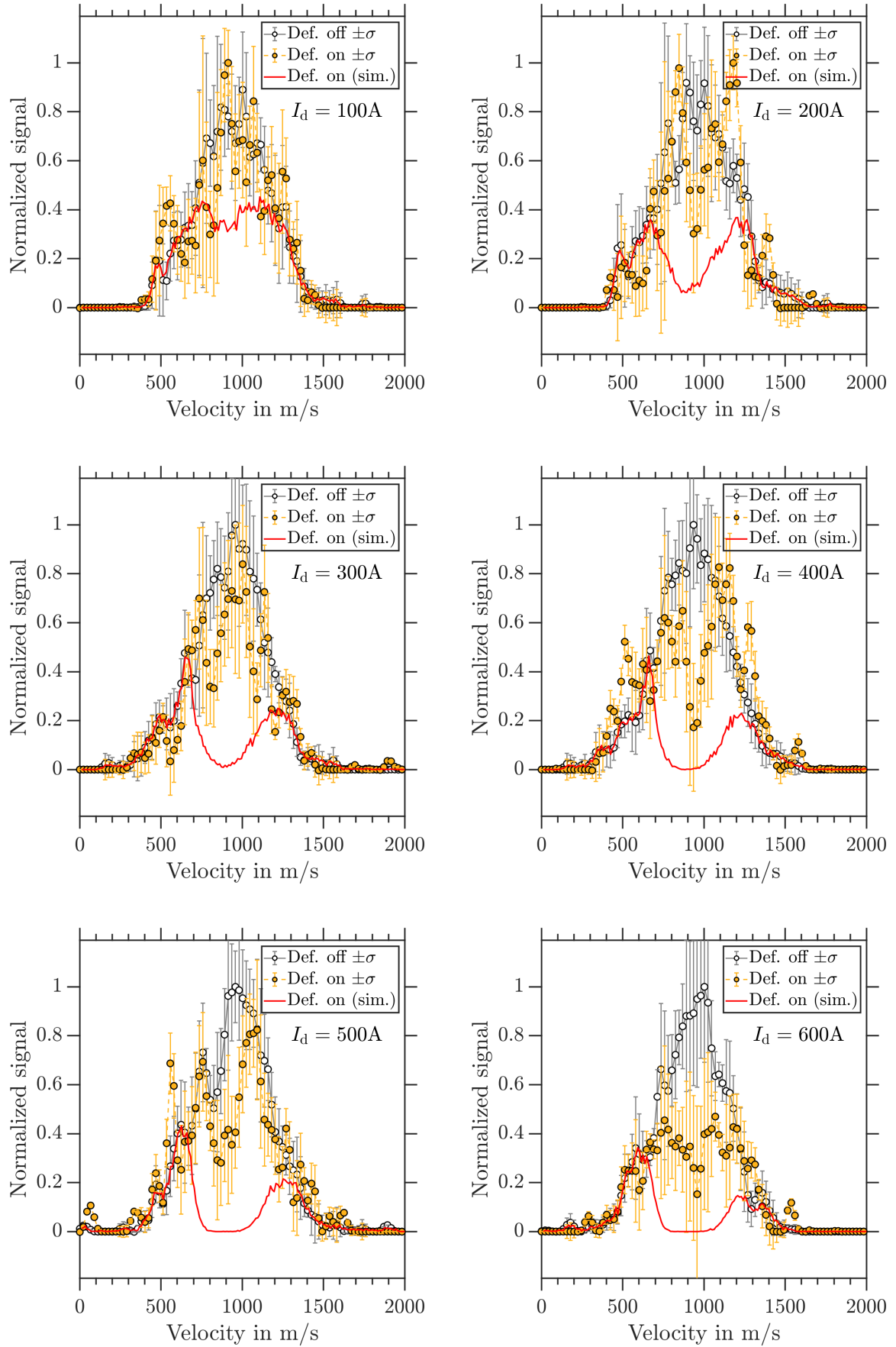


Fig. A.0.7: Photoion VMIs of NaMeOH for deflector ‘off’ and deflector ‘on’ measurements at $100\text{A} \leq I_d \leq 600\text{A}$. The corresponding simulations for $m_S = \pm 1/2$ are shown as red traces.

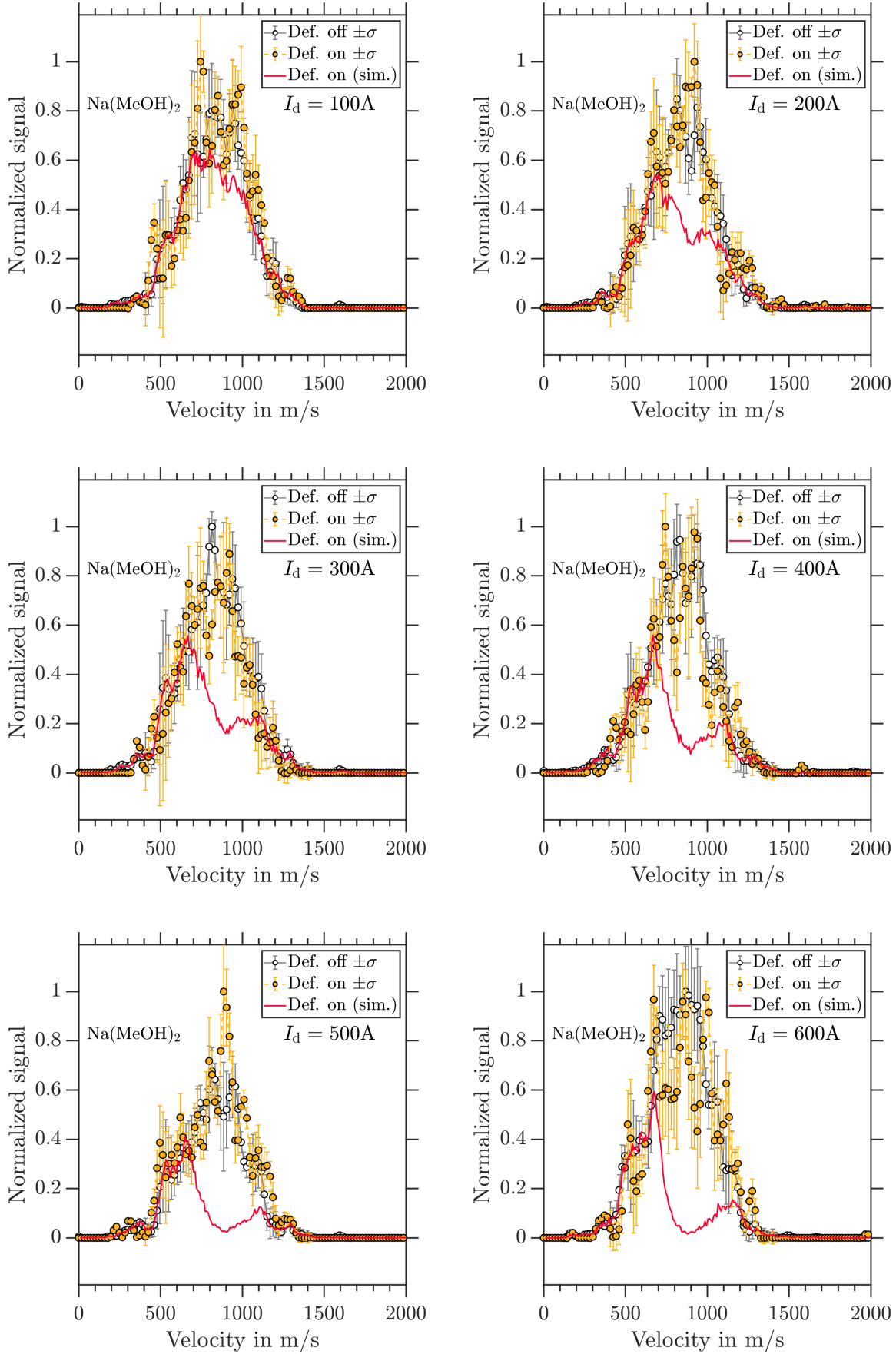


Fig. A.0.8: Photoion VMIs of $\text{Na}(\text{MeOH})_2$ for deflector ‘off’ and deflector ‘on’ measurements at $100\text{A} \leq I_d \leq 600\text{A}$. The corresponding simulations for $m_S = \pm 1/2$ are shown as red traces.

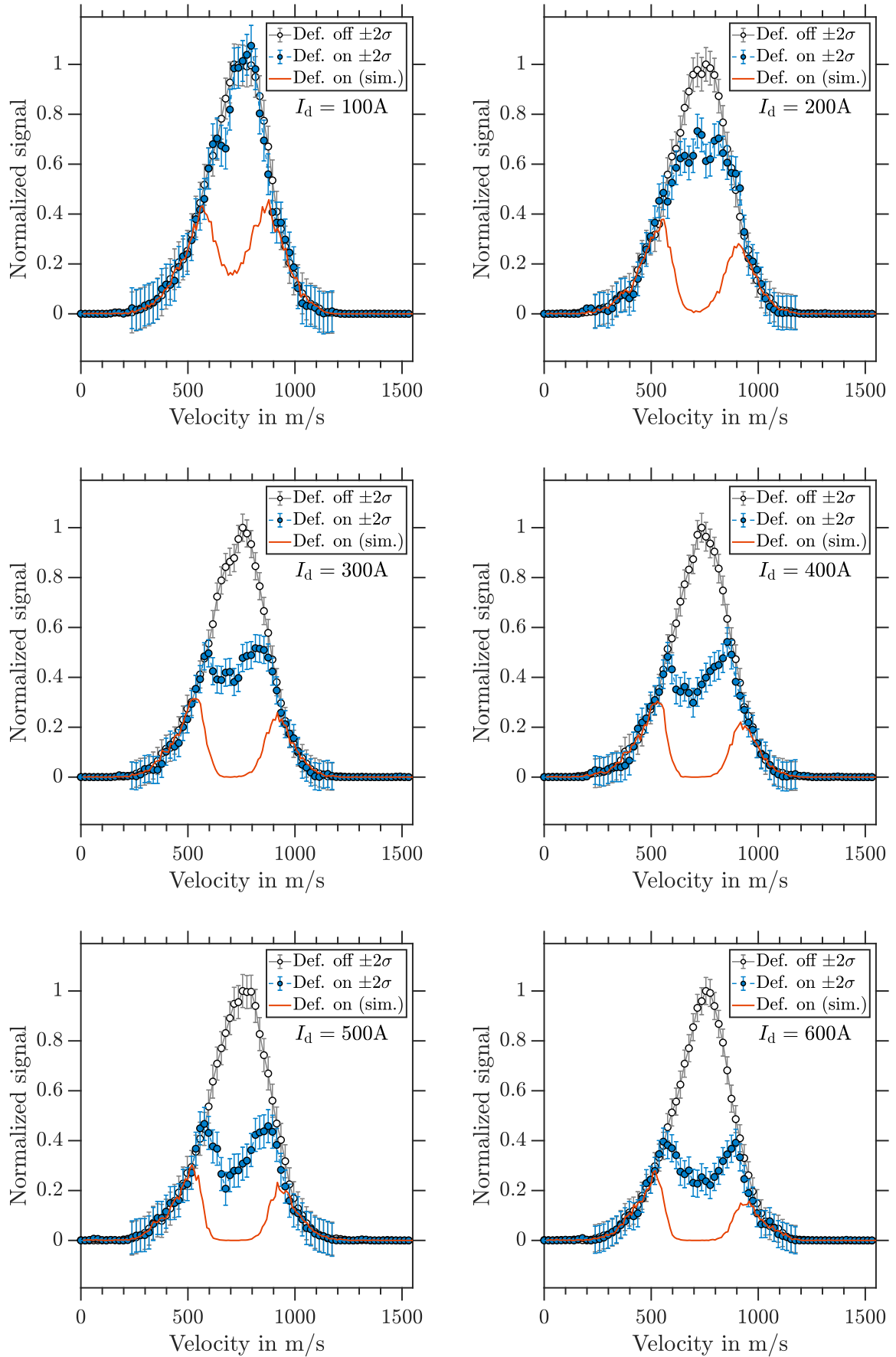


Fig. A.0.9: Photoion VMIs of NaDME for deflector ‘off’ and deflector ‘on’ measurements at $100\text{A} \leq I_d \leq 600\text{A}$. The corresponding simulations for $m_S = \pm 1/2$ are shown as red traces.

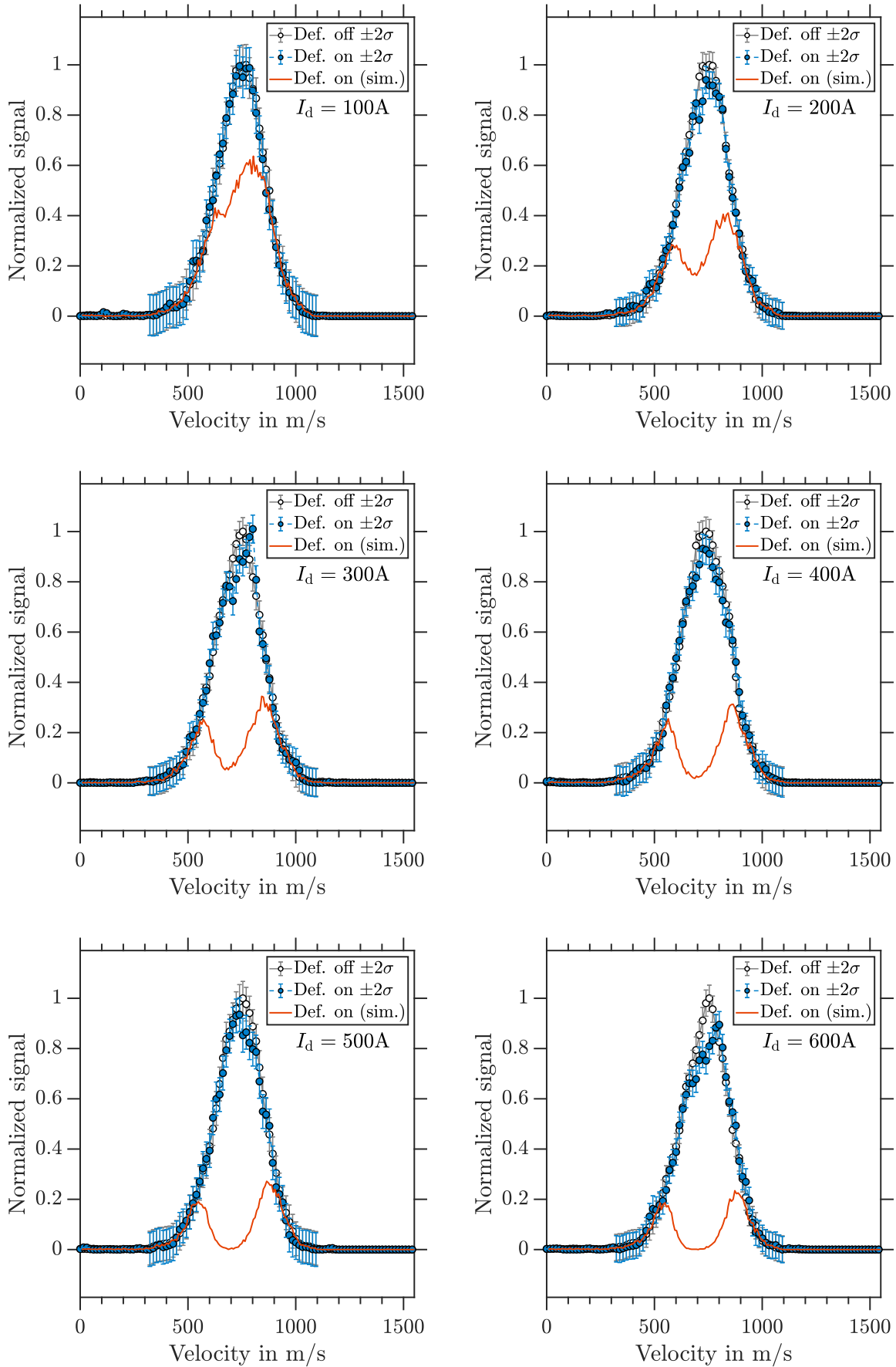


Fig. A.0.10: Photoion VMIs of $\text{Na}(\text{DME})_2$ for deflector ‘off’ and deflector ‘on’ measurements at $100\text{ A} \leq I_d \leq 600\text{ A}$. The corresponding simulations for $m_S = \pm 1/2$ are shown as red traces.

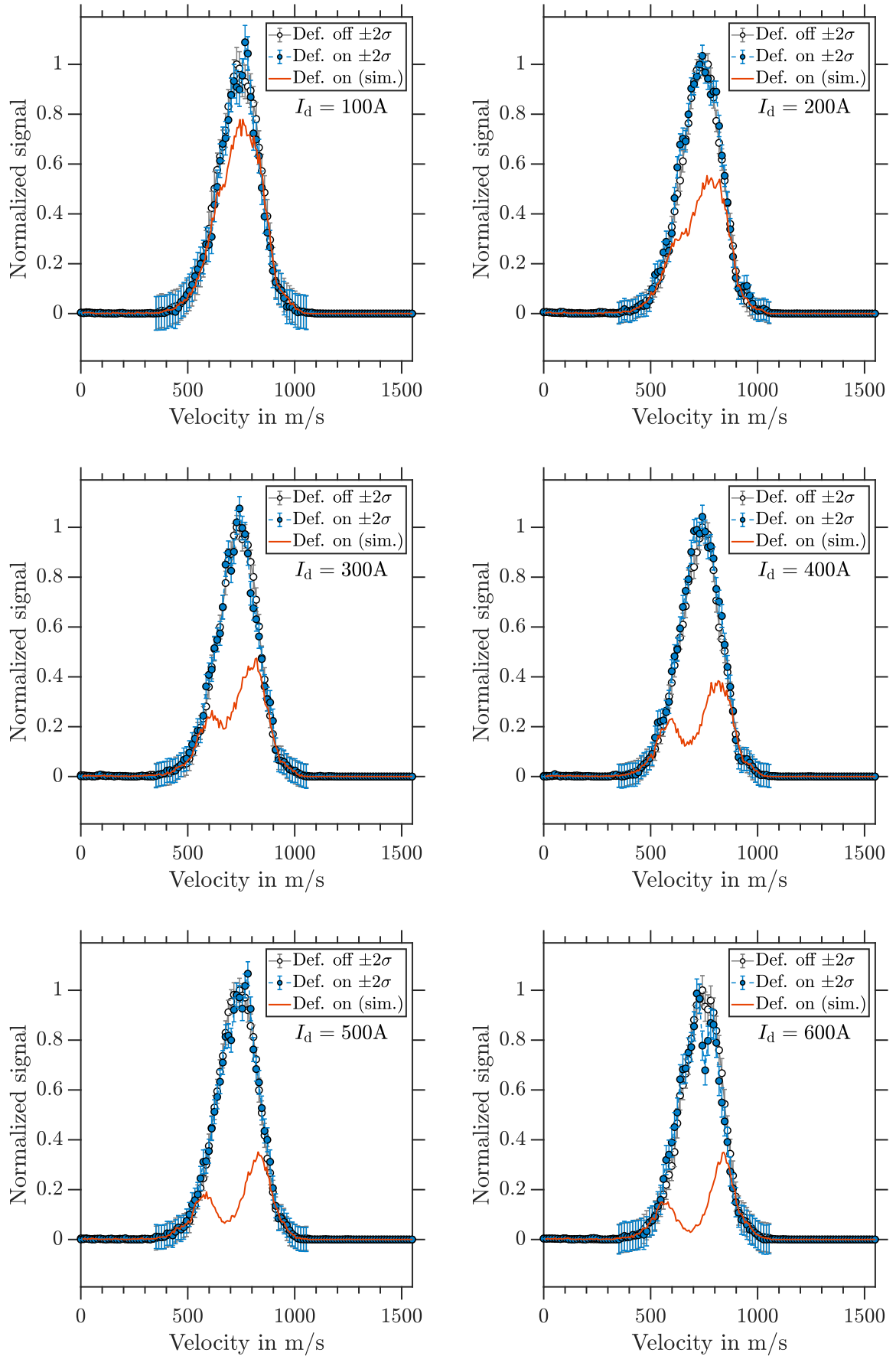


Fig. A.0.11: Photoion VMIs of Na(DME)₃ for deflector ‘off’ and deflector ‘on’ measurements at $100 \text{ A} \leq I_d \leq 600 \text{ A}$. The corresponding simulations for $m_S = \pm 1/2$ are shown as red traces.

Appendix B

Quantum chemical calculations

B.1 Cluster structures

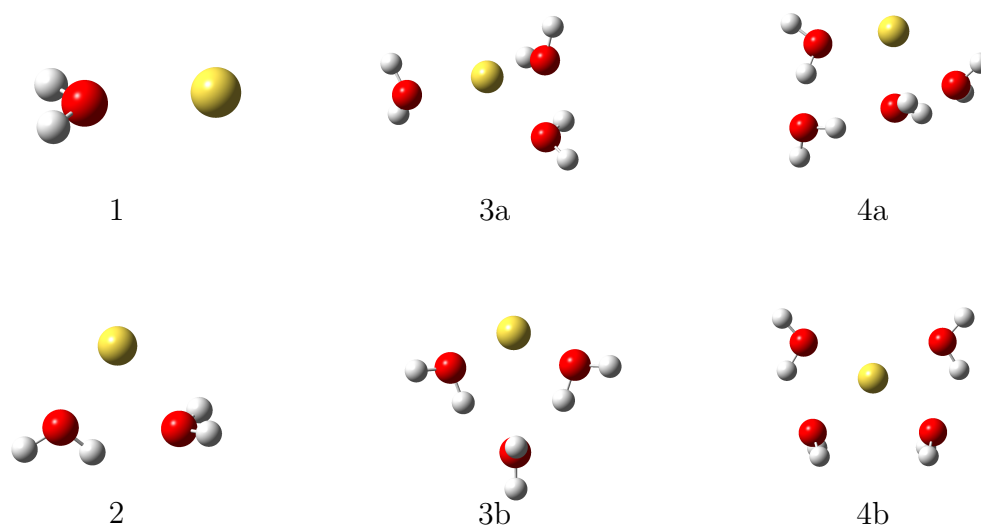


Fig. B.1.1: DFT optimized (ω B97XD/6-31+G^{*}) cluster structures of $\text{Na}(\text{H}_2\text{O})_n$.

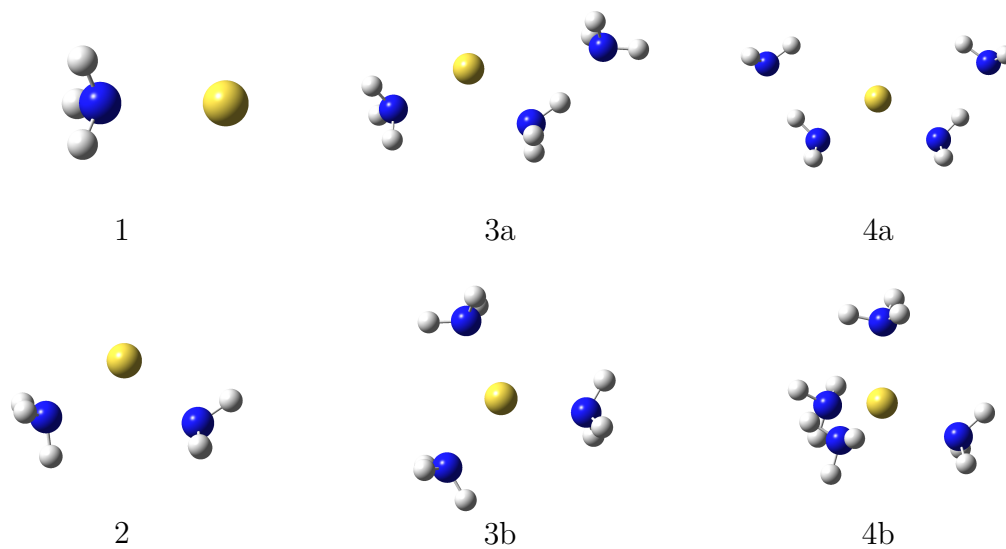


Fig. B.1.2: DFT optimized ($\omega\text{B97XD}/6\text{-}31+\text{G}^*$) cluster structures of $\text{Na}(\text{NH}_3)_n$.

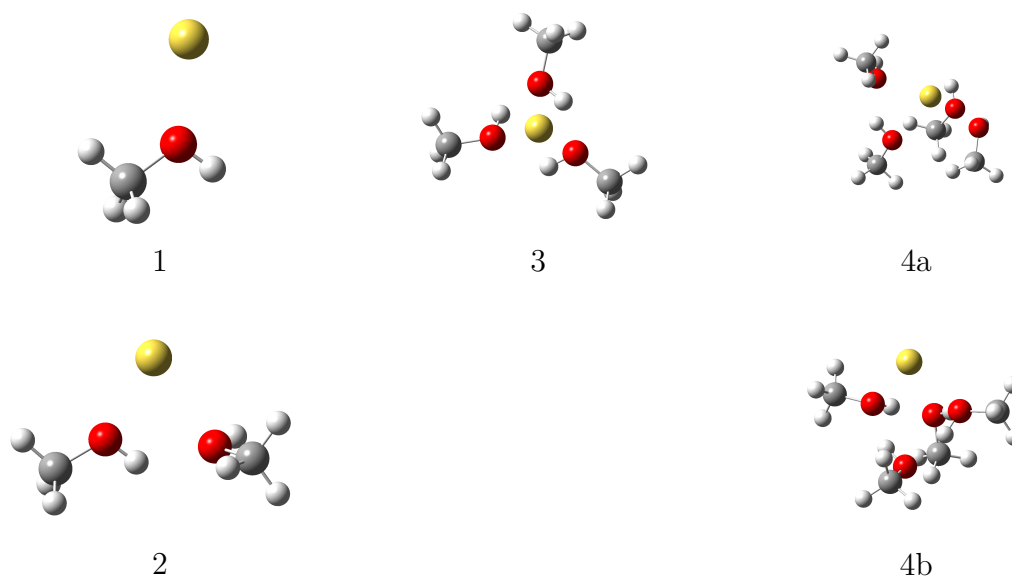


Fig. B.1.3: DFT optimized ($\omega\text{B97XD}/6\text{-}31+\text{G}^*$) cluster structures of $\text{Na}(\text{MeOH})_n$.

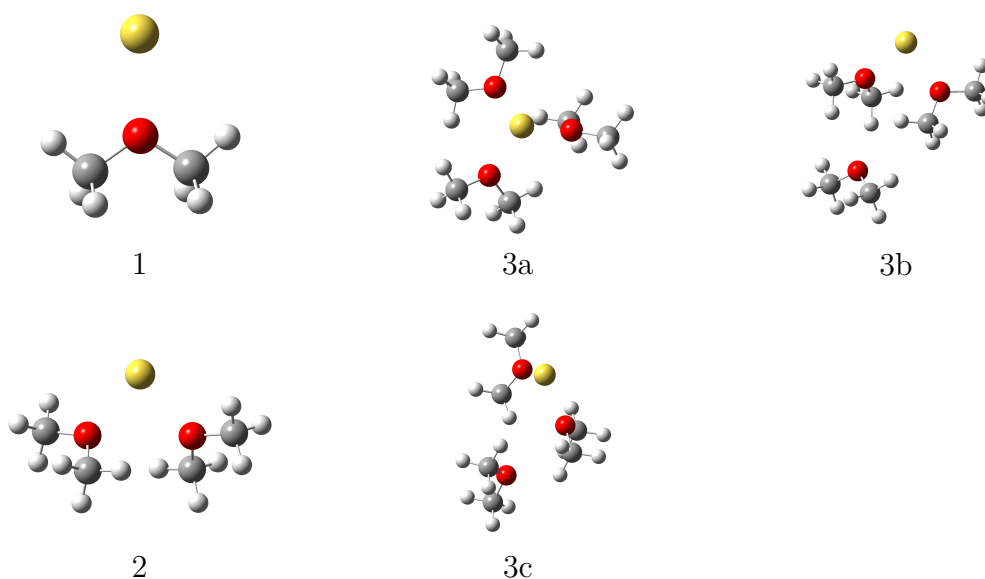


Fig. B.1.4: DFT optimized (ω B97XD/6-31+G^{*}) cluster structures of Na(DME)_n.

B.2 Harmonic frequency calculations

Tab. B.2.1: Harmonic vibrational frequencies $\tilde{\nu}_i$ (ω B97XD/6-31+G^{*}) of Na(H₂O)_n clusters, all frequencies are given in cm⁻¹.

i	$\tilde{\nu}_i(1)$	$\tilde{\nu}_i(2)$	$\tilde{\nu}_i(3a)$	$\tilde{\nu}_i(3b)$	$\tilde{\nu}_i(4a)$	$\tilde{\nu}_i(4b)$
1	45	90	22	71	40	14
2	209	97	26	89	44	47
3	256	183	100	152	77	53
4	1683	186	117	206	101	122
5	3780	231	147	207	130	124
6	3908	309	188	220	169	133
7		338	196	225	205	145
8		407	226	250	235	202
9		511	274	268	243	209
10		1655	287	315	251	211
11		1689	341	347	261	215
12		3696	382	456	275	251
13		3751	398	471	294	290
14		3819	431	691	333	350

15	3925	552	700	368	415
16		1650	1658	418	427
17		1678	1702	448	434
18		1682	1730	496	437
19		3592	3522	696	462
20		3700	3670	756	545
21		3716	3688	848	566
22		3728	3840	1630	1625
23		3838	3874	1685	1645
24		3924	3875	1712	1676
25				1737	1680
26				3473	3504
27				3506	3566
28				3610	3607
29				3645	3630
30				3739	3717
31				3835	3720
32				3911	3929
33				3918	3929

Tab. B.2.2: Harmonic vibrational frequencies $\tilde{\nu}_i$ (ω B97XD/6-31+G*) of $\text{Na}(\text{NH}_3)_n$ clusters, all frequencies are given in cm^{-1} .

i	$\tilde{\nu}_i(1)$	$\tilde{\nu}_i(2)$	$\tilde{\nu}_i(3a)$	$\tilde{\nu}_i(3b)$	$\tilde{\nu}_i(4a)$	$\tilde{\nu}_i(4b)$
1	231	20	17	14	13	16
2	322	31	28	17	16	17
3	323	41	37	20	26	24
4	1199	214	44	31	38	29
5	1716	230	52	33	40	30
6	3482	265	179	39	59	40
7	3622	268	203	188	62	43

8	3623	329	216	244	161	48
9		374	235	247	180	53
10		1188	258	273	203	188
11		1192	305	279	215	239
12		1708	312	305	218	249
13		1710	331	330	235	257
14		1716	395	366	281	270
15		1717	564	370	290	270
16		3473	1168	1198	295	306
17		3474	1187	1199	299	307
18		3616	1249	1200	371	318
19		3616	1708	1704	385	320
20		3619	1710	1704	556	380
21		3620	1712	1705	603	381
22			1717	1710	1168	1196
23			1719	1711	1170	1212
24			1767	1712	1250	1212
25			3367	3450	1252	1217
26			3478	3450	1702	1697
27			3492	3459	1703	1697
28			3558	3594	1712	1703
29			3619	3595	1716	1703
30			3626	3595	1716	1705
31			3626	3606	1719	1705
32			3628	3606	1764	1718
33			3639	3608	1766	1718
34					3365	3410
35					3369	3412
36					3466	3430
37					3469	3488

38	3563	3555
39	3564	3558
40	3601	3558
41	3602	3584
42	3631	3584
43	3631	3587
44	3639	3627
45	3639	3628

Tab. B.2.3: Harmonic vibrational frequencies $\tilde{\nu}_i$ (ω B97XD/6-31+G*) of Na(MeOH)_n clusters, all frequencies are given in cm⁻¹.

i	$\tilde{\nu}_i(1)$	$\tilde{\nu}_i(2)$	$\tilde{\nu}_i(3)$	$\tilde{\nu}_i(4a)$	$\tilde{\nu}_i(4b)$
1	57	40	53	19	42
2	99	44	53	49	47
3	190	66	60	51	61
4	329	88	70	58	71
5	1075	103	77	70	79
6	1100	119	90	84	84
7	1189	125	91	88	93
8	1388	205	113	95	96
9	1504	229	128	98	109
10	1527	393	136	106	114
11	1537	606	154	112	116
12	3063	1070	204	130	121
13	3137	1096	204	135	130
14	3183	1109	205	147	137
15	3835	1131	235	152	162
16		1189	616	162	171
17		1194	620	187	199
18		1371	746	207	222
19		1411	1092	237	235

20	1499	1092	242	264
21	1507	1113	247	287
22	1527	1125	481	743
23	1535	1126	502	785
24	1538	1166	647	910
25	3052	1194	688	930
26	3063	1195	1070	1086
27	3119	1195	1075	1092
28	3140	1405	1100	1096
29	3178	1407	1106	1105
30	3182	1438	1111	1140
31	3749	1504	1114	1150
32	3777	1504	1135	1169

33		1512	1143	1184
34		1528	1187	1196
35		1528	1191	1197
36		1535	1195	1197
37		1537	1198	1203
38		3057	1377	1447
39		3057	1392	1456
40		3059	1431	1493
41		3128	1440	1501
42		3129	1492	1502
43		3130	1493	1503
44		3181	1505	1515
45		3181	1509	1526
46		3182	1519	1528
47		3679	1524	1529
48		3705	1528	1533
49		3707	1533	1540

50			1536	1544
----	--	--	------	------

51	1538	1549
52	1541	1558
53	1554	3048
54	3045	3050
55	3046	3056
56	3054	3058
57	3063	3119
58	3111	3120
59	3111	3131
60	3130	3131
61	3138	3170
62	3157	3171
63	3169	3175
64	3173	3180
65	3179	3391
66	3458	3449
67	3587	3583
68	3677	3608
69	3734	3717

Tab. B.2.4: Harmonic vibrational frequencies $\tilde{\nu}_i$ (ω B97XD/6-31+G*) of $\text{Na}(\text{DME})_n$ clusters, all frequencies are given in cm^{-1} .

i	$\tilde{\nu}_i(1)$	$\tilde{\nu}_i(2)$	$\tilde{\nu}_i(3a)$	$\tilde{\nu}_i(3b)$	$\tilde{\nu}_i(3c)$
1	69	43	14	30	15
2	85	48	20	34	24
3	158	59	38	38	34
4	196	66	40	54	40
5	262	97	49	63	53
6	433	112	67	67	65
7	960	112	74	72	69
8	1141	155	76	90	75

9	1179	171	93	99	85
10	1213	206	99	103	105
11	1225	208	109	114	111
12	1292	270	124	140	134
13	1485	272	150	150	142
14	1510	433	164	176	146
15	1519	437	178	181	176
16	1524	961	195	217	204
17	1525	966	207	221	218
18	1524	1142	214	238	236
19	3033	1142	264	276	262
20	3038	1181	269	293	282
21	3100	1181	273	315	292
22	3106	1214	431	430	431
23	3163	1214	435	440	436
24	3165	1227	437	441	441

25		1228	963	960	963
26		1292	964	967	968
27		1292	970	971	973
28		1482	1142	1143	1144
29		1485	1142	1144	1146
30		1509	1143	1145	1147
31		1512	1180	1181	1181
32		1515	1181	1182	1183
33		1518	1182	1182	1187
34		1522	1214	1214	1213
35		1523	1215	1215	1216
36		1526	1228	1217	1221
37		1530	1231	1222	1228
38		1538	1232	1226	1230
39		1541	1292	1238	1239

40	3026	1292	1286	1288
41	3027	1293	1291	1293
42	3032	1481	1297	1297
43	3034	1482	1479	1483
44	3090	1484	1485	1484
45	3091	1506	1488	1489
46	3099	1509	1508	1510
47	3099	1510	1513	1510
48	3171	1513	1514	1513
49	3171	1514	1515	1519
50	3178	1515	1518	1521
51	3179	1520	1521	1522

52		1522	1524	1523
53		1522	1525	1525
54		1526	1526	1526
55		1529	1529	1530
56		1531	1531	1536
57		1536	1537	1540
58		1538	1540	1543
59		1542	1543	1552
60		3018	1549	3013
61		3022	3009	3021
62		3024	3018	3022
63		3026	3024	3030
64		3029	3031	3030
65		3030	3034	3037
66		3078	3041	3071
67		3087	3067	3078
68		3088	3075	3083
69		3091	3086	3094
70		3095	3097	3102

71	3097	3106	3107
72	3162	3112	3160
73	3163	3160	3165
74	3164	3161	3166
75	3182	3165	3169
76	3182	3168	3169
77	3185	3179	3188
78	3197	3194	3192

Jonathan Barnes

Curriculum Vitae

Stauffacherstrasse 96
8004 Zürich

+41(0)78 660 00 41

✉ jonathan_barnes@web.de

Personal Data

Name Jonathan Vinzent Barnes
Date of birth 31.08.1991
Place of birth Bad Tölz

Education

04/2018 – 12/2022 **Doctoral Studies: Physical Chemistry, ETH Zürich, Switzerland**
Degree: Dr. Sc. Physical Chemistry

10/2014 – 05/2017 **Master Studies: Chemistry, Universität Leipzig, Germany**
Degree: M.Sc. Chemistry

10/2011 – 07/2014 **Bachelor Studies: Chemistry, Universität Leipzig, Germany**
Degree: B.Sc. Chemistry

09/2006 – 07/2011 **School: Gymnasium, Klenze-Gymnasium München, Germany**
Degree: Abitur

09/2003 – 07/2006 **School: Gymnasium, Gabriel-von-Seidl-Gymnasium Bad Tölz, Germany**

Theses

Doctoral Theses *Magnetic and electronic properties of solvated electron precursor systems*
Supervision Prof. Ruth Signorell

Master Theses *Infrarot Laserspektroskopie an Isomer selektierten $D^+(D_2O)_6$ Gasphasenclustern*
Supervision Prof. Knut Asmis

Bachelor Theses *Photoelektronenspektroskopie an $Ge_2Sb_2Te_5$ und $Ge_2Bi_2Te_5$ Einkristallen*
Supervision Prof. Oliver Oeckler

Language Skills

German **native**
English **native**

Conference ontributions

Clustertreffen
2022 Herzogenhorn Germany, oral presentation

EGAS 2021 Online, poster presentation

Bunsentagung
2021 Online, poster presentation

S3C 2020 Davos Switzerland, poster presentation

SCS 2019 Zürich Switzerland, poster presentation

PTPC 2019 Beatenberg Switzerland, oral presentation

Publication List

2021 J. V. Barnes, M. Beck, S. Hartweg, A. Luski,
B. L. Yoder, J. Narevicius, E. Narevicius and R. Signorell,
Magnetic deflection of neutral sodium-doped ammonia cluster
Phys. Chem. Phys. 2021, **23**, 846. DOI: 10.1039/D0CP04647G

2019 J. V. Barnes, B. L. Yoder and R. Signorell, *Magic numbers for the
photoelectron anisotropy in Li-doped dimethyl ether clusters*,
J. Phys. Chem. A 2019, **12**, 2379. DOI: 10.1021/acs.jpca.8b12262